Crystal-scale records of the Gakkel Ridge magma plumbing system

Emma N. Bennett

School of Earth and Ocean Sciences

Cardiff University

Submitted in partial fulfilment of the requirements for the degree of:

Doctor of Philosophy (PhD)

June 2019

Declaration

This is work has not previously been accepted in substance for any degree and is not concurrently submitted in candidature for any degree.

Signed…… (candidate) Date……..

Statement 1

This thesis is being submitted in partial fulfilment of the requirements for the degree of Doctor of Philosophy (PhD).

Signed…… (candidate) Date……..

Statement 2

This thesis is a result of my own independent work and investigation, except where otherwise stated, and the thesis has not been edited by a third party beyond what is permitted by Cardiff University's policy on the Use of Third Party Editors by Research Degree Students. Other sources are acknowledged by explicit references. Views expressed here are my own.

Signed…… (candidate) Date……..

Statement 3

I hereby give consent for my thesis, if accepted, to be available online in the University's Open Access repository and for inter library loan, and for the title and summary to be made available to outside organisations.

Signed…… (candidate) Date……..

Statement 4

I hereby give consent for my thesis, if accepted, to be available online in the University's Open Access repository and for inter library loan, and for the title and summary to be made available to outside organisations after expiry of a bar on access previously approved by the Graduate Development Committee.

Signed…… (candidate) Date……..

Acknowledgements

First and foremost, I would like to thank both my supervisors, Johan Lissenberg and Kathy Cashman. Not only have you both provided me with a wealth of knowledge and expertise, you have been a constant source of inspiration and encouragement throughout the entirety of my PhD. I would like to think that over the years I have grown as a person and a scientist, and I owe no small part of that transformation to the confidence that you have both given me. I feel incredibly lucky and privileged to have worked with you both.

I would also like to thank Tony Oldroyd and Duncan Muir from Cardiff University, Andy Milton from the National Oceanography Centre and Cees-Jan De Hoog from the NERC Ion Microprobe facility for your guidance and expertise during sample preparation and analysis.

Of the PhD students, many of whom have become close friends over the last four years, Andrew Martin (A) and Bianca Kennedy (B) deserve special mention. There are no words that could possibly convey how important you both have been to me over the last four years, suffice to say that you have been the most amazing and supportive friends and have helped make doing a PhD an enjoyable and unforgettable experience.

Finally, I would like to thank my family. You always believed in me even when I didn't believe in myself, and without your continued support and encouragement over the last four years and beyond I would not be where I am today.

Abstract

The global mid-ocean ridge system is the most significant magmatic system on our planet and is the site of 75% of Earth's volcanism. Whilst mid-ocean ridges have been studied for decades, ultraslow-spreading ridges, such as the Gakkel Ridge have received comparably little attention. These ultraslow-spreading ridges are important because, in addition to representing a spreading ridge end-member, they are also volumetrically significant, with ridges exhibiting ultraslow-spreading characteristics making up ~36% of the global mid-ocean ridge system. Despite this, we have very few constraints on the physical nature of the underlying magma plumbing systems or the magmatic processes occurring within them. In order to address this knowledge gap, this thesis presents the first systematic and quantitative analysis of crystal cargo textures and compositions of ultraslow-spreading mid-ocean ridge basalt (Gakkel Ridge, Arctic Ocean). These data are used to infer the physiochemical conditions present within the Gakkel Ridge magma plumbing system.

Using the textures and compositions of >1800 plagioclase crystals, the Gakkel Ridge crystal cargo is shown to be complex, with both individual plagioclase and glomerocrysts showing large variations in crystal habit, zoning and resorption. These textures, in combination with basalt modal crystal contents indicate that the crystal cargo is not generally phenocrystic in origin, and that the processes of undercooling, magma mixing, decompression and mush disaggregation are important processes occurring within the Gakkel Ridge magma plumbing system. Furthermore, the observed relationship between melt inclusion morphologies and specific host crystal textures suggests a link between plagioclase crystallisation processes and melt inclusion entrapment.

To constrain the depths of crystallisation within the Gakkel Ridge magma plumbing system, volatile contents of olivine- and plagioclase-hosted melt inclusions have been determined. The volatile contents of (complexly zoned) plagioclase-hosted melt inclusions correspond to significantly higher crystallisation pressures (mean 270 MPa) than (simply zoned) olivine-hosted melt inclusions (mean 145 MPa). The higher pressures recorded in plagioclase-hosted inclusions, which correspond to crystallisation as deep as 16.4 km below the seafloor, are consistent with both the proposed thickness of the Gakkel Ridge lithosphere and pressures reconstructed from glass compositions. Contrary to previous studies using olivine-hosted melt inclusions alone, these results demonstrate that mid-ocean ridge volcanoes, at least at ultraslow-spreading ridges, have magmatic roots deep in the lithospheric mantle. The observed dichotomy in pressure recorded in olivine vs. plagioclase indicates that a multi-mineral melt inclusion approach is required to constrain the full range of crystallisation depths present in magmatic systems.

Examination of along axis changes in mineral textures, mineral and melt geochemistry, melt inclusion crystallisation pressures, crystal content and ridge bathymetry demonstrates that the nature of the plumbing system and processes occurring within it are variable. For example, magma plumbing systems may be vertically extensive (i.e., trans-lithospheric) and be characterised by both pervasive mush zones and localised melt-rich regions, whilst in some regions well-developed magma plumbing systems may be entirely absent; here aphyric primitive basalts are erupted from depth having undergone minimal compositional modification. There are no systematic changes with decreasing spreading rate along-axis. Instead, both variations in the extent of partial melting and the degree of melt focussing along the base of the lithosphere play a key role in influencing the nature of magma plumbing systems at the Gakkel Ridge. Despite this, crystal content and glass geochemistry correlate with spreading rate at the global scale.

Abstract

Taken together, this thesis builds on our growing understanding of the complexity of processes occurring within mid-ocean ridge magmatic systems. It demonstrates that, contrary to the often-held view that mid-ocean ridges are nominally simple and have shallow magma plumbing systems, the observed textural and compositional complexity and crystallisation depths attest to the presence of vertically extensive plumbing systems within which complex magmatic processes occur.

Table of contents

Page Number

Declaration……..*i*
Acknowledgements ……..…..*iii*
Abstract ……..*v*
Table of contents ……....*vii*
Figure list ……..….*x*
Table list……...……...*xiii*

Chapter 1: Introduction……1
1.1 The global mid-ocean ridge system……..……2
1.2 Why study ultraslow-spreading mid-ocean ridges?.....3
1.3 Crystal-scale records of mid-ocean ridge plumbing systems……..……3
1.3.1 Mineral textures and compositions……..……..3
1.3.2 Melt inclusions……..……..……5
1.4 Aims……..……..5
1.5 Thesis structure……6

Chapter 2: The Gakkel Ridge……..……7
2.1 Location ……..…8
2.2 Current understanding of the Gakkel Ridge.....9
2.2.1 Tectono-magmatic segmentation……..…..……..…9
2.2.1.1 Western Volcanic Zone (WVZ)……..……..…..9
2.2.1.2 Sparsely Magmatic Zone (SMZ)……..……..……11
2.2.1.3 Eastern Volcanic Zoe (EVZ)……..……..11
2.2.2 Formation of the Gakkel Ridge ……..……..……14
2.2.3 Structure of the Gakkel Ridge lithosphere ……..……..…15
2.2.3.1 Crustal thickness and structure……..……..…16
2.2.3.2 Lithospheric thickness and structure…..……..……19
2.2.4 Melt focussing at ultraslow-spreading ridges……..…..……..…22
2.2.5 Mantle heterogeneity……..……..……..…24
2.2.6 Crystal-scale insights into the Gakkel Ridge plumbing system……27
2.2.6.1 Plagioclase diffusion studies……..……..……...27
2.2.6.2 Crystallisation pressures: Olivine-hosted melt inclusions……..27
2.3 Summary……..……..…28

Chapter 3: Samples and analytical methods……..……..……..…29
3.1 Sampling……..……..…30
3.2 Sample preparation.....30
3.2.1 Polished slabs….....…30
3.2.2 Polished blocks….....33
3.3 Analytical SEM……..……..……..……33
3.3.1 Backscatter electron (BSE) image acquisition…….....……..33
3.3.2 Quantitative EDS analysis ……..……...33
3.3.3 Determination of modal mineralogy……..……..……..34

3.4 Plagioclase LA-ICP-MS……..34
3.5 Ion probe melt inclusion analysis……..36
3.5.1 Melt inclusion selection……..36
3.5.2 Instrumentation setup……36
3.5.3 Potential for carbon contamination……..37

Chapter 4: Crystal cargo database……39
4.1 Individual crystal and glomerocryst classification……40
4.1.1 Glomerocryst configuration and component contacts ……40
4.2 Crystal morphologies……42
4.2.1 Plagioclase……42
4.2.2 Olivine……42
4.3 Mineral zoning……42
4.3.1 Zoning complexity……44
4.4 Resorption……47
4.5 Melt inclusion habits……48
4.6 Attached and included components……48

Chapter 5: The significance of plagioclase textures in mid-ocean ridge basalt...51
5.1 Introduction……52
5.2 Controls on plagioclase crystallisation……53
5.3 Results……55
5.3.1 Crystal cargo inventory……55
5.3.2 Textural observations……57
5.3.2.1 Crystal habits ……57
5.3.2.2 Zoning ……58
5.3.2.3 Resorption ……62
5.3.2.4 Glomerocryst configuration and component contacts……64
5.3.3 Plagioclase major element compositions……64
5.3.4 Plagioclase-melt equilibria……66
5.3.5 Plagioclase TiO_2 contents……68
5.3.6 Juxtaposition of chemically and texturally distinct populations……68
5.4 Discussion……70
5.4.1 Significance of plagioclase texture……70
5.4.1.1 Skeletal growth: disequilibrium during undercooling……70
5.4.1.2 Resorption: recharge and decompression……71
5.4.1.3 Patchy zoning: infilling following skeletal growth and resorption...73
5.4.1.4 Glomerocrysts: mush fragments and synneusis……74
5.4.2 Melt inclusion entrapment……77
5.4.3 The origin of plagioclase crystal cargo……78
5.5 Synthesis……81

Chapter 6: Deep roots for mid-ocean ridge volcanoes revealed by plagioclase-hosted melt inclusions ……83
6.1 Introduction……84
6.2 Methods ……86
6.2.1 Post-entrapment crystallisation correction……86

6.2.1.1 Olivine PEC correction……..87
6.2.1.2 Plagioclase PEC correction……89
6.2.2 Pressure calculation……..…93
6.3 Results……96
6.3.1 Textural analysis……..…96
6.3.2 Melt inclusion volatile content and crystallisation pressures..……..98
6.3.3 Crystallisation pressures……..……101
6.3.4 Olivine- vs. plagioclase-hosted melt inclusion record…….……103
6.4 Origin of the plagioclase-olivine crystallisation depth dichotomy……..……103
6.5 Conclusions ……106

Chapter 7: Regional along-axis variations in the nature of the Gakkel Ridge magma plumbing system……...107
7.1 Introduction……..……108
7.2 Data and approach……..……..…109
7.3 Results……..…116
7.3.1 Basalt crystal cargo……..……..116
7.3.2 Basalt glass geochemistry..……....119
7.3.2.1 SiO_2……...…119
7.3.2.2 Mg#……...120
7.3.2.3 $Na_{8.0}$……..120
7.3.2.4 Glass K/Ti……123
7.3.3 Glass Geochemistry correlations ……..……123
7.3.4 Basalt glass temperatures ……..125
7.3.5 Melt flux ……..……..…126
7.3.6 Crystal cargo geochemistry……...…127
7.3.6.1 Plagioclase……..……...…127
7.3.6.2 Olivine……...…131
7.3.6.3 Clinopyroxene……....……...133
7.3.7 Mineral chemistry correlations…….……133
7.3.8 Plagioclase crystal cargo textural analysis……..……..135
7.3.8.1 Zoning complexity……..…..135
7.3.8.2 Resorption……136
7.3.9 Melt inclusion crystallisation pressures and geochemistry ……..……..138
7.3.9.1 Melt inclusion crystallisation pressures……..……..138
7.3.9.2 Melt inclusion geochemistry…….……..…139
7.4 Discussion……..……..140
7.4.1 Physical nature of the Gakkel Ridge magma plumbing system…...…..140
7.4.1.1 Melt vs. crystal mush…….. ……140
7.4.1.2 Mush zone melt content……142
7.4.1.3 Mush zone maturity: hot vs. cold mush zones ……..……143
7.4.1.4 Variations in magma plumbing system maturity …….. ……144
7.4.1.5 The vertical extent of plumbing systems: Presence of trans-lithospheric magmatic systems?……...……147
7.4.2 Along-axis variation in the Gakkel Ridge plumbing system ……..……..150
7.4.3 Controls on the Gakkel Ridge magma plumbing system...…..……153
7.4.3.1 Extent of melting……..…...…153
7.4.3.2 Melt focussing ……156

7.4.4 Comparison to fast- and slow-spreading mid-ocean ridges……157
7.4.4.1 Relationship between spreading rate and mineral and glass chemistry……..158
7.4.4.2 Relationship between spreading rate and crystal content…...…159
7.5 Conclusions……..…163

Chapter 8: Melt transport at the Gakkel Ridge ……165
8.1 Introduction……...166
8.2 Magmatic systems of the Gakkel Ridge……168
8.2.1 2°W Axial Volcanic Ridge……..……..168
8.2.1.1 Local-scale geochemical and textural variation……..169
8.2.2 18°50'E Basement Ridge……..……...171
8.2.2.1 Local-scale geochemical and textural variation……..172
8.3 Discussion……174
8.3.1 Melt transport at the Gakkel Ridge: 2°E Axial Volcanic Ridge and 18°50'E Basement Ridge ……..……..……...174
8.4 Conclusions…..……177

Chapter 9: Synthesis……**179**
9.1 Magmatic processes in mid-ocean ridge plumbing systems…….……..…180
9.2 The melt inclusion record of crystallisation depths at mid-ocean ridges……181
9.3 The physical nature of the Gakkel Ridge magma plumbing system…….....…182
9.4 Future work……..……183

Bibliography……..185

Appendices…….....211
Appendix 1……..…211
Appendix 2……..….219
Appendix 3……..….223

Figure list

Chapter 2

Fig. 2.1: Bathymetric map of the Arctic Ocean (IBCAO) showing the locations of The Gakkel ridge and other regional features…….8
Fig. 2.2: Bathymetric map of the Gakkel Ridge with tectono-magmatic segments highlighted……...…..10
Fig. 2.3: Along-axis lithological variation showing basalt was more commonly recovered from the EVZ and WVZ……11
Fig. 2.4: Bathymetric map highlighting the features of the Western Volcanic Zone (WVZ) ……12
Fig. 2.5: Bathymetric map highlighting the features of the Sparsely Magmatic Zone (SMZ).....13
Fig. 2.6: Bathymetric map highlighting the features of the Eastern Volcanic Zone (EVZ)……..14
Fig. 2.7: Tectonic history of the Gakkel Ridge……..…15
Fig. 2.8: Schematic of the current tectonic configuration of the Gakkel Ridge and surrounding ocean basins…….……16
Fig. 2.9: Mid-ocean ridge crustal accretion models……..…18

Fig. 2.10: Gakkel Ridge crustal thickness map generated using 3D gravity models ……..20
Fig. 2.11: Along-axis variation in basalt $Fe_{8.0}$ and $Na_{8.0}$……..……..……..21
Fig. 2.12: $Fe_{8.0}$ and $Na_{8.0}$ values of melt inclusions from the EVZ……21
Fig. 2.13: Schematic illustration of the Gakkel Ridge demonstrating the distribution of magmatic and amagmatic lithosphere……..…22
Fig. 2.14: Bathymetric (a) and magnetic (b) map of the Gakkel Ridge highlighting the locations of basement ridges and structure of magnetic anomalies…….24
Fig. 2.15: $\Delta 8/4$ variation along-axis (a) and $^{87}Sr/^{86}Sr$ vs. $^{206}Pb/^{204}Pb$ (b) for Gakkel Ridge basalts……26

Chapter 3
Fig. 3.1: Bathymetric map of the Gakkel Ridge showing sample locations……31
Fig. 3.2: Examples of polished slabs used for analysis…….……..32
Fig. 3.3: Two examples of polished slabs and their corresponding modal maps…….35
Fig. 3.4: ^{12}C counts per cycle for selected melt inclusion CO_2 analyses…….……38
Fig. 3.5: $^{12}C/^{30}Si$ RSE (%) and standard deviation (SD) vs. ^{12}C counts of the last five analytical cycles in standards and analysed melt inclusions…….……38

Chapter 4
Fig. 4.1: Glomerocryst configuration and component contacts……..…41
Fig. 4.2: Plagioclase zoning patterns..……..…44
Fig. 4.3: Patchy zoning scale……..…45
Fig. 4.4: Olivine zoning……46
Fig. 4.5: Clinopyroxene zoning.……..…47
Fig. 4.6: Plagioclase resorption characteristics…..……..…48
Fig. 4.7: Melt inclusion habits……..……..…49

Chapter 5
Fig. 5.1: Controls on plagioclase composition and morphology……55
Fig. 5.2: Relationships between total phenocryst % and proportion of plagioclase ((modal% plagioclase/Total % crystals) x100) (red) and the relationship between the modal % of olivine and plagioclase (green)……56
Fig. 5.3: Modal maps of four samples from the Gakkel Ridge ……..56
Fig. 5.4: Plagioclase crystal habits……..……57
Fig. 5.5: Relationship between crystal habit, core anorthite content and the size of both individual plagioclase (a) and glomerocrysts (b)……58
Fig. 5.6: Glomerocryst configuration and contact types……59
Fig. 5.7: Variations in plagioclase zoning……..…60
Fig. 5.8: Relationship between the size of individual plagioclase crystals and zoning complexity ……..…..60
Fig. 5.9: Type 1 and 2 patchy zoning in plagioclase……61
Fig. 5.10: Types of plagioclase resorption……62
Fig. 5.11: Relationship between crystal area and number of resorption events……...63
Fig. 5.12: Relationship between crystal size and the size of different types of melt inclusions……...63
Fig. 5.13: Anorthite content of plagioclase analyses……..…65
Fig. 5.14: Relationship between average core anorthite and crystal type……65
Fig. 5.15: Histograms of ΔAn for each crystal location split by crystal type……..……67
Fig. 5.16: Relationship between plagioclase TiO_2 and An content (a), and between ΔAnR and ΔTiO_2 (b)……..……..68
Fig. 5.17: Juxtaposition of chemically and texturally distinct plagioclase crystals……69
Fig. 5.18: Modal map of sample PS59-223-25 showing the presence of two plagioclase populations.....…69

Fig. 5.19: Schematic phase diagram showing the formation of Type 1 and Type 2 patchy zoning……75
Fig. 5.20: Schematic showing the effect of sectioning on the observed plagioclase zoning pattern……...76
Fig. 5.21: Histogram of ΔAn for plagioclase from dredge HLY0102-D27……81
Fig. 5.22: Schematic model for the processes occurring within the Gakkel Ridge plumbing system……..……...82

Chapter 6

Fig. 6.1: Melt inclusion sampling locations……87
Fig. 6.2: Olivine post-entrapment crystallisation correction methods……...88
Fig. 6.3: Major element compositions of plagioclase-hosted melt inclusions following different post-entrapment crystallisation corrections……..90
Fig. 6.4: Comparison of the different amount of post-entrapment crystallisation correction required by different correction schemes……..91
Fig. 6.5: Plagioclase-hosted melt inclusion post-entrapment crystallisation correction..92
Fig. 6.6: Relationship between post-entrapment crystallisation correction and crystallisation depths……93
Fig. 6.7: Comparison of experimental pressures to pressures determined using different parameterisations……94
Fig. 6.8: Comparison of pressures calculated using MagmaSat and Iacono-Marziano et al. (2012) parameterisations……...95
Fig. 6.9: Comparisons of plagioclase- and olivine-hosted melt inclusion pressures calculated using MagmaSat and Iacono-Marziano et al. (2012) parameterisations……96
Fig. 6.10: Textural complexity of olivine and plagioclase and melt inclusion distribution……97
Fig. 6.11: Volatile contents of Gakkel Ridge olivine- and plagioclase-hosted melt inclusions compared to datasets that have all used volatiles to investigate crystallisation pressures. ……..……..99
Fig. 6.12: Relationship between melt inclusion size and CO_2 content……100
Fig. 6.13: Relationship between melt inclusion Mg# and CO_2 content……...100
Fig. 6.14: Crystallisation depth of olivine- and plagioclase-hosted melt inclusions (a) and olivine-hosted melt inclusions split by olivine habit (b)……..……101
Fig. 6.15: Comparison of melt inclusion saturation pressures calculated using different parameterisations of and corrected using different correction schemes……102
Fig. 6.16: Comparison of crystallisation depths recorded in melt inclusions at different scales……...103
Fig. 6.17: Crystallisation depths recorded by melt inclusions from individual samples.104
Fig. 6.18: Textural relationship of high-pressure olivine-hosted melt inclusion found in a plagioclase-olivine glomerocryst……..106

Chapter 7

Fig. 7.1: Melt flux parameter determination along the Gakkel Ridge……..113
Fig. 7.2: Along-axis variation in basalt modal mineralogy……118
Fig. 7.3: Plagioclase (**a**) and olivine (**b**) content as a function of total crystal content..119
Fig. 7.4: Discrete along-axis plot displaying the proportions of individual plagioclase and poly- and mono-mineralic glomerocrysts……..……...119
Fig. 7.5: Along-axis variation in basalt geochemistry……121
Fig. 7.6: Binary plots of Na_2O vs. MgO for Gakkel Ridge basalt glass data……122
Fig. 7.7: Glass geochemistry correlations between $Na_{8.0}$ and SiO_2 (**a**), K/Ti (**b**) and Mg# (**c**) and between Mg# and K/Ti (**d**)……124
Fig. 7.8: Histogram of glass SiO_2 contents……124

Fig. 7.9: Relationship between glass temperature and both total crystal content (**a**) and glass $Na_{8.0}$ (**b**). ……125
Fig. 7.10: Relationship between melt flux and $Na_{8.0}$ (**a),** olivine content (%) **(b),** plagioclase content (%) **(c)** and plagioclase : olivine ratio **(d)**……..126
Fig. 7.11: Relationship between melt flux and glass Mg#……..……..127
Fig. 7.12: Along-axis change in plagioclase (**a**), olivine (**b**) and clinopyroxene (**c**) mineral chemistry……129
Fig. 7.13: Along-axis variations in ∆AnV for each plagioclase crystal plotted against longitude (**a**) and for each individual dredge arranged by longitude (**b**)…….130
Fig. 7.14: Longitudinal variations in plagioclase-melt equilibrium for plagioclase cores (**a**) and rims (**b**)……130
Fig. 7.15: Rhodes diagram of olivine forsterite content against host glass Mg# (**a**) and olivine-melt equilibrium plotted along axis (**b**)……..……132
Fig. 7.16 Along-axis variation in olivine ∆Fo……132
Fig. 7.17: Composition of plagioclase and olivine in poly-mineralic glomerocrysts with and without clinopyroxene (**a**) and temperature of melts in equilibrium with glomerocryst clinopyroxene (**b**)……..133
Fig. 7.18: Composition of plagioclase and clinopyroxene from the Gakkel Ridge compared to a global compilation of mineral compositions……134
Fig. 7.19: Correlations between: melt flux and plagioclase anorthite content (**a**) and olivine forsterite content (**b**); and plagioclase anorthite content and glass Mg# (**c**)……..…134
Fig. 7.20: Along-axis variations in zoning complexity plotted against longitude (**a**) and for each individual dredge arranged by longitude (**b**)……135
Fig. 7.21: Relationship between melt flux and zoning complexity for plagioclase crystal cargo……135
Fig. 7.22: Discrete plots of the number of resorption stages recorded in individual plagioclase from each dredge (**a**) and the proportions of plagioclase showing different resorption types (i.e., internal or external) (**b**) and zoning following the resorption interface (**c**)……..137
Fig. 7.23: Relationship between melt flux and both resorption magnitude (**a**) and number of resorption stages (**b**)……137
Fig. 7.24: Along axis variation in olivine- and plagioclase-hosted melt inclusion crystallisation pressures……138
Fig. 7.25: Range of crystallisation pressures recorded in individual dredges……138
Fig. 7.26: Variations in olivine- and plagioclase- hosted melt inclusion Mg# with depth below the seafloor at 3°E Seamounts (**a**), 18°50'E Basement Ridge (**b**), 31°E Basement Ridge (**c**) ……..……139
Fig. 7.27: Variations in plagioclase-hosted melt inclusion host anorthite compositions with depth……..……..140
Fig. 7.28: Glomerocryst melt content……...144
Fig. 7.29: Schematic of the Gakkel Ridge magma plumbing system……152
Fig. 7.30: Total iron contents vs. SiO_2 contents of MORB glasses ……156
Fig. 7.31: Comparison of glass Mg# (**a**), plagioclase An (**b**) and olivine Fo (**c**) content of samples from the East-Pacific Rise (EPR; fast-spreading ridge), Mid-Atlantic Ridge (MAR; slow-spreading ridge) and the Gakkel Ridge (ultraslow-spreading ridge)……159
Fig. 7.32: Comparison of the total crystal (**a**), plagioclase (**b**), olivine (**c**) and clinopyroxene (**d**) content in MORB erupted at the East Pacific Rise, Mid-Atlantic Ridge and Gakkel Ridge……162

Chapter 8

Fig. 8.1: Bathymetric map of 2°W Axial Volcanic Ridge……169
Fig. 8.2: Local-scale variation at 2°W Axial Volcanic Ridge……170

Fig. 8.3: Bathymetric map of 18°50'E Basement Ridge……171
Fig. 8.4: Local-scale variation at 18°50'E Basement Ridge……173
Fig. 8.5: K/Ti variation versus MgO of basalts from 18°50'E Basement Ridge……176

Table list

Chapter 2

Table 2.1: Summaries of each tectono-magmatic segment……9

Chapter 3

Table 3.1: Study sample locations……30
Table 3.2: Crystal cargo imaging and analysis……34

Chapter 4

Table 4.1: Glomerocryst component contacts and structure……41
Table 4.2: Plagioclase and olivine crystal habits……42
Table 4.3: Zoning patterns in plagioclase, olivine and pyroxene……43
Table 4.4: Mineral zoning……43
Table 4.5: Plagioclase zoning complexity code……44
Table 4.6: Location of resorption in plagioclase……48
Table 4.7: Melt inclusion habit……49

Chapter 7

Table 7.1: Supplementary data sources……110
Table 7.2: Melt flux parameters……111
Table 7.3: Total crystal content variations of Gakkel Ridge basalts……117
Table 7.4: Compositional variations of Gakkel Ridge glasses……123
Table 7.5: Temperature variations of Gakkel Ridge glasses……126
Table 7.6: Anorthite content of Gakkel Ridge basalt plagioclase crystal cargo……128
Table 7.7: Forsterite content of Gakkel Ridge basalt olivine crystal cargo……131
Table 7.8: Plagioclase resorption statistics……136
Table 7.9: Plagioclase and olivine literature analyses data sources……160
Table 7.10: Comparative glass and mineral chemistry statistics……160
Table 7.11 Modal mineralogy data sources……161
Table 7.12: Comparative crystal cargo statistics……162

Chapter 8

Table 8.1: Number of samples analysed from 2°W Axial Volcanic Ridge ……168
Table 8.2: Number of samples analysed from 18°50'E Basement Ridge ……172

Chapter 1
Introduction

Chapter 1

1.1 The global mid-ocean ridge system

The global mid-ocean ridge system is the most significant magmatic system on our planet and is the site of 75% of Earth volcanism (Crisp 1984) which produces oceanic crust that covers 2/3 of the Earth's surface. In addition, this volcanism drives hydrothermal circulation which acts to modify and control seawater chemistry (e.g., Elderfield and Schultz 1996), has the potential to form economic mineral deposits (e.g., Humphris et al. 1995) and provides an extreme environment within which extreme faunal communities and chemosynthetic micro-organisms thrive (e.g., Rona et al. 1986; Kelley et al. 2001; Connelly et al. 2012). More importantly here, mid-ocean ridge basalts (MORBs) erupted from these systems have allowed scientists to indirectly study the composition of the upper mantle (e.g., major, trace element and isotopic composition) (Allègre et al. 1984; Sun and McDonough 1989; Gale et al. 2013); determine processes of mantle melting and melt migration (e.g., Langmuir et al. 1992; Kelemen et al. 1997b; Niu and O'Hara 2008; Rubin et al. 2009 (for an overview); Gale et al. 2014); and to study the processes which act to modify MORBs after their generation in the mantle (e.g., Grove et al. 1992; Lissenberg and Dick 2008; Kimura and Sano 2012; Lissenberg et al. 2013).

However, the analysis of glass and whole rock samples alone results in the loss of information recorded within the basalt crystal cargo in the form of mineral textures, compositions and their melt inclusions. This is important because the textures and compositions of minerals can be used to infer the physiochemical conditions present within magmatic systems (Vance 1965; Meyer and Shibata 1990; Ginibre et al. 2002a; Pan and Batiza 2002; Ridley et al. 2006; Pietranik et al. 2006; Ginibre and Wörner 2007; Hellevang and Pedersen 2008; Viccaro et al. 2010; Cashman and Blundy 2013; Neave et al. 2014; Bouvet de Maisonneuve et al. 2016; Coote and Shane 2016). Similarly, because melt inclusions become trapped within crystallising minerals in different portions of the magmatic system, they offer a means of studying magmatic plumbing systems (i.e., the interconnected magma transport network made up of reservoirs and conduits) at a fine-scale (e.g., Sobolev and Shimizu 1993; Chesner and Luhr 2010; Shaw et al. 2010; Moune et al. 2012; Wanless and Shaw 2012; Cashman and Blundy 2013; Wanless et al. 2014a, b; Colman et al. 2015; Coumans et al. 2015, 2016).

1.2 Why study ultraslow-spreading mid-ocean ridges?

Whilst mid-ocean ridges such as the East Pacific Rise and Mid-Atlantic Ridge have been studied for decades, ultraslow-spreading ridges, a relatively new class of spreading ridge characterised by spreading rates <20 $mmyr^{-1}$, intermittent volcanism and lack of transform faults (Dick et al. 2003), have received comparatively little attention. These ultraslow-spreading ridges are important because they are volumetrically significant and make up ~36% of the global ridge system (Solomon 1989; Michael et al. 2003). These ridges have remained little studied in part due to their location in either deep high seas (e.g., Southwest Indian Ridge (SWIR)) or under permanent pack ice cover (e.g., Gakkel Ridge). The Gakkel Ridge, the focus of this thesis, is the end-member ultraslow-spreading ridge in the global mid-ocean ridge system. Here, spreading rates decrease from 14.6 $mmyr^{-1}$ in the west to 6.3 $mmyr^{-1}$ in the east (DeMets et al. 1990). To date, a large proportion of the literature concerning the Gakkel Ridge concentrates on the recovery of abyssal peridotites that, due to the low degrees of mantle melting occurring at these ridges, offer the opportunity to study relatively fertile mantle compositions (e.g., Hellebrand et al. 2002; Goldstein et al. 2008; Liu et al. 2008; Stracke et al. 2011; D'Errico et al. 2016). A more detailed background on our current understanding of the Gakkel Ridge will be given in Chapter 2. To achieve better constraints on the nature of ultraslow-spreading magma plumbing systems, crystal cargo in erupted lavas can be studied: it preserves a record of the physiochemical conditions during crystal growth, which, in turn, is a function of magma chamber dynamics.

1.3 Crystal-scale records of mid-ocean ridge plumbing systems

1.3.1 Mineral textures and compositions

Textures and compositions of minerals record the physiochemical conditions and processes occurring within magmatic systems (Vance 1965; Meyer and Shibata 1990; Ginibre et al. 2002; Pan and Batiza 2002; Pietranik et al. 2006; Ridley et al. 2006; Ginibre and Wörner 2007; Hellevang and Pedersen 2008; Viccaro et al. 2010; Cashman and Blundy 2013; Neave et al. 2014; Coote and Shane, 2016; Bouvet de Maisonneuve et al. 2016) and thus provide petrologists with an observable record of what magmatic processes have occurred within the magmatic system. Whilst both olivine and plagioclase are common erupted phases in MORBs, plagioclase is particularly useful for studying magmatic processes because slow inter-diffusion of CaAl-NaSi prevents equilibration of adjacent compositional zones thus preserving textures over long timescales (Grove et al. 1984; Morse 1984); major element diffusion is comparatively fast in olivine (Chakraborty 1997).

To date, mineral-scale studies have revealed mid-ocean ridges to be chemically and physically dynamic open systems within which multiple processes operate. Magma mixing is often used to explain several common features of MORBs: (1) mixed chemical and textural populations (Dungan et al. 1979; Meyer and Shibata 1990; Pan and Batiza 2003); (2) plagioclase morphologies indicative of resorption (i.e., superheating) and skeletal growth (i.e., supercooling) (Kuo and Kirkpatrick 1982); and (3) the presence of plagioclase and olivine that is too anorthitic and forsteritic respectively to be in equilibrium with its host melt (Dungan et al. 1979). Diffusion studies also suggest that at some mid-ocean ridges, eruptions are preceded by mush disaggregation that results directly from magma mixing and melt replenishment (Costa et al. 2009; Moore et al. 2014). Mush disaggregation itself has been proposed to explain the origin of both anorthitic plagioclase xenocrysts (Ridley et al. 2006) and open-structured crystal networks in MORB (Pan and Batiza 2003) as well as the formation of plagioclase ultraphyric basalts (PUBs) commonly sampled at ultraslow- to intermediate-spreading ridges (Lange et al. 2013). The importance of interactions between percolating melt and pre-existing mush zones is demonstrated by compositional zoning and dissolution textures present in both individual plagioclase (Coumans et al. 2015) and plagioclase in cumulate xenoliths from the East Pacific Rise (Ridley et al. 2006). Undercooling, distinct to that occurring upon quench crystallisation, has been shown to occur within the magma plumbing systems of the Mohns and Knipovich Ridges, where crystal-rich magmas advance into cool regions of the plumbing system (Hellevang and Pedersen 2008).

Using diffusion modelling, compositional profiles present within minerals (e.g., Fe-Mg, Ti, Ca in olivine and Mg, Sr, REE in plagioclase) can also be utilised to determine the timescales of magmatic processes (e.g., magma mixing, mush zone disaggregation). Such modelling relies on the identification of chemical or isotopic disequilibrium within crystals or between crystals and the host melt (Chakraborty 2008; Moore et al. 2014) in addition to the accurate determination of initial and boundary conditions and appropriate choice of diffusion coefficients. Whilst diffusion modelling has been shown to be a powerful tool for studying magmatic processes in volcanic systems (e.g., Zellmer et al. 1999; Ginibre et al. 2002; Costa et al. 2003; Costa and Dungan 2005; Oeser et al. 2015) relatively few studies have utilised it for studying timescales of processes occurring in mid-ocean ridges (e.g., Nabelek and Langmuir 1968; Humler and Whitechurch 1988; Pan and Batiza 2002; Costa et al. 2009; Zellmer et al. 2011, 2012; Moore et al. 2014). The majority of timescale estimates for the occurrence of processes such as magma mixing and crystal mush disaggregation are on the order or days to years, however longer timescales suggest that some crystals remain within the magmatic system for

prolonged periods, thus providing constraints on the temporal evolution of magmatic systems (e.g., Costa et al. 2009; Moore et al. 2014).

1.3.2 Melt inclusions

Melt inclusions are small volumes of melt which become trapped within crystallising minerals as they ascend through magmatic systems. Because of this, melts that exist at different times and in different locations within the plumbing system can become trapped, thus providing a fine-scale record of both the geochemical heterogeneity and evolution of melts within the magmatic system. Mid-ocean ridge basalts do not record this heterogeneity because primary mantle melts, generated through partial melting of decompressing mantle (M^{c}kenzie and Bickle 1988; Kelemen et al. 1997a), aggregate together and become modified through magma mixing (Dungan et al. 1978; Grove et al. 1992; Pan and Batiza 2003; Ridley et al. 2006), fractional crystallisation (Grove et al. 1992; Rubin and Sinton 2007) and reaction with lower crustal lithologies (Gao et al. 2007; Kvassnes and Grove 2008; Lissenberg and Dick 2008; Lissenberg et al. 2013). These processes lead to chemical (major- and trace-element and isotopic) homogenisation (Saal et al. 2005) and a loss of information regarding the characteristics of the melts that contributed to MORB formation (Sobolev 1996). Major- and trace-element, as well as volatile and isotopic composition of mid-ocean ridge basalt melt inclusions provide information on: (1) the compositional heterogeneity of melts within the system (e.g., Maclennan 2008); (2) the composition of the mantle source (e.g., Wanless et al. 2014a); (3) the pressures at which crystallisation occurs (e.g., Sobolev and Shimizu 1993; Shaw et al. 2010; Wanless and Shaw 2012; Wanless et al. 2014a,b; Colman et al. 2015; Coumans et al. 2015, 2016); and (4) mantle melting processes (e.g., Sobolev and Shimizu 1993).

1.4 Aims

The overarching aim of this work is to reconstruct the magma plumbing system of the Gakkel Ridge. Through crystal-scale studies, and using a combination of back-scattered electron images, mineral- and glass geochemistry and melt inclusion volatile data, the following questions will be addressed:

- What is the relative importance of the different magmatic processes occurring within the Gakkel Ridge magma plumbing system, and what is their record on the crystal scale?
- What is the vertical extent of the Gakkel Ridge plumbing system?

- What is the physical nature (i.e., crystal vs. melt content and chemical maturity) of the Gakkel Ridge magma plumbing system?
- Do any of the above change along axis and/or correlate with spreading rate?

1.5 Thesis structure

This thesis comprises 9 chapters. Following this introduction Chapter 2 reviews our current understanding of the Gakkel Ridge. Chapters 3 and 4 cover first the analytical techniques used in this study and second the classification schemes used to construct the textural database which forms the foundation of the work presented herein. Chapter 5 investigates the significance of plagioclase textures, whilst Chapter 6 compares the crystallisation pressure records of olivine- and plagioclase hosted melt inclusions. Using that presented in Chapters 5 and 6, Chapters 7 and 8 examine regional along-axis variations in the nature of the Gakkel Ridge magma plumbing system and melt transport at the Gakkel Ridge respectively. Finally, Chapter 9 presents a synthesis of the previous chapters.

Chapter 2
The Gakkel Ridge

Chapter 2

2.1 Location

The Gakkel ridge is located within the Eurasia Basin (Arctic Ocean) and is the northern extension of the Mid-Atlantic Ridge (MAR). The ridge connects to the MAR in the south along the Spitsbergen and Molloy Fracture Zones and the Lena Trough (Herron et al. 1974; Brozena et al. 2003) and extends eastwards over 1,800 km into the Leptev Sea where seafloor spreading transforms into continental extension on the Leptev margin (Sekretov 2002; Dick et al. 2003; Michael et al. 2003) (Fig 2.1); spreading rates decrease from 14.6 mmyr^{-1} to 6.3 mmyr^{-1} from west to east along the ridge (DeMets et al. 1990). The ridge divides the Eurasia Basin into the Amundsen (northern) and Nansen (southern) Basins and is bound by the Lomonosov Ridge, Greenland and the Eurasian margin (Barents, Kara and Leptev Seas) (Fig 2.1).

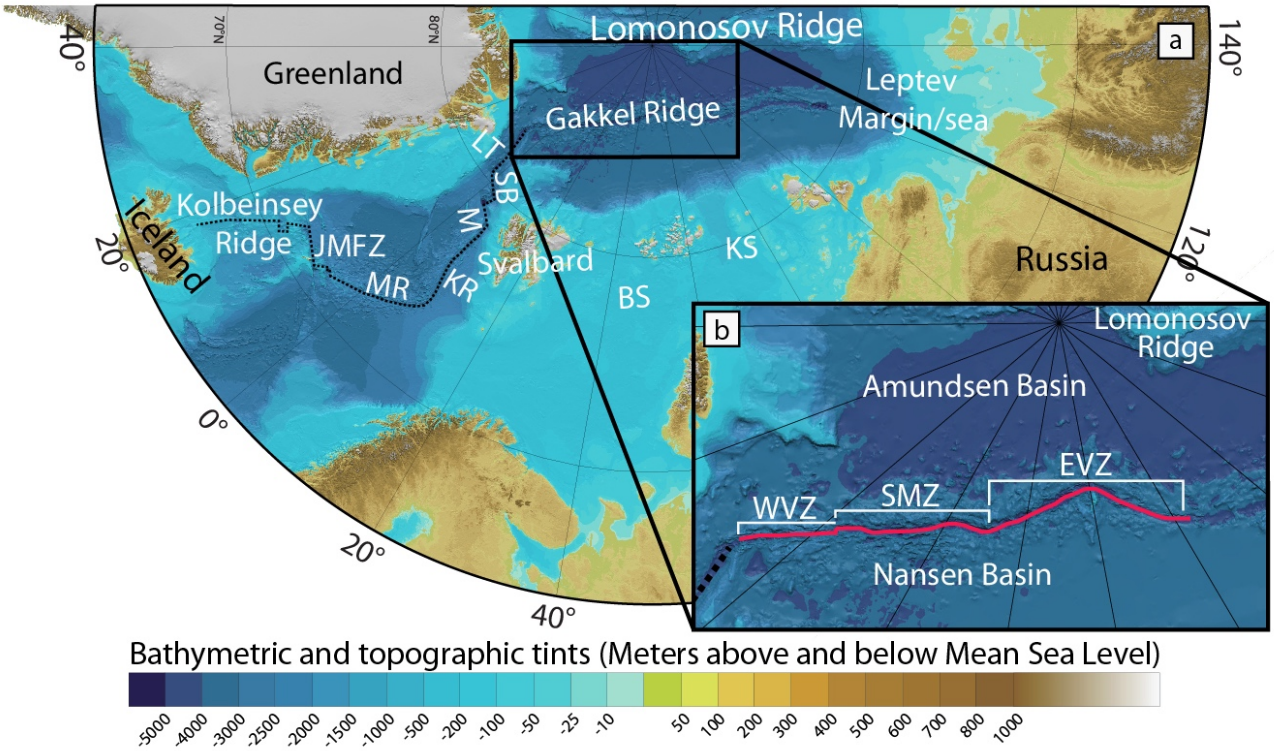

Fig. 2.1: **a** Bathymetric map of the Arctic Ocean (IBCAO) showing the locations of The Gakkel ridge and other regional features. **b** The Gakkel ridge is split into its three tectono-magmatic segments: Western Volcanic Zone, WVZ; Sparsely Magmatic Zone, SMZ; and Eastern Volcanic Zone, EVZ. LT, Lena Trough; SB, Spitsbergen fracture zone; M, Molloy fracture zone; KR, Knipovich Ridge; MR, Mohns Ridge; JMFZ, Jan Mayen Fracture Zone; KS, Kara Sea; BS, Barents Sea. IBCAO data from Jakobsson et al. (2012).

2.2 Current understanding of the Gakkel Ridge

2.2.1 Tectono-magmatic segmentation

The Gakkel Ridge, unlike faster spreading ridges such as the East Pacific Rise (EPR), lacks transform fault offsets along its length. Instead, based on bathymetric data and sample lithologies (Fig. 2.2 and 2.3), the ridge has been split into three tectono-magmatic segments that exhibit alternating modes of volcanic and avolcanic crustal accretion; the Western Volcanic Zone (WVZ), Sparsely Magmatic Zone (SMZ) and Eastern Volcanic Zone (EVZ) (Dick et al. 2003; Michael et al. 2003) (Fig 2.1 and 2.2). The features of each segment in terms of their extent, dominant morphology and mode of crustal accretion are summarised in Table 2.1 and in the following sections.

Table 2.1 Tectono-magmatic segments of the Gakkel Ridge

Segment	Extent	Sampling locations containing:				Mode of crustal accretion	Dominant volcanic morphology
		Number of sampling locations	Basalt (%)	Peridotite (%)	Gabbro (%)		
Western Volcanic Zone (WVZ)	7°W-3°E	49	96	0	6	Magmatic	Axial volcanic ridges and small seamounts
Sparsely magmatic zones (SMZ)	3°E-29°E	54	54	56	9	Avolcanic	Basement perpendicular ridge and an immature axial volcanic ridge
Eastern Volcanic Zone (EVZ)	29°E-85°E	88	94	7	1	Magmatic	Large roughly circular seamounts and basement perpendicular ridges

2.2.1.1 Western volcanic zone (WVZ)

From the Lena Trough, the WVZ extends 220 km from 7°W to 3°E where the transition to the SMZ is marked by a left-stepping, non-transform ridge offset (Michael et al. 2003) (Fig. 2.2 and 2.4). The rift valley (7-20 km wide) is characterised by a relatively shallow axial valley floor (~4200 mbsl) bounded by inward dipping faults that form a series of scarps and terraces that appear to become larger to the east (Dick et al. 2003; Michael et al. 2003). Within the WVZ, volcanic landforms are varied and include five elongated axial volcanic ridges and numerous small seamounts that are located both on the axial valley floor and on its walls (Dick et al. 2003; Michael et al. 2003). A total of 156 seamounts measuring >50 m in height are present within the WVZ, 76 are located on the rift valley floor (Cochran et al. 2008). The dominant lithology recovered along this

segment of the ridge is basalt (Table 2.1), suggesting that crustal accretion is magmatic; no peridotite was recovered (Michael et al. 2003).

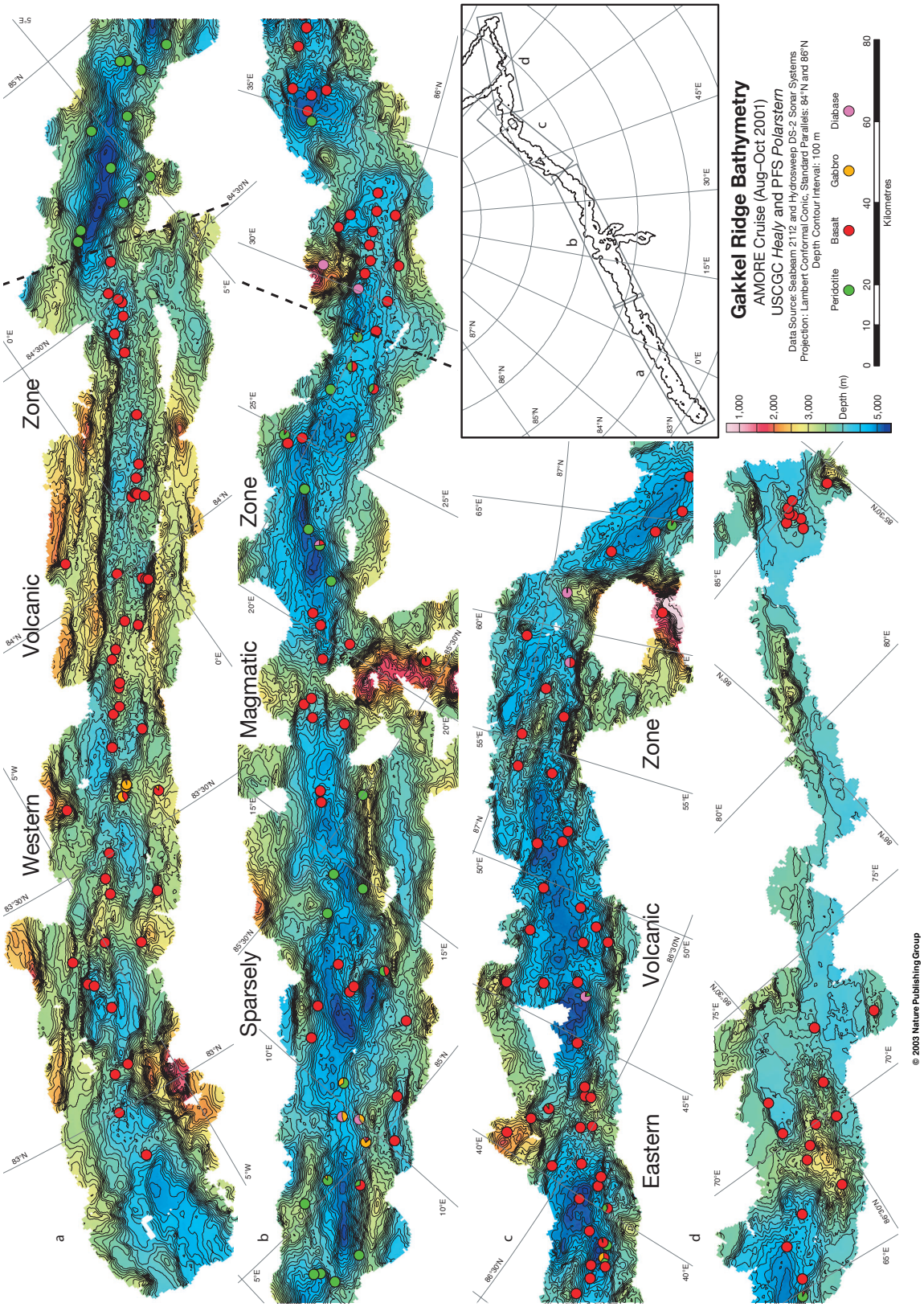

Fig. 2.2: Bathymetric map of the Gakkel Ridge with tectono-magmatic segments highlighted. Pie charts illustrate the distribution of recovered lithologies. Figure from Michael et al. (2003).

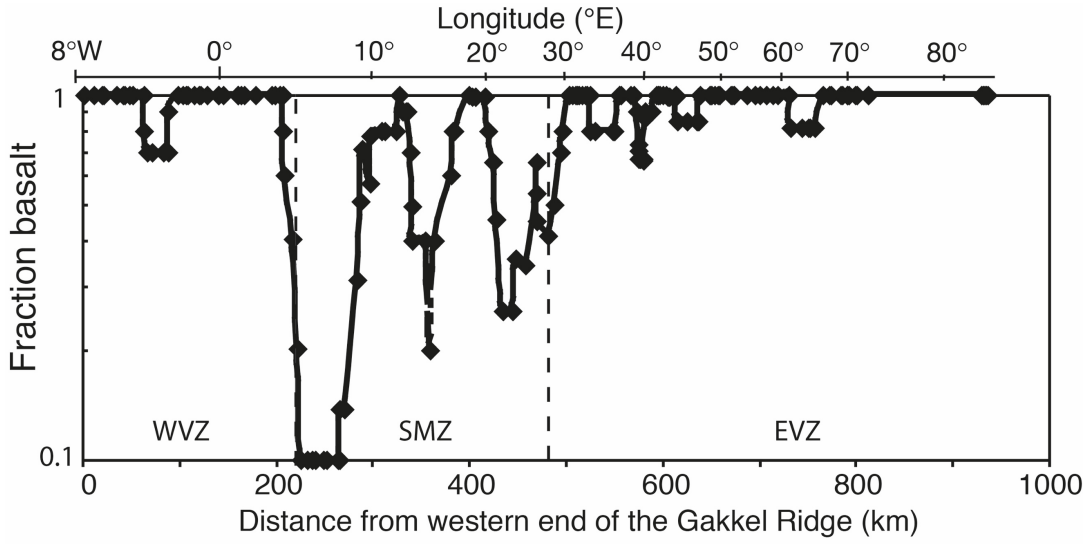

Fig. 2.3: Along-axis lithological variation showing basalt was more commonly recovered from the EVZ and WVZ. Figure adapted from Michael et al. (2003).

2.2.1.2 Sparsely magmatic zone (SMZ)

The transition from the WVZ to the SMZ is marked by a left-stepping non-transform offset (10 km) and accompanying ~1 km deepening of the ridge axis (Michael et al. 2003) (Fig. 2.2 and 2.5). The SMZ extends for ~300 km, with its axial valley bounded by low angle slopes, many of which are interpreted as large-throw fault surfaces (Michael et al. 2003). The axial valley is dominated by peridotite, and contains no axial volcanic ridges such as those found in the WVZ, but it does contain a total of nine seamounts >50 m in height (Cochran 2008). From 3°E for 80 km only peridotite was recovered, with gabbroic lithologies recovered from dredges around 10°E (Michael et al. 2003). Whilst an immature axial volcanic ridge at 13°E marks the first appearance of volcanism within the SMZ, a dredge at ~8°E also recovered basalts. Unlike the WVZ where basalt was abundant, here less than 20% of the rift valley is thought to be covered with basalt suggesting accretion in this portion of the ridge is amagmatic (Michael et al. 2003). One of the most prominent features within the SMZ is a basement perpendicular ridge located at 19°E where the rift valley shoals significantly to 3500 mbsl (Cochran et al. 2003). This basement ridge extends NW and SE off-axis for ~100 km. From 17.8°E to 20.2°E the ridge axis is marked by a volcanic ridge. A second immature basement ridge, extending NW and SE ~50 km off-axis, is located at 10°E.

2.2.1.3 Eastern volcanic zone (EVZ)

Following the SMZ, the EVZ marks the return of abundant volcanism (Fig. 2.2 and 2.6). However, volcanic landforms here are very different to those in the WVZ. To start, the axial rift valley within the EVZ is much deeper (~5000 mbsl). Located within this deeper

rift valley are six large (15-50 km along axis) roughly circular volcanic edifices (31°E, 37°E, 43°E, 55°E, 69°E, 85°E) spaced 50-160 km apart. Three of these volcanic centres are associated with basement perpendicular ridges located at 31°E, 42°E, 62°E and 70°E; the basement ridge located at 62°E is not associated with a large volcanic edifice. Closely associated with these volcanic centres are a total of 62 seamounts (>50 m in height) (Cochran 2008). Similar to the WVZ, abundant volcanism suggests crustal accretion is magmatic (Michael et al. 2003). Within the EVZ the rift valley shows two abrupt changes in trend at ~32°E and 63°E; the trend of the ridge axis changes from N60°E in the SMZ, to N50°E and subsequently N140°E at 32°E and 63°E respectively in the EVZ (Cochran et al. 2003). Between ~32-63°E, ridge obliquity is explained by the presence of non-transform discontinuities that cause the ridge axis to become offset to the north by 15-14 km (Cochran et al. 2003). Basement perpendicular ridges are present at both locations where the ridge trend changes. Seamounts situated on inside corner highs of these basement ridges are interpreted by Michael et al. (2003) to be tectonic rather than volcanic in origin due to the recovery of only altered diabase from dredges.

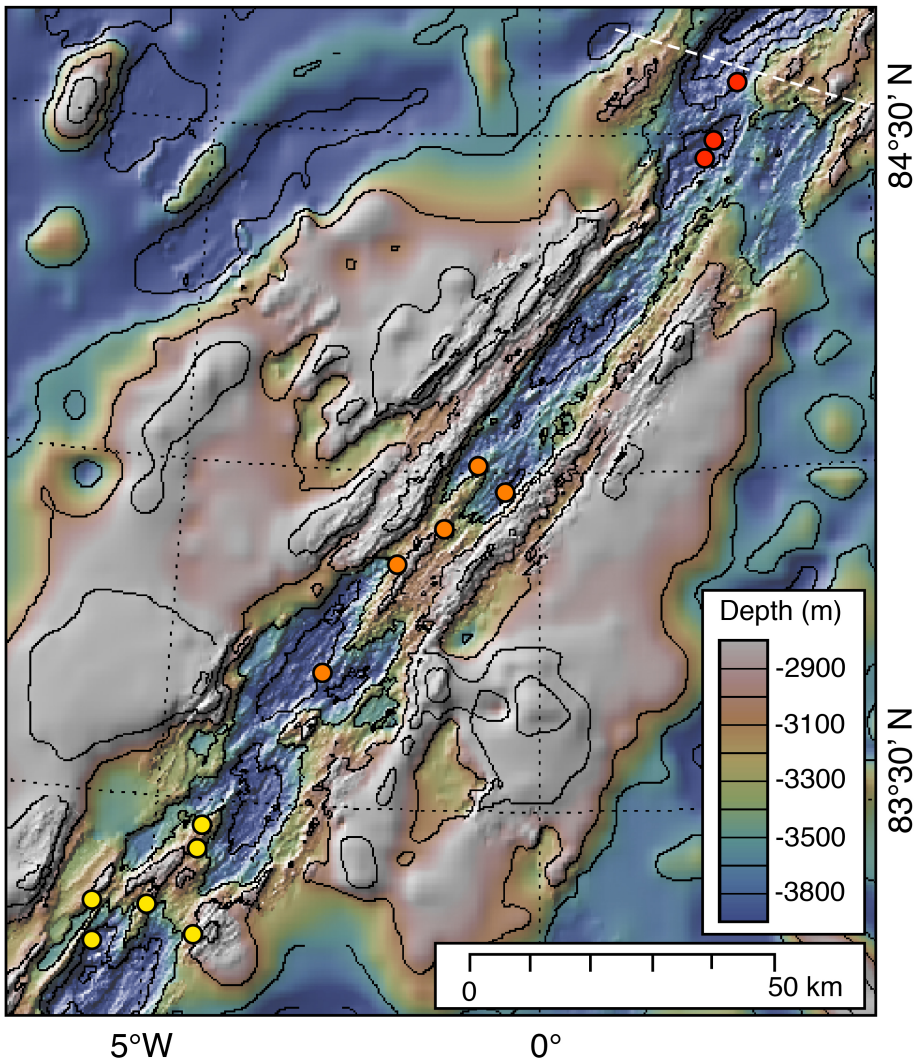

Fig. 2.4: Bathymetric map highlighting the features of the Western Volcanic Zone (WVZ). Sampling locations are shown by coloured dots and correspond to the following locations: yellow, 5°W axial volcanic ridge; orange, 2°W axial volcanic ridge; red, 3°E Seamounts. The bathymetric map is a combination of IBCAO V.3 30 arc-second resolution bathymetry (Jakobsson et al. 2012) and Gakkel Ridge 100 m resolution bathymetry (Michael et al. 2003). Contour interval is 500 m. White dashed line marks the junction with the SMZ.

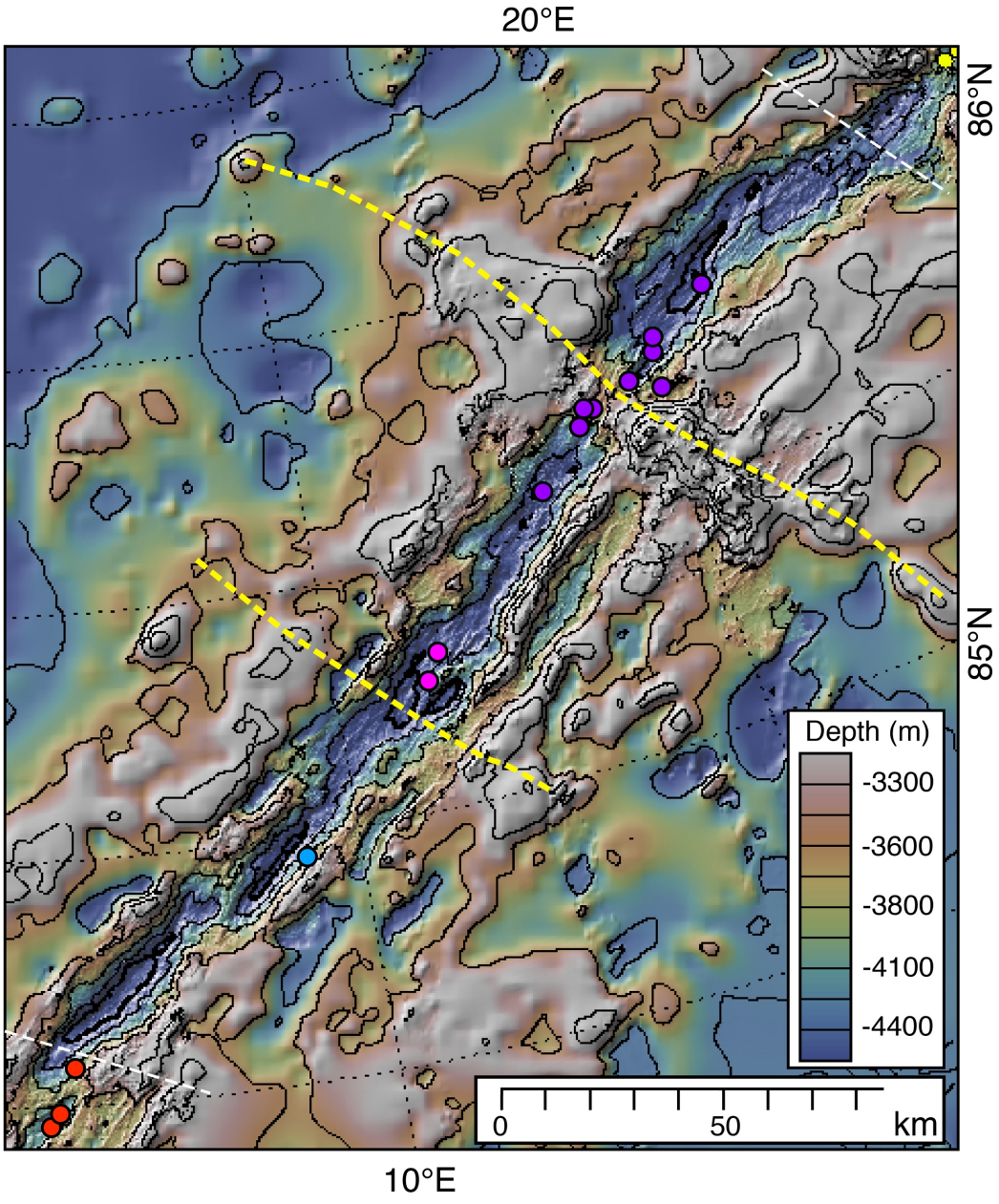

Fig. 2.5: Bathymetric map highlighting the features of the Sparsely Magmatic Zone (SMZ). Two basement perpendicular ridges (yellow dashed lines) are marked. Sampling locations are shows by coloured dots and correspond to the following locations: blue, 9°E valley wall; pink, 12°40'E axial volcanic ridge; purple, 18°50'E basement ridge. Red and yellow points correspond to locations in the WVZ and EVZ, respectively. Contour interval is 100 m. The bathymetric map is a combination of IBCAO V.3 30 arc-second resolution bathymetry (Jakobsson et al. 2012) and Gakkel Ridge 500 m resolution bathymetry (Michael et al. 2003). Basement perpendicular ridges have been drawn from Jokat and Schmid-Aursch (2007).

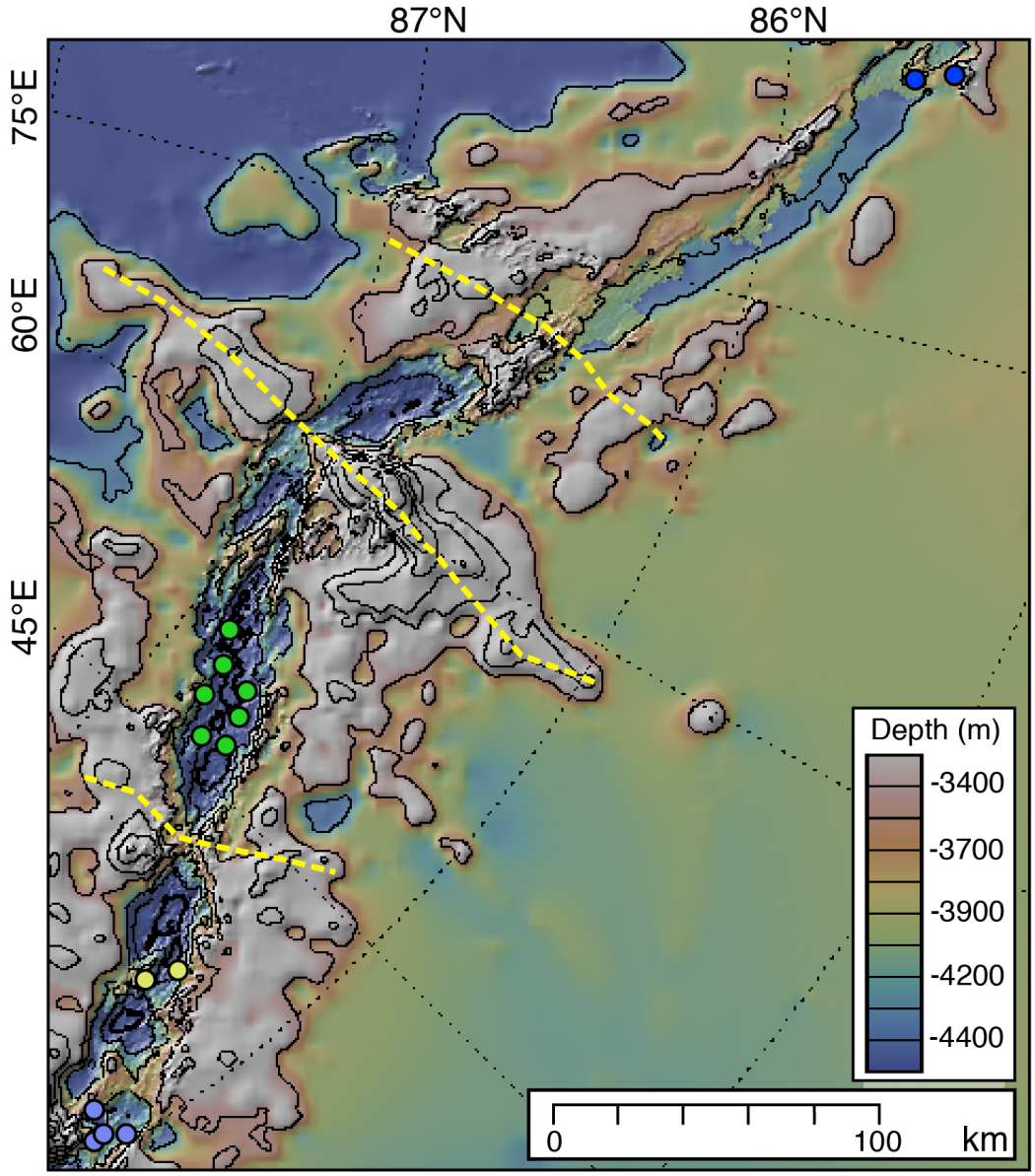

Fig. 2.6: Bathymetric map highlighting the features of the Eastern Volcanic Zone (EVZ). Four basement perpendicular ridges (yellow dashed lines) are marked. Sampling locations are shown by coloured dots and correspond to the following locations: violet, 31°E basement ridge; yellow, 37°E seamount and 38°E random basalt; green, 48°E deep sea floor; blue 84°40'E seamounts. Contour interval is 500m. The bathymetric map is a combination of IBCAO V.3 30 arc-second resolution bathymetry (Jakobsson et al. 2012) and Gakkel Ridge 100 m resolution bathymetry (Michael et al. 2003). Basement perpendicular ridges have been drawn from Jokat and Schmid-Aursch (2007).

2.2.2 Formation of the Gakkel Ridge

The opening of the Eurasia Basin initiated with the rifting of the Lomonosov Ridge from Eurasia during the early Eocene at or before magnetic anomaly twenty-four (53.3 Ma, chron C24 (Vogt et al. 1979; Blythe and Kleinspehn 1998; Mosar et al. 2002) or at chron C25 (Brozena et al. 2003; Schmidt-Aursch and Jokat 2016)). The configuration of this initial break-up is preserved in the conjugate shape of the Lomonosov Ridge and Eurasia margin (Brozena et al. 2003; Cochran et al. 2003).

Using a 3D gravity model in combination with geophysical and petrological data, Schmidt-Aursch and Jokat (2016) propose that the EVZ and SMZ are older than the WVZ (Fig. 2.7). They suggest that amagmatic or weakly volcanic spreading occurred in the vicinity of the EVZ and SMZ following the separation of the Lomonosov Ridge from Eurasia (~chron 25); spreading in the vicinity of the WVZ initiated following the separation of the Morris Jesup Rise and Yermak Plateau in the southwest at approximately chron 13 to produce thin oceanic crust similar to that found further west. As will be explored in greater detail in the following sections, separation of Greenland from Svalbard at chron 5/6 resulted in the influx of North Atlantic mantle northward into the WVZ; geochemical evidence suggests propagation extended half way into the WVZ. It is this mantle influx that is attributed to the differences between the WVZ and SMZ and EVZ (Fig. 2.8).

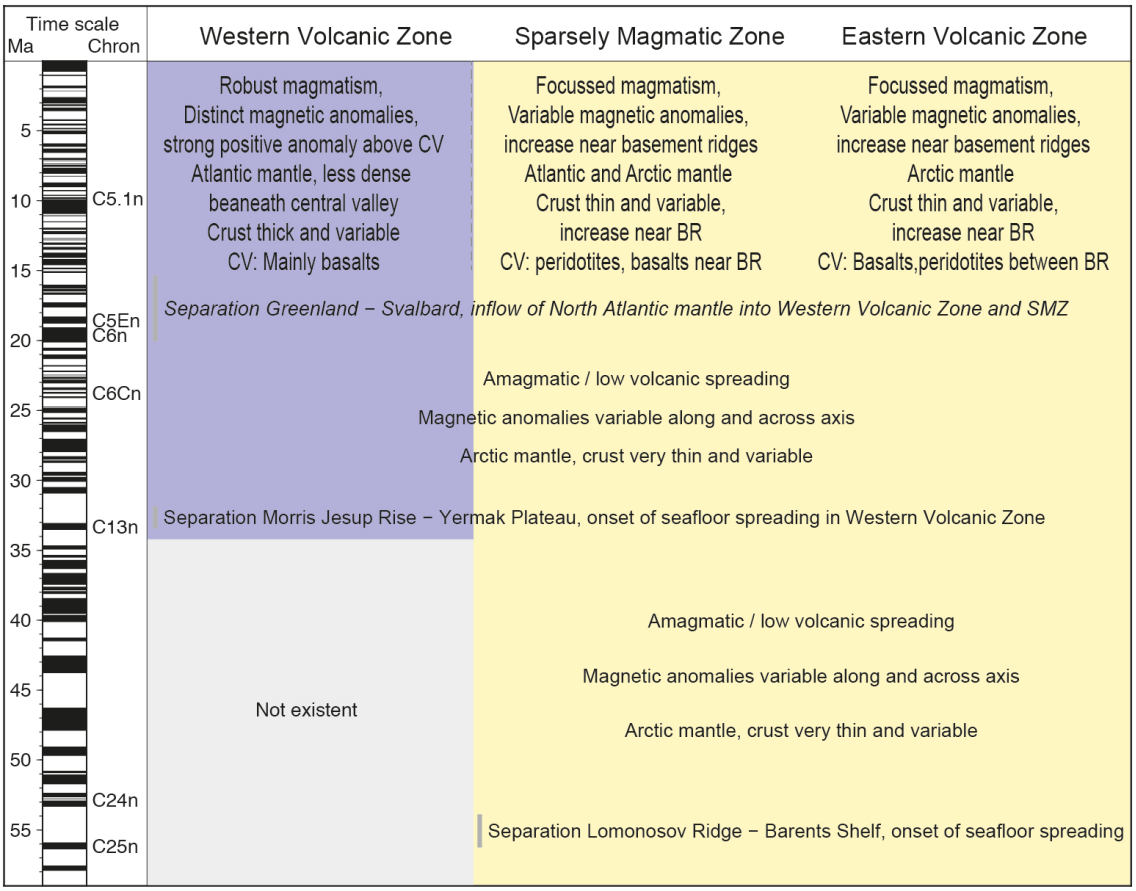

Fig. 2.7: Tectonic history of the Gakkel Ridge outlining the evolution of the Sparely Magmatic Zone, Eastern Volcanic Zone and Western Volcanic Zone. Colours correspond to those in Figure 2.8. Abbreviations are as follows: CV, central valley; BR, basement ridge. Re-drawn from Schmidt-Aursch and Jokat (2016)

2.2.3 Structure of the Gakkel Ridge Lithosphere

At spreading rates below 15-20 mmyr^{-1}, melting models predict that melt production, and in turn crustal thickness, will reduce significantly due to more efficient conductive cooling

of the slowly upwelling mantle; lithospheric and crustal thickness will in turn increase and decrease respectively (Reid and Jackson, 1981; Bown and White 1994; Coakley and Cochran 1998). More efficient conductive cooling effectively truncates the top of the melting column causing melting to occur at greater depth beneath the axis thus reducing the amount of melt produced through decompression (Bown and White 1994; Coakley and Cochran 1998). Below, the structure of the crust and lithosphere shall be discussed in detail separately.

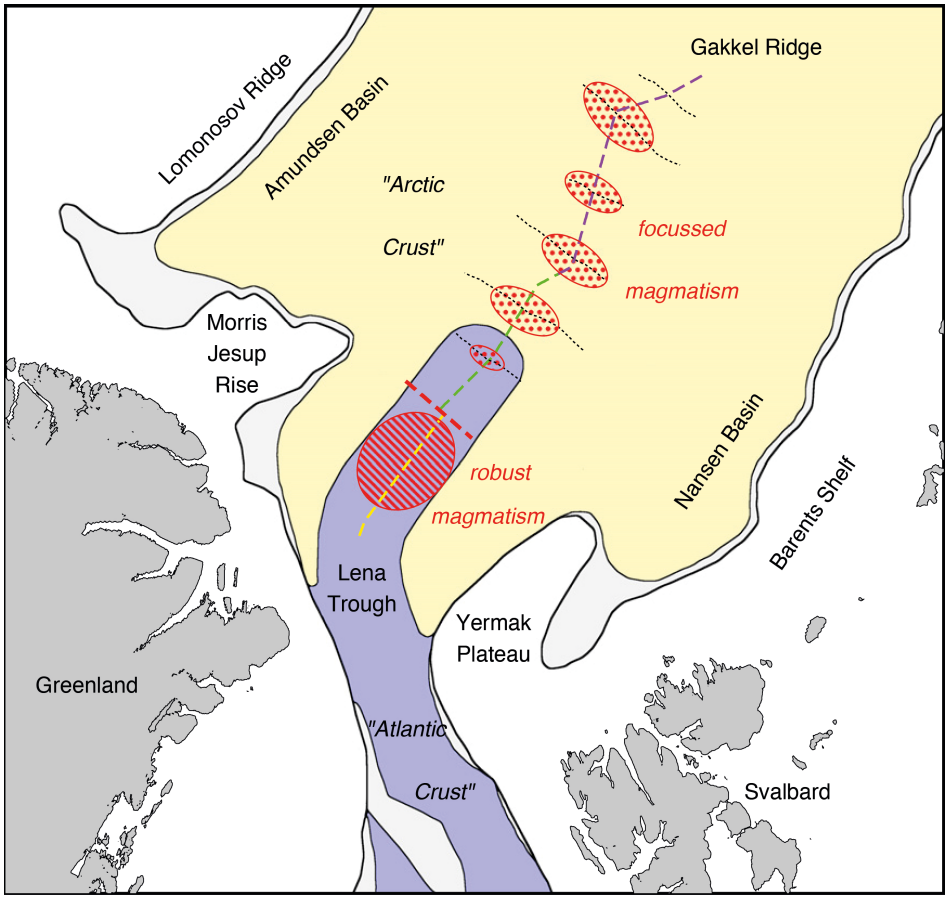

Fig. 2.8: Schematic of the current tectonic configuration of the Gakkel Ridge and surrounding ocean basins. Areas of yellow oceanic crust were accreted prior to the separation of Greenland and Svalbard. Subsequent to this separation North Atlantic mantle propagated northwards into the WVZ and partly into the SMZ resulting in robust magmatism in the WVZ. In contrast, magmatism in the SMZ and EVZ is highly focused. Trace of the Gakkel Ridge is shown by the dashed lines, colours indicate the following; yellow, WVZ; green, SMZ; purple, EVZ. Re-drawn from Schmidt-Aursch and Jokat (2016).

2.2.3.1 Crustal thickness and structure

Multiple methods have been implemented to investigate the nature of the crust along the Gakkel Ridge. Early seismic refraction studies at off-axis locations toward the western extent of the Gakkel Ridge retrieved crustal thicknesses of 2-3 km (Jackson et al. 1982), significantly less than the 6-7 km thick Penrose crust present at intermediate- to fast-spreading ridges (Jokat et al. 2003; Snow and Edmonds 2007) (Fig. 2.9). However, in

order to determine whether the off-axis crust is representative of current oceanic crust forming at the ridge axis, more recent seismic studies have investigated the on-axis crustal thickness (e.g., Jokat et al. 2003; Jokat and Schmidt-Aursch 2007); they obtained similar crustal thicknesses of 1.9 to 3.3 km (Jokat et al. 2003). Contrary to model predications, crustal thickness does not vary systematically along axis; the crust does not become thinner toward the east as spreading rate decreases (Jokat et al. 2003). This is corroborated by Jokat and Schmidt-Aursch (2007), who show that there is no systematic decrease in crustal thickness with decreases spreading rate moving east, the WVZ (2.2 to 4.9 km) and EVZ (2.7 to 3.3 km) having similar crustal thicknesses; the central SMZ (1.4 to 2.1 km) exhibits slightly thinner crust with the absence of volcanics along much of this segment indicating the complete absence of basaltic crust. This suggests that crustal thickness is not a function of spreading rate, but is likely highly dependent on the nature of melt delivery and ridge magmatism (Jokat et al. 2003).

In support of these seismic studies, crustal thickness can be determined from gravity anomalies (e.g., Coakley and Cochran 1998; Schmidt-Aursch and Jokat 2016). Early gravity studies showed that crustal thickness was variable (1-4 km) and became vanishingly thin in the east. Building on this, a recent study that combined 3D gravity models with geophysical and petrological data demonstrated that crustal thickness can be highly variable along the Gakkel Ridge, reaching up 6.6 km thick in the WVZ (Schmidt-Aursch and Jokat 2016) (Fig. 2.10); seismic refraction data show the crust in the WVZ can be up ~5 km thick (Jokat and Schmidt-Aursch 2007). This thickened crust in the WVZ is attributed to more robust melt supply as a result of the influx of North-Atlantic mantle from the south following the breakup of Greenland and Svalbard around chrons C5/C6. It should be noted that extensive peridotite exposure at the seafloor (Fig. 2.3) in the SMZ indicates that at points, there is no magmatic crust, with lithospheric mantle being exposed directly at the seafloor.

Geophysical studies not only provide insight into crustal thickness, but also its structure. Typical layered oceanic crust (i.e., Penrose crust), such as that formed at fast-spreading ridges, consists of pillow basalts, sheeted dykes and gabbros overlying residual mantle peridotites (Anonymous 1972) (Fig. 2.9a). However, along the Gakkel Ridge seismic velocities typical of layer three (i.e., gabbros, 6.5 to 7.2 kms^{-1}) are missing, indicating that layer three is either entirely absent or cannot be resolved (Jokat et al. 2003; Jokat and Schmidt-Aursch 2007). Whilst gabbro has been recovered from three locations along the Gakkel Ridge, suggesting layer three may be locally present (Fig. 2.2; WVZ, 3°W; SMZ, 10°E; EVZ, 39°E), the predominance of peridotite at the seafloor in the SMZ and absence of seismic velocities typical of layer three supports the absence of a magmatic crust

typical of faster spreading ridges (Michael et al. 2003). Instead, ultraslow-spreading ridges have alternating magmatic and amagmatic crustal accretionary segments, and may, unlike that depicted in Figure 2.9d, entirely lack gabbroic lithologies, instead being comprised of a basaltic cap directly overlying mantle peridotites (Dick et al. 2003; Michael et al. 2003). However, it seems unlikely that gabbroic lithologies are entirely absent seeing as basalts erupted are not primary and have undergone variable degrees of fractionation within the plumbing system. Therefore, whilst it may hold that layered 'Penrose-type' crust typical of fast-spreading ridges is absent at ultraslow-spreading ridges, gabbroic lithologies are likely present within the system.

Alternatively, spinel geochemistry can be used to determine crustal thickness. Due to Cr and Ti being compatible and incompatible in spinel respectively spinel Cr# (100 x Cr/[Cr + Al]) will increase during progressive melting (Dick and Bullen 1984). Therefore, because Cr# can be used to infer how much melting has occurred, the resulting crustal thickness can be calculated. Using the above rationale and spinel from an abyssal peridotite from the SMZ, Hellebrand et al. (2002) showed that a Cr# of 0.24, generated through ~9.7% melting, corresponds to a crustal thickness of 5.4 km. This value is greater than any seismically determined crustal thickness for the SMZ, and is proposed to reflect enhanced melt focusing (Hellebrand et al. 2002). However, crustal thickness estimates inferred from spinel geochemistry are only valid if it can be shown there has only been a recent single melting event; in the case of the Gakkel Ridge, Os isotopic studies have shown that there has been more than one partial melting event here (e.g., Liu et al. 2008).

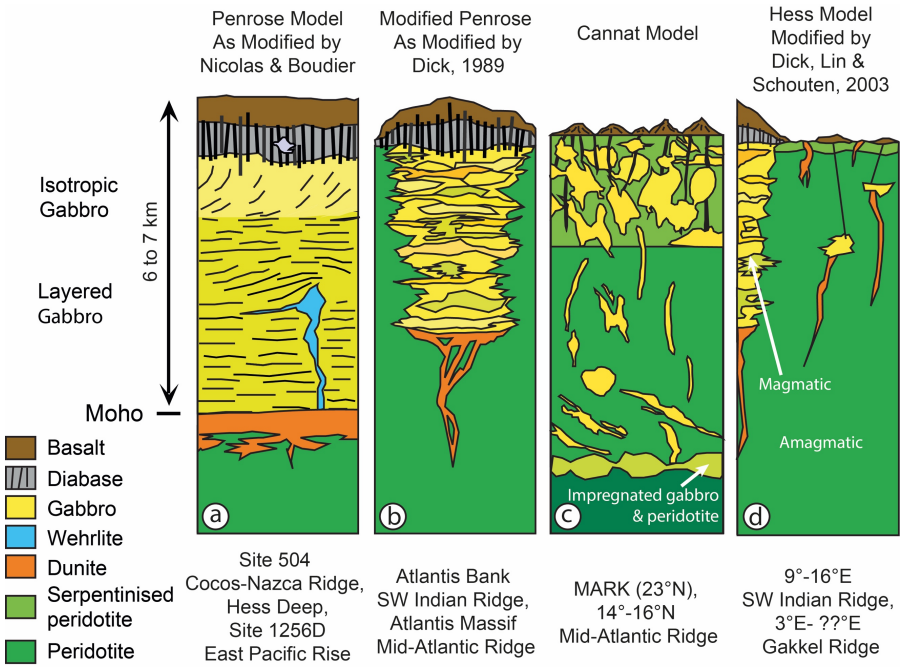

Fig. 2.9: Mid-ocean ridge crustal accretion models. **a** Layered Penrose oceanic crust typical of fast-spreading ridges comprising pillow basalts, dykes, gabbro and peridotite. **b** Oceanic crust typical of slow-spreading ridges. **c** Anomalous crustal structure at 14-16°N along the slow-spreading MAR. **d** Ultraslow-spreading oceanic crust, typical of the Gakkel Ridge, comprising alternating magmatic and amagmatic accretionary segments. Figure modified from Dick et al. (2006).

2.2.3.2 Lithospheric thickness and structure

The thickness of the lithosphere is predicted to increase at slower spreading rates due to the effects of conductive cooling. Therefore, the lithospheric thickness should increase towards the east along the Gakkel Ridge. To assess this, $Fe_{8.0}$ values of basalts, an index for the pressure of melting, can be used; this value is the FeO abundance corrected for the effects of fractionation and is the concentration of FeO at 8 wt.% MgO (Klein and Langmuir 1987). Higher values of $Fe_{8.0}$ are taken to indicate increased pressure of melting and in turn thicker lithosphere (Klein and Langmuir 1987). Data from Michael et al. (2003) reveal a trend of increasing $Fe_{8.0}$ towards the east is present along two portions of the Gakkel Ridge, within the WVZ and combined SMZ and EVZ (Fig. 2.11a); the increase in the former is much great than in the latter. Similarly, $Fe_{8.0}$ values of olivine-hosted melt inclusions increase toward the east (Wanless et al. 2014a) (Fig. 2.12). However, modification of the initial $Fe_{8.0}$ of the melt inclusions may have occurred through diffusive Fe-Mg equilibration (Wanless et al. 2014a). If only melt inclusion host glass values are considered from the study of Wanless et al. (2014a), there appears to be no systematic change in pressure of melting along the EVZ unlike that shown by glass $Fe_{8.0}$ values reported by Michael et al. (2003) for the entire ridge. In addition, there has been recent debate as to whether $Fe_{8.0}$ is a useful and meaningful parameter (e.g., Niu and O'Hara 2008; Gale et al. 2014; Niu 2016). Whilst Gale et al. (2014) defend conclusions drawn from the use of $Fe_{8.0}$, two criticisms of $Fe_{8.0}$ by Niu and O'Hara (2008) and Niu (2016) are that: (1) $Fe_{8.0}$ does not account for MgO, which along with FeO, is pressure sensitive; and (2) that erupted MORBs will have undergone sub-solidus re-equilibration during decompression which would result in the loss of the initial signature of depth of melting.

Seismic studies have also been undertaken to constrain the lithospheric thickness at both the ultraslow-spreading Southwest Indian Ridge (SWIR) and Knipovich Ridge (Schlindwein and Schmid 2016). Through determining micro-earthquake hypocentre depths, they show that earthquakes occur up to 35 km deep beneath peridotite dominated regions, and that the lower boundary of seismicity defining the extent of the lithosphere that behaves elastically can shallow up to 15 km beneath volcanic centres. This suggests the lithospheric thickness beneath ultraslow-spreading ridges can be highly variable. Using this seismic data, two types of ultraslow-spreading lithosphere are identified, magmatic and amagmatic (Fig. 2.13). Magmatic lithosphere is present beneath areas of volcanic activity and is both stronger and thinner than amagmatic lithosphere present in areas of peridotite exposure that exhibit serpentinisation. Whilst thinning of the lithosphere occurs in the vicinity of magmatic activity, top-down cooling due to deep serpentinisation can influence the topography of the base of the elastic

lithosphere (Schlindwein and Schmid 2016). Whilst the Gakkel Ridge was not directly investigated in this study, teleseismic earthquake records revealed the occurrence of strong earthquakes in the WVZ (strong magnetic anomalies and extensive basalt exposure) as opposed to the reduced seismicity in the SMZ (no large magnetic anomalies and extensive peridotite exposure); this is in agreement with that observed along the Knipovich and SWIR. This seismic study reveals the thickness of the lithosphere is highly variable along ultraslow-spreading ridges, with attenuation of the lithosphere thickness occurring in regions of magmatism; the significance of topography at the base of the elastic lithosphere is discussed in the following section.

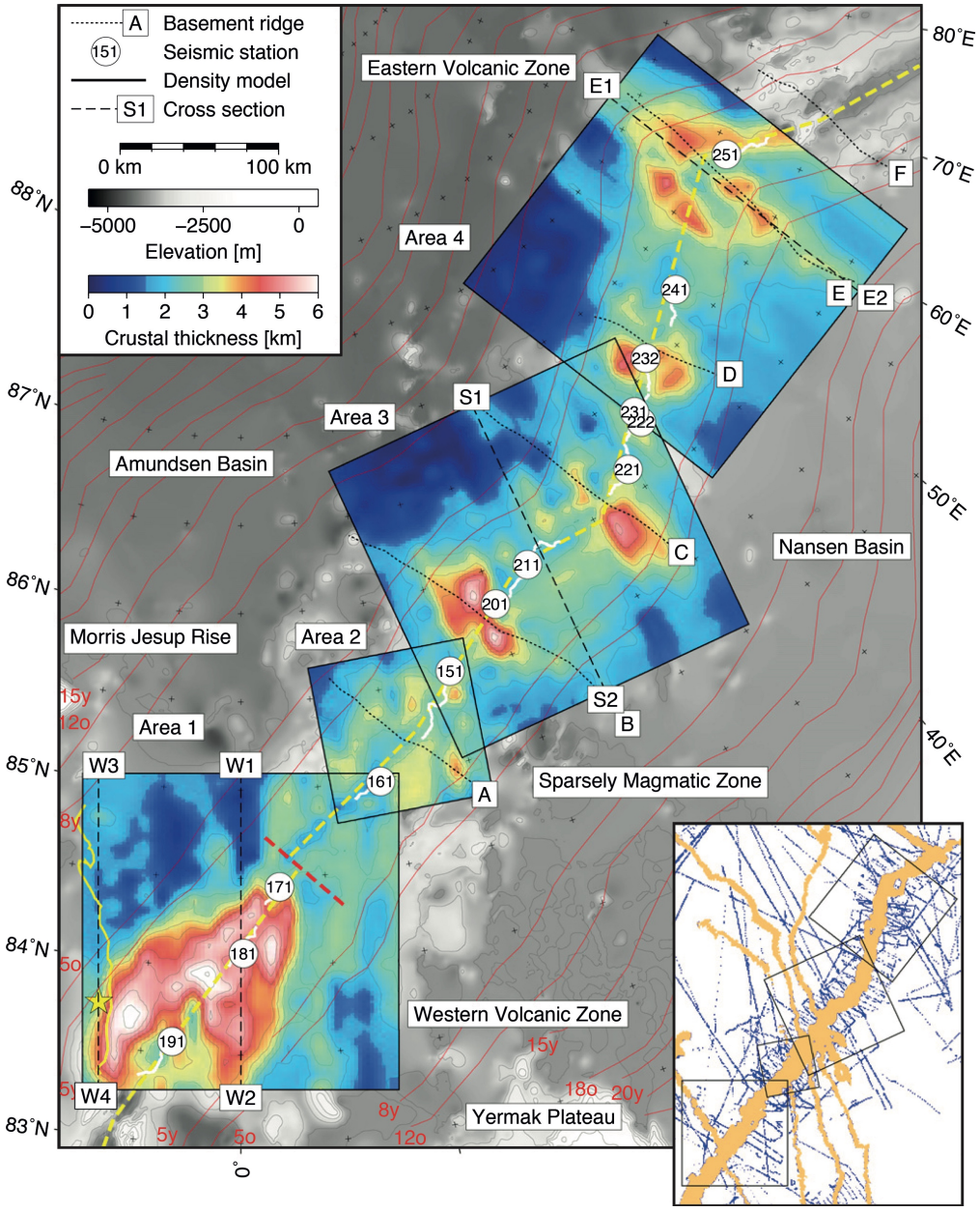

Fig. 2.10: Crustal thickness map generated using 3D gravity models. The greatest crustal thickness is found in the WVZ, whilst crustal thickness is highly variable in the SMZ and EVZ. Crustal thickness contour interval within each individual square is 0.5 km. Red lines indicate magnetic isochrons. The inset shows sonar (orange) and single beam (blue) measurement areas. Figure modified from Schmidt-Aursch and Jokat (2016).

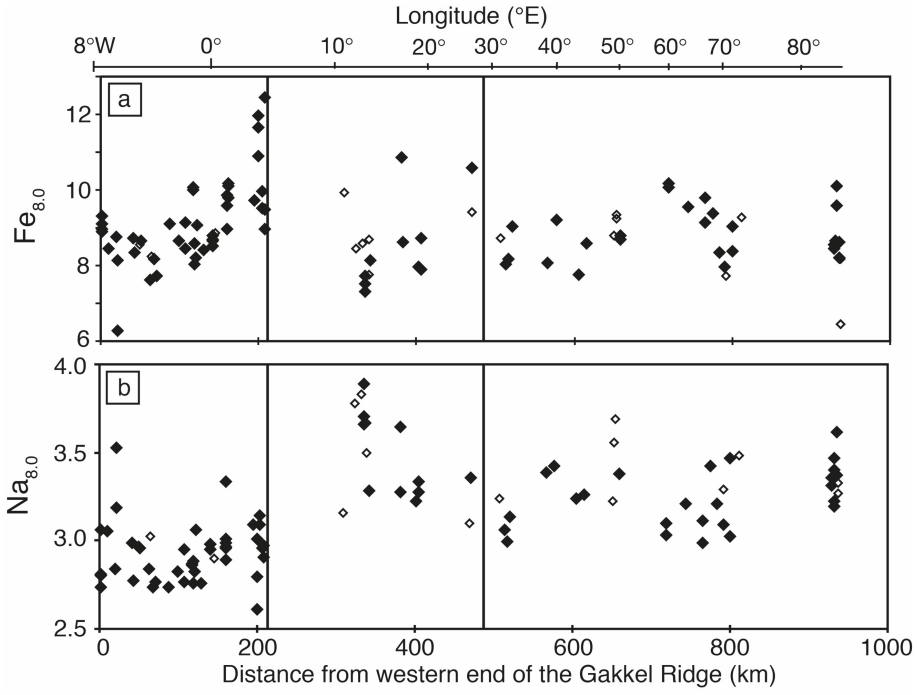

Fig. 2.11: a $Fe_{8.0}$ along-axis variation showing the pressure of melting increases toward the WVZ-SMZ boundary; $Fe_{8.0}$ does not appear to change much within the SMZ and EVZ. **c** $Na_{8.0}$ values, indicative of the extent of melting, are lower in the EVZ compared to both the SMZ and EVZ, indicating the extent of melting is higher. Redrawn from Michael et al. (2003).

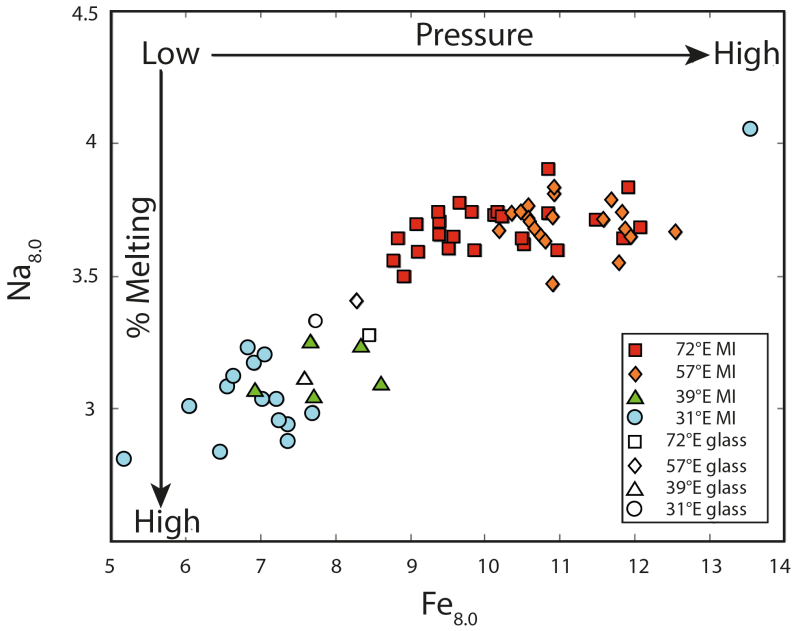

Fig. 2.12: $Fe_{8.0}$ and $Na_{8.0}$ values of olivine-hosted melt inclusions from the EVZ. Values indicate that melting pressure and extent become lower and higher respectively towards the west, host glass $Fe_{8.0}$ and $Na_{8.0}$ values do not show the same trend. Redrawn from Wanless et al. (2014a).

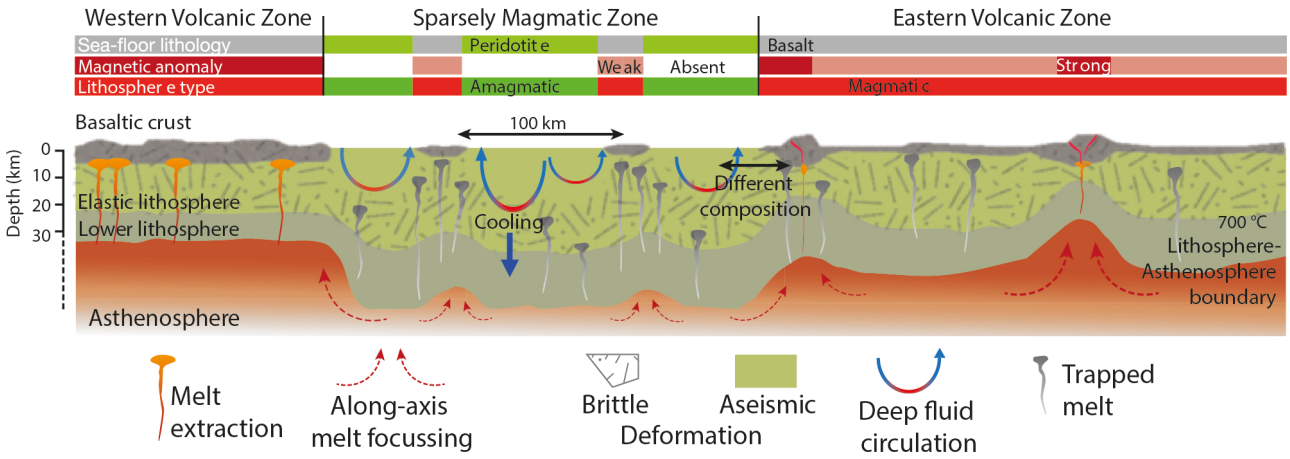

Fig. 2.13: Schematic of the Gakkel Ridge demonstrating the distribution of magmatic and amagmatic lithosphere and how shallowing of the lithosphere beneath magmatic centres creates topography at the lithosphere-asthenosphere boundary that can in turn enhance along-axis melt focusing. Modified from Schlindwein and Schmid (2016).

2.2.4 Melt focusing at ultraslow-spreading ridges

At mid-ocean ridges, melts produced in a broad ~50-100 km region become focused into a narrow <2 km zone located at the ridge axis (Phipps-Morgan 1987). In the literature, several hypotheses exist that attempt to explain how melts become focused beneath mid-ocean ridges: (1) migration of melt towards the ridge axis due to lateral pressure gradients generated by plate-driven asthenospheric corner flow (Morgan 1987; Spiegelman and McKenzie 1987); (2) melt migration within high porosity melt bands (Katz et al. 2006); and (2) 3D melt migration along a sloping high porosity boundary layer at the top of the melting column beneath mid-ocean ridges (Sparks and Parmentier 1991; Magde and Sparks 1997). Melt flow along an undulating boundary layer is especially key at ultraslow-spreading ridges where this mechanism is used to explain the extreme variations observed in crustal thickness (Cannat et al. 2003; Standish et al. 2008; Montési et al. 2011). Indeed, geophysical data have shown that the base of the elastic lithosphere at ultraslow-spreading ridges has significant topography; if the lithosphere-asthenosphere boundary mirrors this topography, melt focusing toward segment centres would be greatly enhanced (Schlindwein and Schmid 2016) (Fig. 2.13).

Regardless of the mechanism of melt focusing, first-order insights into melt delivery beneath mid-ocean ridges are provided by observations of volcanic landforms. Melt focusing from the mantle occurs at all spreading rates, however more efficient melt focusing at slower spreading rates (Cochran 2008) results in concentrated seamount

volcanism (MAR, SWIR, Gakkel Ridge and Knipovich Ridge (Okino et al. 2002; Dick et al. 2003; Jokat et al. 2003; Michael et al. 2003; Cochran 2008; Wanless et al. 2014a)) in comparison to elongate fissure volcanism at faster spreading ridges. Additionally, more efficient highly focused melt delivery along the ultraslow-spreading SWIR results in markedly larger seamounts than those found along the slow-spreading MAR (Cannat et al. 2003; Sauter et al. 2004). Similar volcanic morphologies are present along the Gakkel Ridge, with a change from elongate axial ridges in the WVZ (Fig. 2.4) to large roughly circular seamounts in the EVZ (Fig. 2.6) suggesting melt focusing becomes more efficient towards the east as spreading rate drops.

Aeromagnetic surveys provide additional evidence for the presence of discrete regions of melt focusing along the Gakkel Ridge (Jokat et al. 2003; Jokat and Schmidt-Aursch 2007) (Fig. 2.14). Each tectono-magmatic domain can be distinguished based on its magnetic characteristics. The magmatically robust WVZ is characterised by a high amplitude magnetic anomaly along most of its length that is associated with low seismic velocities (Jokat and Schmidt-Aursch 2007) (Fig. 2.14b). Both the magnetic anomaly and low seismic velocities combined with the abundance of basalts are taken as evidence for the presence of hotter mantle beneath the WVZ that allows for greater melt production (Jokat and Schmidt-Aursch 2007). Greater melt production is supported by low $Na_{8.0}$ values of basalts from the WVZ (Fig. 2.11b); Na is an incompatible element and becomes diluted as melting progresses resulting in lower $Na_{8.0}$ (e.g., Klein and Langmuir 1987). Magmatism within the WVZ is focused into elongate axial volcanic ridges similar to those found at faster spreading ridges. Magnetic anomalies within the SMZ and EVZ, as with volcanic morphology, are different to those in the WVZ, with high magnetic anomalies associated with basement ridges and basalt cover; magnetic anomalies in the intervening areas of deeper seafloor and peridotite exposure in the SMZ can drop to zero (Jokat et al. 2003; Jokat and Schmidt-Aursch 2007) (Fig. 2.14b). These magnetic anomalies are interpreted as the locus of strongly focused and prolonged melt supply from the mantle that has formed basement ridges that can be traced off-axis for up to 25 Myr (Jokat et al. 2003) (Fig. 2.14a). The lack of crustal thickening beneath two of the six basement ridges is attributed to (1) a very narrow region of melt supply, or (2) the effect of the melt supply region not being resolved in the seismic data (Jokat et al. 2003). Whilst $Na_{8.0}$ values of SMZ and EVZ glasses are not as low as basalts from the WVZ, basalts in the vicinity of three of basement ridges (31°E, 62°E and 70°E) (Fig. 2.11b) are slightly lower than adjacent locations, suggesting elevated melt production in their vicinity. An increase in the extent of melting westwards within the EVZ is suggested by $Na_{8.0}$ values of both glass (~80-55°E) (Fig. 2.11b) and olivine hosted melt inclusion (72-31°E) that get lower toward the west (Fig. 2.12).

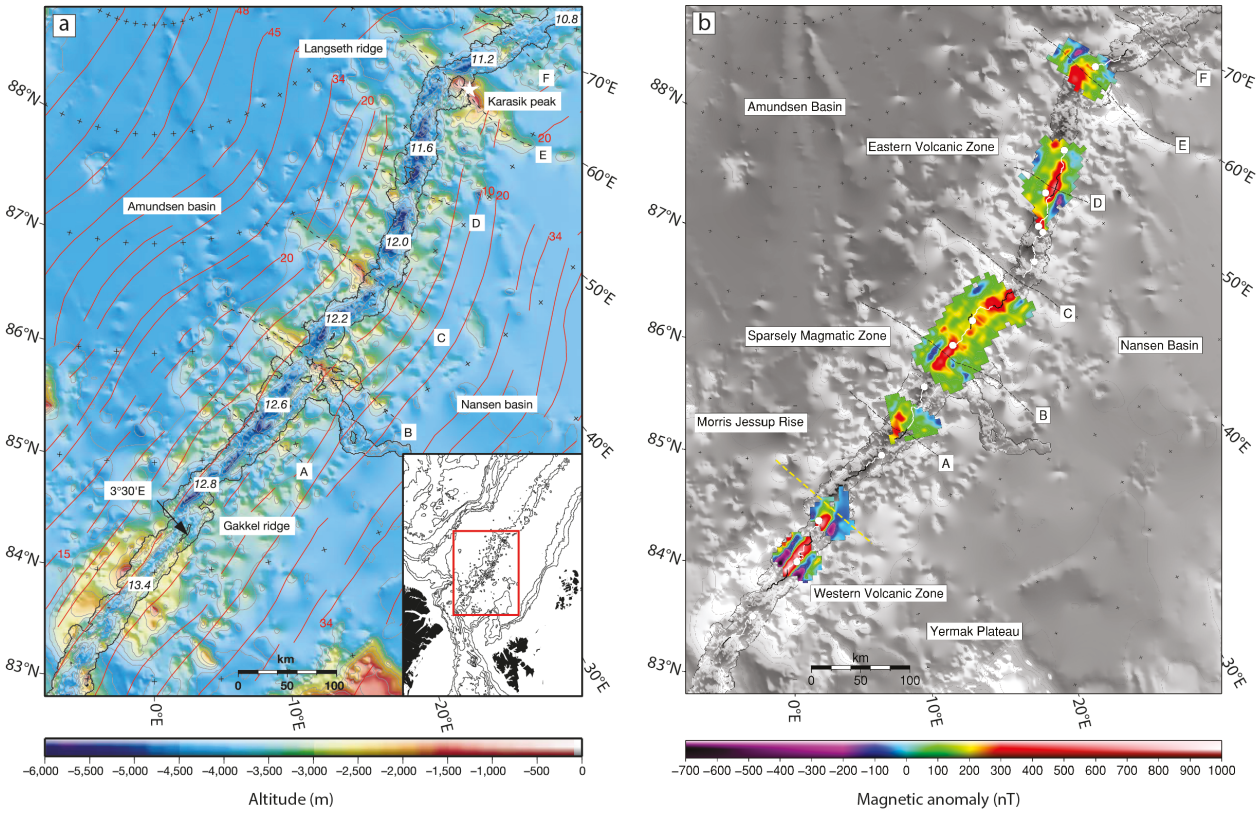

Fig. 2.14: a Bathymetric map showing the locations of six (a-f) basement perpendicular ridges. **b** Magnetic data from the Gakkel Ridge superimposed on Gakkel Ridge bathymetry (grey). More robust magmatism in the Western Volcanic Zone is associated with a more continuous magnetic anomaly compared to focusfocused magnetic anomalies associated with basement ridges in both the Sparsely magmatic and Eastern Volcanic zones. **a** adapted from (Jokat et al. (2003); **b** adapted from Jokat and Schmidt-Aursch (2007)

2.2.5 Mantle heterogeneity

Multiple studies using MORB, olivine-hosted melt inclusions and abyssal peridotites have shown the Gakkel Ridge mantle source to be highly heterogeneous (Mühe et al. 1993; Mühe et al. 1997; Goldstein et al. 2008; Liu et al. 2008; Wanless et al. 2014a; D'Errico et al. 2016).

The first insights into the nature of the Gakkel Ridge mantle were provided by three E-MORBs that revealed, contrary to earlier whole mantle convection and geochemical models developed by Hart (1984, 1988), that the Arctic mantle has DUPAL signatures (Mühe et al. 1993; Mühe et al. 1997). The DUPAL anomaly was originally described as a large southern hemisphere isotopic mantle domain characterised by higher Δ8/4, Δ7/4 and ΔSr (Hart 1984). DUPAL anomalies can be determined by quantifying: (1) $^{208}Pb/^{204}Pb$ and $^{207}Pb/^{204}Pb$ deviation from the Northern Hemisphere Reference Line

(NHRL); and (2) the absolute value of $^{87}Sr/^{86}Sr$ (Hart 1984). The NHRLs are defined by the following equations:

$$^{208}Pb/^{204}Pb = 0.1084(^{206}Pb/^{204}Pb) + 13.491$$

$$^{207}Pb/^{204}Pb = 1.209(^{206}Pb/^{204}Pb) + 15.627$$

The values of Δ8/4 and Δ7/4 can subsequently be determined by calculating the difference between the $^{208}Pb/^{204}Pb$ and $^{207}Pb/^{204}Pb$ values of a dataset (DS) and the NHRLs:

$$\Delta 8/4 = [(^{208}Pb/^{204}Pb)_{DS}-(^{208}pb/^{204}Pb)_{NHRL}]\times 100$$

$$\Delta 7/4 = [(^{207}Pb/^{204}Pb)_{DS}-(^{207}pb/^{204}Pb)_{NHRL}]\times 100$$

Whilst ΔSr, the magnitude of the $^{87}Sr/^{86}Sr$ ratio, is determined using:

$$\Delta Sr = [(^{87}Sr/^{86}Sr)_{DS}-0.7]10^4$$

The presence of a DUPAL signature in Gakkel MORB has been confirmed by Goldstein et al. (2008) using Sr-Nd-Pb isotope systematics. This anomaly is not present along the entire length of the Gakkel Ridge and is restricted to the WVZ and western section of the SMZ; the isotopic composition of the mantle changes abruptly at a boundary located in the middle of the SMZ (Fig. 2.15a). Basalts from the EVZ are geochemically similar to Atlantic and Pacific MORB, whilst WVZ basalts are similar to Spitsbergen lavas and Indian and Atlantic MORBs showing the DUPAL anomaly (Fig. 2.15b). The similarity of WVZ MORBs to Spitsbergen lavas and Indian and Atlantic MORBs is attributed to the influx of North Atlantic mantle following the separation of Greenland from Svalbard (Goldstein et al. 2008; Schmidt-Aursch and Jokat 2016). Recent Pb isotope studies support the absence of the DUPAL anomaly within the EVZ (Elkins et al. 2014). Goldstein et al. (2008) propose the source of the DUPAL signature in the WVZ is delaminated subcontinental lithospheric mantle (SCLM) that became incorporated into the asthenosphere during initial spreading, with the boundary between the two isotopic regions marking the junction between two isolated mantle domains. However, the origin of the DUPAL signature is not agreed upon, and is instead proposed to be due to a lower continental crust component in the source of Indian MORB (Escrig et al. 2004). It is possible that the DUPAL signature in the Indian and Arctic Oceans may arise through the contribution of different components to the mantle source.

Variable peridotite composition that cannot be explained by melting of a homogeneous upper mantle (e.g., LREE enriched refractory harzburgites) provide insights into the heterogeneous nature of the Gakkel Ridge mantle (D'Errico et al. 2016). It is proposed that the variability in peridotite compositions arises due to the occurrence of previous melting event(s) and depletion followed by subsequent melt infiltration and refertilisation; this produces a heterogeneous mantle comprising both depleted and fertile components

(D'Errico et al. 2016). In support of this, osmium isotopes reveal the presence of both fertile (radiogenic $^{187}Os/^{188}Os$) and refractory (unradiogenic $^{187}Os/^{188}Os$) domains within abyssal peridotites, with the depleted $^{187}Os/^{188}Os$ ratios supporting the occurrence of ancient partial melting events with ages up to 2 Ga (Liu et al. 2008). D'Errico et al. (2016) suggests that these ancient partial melting events may explain the abnormally high crustal thickness of 5.4 km yielded by studies of abyssal peridotite spinel compositions (e.g., Hellebrand et al. 2002). Importantly, the presence of both refractory and fertile domains within the upwelling mantle beneath mid-ocean ridges has implications for the use of MORBs to infer the composition of the asthenospheric mantle. Indeed, MORBs will preferentially sample the fertile mantle domains because refractory domains will not undergo subsequent partial melting (Liu et al. 2008).

Finally, the geochemical variability of olivine-hosted melt inclusion also suggest the presence of a heterogeneous mantle source beneath the EVZ (Wanless et al. 2014a). Wanless et al (2014a) attribute this variability to the presence of a mantle source comprising both depleted MORB and metasomatized mantle components. Using the water contents of olivine-hosted melt inclusions (0.15-0.43 wt.%) this metasomatized component has been suggested to contain up to 500 ppm H_2O (Wanless et al. 2014a). The presence of a metasomatized component (e.g., subcontinental lithosphere) was similarly identified to the west by Goldstein et al. (2008) using isotope and trace element systematics, however, Wanless et al. (2014a) highlight that due to the absence of isotopic signatures within the EVZ that are indicative of subcontinental lithosphere, the two metasomatized mantle components are not the same.

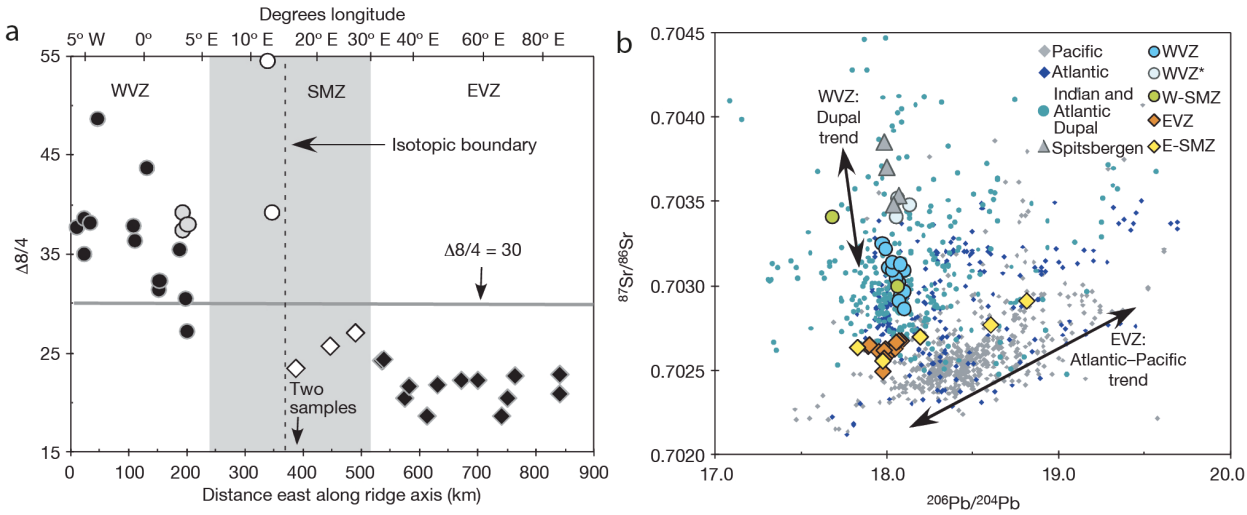

Fig. 2.15: a Δ8/4 variation along-axis. Two isotopically distinct regions, the Western Volcanic Zone (WVZ) and Eastern Volcanic Zone (EVZ), are identified and separated by an abrupt boundary located within the Sparsely Magmatic Zone (SMZ). **b** $^{87}Sr/^{86}Sr$ vs. $^{206}Pb/^{204}Pb$ for Gakkel Ridge basalts. Basalts from the EVZ form a trend similar to that defined by Atlantic and Pacific MORBs, whilst WVZ basalts have a trend similar to the basalts possessing the DUPAL anomaly (Indian and South Atlantic MORBs). **a** and **b** adapted from Goldstein et al. (2008).

2.2.6 Crystal-scale insights into the Gakkel Ridge plumbing system

To date there exists only three studies that use MORB crystal cargo (e.g., plagioclase and olivine and olivine-hosted melt inclusions) to investigate the magmatic plumbing system of the Gakkel Ridge (e.g., plagioclase, Zellmer et al. (2011); and olivine, Shaw et al. (2010) and Wanless et al. (2014a)).

2.2.6.1 Plagioclase diffusion studies

Using Sr diffusion systematics in plagioclase, Zellmer et al. (2011) propose that crystal residence times of the order of days to several months are consistent with plagioclase crystallisation occurring almost entirely during dyke injection. This precludes prolonged storage and crystallisation within an axial melt lens. However, as shall be discussed in greater detail in Chapter 5, this study has drawn its conclusions from a single sample from the WVZ of the Gakkel Ridge and analysed only simple, large (<2 mm) individual plagioclase that showed either concentric or no visible zonation; as will be shown in Chapter 5, such crystals are highly atypical of the plagioclase crystal cargo from the Gakkel Ridge.

2.2.6.2 Crystallisation pressures: Olivine-hosted melt inclusions

In addition to providing insights into the composition of the mantle source (section 2.2.5) and extent (section 2.2.4) and depth of melting (section 2.2.3.2) (Shaw et al. 2010; Wanless et al. 2014a,b) volatile contents of olivine-hosted melt inclusions have been used to constrain crystallisation depths within Gakkel Ridge plumbing system (Shaw et al. 2010; Wanless and Behn 2017). Using the pressure dependence of CO_2 and H_2O (e.g., Dixon and Stolper 1995; Dixon et al. 1995), Shaw et al. (2010) show that crystallisation occurs within the Gakkel Ridge from seafloor depths up to 9 km below the seafloor. The volatile contents of melt inclusions from the Juan de Fuca Ridge (JdFR) and EPR reveal similar maximum depths of crystallisation to the Gakkel Ridge of 0.31-9.6 km and 0.29-7.14 km below the seafloor, respectively (Wanless and Shaw 2012).

Whilst greater crystallisation depths along the JdFR compared to the EPR are consistent with reduced spreading rates that result in diminished magma flux, cooler crust and thicker lithosphere (Wanless and Shaw 2012), maximum depths of crystallisation at the JdFR are remarkably similar to crystallisation depths at the Gakkel Ridge. This is somewhat surprising seeing as, compared to the JdFR, melt flux and lithospheric thickness at the Gakkel Ridge are predicted to be both significantly lower and higher respectively; in turn one might expect greater depths of crystallisation at progressively

slower spreading rates. Indeed, such a relationship is shown by basalt major element barometers, with crystallisation pressures increasing and becoming more variable with decreasing spreading rate (Wanless and Behn 2017). Major element barometers will be discussed in more detail in Chapter 6.

2.3 Summary

Whilst the Gakkel Ridge has been studied for several decades, it is clear that much of the research has focused on constraining the physical structure of the ridge (e.g., crustal structure and nature of melt supply) and using exposed mantle peridotites to gain insights into the composition of the mantle. Therefore, there are very few studies which provide direct insights into the nature of the Gakkel Ridge magma plumbing system or the processes occurring within it.

Chapter 3

Samples and analytical methods

Chapter 3

3.1 Sampling

Samples used in this thesis were collected during the international Arctic Mid-Ocean Ridge Expedition (AMORE, 2001) using two research ice-breakers (PFS Polarstern (Alfred Wegener Institute for Polar and Marine Research, Bremerhaven, Germany) and USCGC Healy (Seattle, USA)) which obtained both dredge samples and geophysical data. A total of ten sampling areas were chosen to ensure that each ridge environment and volcanic morphology present within the axial valley was represented in the sample set (Table 3.1; Fig. 3.1). Samples were collected from Woods Hole Oceanographic Institution, Massachusetts. Hand sample descriptions are in Electronic Appendix 1. Additional samples from within the EVZ were collected but not used in this study.

Table 3.1 Study sample areas

Segment	Location name	Location	Sample site description
WVZ	5°W AVR	5°W	Elongate axial volcanic ridge
	2°W AVR	2°W	Elongate axial volcanic ridge
	3°E Seamounts	3°E	Basalts immediately before WVZ-SMZ boundary in the vicinity of seamounts
SMZ	9°E Valley Wall	9°E	Isolated basalt outcrop amongst peridotite
	12°40'E AVR	12°40'E	Elongate axial volcanic ridge
	18°50'E Basement Ridge	18°50'E	Transect across basement perpendicular ridge
EVZ	31°E Basement Ridge	31°E	Transect across basement perpendicular ridge
	37°E Seamount and 38°E random basalt	37°E 38°E	Seamount and random basalt on valley wall
	48°E Deep Sea Floor	48°E	Deep seafloor
	84°40'E Seamounts	84°40'E	Small flat-topped seamount to the west, large circular volcanic edifice

3.2 Sample preparation

3.2.1 Polished slabs

To maximise the sample surface area and minimise crystal cargo destruction, large polished slabs were made of 114 samples (Fig. 3.2). Polished slab preparation involved three stages; sawing, grinding and polishing. Once target areas had been sawn, each sample was ground by hand using progressively finer silicon carbide grit (220-1000) to remove any surface topography. Samples with excess topography were initially ground flat using a diamond grinding wheel. Samples were then each washed for 10 minutes in an ultrasonic bath before being polished by hand using a polishing wheel and 0.3 μm aluminium oxide powder mixed 1:1 with water. Some smaller blocks were polished using

an automatic polishing machine. All samples were then washed in an ultrasonic bath a second time.

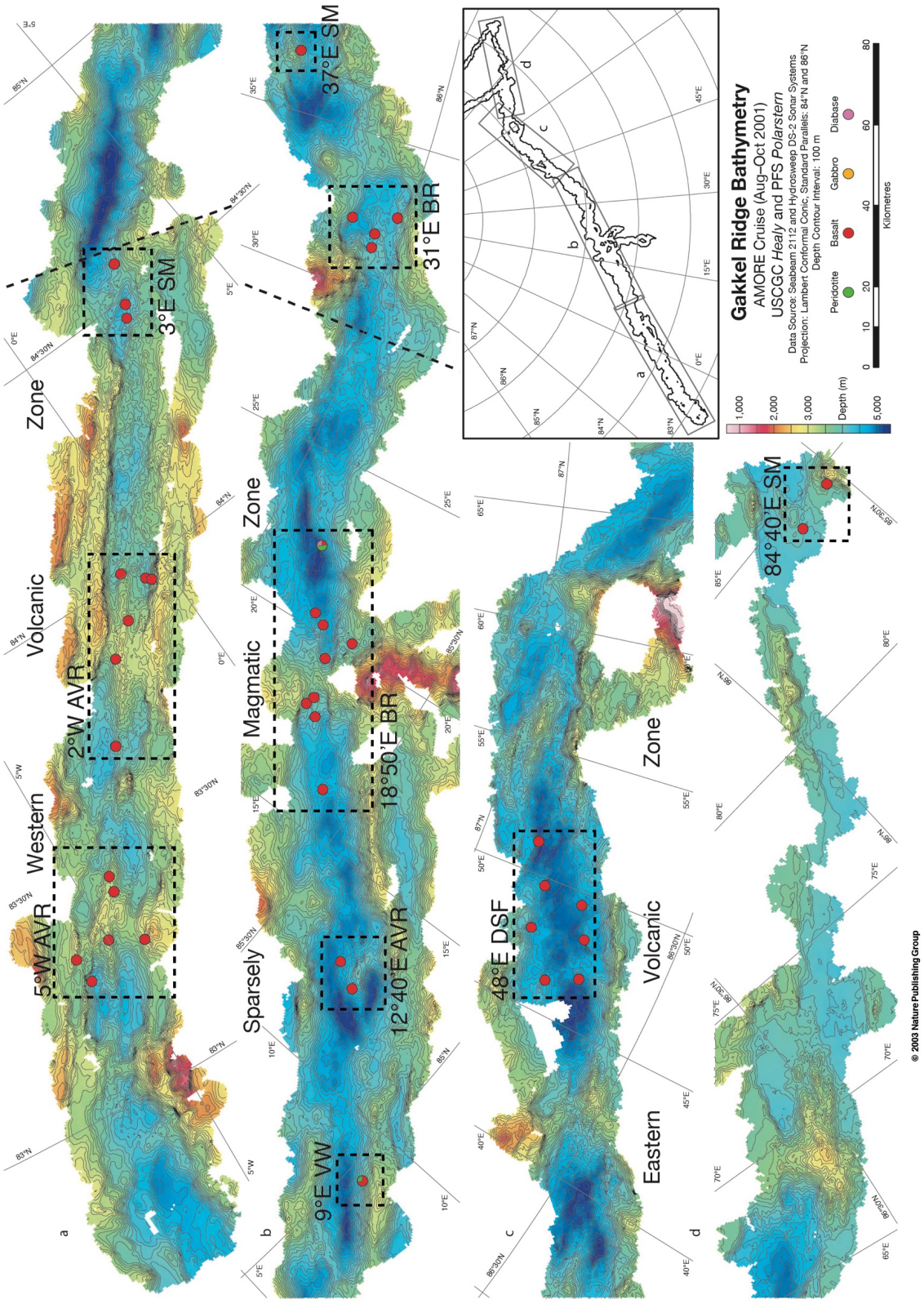

Fig. 3.1: Bathymetric map of the Gakkel Ridge showing each of the ten sampling locations. Adapted from Michael et al. 2003.

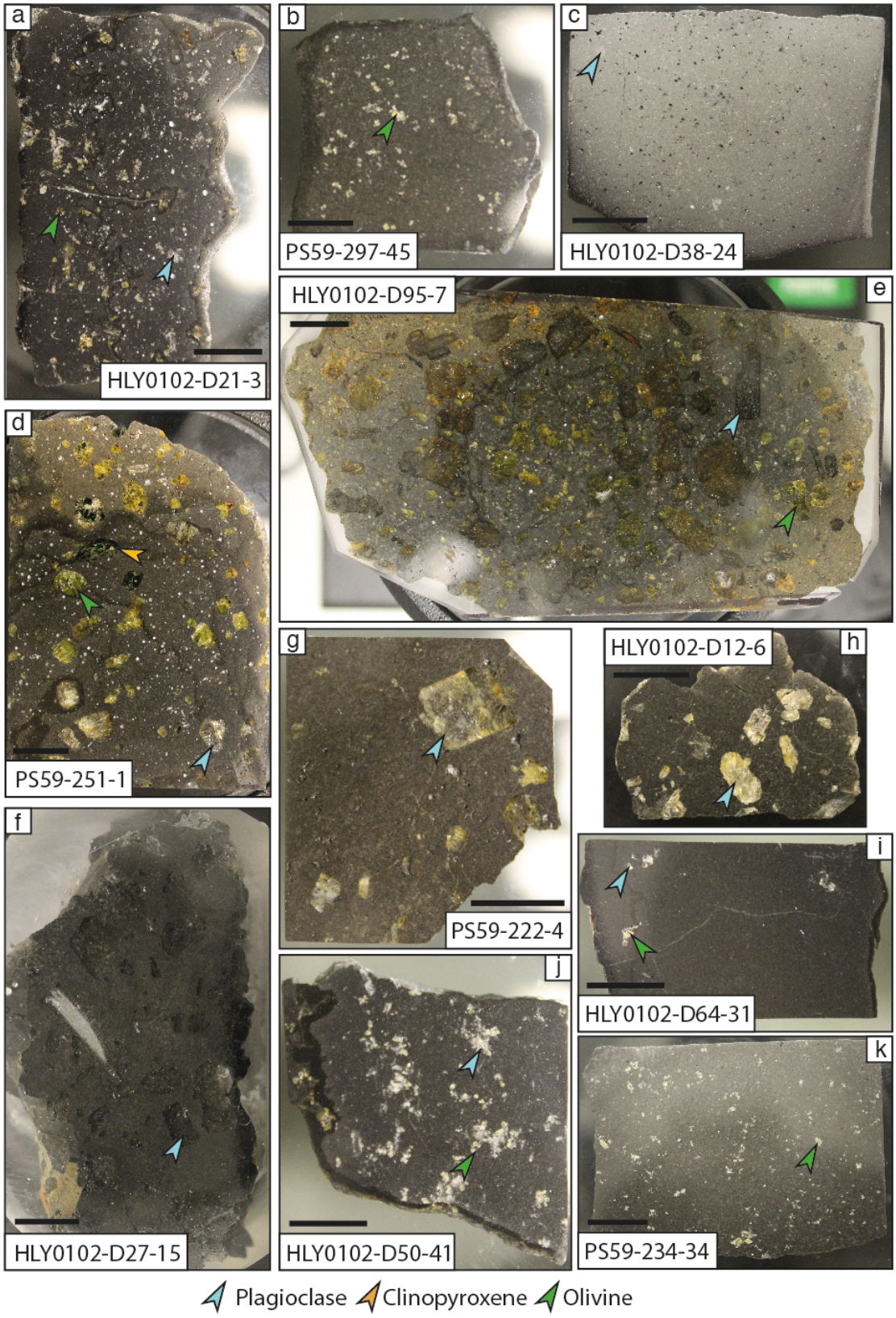

Fig. 3. 2: Examples of polished slabs used in the project. Samples shown are representative of the different types of basalts. Basalts can contain crystal cargo of olivine (**b**, **k**), plagioclase (**c**, **g**, **f**, **h**), plagioclase and olivine (**a**, **e**, **l**, **j**), olivine, plagioclase and clinopyroxene (**d**). and clinopyroxene. All scale bars are 1 cm.

3.2.2 Polished blocks

Polished blocks were made for glass and melt inclusion analysis; all polished blocks were 1 inch in diameter. For the former, glass chips were stuck down to double sided tape and set in Araldite 2020 epoxy mixed according to package instructions. These blocks were then ground and polished to expose the glass chips. To make the polished blocks for melt inclusion analysis, the target crystals containing the melt inclusions were first cut out of the larger polished slabs. The polished surfaces were stuck to double sided tape; the chips were then set in EpoThin^{TM} 2 Epoxy Resin and Hardener. These blocks did not require further grinding or polishing; in some cases, excess resin was peeled from the polished surface of some chips. Epoxy blocks were left for >2 months before Ion Probe analysis was undertaken.

3.3 Analytical SEM

Crystal cargo imaging and mineral and glass major element analysis was carried out using a Zeiss Sigma HD Field Emission Gun analytical scanning electron microscope (ASEM) outfitted with dual 150 mm^2 Oxford X-MaxN silicon drift detector energy dispersive spectrometers in the School of Earth and Ocean Science, Cardiff University (UK).

3.3.1 Backscatter electron (BSE) image acquisition

Other than avoiding crystals that had been cut through at the margins of the samples, there were no selection criteria for imaged crystals to ensure the image database collected was not biased. Optimal contrast and brightness settings were selected for each phase during BSE image acquisition. Depending on the crystal size, individual or multiple images were collected, with multiple images of one crystal later montaged together using Oxford Instrument Aztec software. The total number of crystal images acquired is shown in Table 3.2.

3.3.2 Quantitative EDS analysis

Quantitative EDS analysis used a 1 nA beam current, 20.0 kV accelerating voltage, a fixed working distance of 8.9 mm and a 60 nm aperture. The beam current was measured using a stage-mounted faraday cup. EDS spectra were acquired over 20-30s live time using both detectors with an output count rate of ~136 kcps. A defocused beam rastering over 5-10 μm^2 areas was used to minimise Na loss in both plagioclase and glasses. Oxford Instruments Aztec Software was used to process and quantify raw data using the internal XPP matrix correction. The total number of minerals analysed is shown in Table

3.1. Mineral and glass data can be found in Electronic Appendix 2. A comprehensive suite of standards (Appendix 1) were used to calibrate EDS analysis of all mineral phases and glass; precision and accuracy of mineral and glass standard measurements, and equations used to calculate these values, can be found in Appendix 1.

Table 3.2 Crystal cargo imaging and analysis

Crystal type	Individual plagioclase	Individual olivine*	Individual clinopyroxene	Mono-mineralic glomerocryst	Poly-mineralic glomerocrysts
Number imaged	1252	2110	69	167	377
Number analysed	590	372	69	77	75

* This includes mono-mineralic olivine glomerocrysts.

3.3.3 Determination of modal mineralogy

Modal mineralogy was determined by collecting element maps of 95 samples. Maps were collected using a 120 nm aperture and 20.0 kV accelerating voltage with a resulting beam current of ~4 nA. Maps were run at 95-110x magnification, with a step size of 20-22 μm, a dwell time between 3200-4000 μs and a process time of 0.5 μs. All maps were background corrected and overlaps were deconvolved using Oxford Instruments Aztec software. To determine sample modal mineralogy the maps were processed using the clustering algorithm of the AutoPhaseMap function in Aztec (Statham et al. 2013). The clustering algorithm determines what phases (e.g., plagioclase, olivine, clinopyroxene and spinel) are present by identifying groups of pixels within each element map which show similar spectral profiles. Pixels at the boundaries between phases are often excluded from phases analysis because their spectra are a mixture of two phases, hence the spectra cannot be assigned to one particular phase. Phase maps of each sample analysed for its modal mineralogy are are available directly from the author (e.bennett@hotmail.co.uk); two examples are shown in Figure 3.3.

3.4 Plagioclase LA-ICP-MS

Plagioclase minor- and trace elements were measured at the National Oceanography Centre at the University of Southampton (UK) using a New Wave UP193FX laser ablation system coupled to a HR-ICP-MS Thermo Fisher Scientific ELEMENT 2XR mass spectrometer. Beam spot sizes of 10 μm, 20 μm and 50 μm were used depending on the size of the feature being analysed. Target locations were pre-determined from BSE images. The laser fired with a frequency of 5 Hz at 80% energy over 35 seconds. 35 s

gas blanks were run at the start and end of each sample run, with standards (NIST 610, NIST 612, BCR-2G and BHVO-2G) analysed at the start of each sample run. Data was processed according to spot size and additionally gas blank corrected, with the CaO content determined through EDS analysis serving as an internal standard. Plagioclase LA-ICP-MS data along with precision and accuracy of standard measurements can be found in Electronic Appendix 4.

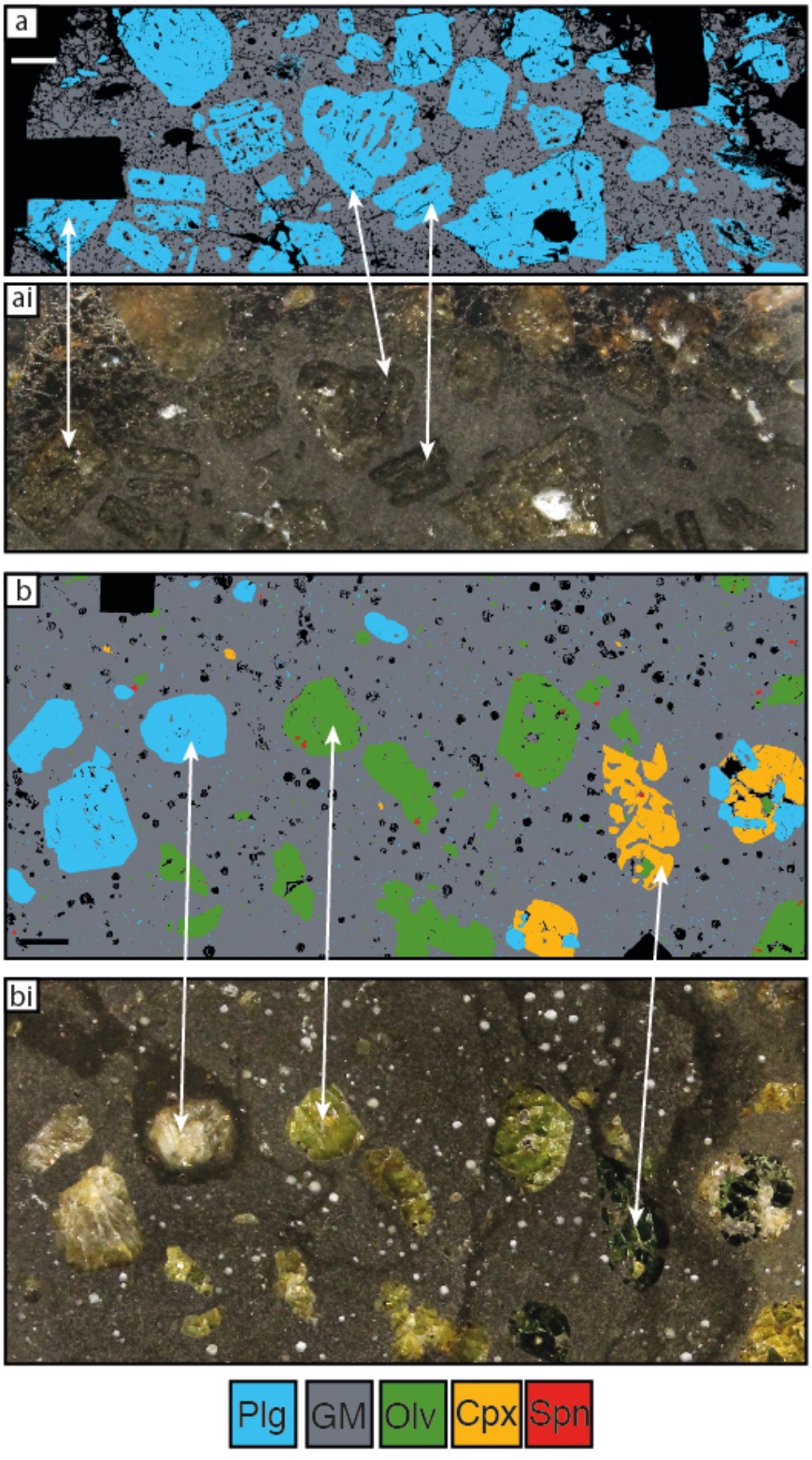

Fig. 3. 3: Images of polished blocks with their corresponding modal maps. The locations of crystals within the blocks and maps are linked by white arrows. Abbreviations are as follows: Plg, plagioclase; GM, groundmass; Olv, olivine; Cpx, clinopyroxene; Spn, spinel. Scale bars in the modal maps are 2.5 cm.

3.5 Ion probe melt inclusion analysis

3.5.1 Melt inclusion selection

Potential target melt inclusions were identified from BSE images (section 3.3.1). For volatile analysis, melt inclusions were selected that were glassy, had no visible gas bubbles (except two), and had diameters greater than 20 μm. These criteria were evaluated using BSE and secondary electron (SE) images of each potential melt inclusion. After samples had been characterised texturally, carbon coats were removed by polishing with MetaDi^{Tm} Supreme Polycrystalline Diamond Suspension (0.25 μm). Subsequentially, samples were cleaned with acetone and then washed in an ultrasonic bath for 10 minutes; this process was repeated twice. For ion probe analysis, samples were gold coated.

3.5.2 Instrumentation setup

Melt inclusion CO_2, H_2O, K_2O and B contents were measured using the Cameca IMS4f ion microprobe at the Edinburgh Ion Microprobe Facility (UK). A ~5 nA $^{16}O^-$ primary beam with a 14.5 kV impact energy beam was used. Melt inclusions were analysed for CO_2 first in a separate measurement before H_2O and other elements, with CO_2 measured at high mass resolution (M/ΔM = 1200) sufficient to avoid interference between $^{24}Mg^{2+}$ and $^{12}C^+$. Energy filtering of the secondary ions was applied, using offsets of 75 eV and 50 eV for H_2O and CO_2, respectively, using a 50 eV energy window. Image fields of 25 μm and 50 μm and field apertures with effective diameters of 8 μm and 16 μm were used during H_2O and CO_2 analysis, respectively. Prior to each measurement the beam was aligned relative to the centre of the field aperture. H_2O and CO_2 target locations were rastered for 2 and 4 minutes prior to each analysis using analysis beam conditions to remove surface contamination; during this time peak mass positions were centred. Each analysis ran for 4 minutes following rastering and comprised ten cycles. For H_2O and CO_2 measurements, counts were normalised to ^{30}Si and corrected for known SiO_2 content of the samples, except $^1H/^{30}Si$ as this has been shown to have a matrix effect proportional to the material's SiO_2 content. The analyses were calibrated against a set of basaltic glass standards of known CO_2 (0-2183 ppm) and H_2O (0.00-3.07 wt.%) contents (Shishkina et al. 2010). Instrumental blank measurements for H_2O and CO_2 were made on plagioclase in each mount and subtracted from the raw count rates: targets in 12 mounts were analysed. Uncertainty and accuracy of SIMS analysis can be found in Appendix 1. Raw volatile element data are present in Electronic Appendix 5.

3.5.3 Potential for carbon contamination

Having previously carbon coated samples for initial textural characterisation using SEM, residual carbon may have been left on the surface of the melt inclusions; this may have resulted in high melt inclusion CO_2 content. However, multiple steps were taken to minimise and identify carbon contamination.

1) All carbon coats were thoroughly removed, and samples were cleaned, after SEM analysis.
2) Prior to each analysis, the surface was pre-sputtered (i.e., rastered) for 4 minutes over an area larger than the analytical area to remove any carbon at the surface. The effectiveness of this was tested by measuring backgrounds on both olivine and plagioclase; these backgrounds were then subtracted from all analyses. Any additional contamination would have come from somewhere other than the surface, such as cracks. However, melt inclusions with visible cracks, within which carbon may have been trapped, were avoided.
3) The average $^{12}C^+$ value of the last six analysis cycles was used to calculate melt inclusion CO_2 contents; this avoids including cycles closer to the surface which may have been affected by residual carbon. Analyses affected by surface contamination would show cycles with $^{12}C^+$ counts that drop off from the surface; two examples of such analyses are shown in Fig. 3.4 (j and l) and were removed. Furthermore, if a cycle hit a crack containing residual C, a significant peak in $^{12}C^+$ counts would be expected; only one groundmass glass analysis shows a significant peak in $^{12}C^+$ (Fig. 3.4k).
4) Finally, melt inclusion analyses show similar trends in C/Si RSE (%) and standard deviation (SD) vs. ^{12}C counts as standards analysed during melt inclusion analysis (Fig.3.5).

Accounting for the above, the CO_2 content of melt inclusions is not a result of carbon contaminating and reflects natural variation.

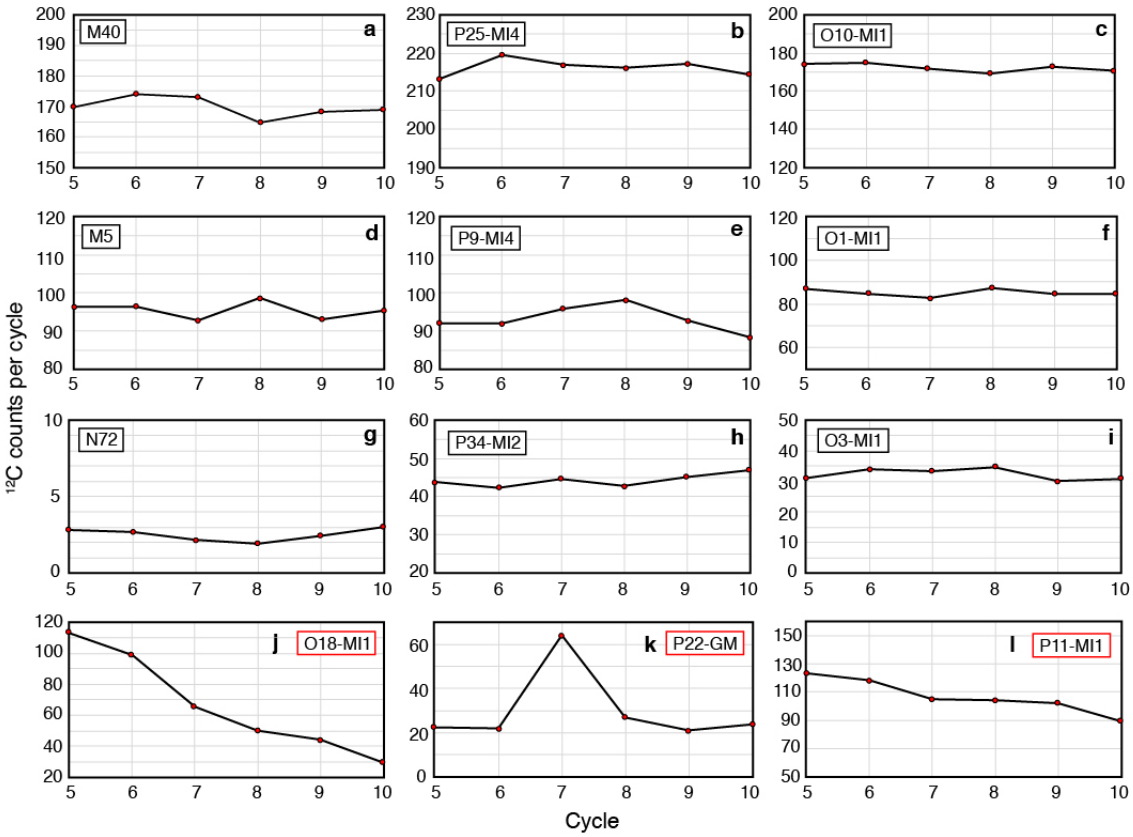

Fig. 3.4: ^{12}C counts per cycle for selected melt inclusion CO_2 analyses: standards, **a**, **d**, and **g**; plagioclase, **b**, **e**, and **h**; and olivine **c**, **f** and **i**. Melt inclusion CO_2 contents was determined using the average ^{12}C of cycles 5-10 of each analysis. Profiles of three standards, M40, M5 and N72, are shown in **a**, **d** and **g**, respectively; the CO_2 contents of these standards are 2183, 990 and 0 ppm. Excluded analyses are those characterised by constantly dropping ^{12}C counts (**j** and **l**), and those with large peaks in ^{12}C (**k**).

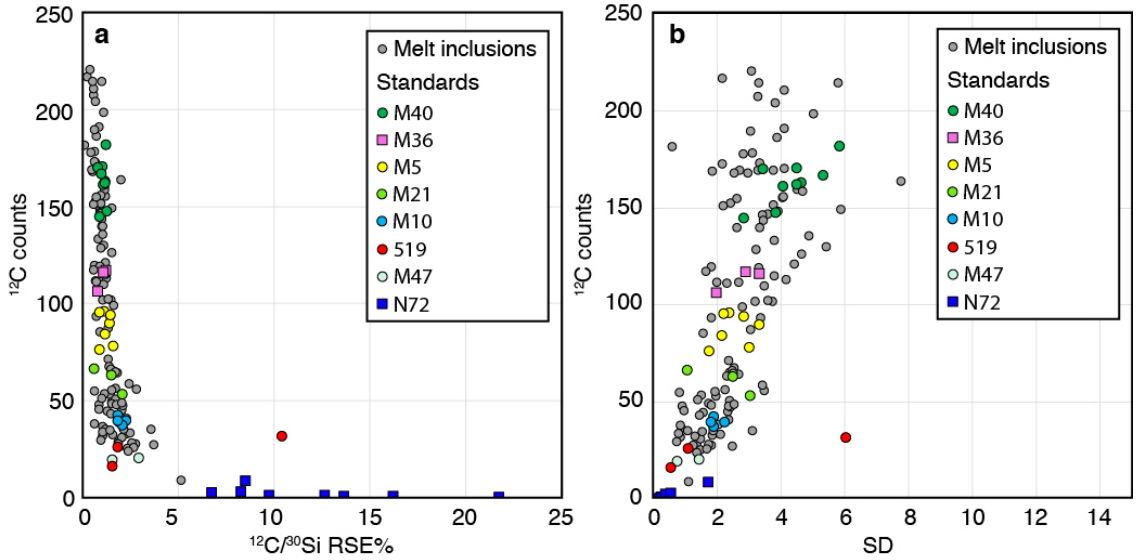

Fig. 3.5: $^{12}C/^{30}Si$ RSE (%) and standard deviation (SD) vs. ^{12}C counts of the last five analytical cycles in standards and analysed melt inclusions. Standards and melt inclusions show similar distributions to one another. $^{12}C/^{30}Si$ RSE (%) for both standards and melt inclusions increases with decreasing ^{12}C counts (**a**). The SD increases with increasing ^{12}C counts for both melt inclusions and standards (**b**).

Chapter 4
Crystal cargo database

Chapter 4

4 Crystal cargo database

Using back-scattered electron (BSE) images, a database documenting and quantifying crystal cargo textures has been created. The following chapter outlines the classification of olivine, plagioclase and pyroxene crystals, as well as mono- and poly-mineralic glomerocrysts. This methodology provides details about variables in the database that are most important for the following chapters. The full crystal cargo database and classification tables can be found in Electronic Appendix 6.

4.1 Individual crystal and glomerocryst classification

Individual crystals are present as either macrocrysts (>1 mm) or microcrysts (<1 mm), the former commonly having attached components. Glomerocrysts are defined as crystal clusters comprised of two or more similarly sized components; they can be mono- or poly-mineralic. Poly-mineralic glomerocrysts are classified using a similar classification to the mono-mineralic glomerocrysts with more phases taken into account.

Individual plagioclase and olivine crystal sizes are measured as their apparent maximum length; the aspect ratio is calculated using the width of the crystal normal to this. If the crystal is not euhedral, the width is taken as the widest part of the crystal perpendicular to the maximum length. Glomerocrysts (mono- and poly-) are measured as a whole, the maximum length being the longest dimension accounting for all components, with the width measured as the maximum width of that crystal cluster perpendicular to the length. The size range of each phase within the glomerocrysts and grouped olivines is recorded. If there is only one component of a phase present in a glomerocryst its size is recorded as the maximum length. It must be noted that the size recorded for each crystal may not be its maximum length due to the 3D nature of the crystals.

4.1.1 Glomerocryst configuration and component contacts

Components within glomerocrysts can exhibit three different contact types; point, planar and embedded (Table 4.1, Fig. 4.1). Accounting for these different types, glomerocryst configurations can be classified as either open or closed (Table 4.1). Open configurations are those with cavities between the glomerocryst components (Fig. 4.1b), whilst closed configurations have no cavities (Fig. 4.1d).

Table 4.1 Glomerocryst component contacts and structure

Feature	Categories			
Glomerocryst component contacts	Embedded		Planar	Point
Glomerocryst structure	Open (voids)		Closed (no voids)	

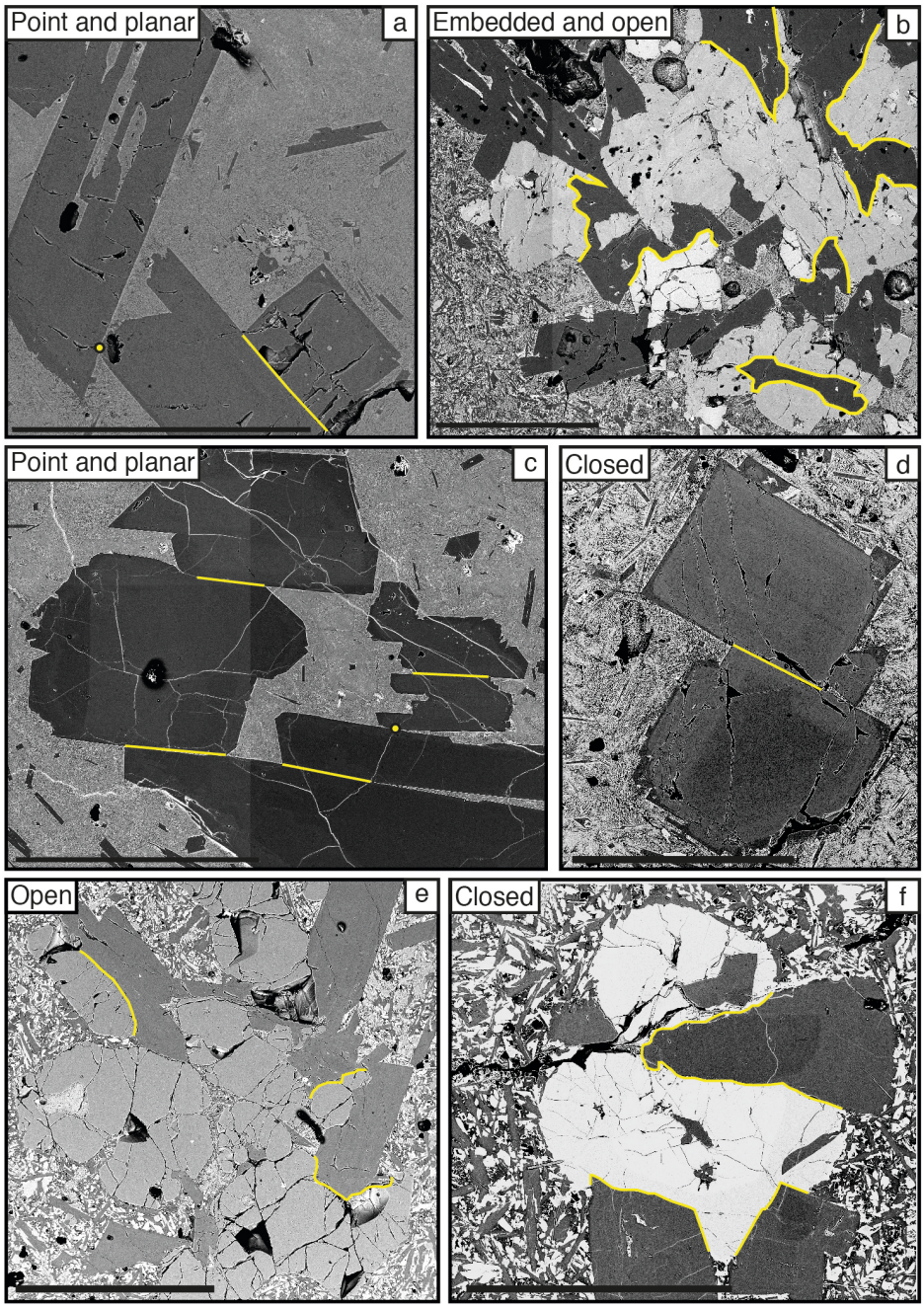

Fig. 4.1: Glomerocryst configuration and component contacts. Glomerocryst configuration: open, a-c, e; closed, d, f. Glomerocryst contacts: point (yellow dots), a, c; planar (straight lines), a, c, d; and embedded (curved yellow lines), b, e, f. Scales 1 cm.

4.2 Crystal morphologies

4.2.1 Plagioclase

Plagioclase morphologies are described in two ways, first by assigning a crystal habit (Table 4.2) and second a number from 1-5 relating to how euhedral (1) or anhedral (5) the crystal is. For example, crystals with tabular and resorbed morphologies tend to have lower and higher values, respectively; tabular crystals can be subhedral as long as the tabular crystal habit is recognisable. All skeletal morphologies are assigned a value of 2. The same classification is used for individual plagioclase and plagioclase in both mono- and poly-mineralic glomerocrysts.

Table 4.2 Mineral habits

Mineral	Categories			
Plagioclase	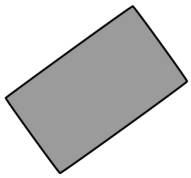 Tabular	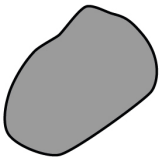 Resorbed	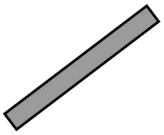 Acicular	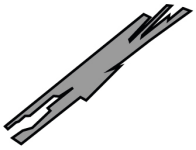 Skeletal
Olivine	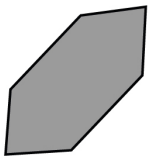 Euhedral	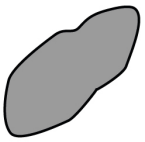 Resorbed/ Anhedral	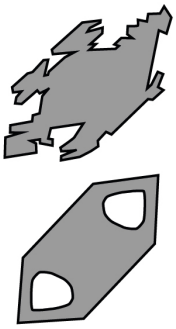 Skeletal/ Hopper	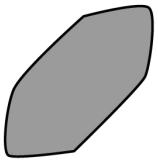 Subhedral

4.2.2 Olivine

Olivine, present as an individual crystal or a grouping of crystals, is classified as one of four morphologies (Table 4.2). For grouped olivines, the number and size range of components is determined, and the types of zoning and habit recorded. Pyroxene has the same habit classification scheme as olivine.

4.3 Mineral zoning

The type of zoning in plagioclase (Fig. 4.2), olivine (Fig. 4.4) and pyroxene (Fig. 4.5) is defined based on patterns in back-scatter intensity (Table 4.3). Other than patchy zoning, the type of zoning (Table 4.4) present in each individual phase or glomerocryst component is recorded as present or absent (1 or 0 respectively). Patchy zoning is defined here as discontinuous patches (sometimes a mottled appearance) of either

higher or lower anorthite/forsterite than the surrounding crystal. Patchy zoning is classified on a scale of 0 to 5; when absent a value of 0 is assigned. In plagioclase, if present, patchy zoning is assigned a value between 1 and 5 based on its intensity, 1 being low and 5 high (Fig. 4.3); patchy zoning is marked as present (1) or absent (0) in olivine and pyroxene. Oscillatory zoning in olivine and plagioclase is defined differently. Oscillatory zoning in plagioclase is identified as fine-scale compositional oscillations, whilst in olivine it is identified as coarse compositional reversals (Table 4.4). Plagioclase with concentric zoning is classified as having both normal and reverse zoning; there is no separate classification for concentric zoning. Classification of pyroxene zoning is most similar to olivine; however pyroxenes exhibit sector zoning.

Table 4.3 Zoning patterns in plagioclase, olivine and pyroxene

Zoning	Phase	BSE intensity	Explanation
Normal	Plagioclase	Light→dark	Higher An followed by lower An
	Olivine/Pyroxene	Dark→Light	Higher Fo followed by lower Fo
Reverse	Plagioclase	Dark→Light	Lower An followed by higher An
	Olivine/Pyroxene	Light→dark	Lower Fo followed by higher Fo
Oscillatory	Plagioclase	Alternating light-dark bands	Fine scale oscillations in composition (plagioclase) or coarse compositional reversals (olivine)
	Olivine/Pyroxene		
Patchy	Plagioclase	Irregular distribution of dark and light patches	Patches can be higher or lower intensity than the including composition
	Olivine/Pyroxene		
Sector	Plagioclase/ pyroxene	Bright and dark sectors controlled by crystallographic orientations	Triangular shapes in the zoning pattern, the crystal is split into sections

Table 4.4 Mineral zoning

Mineral	Categories
Plagioclase	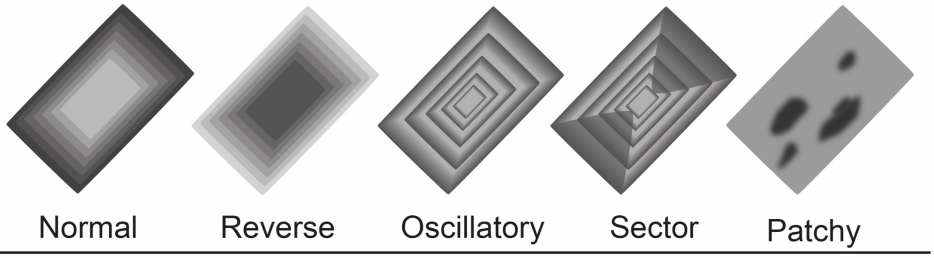
	Normal Reverse Oscillatory Sector Patchy
Olivine	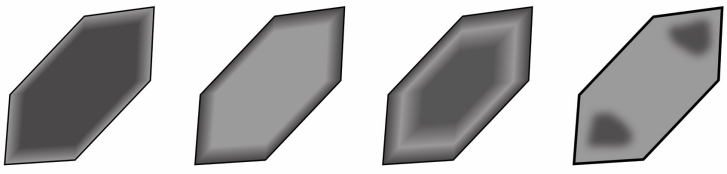
	Normal Reverse Oscillatory Patchy

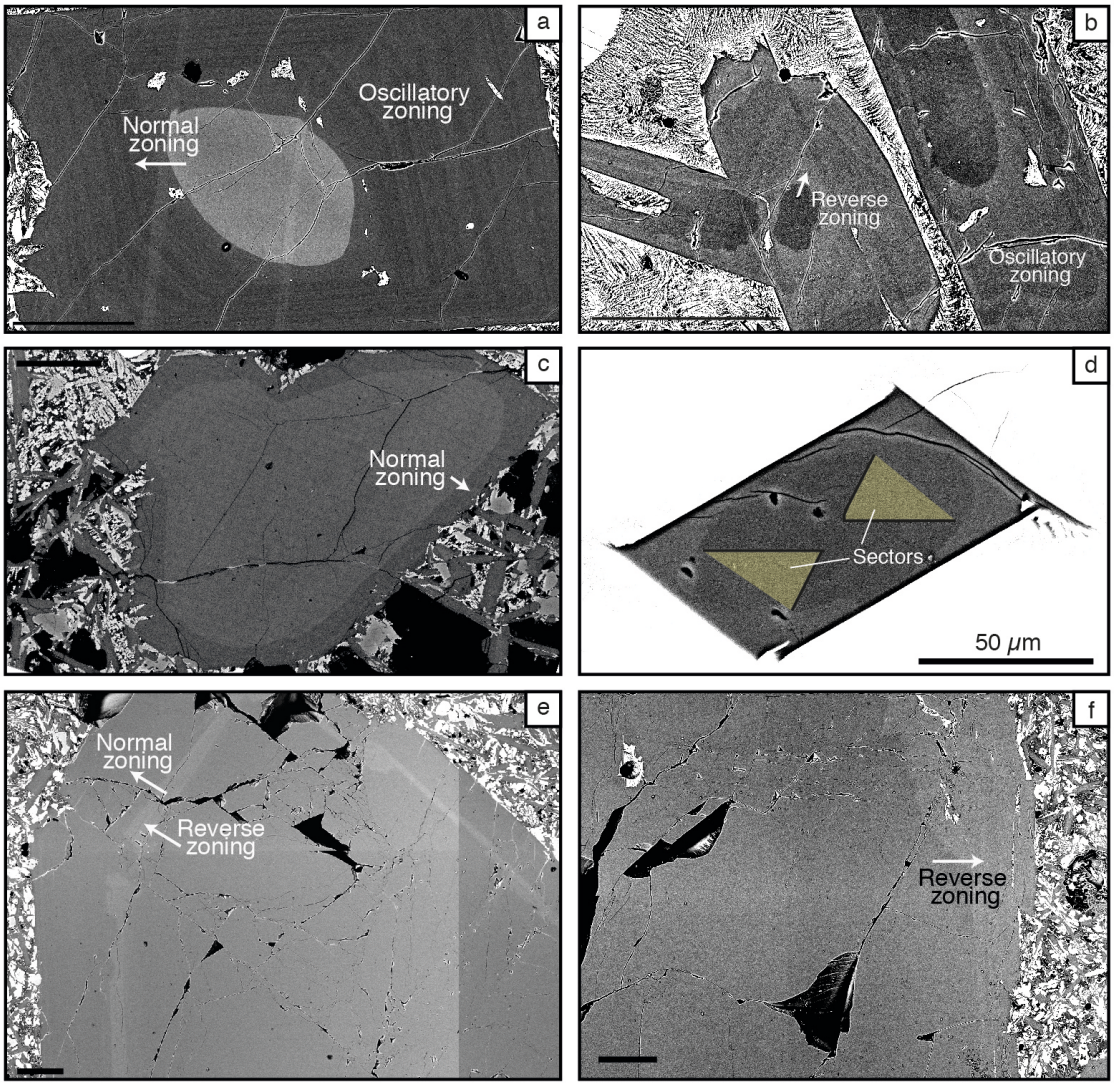

Fig. 4.2: Plagioclase zoning patterns. **a,** Normal and oscillatory zoning. **b,** Reverse and oscillatory zoning. **c,** Normal zoning. Note: in addition to the normally zoned rim there is a quench rim. **d,** Sector zoning characterised by triangular-shaped regions of different composition. **e,** Normal and reverse zoning. **f,** Reverse zoning. All scales are 0.25 cm unless otherwise stated.

4.3.1 Zoning complexity

Many plagioclase, clinopyroxene and to a lesser extent olivine exhibit multiple types of zoning. For easy comparison of the zoning in individual crystals, a single digit complexity code can be calculated. This code is a sum of the values within the zoning categories (Table 4.5), the higher the number the more complex the crystal is interpreted to be.

Table 4.5 Plagioclase zoning complexity code

Zoning	Oscillatory	Patchy	Normal	Reverse	Sector	Complexity code
Crystal 1	0	0	1	1	0	2
Crystal 2	1	4	1	0	0	6

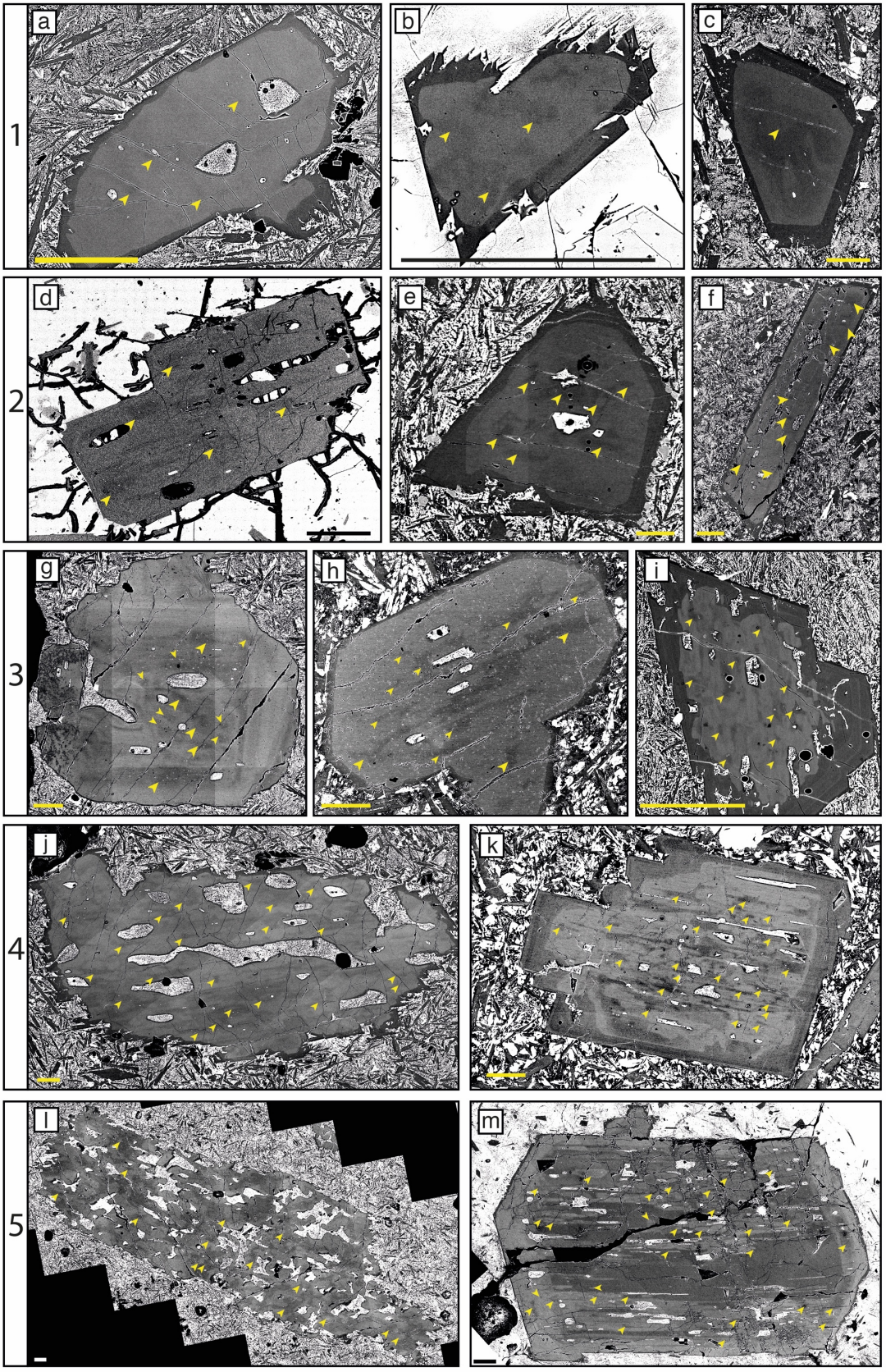

Fig. 4.3: Patchy zoning scale used to assign patchy zoning values to plagioclase crystal cargo. Note: patchy zoning is a continuous scale, hence multiple examples are shown for each category. Scale bars are all 2.5 mm

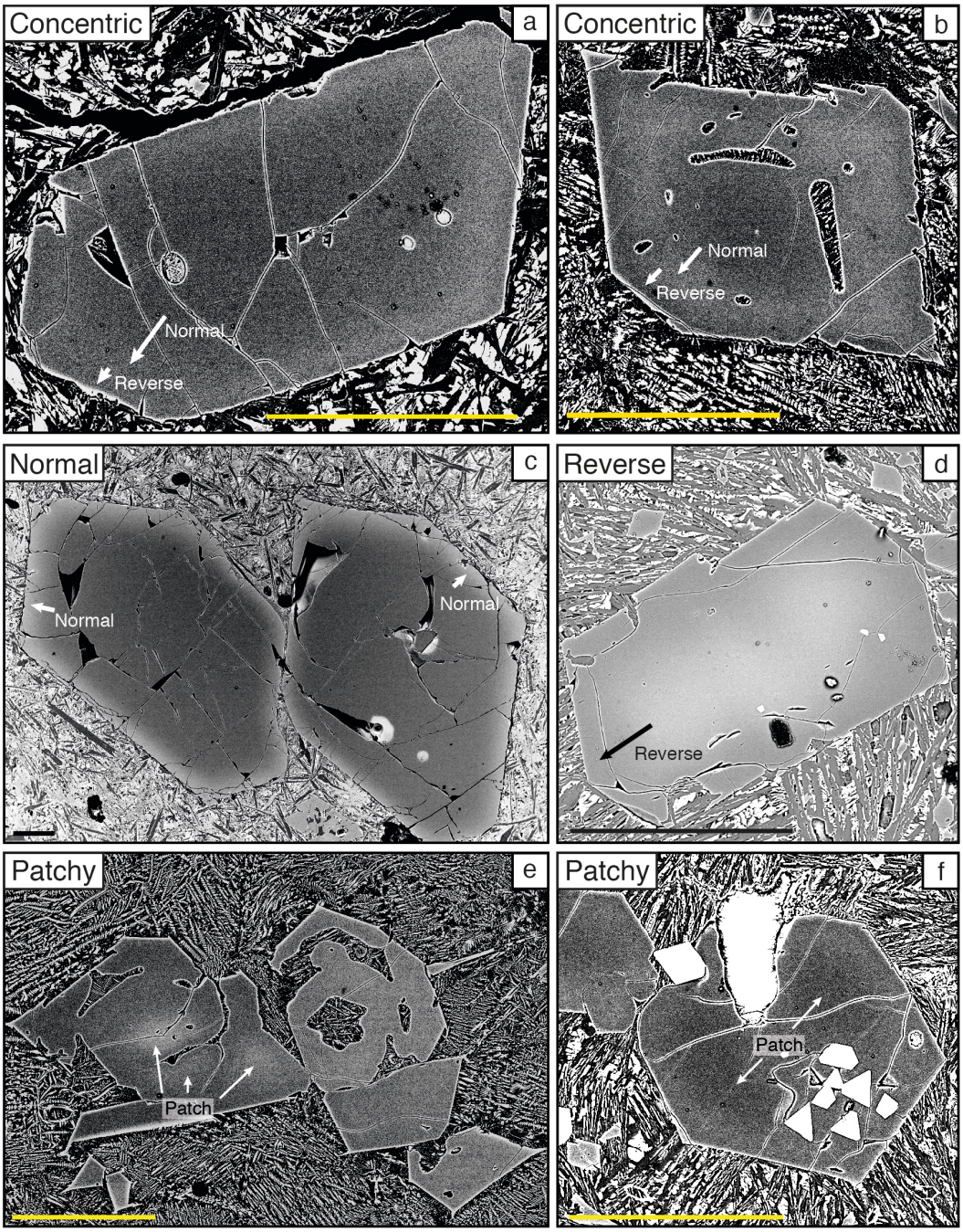

Fig. 4.4: Olivine zoning. **a, b,** Concentric zonation in olivine comprising both normal and reverse zoning. **c,** Normal zoning in two olivine crystals. **d,** Reverse zoning. **e, f,** Patchy zoning in olivine shown as individual isolated patched of lower (**e**) and higher (**f**) forsterite contents than the surrounding olivine. Scale bars are all 0.25 mm

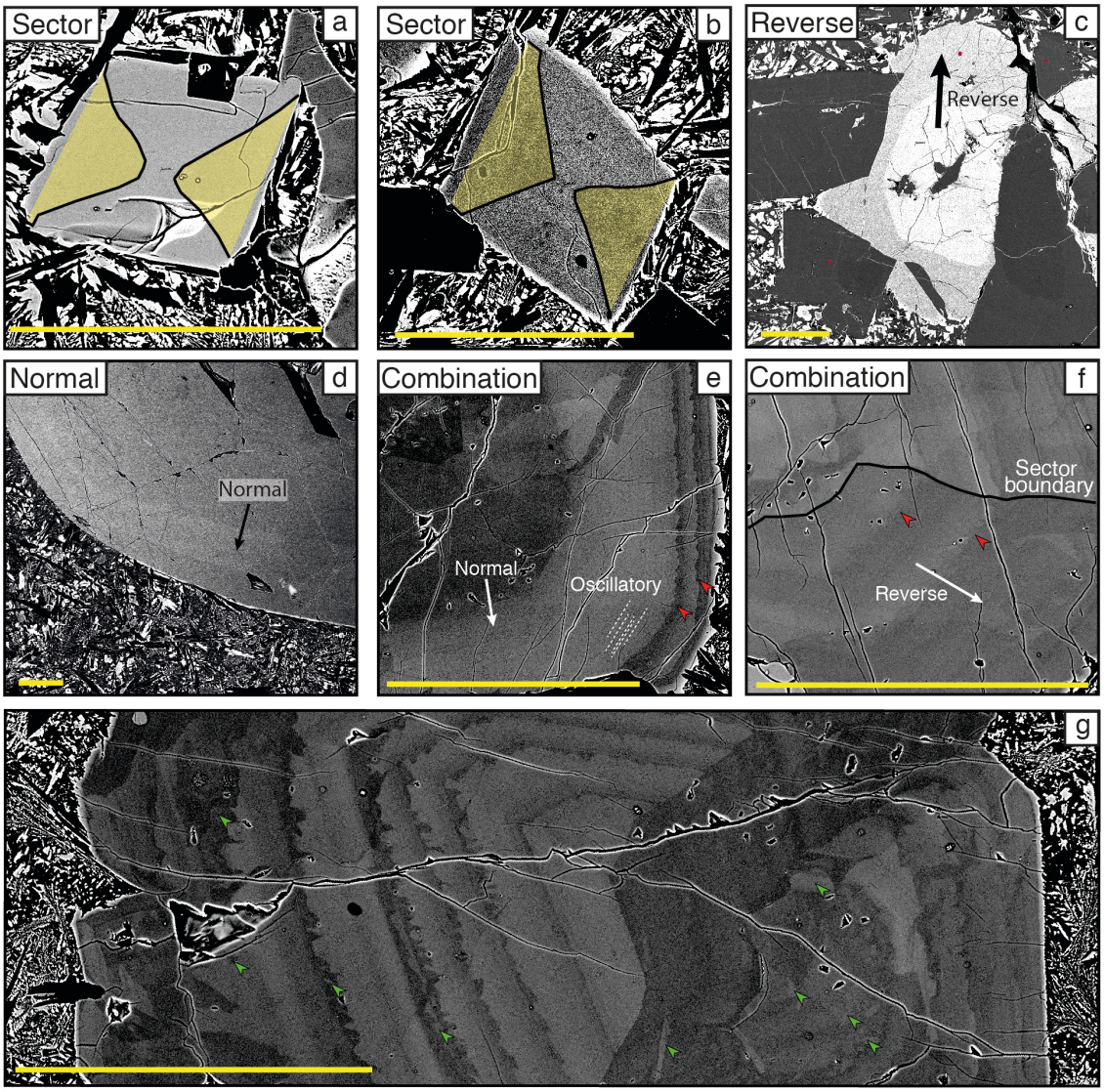

Fig. 4.5: Clinopyroxene zoning. **a, b,** Sector zonation. **c,** Reverse zoning. **d,** Normal zoning. **e, f,** Combination zoning in clinopyroxene. **g,** Complexly zoned clinopyroxene showing complex disaggregated resorption interfaces and patchy zoning (green arrows indicate patches). Red arrows indicate resorption interfaces. Scale bars are all 0.25 mm

4.4 Resorption

Resorption is classified based on: (1) the number of events, (2) the location of the resorption events (Table 4.6, Fig. 4.6) and (3) the intensity of those events based on a scale from 1-5. An intensity of 1 indicates minor resorption (e.g., presence of minor surface undulations) whilst an intensity of 5 relates to major resorption (e.g., major embayment, sieve textures). An internal resorption event is one followed by subsequent crystallisation prior to quench crystallisation, whilst an external resorption event is one followed directly by quench crystallisation (Table 4.6). If there is more than one resorption event, the value relating to the intensity of resorption is effectively an average value accounting for the intensity of each event. The presence and extent of resorption is only recorded in individual plagioclase crystals and plagioclase glomerocrysts (mono-

mineralic). The presence but not extent of resorption is recorded in plagioclase crystals within poly-mineralic glomerocrysts. Resorption is not recorded in olivine other than it being an individual habit category.

Table 4.6 Location of resorption in plagioclase

Type	Internal	External	Internal and external
Appearance	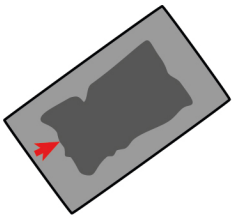	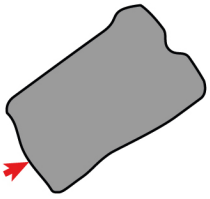	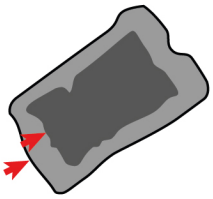

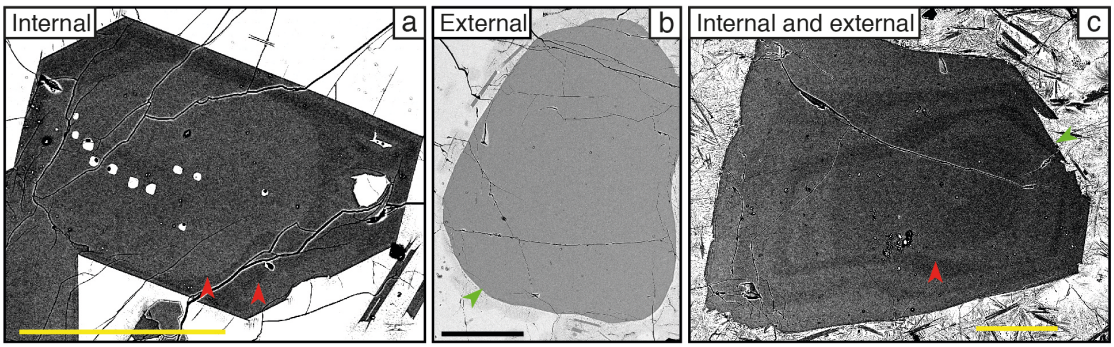

Fig. 4.6: Resorption characteristics in plagioclase. **a,** Multiple internal zoning interfaces within plagioclase. **b,** External resorption interface. **c,** Internal and external resorption interfaces in plagioclase. Red and green arrows indicate internal and external resorption interfaces respectively. Scale bars are all 0.25 mm

4.5 Melt inclusion habits

Melt inclusions are defined here as any void present within a crystal and may be connected to the matrix in 3D. Whether these voids are fresh glassy inclusions or microcrystalline is recorded separately. In all individual crystals, melt inclusion habits (Table 4.7, Fig. 4.7) and their size ranges are recorded. For glomerocrysts, the presence of melt inclusions is noted, with the size and habit recorded for mono- but not poly-mineralic glomerocrysts. The percentage of melt inclusions in an individual olivine or plagioclase is the percentage area of the crystal made up of melt inclusions. In mono-mineralic glomerocrysts, the percentage of melt inclusions is the percentage of the combined area of the glomerocryst components made up of melt inclusions.

4.6 Attached and included components

When a crystal component is not the same size as the crystal it is attached to, that component is classed as an attached component. Attached components are always smaller than the crystal they are attached too. The sizes of attached components are recorded in the plagioclase classification scheme but not in the glomerocryst

classification. The presence and number of included phases (e.g., plagioclase, olivine, pyroxene or spinel) is also recorded.

Table 4.7 Melt inclusion habit

Type	Elongate	Circular	Negative crystal	Boxy	Amoeboid
Appearance			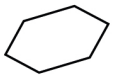	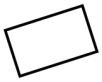	

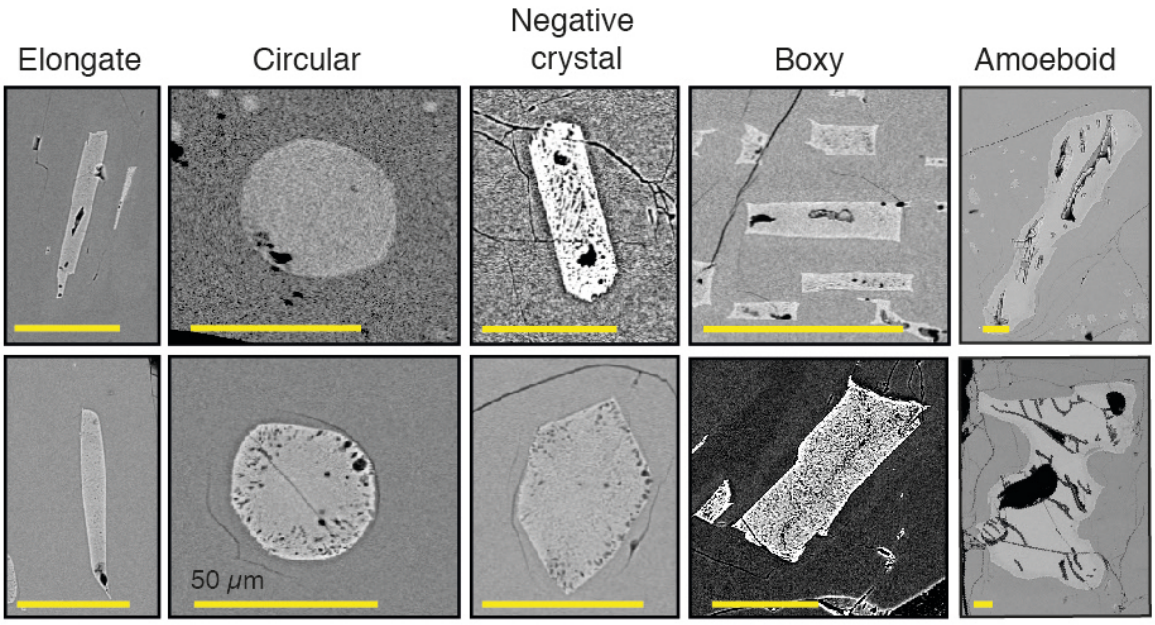

Fig. 4.7: Plagioclase melt inclusion habits, elongate, negative crystal, boxy and amoeboid. Scale bars are all 0.1 mm unless otherwise stated.

Blank page

Chapter 5

The significance of plagioclase textures in mid-ocean ridge basalt

This chapter is based upon the following published paper:

Bennett, E.N., Lissenberg, C.J. and Cashman, K.V. 2019. The significance of plagioclase textures in mid-ocean ridge basalt. Contributions to Mineralogy and Petrology, 174: 49. https://doi.org/10.1007/s00410-019-1587-1

Author contribution and declaration:

E.N.B conducted all data collection and analysis and wrote the manuscript and chapter; C.J.L and K.V.C, were involved in critical discussion throughout. Michael Perfit and François Faure provided constructive reviews of the published manuscript.

Chapter 5

5.1 Introduction

That plagioclase is a useful tool for investigating magmatic processes was discussed in Chapter 1. Not only is plagioclase abundant in lavas from a range of geotectonic settings (e.g., continental arcs (Ginibre et al. 2002); ocean islands (Cullen et al. 1989); mid-ocean ridges (Meyer and Shibata 1990); layered intrusions (Maaløe 1976)), the slow inter-diffusion of CaAl-NaSi prevents equilibration of adjacent compositional zones (Morse et al. 1984; Grove et al. 1984). This slow diffusion preserves textures over long timescales, providing petrologists with an observable record of the processes occurring within a magmatic system. Mid-ocean ridges are an ideal end-member magmatic system in which to study plagioclase textures because, unlike wet, compositionally variable volcanic arcs, mid-ocean ridge basalts (MORB) have relatively uniform compositions (i.e., tholeiitic basalts), have low water contents (Michael 1995; Danyushevsky 2001) and either experience variable (Soule et al. 2012) or no volatile degassing (Saal et al. 2002). The relative compositional simplicity of this system is advantageous, because fewer variables need to be considered when reconciling plagioclase textures with magmatic processes.

Whilst plagioclase textures to data have shown that mid-ocean ridges are dynamic open systems within which magma mixing and mush disaggregation, in addition to fractional crystallisation, are important processes (see Chapter 1), understanding plagioclase growth mechanisms and textures also has implications for the interpretation of melt inclusions, because disequilibrium processes that form melt inclusions may act to modify their compositions (Nakamura and Shimatika 1998; Danyushevsky et al. 2002; Michael et al. 2002). During skeletal growth and resorption, a chemical boundary layer may form at the melt-crystal interface enriched in plagioclase incompatible (e.g., Fe, Mg, Ti) (Bottinga et al. 1966) and compatible (e.g., Ca, Na) (Nakamura and Shimatika 1998; Danyushevsky et al. 2002) elements respectively. In both cases, the composition of the final melt inclusion depends on element diffusivities being rapid enough to dissipate the boundary layer prior to melt inclusions becoming occluded (Danyushevsky et al. 2002). Understanding the processes that form melt inclusions and associated textures is therefore vital in order to use melt inclusion compositions to determine the compositional heterogeneity of melts within magmatic systems as is commonly done (e.g., Nielsen et al. 1994; Kamenetsky et al. 1998; Sours-Page et al. 1999; Maclennan 2008).

Whilst studies of mid-ocean ridge plagioclase exist (Dungan et al. 1978; Kuo and Kirkpatrick 1982; Meyer and Shibata 1990; Pan and Batiza 2003; Ridley et al. 2006; Hellevang and Pedersen 2008; Lange et al. 2013), there are currently no studies that rigorously investigate the significance of different plagioclase textures and/or place quantitative constraints on the relative importance of the processes that form the textures. Additionally, whilst plagioclase has been used to track magmatic processes at fast- and slow-spreading ridges such as the East Pacific Rise (Pan and Batiza 2003; Ridley et al. 2006; Zhang et al. 2008; Moore et al. 2014; Zeng et al. 2014) and Mid-Atlantic ridge (Rhodes et al. 1979; Flower 1980; Kuo and Kirkpatrick 1982; Meyer and Shibata 1990; Faure and Schiano 2004; Costa et al. 2009; Lange et al. 2013), plagioclase from ultraslow-spreading ridges, such as the Gakkel Ridge, has received comparatively little attention (Hellevang and Pedersen 2008; Zellmer et al. 2011, 2012). These ultraslow spreading ridges are of interest because, not only are they a spreading ridge end-member, they are also volumetrically significant, with ridges exhibiting ultraslow spreading ridge characteristics making up ~36% of the Global mid-ocean ridge system (Dick et al. 2003).

Here, using a large catalogue of back-scattered electron (BSE) images in combination with mineral major- and minor-element data, this study presents a systematic quantitative study of plagioclase from the ultraslow-spreading Gakkel Ridge, with the aim of identifying what processes occur within the magma plumbing system, and what their relative importance is. The following demonstrates that complex plagioclase textures can be linked to the occurrence of multiple processes within the magmatic plumbing system, including magma mixing, mush disaggregation, undercooling and decompression; magma mixing and mush disaggregation are the two dominant processes. In addition, the correlation between melt inclusion morphology and host crystal textures indicates different morphologies result from different processes.

5.2 Controls on plagioclase crystallisation

The composition and morphology of plagioclase is controlled by changes in temperature, pressure, melt composition (including water content) and growth, dissolution and nucleation kinetics. The effect these have on plagioclase compositions and morphologies can be visualised using phase diagrams (Fig. 5.1a,b). At constant pressure and low water content, decreasing temperature drives crystallisation which can cause magmatic differentiation (black arrow in Fig. 5.1a). As differentiation proceeds, the corresponding equilibrium plagioclase composition becomes progressively more sodic (red arrow in Fig. 5.1a). Alternatively, if the ambient temperature of the system increases, with no corresponding change in bulk melt composition (e.g., from an adjacent or

underlying melt intrusion), pre-existing plagioclase may become superheated (ΔT_{SH}) with respect to the solidus and become resorbed (blue arrow in Fig. 5.1a). Resorption within dry systems such as mid-ocean ridges can also occur during H_2O-undersaturated decompression (Nelson and Montana 1992). At high pressures, equilibrium plagioclase is more sodic than at lower pressures (Yoder 1968; Panjasawatwong et al. 1995; Ustunisik et al. 2014) (Fig. 5.1a); hence, decompression from high to low pressures (yellow to green lines in Fig. 5.1a) causes resorption and crystallisation of more calcic plagioclase (i.e., reverse zoning) (Nelson and Montana 1992). In contrast, decompression under water-saturated conditions results in degassing and crystallisation of more sodic plagioclase (Blundy and Cashman 2005). Whilst the addition of water depresses the plagioclase loop causing the equilibrium plagioclase composition to become more anorthitic (green to purple lines in Fig. 5.1a) (e.g., Yoder 1968), the effect of water in mid-ocean ridge systems is small because MORBs have uniformly low water contents (Michael 1995).

Magma mixing can change both the bulk composition and temperature of the magmatic system. Figure 5.1b shows how mixing between melts of composition L_1 and L_2 can cause periods of disequilibrium that can trigger undercooling (ΔT_U, X_1-X'_1) and/or superheating (i.e., resorption) (ΔT_{SH}, X_2-X'_2). Both plagioclase composition and morphology have been shown experimentally to be a function of the degree of undercooling (Lofgren, 1972; 1974). Increasing the degree of undercooling has multiple effects: (1) a progressive change from tabular (at equilibrium) to skeletal, dendritic and eventually spherulitic plagioclase morphologies; and (2) crystallisation of plagioclase that is more sodic than at equilibrium. Crystallisation experiments of Lofgren (1974) have produced skeletal plagioclase crystals under conditions of strong undercooling that show reverse zoning. This reverse zoning is proposed to be the result of the crystal attempting to re-attain equilibrium growth conditions (Smith and Lofgren 1979) (S_1-S) (Fig. 5.1b). Rapid growth can also cause disequilibrium partitioning of minor- and trace-elements to form a chemical boundary layer at the plagioclase-melt interface (Bottinga et al. 1966) enriched in plagioclase incompatible elements (e.g., Mg, Fe, Ti). During continued crystal growth, these incompatible elements can become incorporated into the crystal at concentrations different to that expected during equilibrium crystallisation. Within mid-ocean ridges, three additional processes have been suggested to cause undercooling; (1) quench crystallisation upon eruption (Kirkpatrick and Jolla 1976); (2) intrusion of melts into a cool region of the plumbing system (Meyer and Shibata 1990; Hellevang and Pedersen 2008); and (3) nucleation delay which has been attributed to the formation of skeletal plagioclase found in oceanic gabbros drilled from the Cocos Plate (e.g., Koepke

et al. 2011). Magma mixing can also cause partial dissolution resulting in the formation of dissolution-reprecipitation reaction textures (e.g., Nakamura and Shimatika 1998).

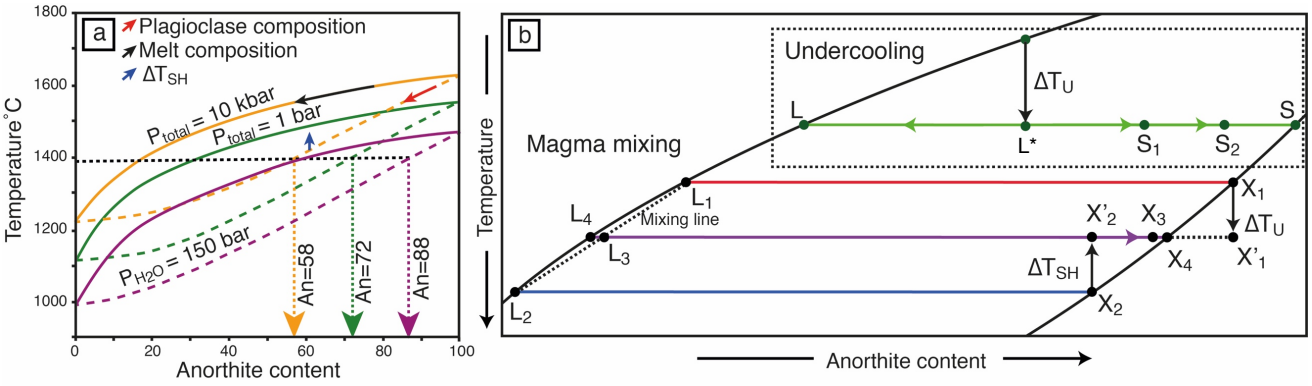

Fig. 5.1: The controls on plagioclase composition and morphology. **a** Schematic phase diagram in the albite-anorthite system showing the effect of changing intensive variables (e.g., temperature, pressure and water content) on plagioclase composition. At the same temperature, plagioclase anorthite content increases with increasing and decreasing water content (purple) and pressure (green) respectively. **b** Schematic phase diagram in the albite-anorthite system showing the effect of (1) undercooling and (2) mixing between two liquids (L_1 and L_2 to form L_3) on both plagioclase composition and morphology. During magma mixing, pre-existing plagioclase (X_2) experience superheating (ΔT_{SH}) and resorption (X_2-X'_2). If plagioclase is not completely dissolved the resorbed plagioclase become overgrown and infilled with more anorthitic plagioclase (i.e., reverse zoning) as the system moves toward equilibrium.

5.3 Results

Each plagioclase and glomerocryst has been classified using the parameters outlined in Chapter 4; the full database can be found in Electronic Appendix 6. In the following, results that are both the most significant and provide the most insight into the processes occurring in the magmatic system are shown. Summary tables of individual parameters can be found in Appendix 2.

5.3.1 Crystal cargo inventory

The basaltic lavas sampled from the Gakkel Ridge range from aphyric to plagioclase phyric, having a total crystal content (e.g., plagioclase + olivine + clinopyroxene macrocrysts and microcrysts) between 0.4 % and 50% (Fig. 5.2) with an average of 11% and a median of 6%. Modal plagioclase content ranges from 0-49 % (average 9%). Figure 5.2 shows that plagioclase is the dominant mineral phase, and its proportion of the total crystal population ((modal % plagioclase/total % crystals) x100)) increases with increased phenocryst content; modal olivine contents are 0-13% (average 2%). Spinel and clinopyroxene are the least common mineral phases, only present in a small number of samples (9 and 13 basalts respectively). Modal maps of four representative samples are shown in Figure 5.3; all modal maps are available directly from the author.

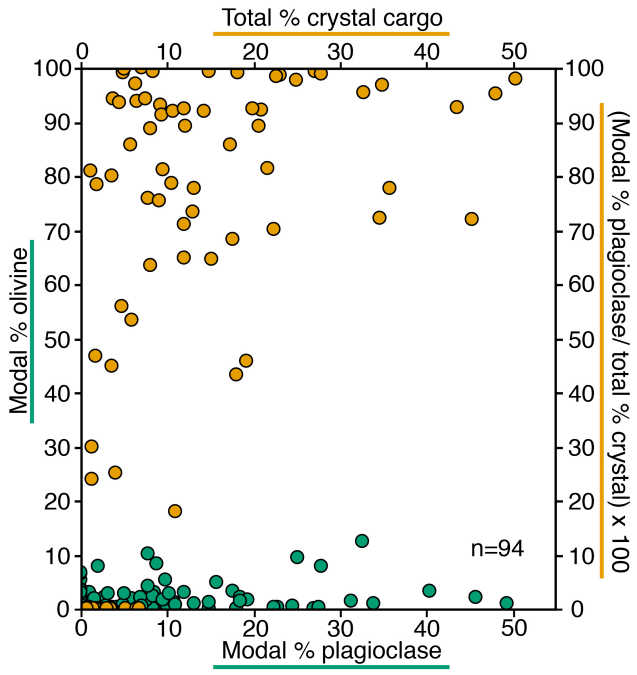

Fig. 5.2: Relationships between total phenocryst % and proportion of plagioclase ((modal% plagioclase/Total % crystals) x100) (orange) and the relationship between the modal % of olivine and plagioclase (green). Samples analysed contain more plagioclase than olivine and as the total crystal content increases, plagioclase content increases. Modal data can be found in Electronic Appendix 3.

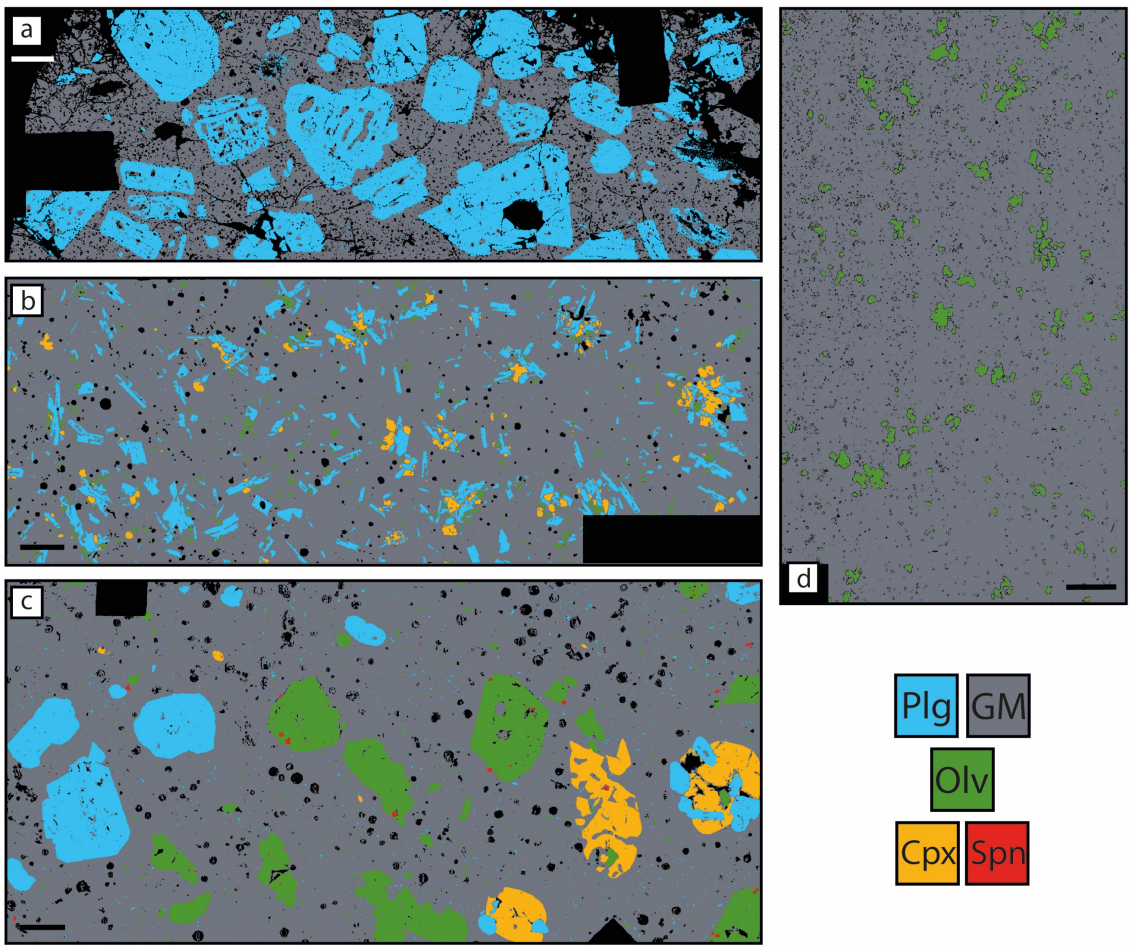

Fig. 5.3: Modal maps of four samples from the Gakkel Ridge; **a**, plagioclase-phyric basalt characterised by large macrocrysts, HLY0102-D41-5; **b**, plagioclase-phyric basalt characterised by poly-mineralic glomerocrysts and individual plagioclase, HLY0102-D49-3; **c**, phyric basalt characterised by plagioclase, olivine and clinopyroxene macrocrysts and minor spinel, PS59-251-1; **d**, olivine micro-phyric basalt, PS59-299-9. Scale bars are all 2.5 mm. Abbreviations are as follows: plagioclase, Plg; olivine, Olv; clinopyroxene, Cpx; spinel, Spn; and groundmass, Gm.

5.3.2 Textural observations

5.3.2.1 Crystal habits

Plagioclase show a range of crystal morphologies (Fig. 5.4). The most abundant and largest crystals are those with tabular habits (Fig. 5.4a and 5.5a). Resorbed crystals have a similar size range (Fig. 5.5a) and comprise ~1/3 of all individual plagioclase (Fig. 5.4b). In comparison, individual skeletal and acicular crystals are both rarer (Fig. 5.4c,d) and smaller (Fig. 5.5a). Similar to individual plagioclase crystals, tabular and resorbed plagioclase are the most common components in mono-mineralic glomerocrysts (e.g., Fig. 5.6b,c; Table A2.1). Acicular and skeletal components are less common and are each only present in 5% of mono-mineralic glomerocrysts. In contrast, the most common crystal habits in poly-mineralic glomerocrysts are tabular and skeletal.

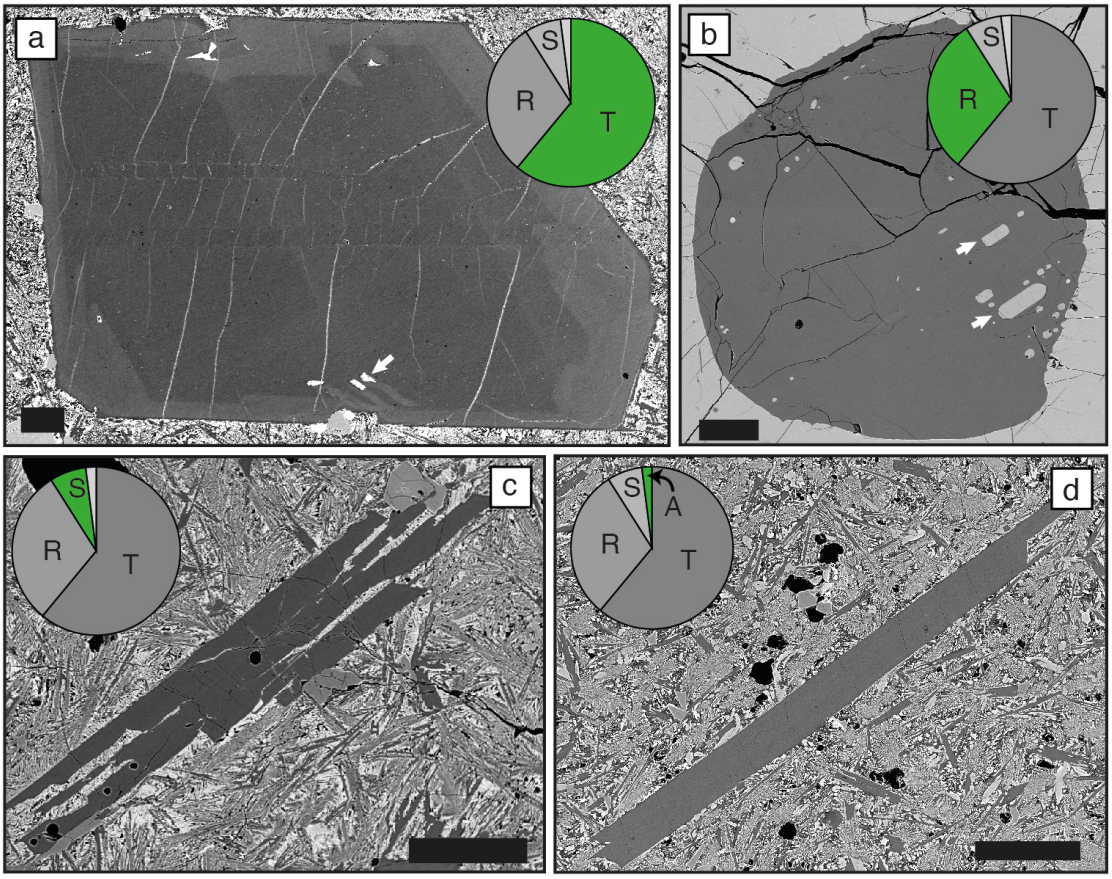

Fig. 5.4: Plagioclase crystal habits. **a** Tabular plagioclase showing internal resorption and reverse zoning. **b** Resorbed plagioclase with no zoning. **c** Skeletal plagioclase. **d** Acicular plagioclase. Pie charts illustrate the proportions of each crystal habit present in the entire individual plagioclase database. White arrows in **a** and **b** indicate melt inclusions. Pie chart abbreviations are as follows: T, tabular; R, resorbed; S, skeletal; A, acicular. All scale bars are 0.25 mm.

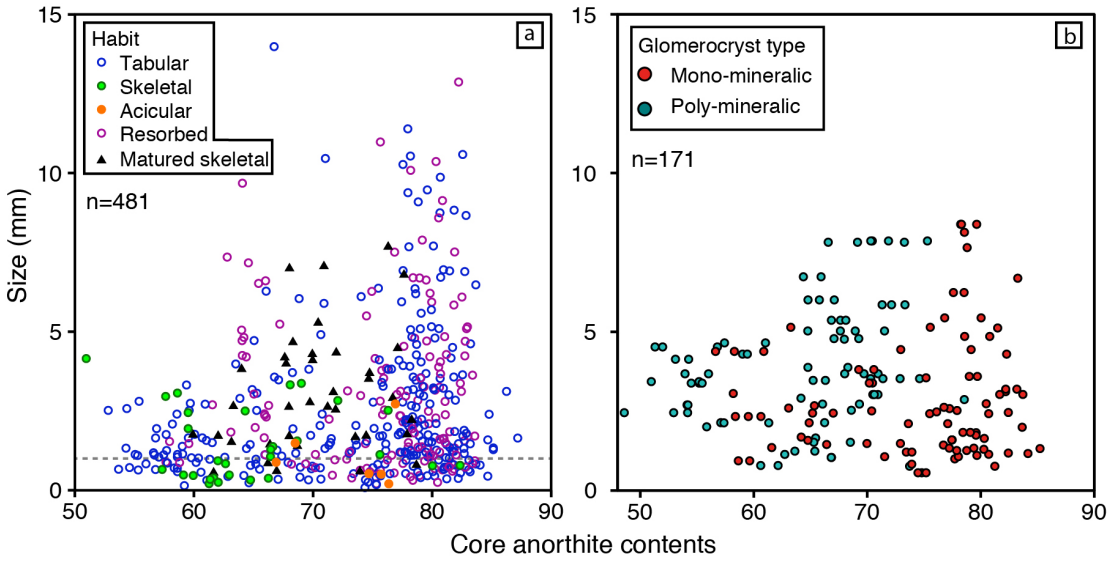

Fig. 5.5: Relationship between habit, core anorthite contents and the size of both individual plagioclase (**a**) and glomerocrysts (**b**). **a** Tabular and resorbed plagioclase have the greatest range in sizes and cluster at higher anorthite content compared to skeletal and acicular crystals which are both smaller and generally restricted to lower anorthite content. **b** Poly- and mono-mineralic glomerocrysts have a similar size range, however, poly- and mono-mineralic glomerocrysts extend to lower and higher anorthite contents respectively. Note: (1) where more than one measurement was taken of an individual plagioclase core, the values in **a** are an average; (2) despite the anorthite content of multiple components in a glomerocrysts being measured, the size used is the overall size of the glomerocryst, not the size of the individual plagioclase. The grey line in **a** represents the change from microcryst (<1 mm) to macrocrysts (>1 mm).

5.3.2.2 Zoning

Complex zoning in individual crystals is common (e.g., Fig. 5.7a): only 19% contain one type of zoning (e.g., Fig. 5.7b,c) and 8% are unzoned (Table A2.2). There is no clear relationship between crystal size and zoning complexity (Fig. 5.8). Where plagioclase exhibits only one type of zoning, reverse (Fig. 5.7b) and patchy (Fig. 5.9e) zoning are the most common types (Table A2.3); in plagioclase exhibiting multiple types of zoning, reverse zoning is the most common (Table A2.4). The remainder of the crystals have complex zoning combinations (e.g., Fig. 5.7a and 8c,d). Sector zoning such as that shown in Figure 5.7d is the least common zoning type in individual crystals. An important result is that tabular and resorbed crystals have higher zoning complexity (0-10; median 2) than skeletal and acicular crystals (0-5; median 1 and 0 respectively).

As with individual crystals, glomerocrysts often exhibit complex zoning; only 3-4% of glomerocrysts (poly- and mono-mineralic respectively) have unzoned components (Table A2.2 and A2.3). Oscillatory zoning (Fig. 5.6a) is the most common individual zoning type in both mono- and poly-mineralic glomerocrysts. Zoning in mono-mineralic glomerocrysts is more complex than that in poly-mineralic glomerocrysts (e.g., Fig. 5.6c)

(Table A2.2 and A2.3). Sector zoning, as with individual plagioclase, is the least common type of zoning in glomerocrysts.

Two distinct end-member types of patchy zoning are identified in both individual plagioclase and glomerocryst components: geometric/boxy (Type 1) (Fig. 5.9a,b) and amoeboid (Type 2) (Fig. 5.9c-g). Type 1 zoning is common in individual plagioclase that have low An skeletal cores (e.g., Fig. 5.9a,b); here these are termed matured skeletal crystals. Type 2 patchy zoning is found in plagioclase that shows evidence of resorption (e.g., Fig. 5.7a and 8c-g). Patches in both types of zoning are often closely associated with melt inclusions; boxy and amoeboid patches are associated with boxy (Fig. 5.9a,b) and amoeboid melt inclusions (Fig. 5.7a and 8c-f) respectively. Patches can be either higher or lower An than the surrounding plagioclase (e.g., Fig. 5.9b) and, whilst more often randomly distributed throughout the crystal (e.g., Fig. 5.9e), patches can show a degree of crystallographic alignment (Fig. 5.9c).

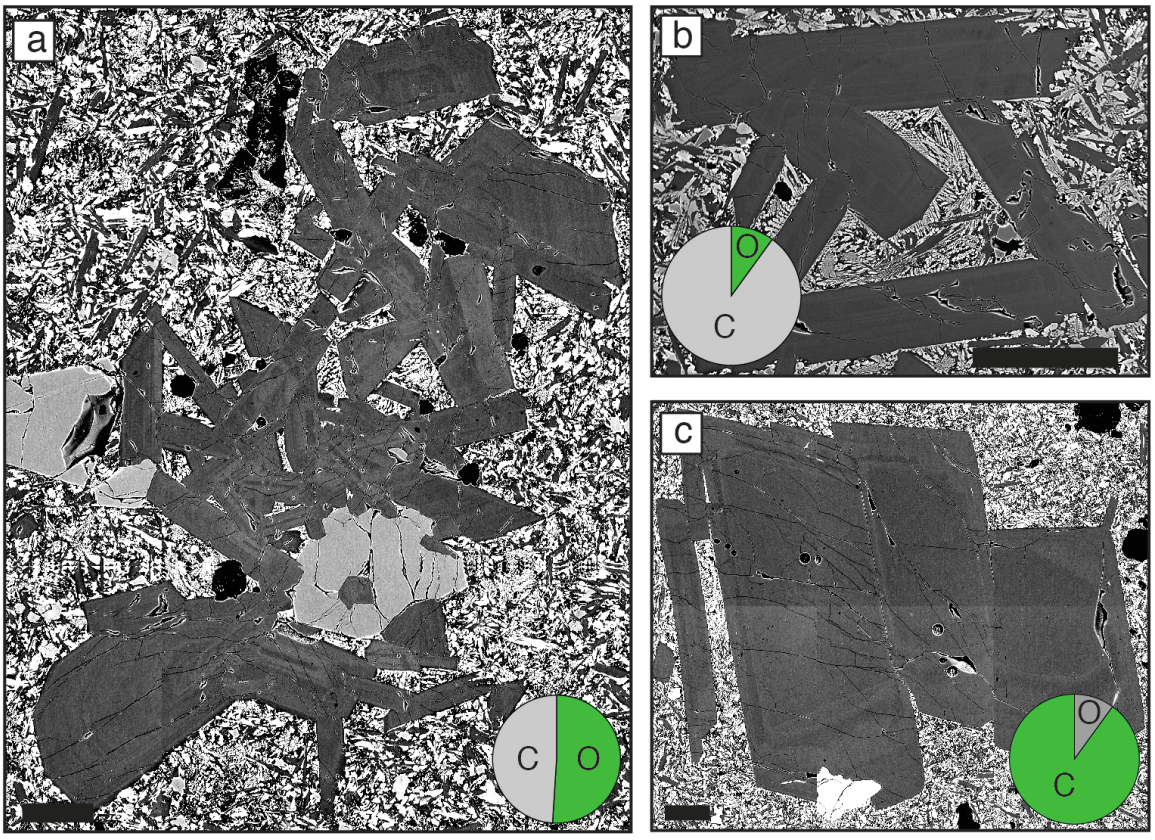

Fig. 5.6: Glomerocryst configuration and contacts. **a** Poly-mineralic glomerocryst showing an open structure with plagioclase at high angles to one another. Mono-mineralic glomerocrysts show both open (**b**) and closed structures (**c**) characterised by high and low (planar) angle component contacts respectively. Pie charts illustrate the proportions of each type of glomerocryst configuration in all mono- and poly-mineralic glomerocrysts in the database. Pie chart abbreviations are as follows: O, open; C, closed. All scale bars are 0.25 mm.

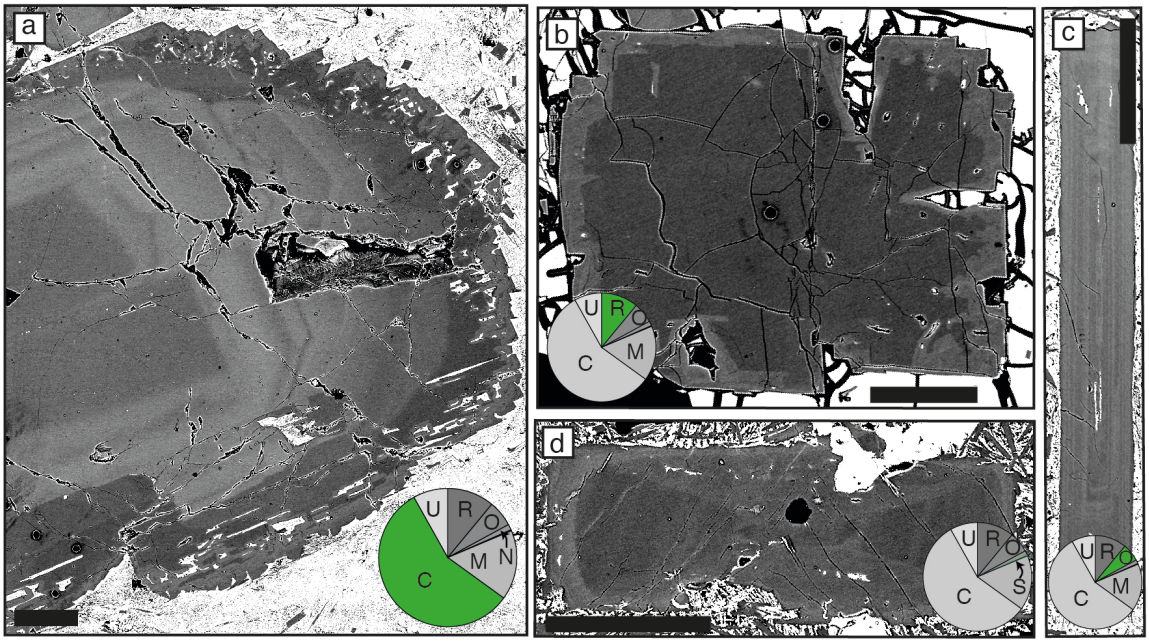

Fig. 5.7: Variation in plagioclase zoning. **a** An example of complex zoning combinations in plagioclase including reverse, normal, oscillatory and patchy zoning. **b** Reverse zoning. **c** Oscillatory zoning. **d** A plagioclase showing sector and reverse zoning. Pie charts illustrate the proportions of each zoning type present on its own in the entire individual plagioclase database. Complex zoning includes plagioclase that have >1 type of zoning present. Pie chart abbreviations are as follows: C, complex; U, unzoned; R, reverse; O, oscillatory; N, normal; S, sector; P, patchy. All scale bars are 0.25 mm.

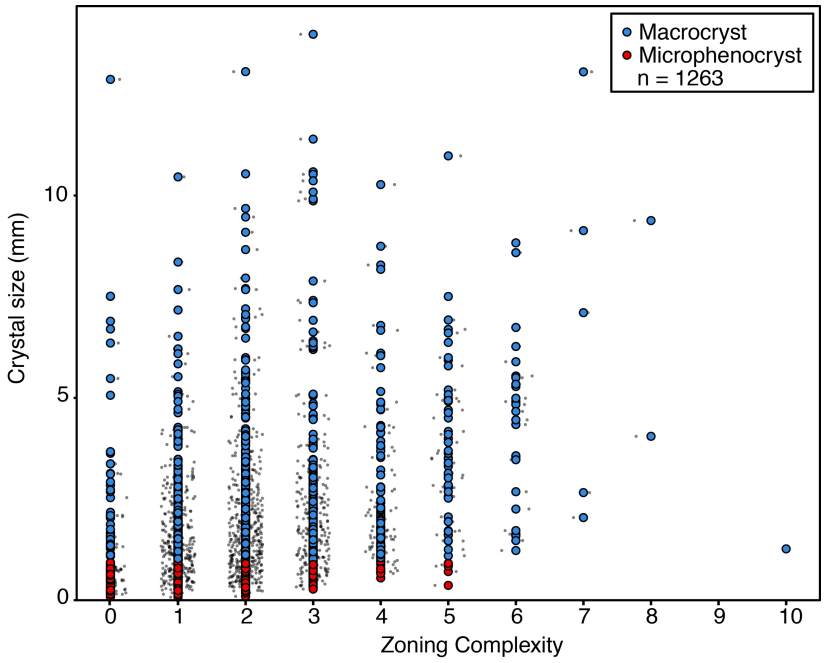

Fig. 5.8: Relationship between crystal size and zoning complexity. Larger plagioclase do not have higher zoning complexity than smaller plagioclase. Similarly there is no different in zoning complexity between micro- and macro-crysts. Small grey points represent the same data but jittered to show the distribution.

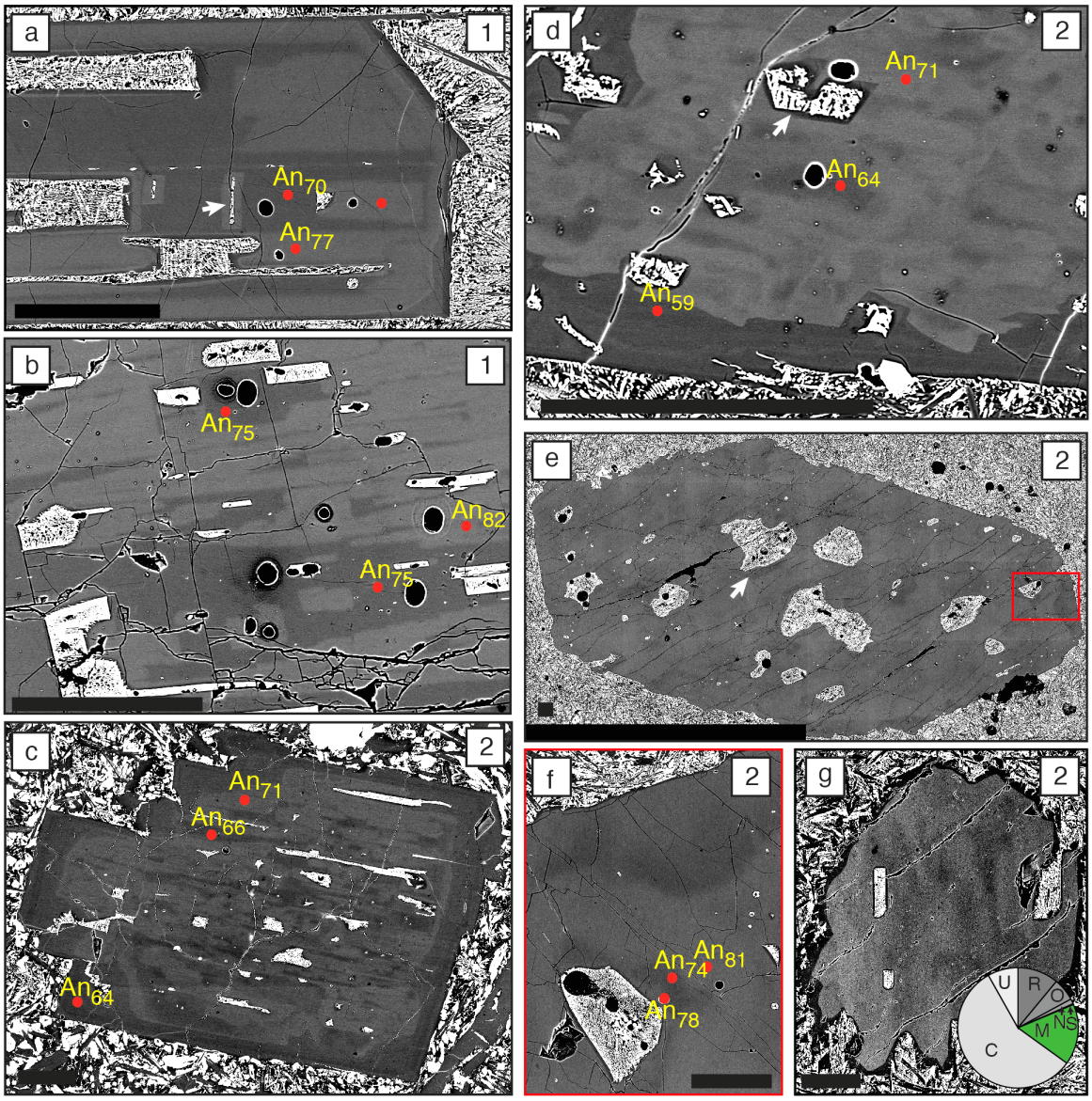

Fig. 5.9: Type 1 (**a**,**b**) and Type 2 (**c**-**g**) patchy zoning in plagioclase; the zoning type is indicated in the top right of each panel. **a** Geometric Type 1 zoning with a skeletal geometric low anorthite core containing patches of higher anorthite similar in composition to the surrounding mantle. **b** The low anorthite skeletal core contains patches of higher anorthite, higher anorthite regions also contain low anorthite patches similar in composition to the skeletal core. **c** Plagioclase exhibiting Type 2 patchy zoning characterised by low anorthite amoeboid patches that show a degree of crystallographic alignment along cleavage planes. These patches have similar anorthite contents to the outer region of the crystal. **d** Resorbed high anorthite core exhibiting Type 2 patchy zoning and outer oscillatory zoning. **e** Plagioclase exhibiting Type 2 patchy zoning. Here individual patches are present as well as voids that show zoning around their margins (**f**) similar to zoning on the exterior of the crystal. **g** Plagioclase showing a mottled core. White arrows indicate melt inclusions. The pie chart in **g** shows the proportions of each zoning type present in the entire individual plagioclase database. Pie chart abbreviations are as follows: C, complex; U, unzoned; R, reverse; O, oscillatory; N, normal; S, sector; P, patchy. White-rimmed black circles (e.g., a) are laser ablation spots. All scale bars are 0.25 mm.

5.3.2.3 Resorption

84% of individual plagioclase crystals show evidence of resorption. This resorption is expressed in several ways including resorbed crystal habits (i.e., external resorption) (Fig. 5.4b and 10a) and resorption interfaces within the plagioclase crystals (i.e., internal resorption) (Fig. 5.6c, 7a,b,d and 10a-c). Figure 5.10a shows that some plagioclase have both internal and external resorption; internal resorption is the most common type of resorption (Fig. 5.10b; Table A2.5). Zoning outboard of internal resorption events is more often reverse (63%) than normal (37%); some resorption events are followed by thin normally zoned bands that may or may not be melt inclusion rich. Tabular and resorbed crystals show more evidence of resorption (e.g., average number of events per crystal and total number of events) compared to skeletal and acicular crystals (Table A2.6); there is no relationship between crystal area and number of resorption events (Fig. 5.11). Amoeboid melt inclusions are often found in plagioclase that show evidence of resorption (Fig. 5.9c,e); they are the largest type of melt inclusion (Fig. 5.12, Table A2.7). Melt inclusions can also be associated with internal resorption interfaces (e.g., Fig. 5.4a and 10b). Similar to individual crystals, resorption in mono-mineralic glomerocrysts is most commonly internal (e.g., Fig. 5.6c), with 81% recording at least one event. Whilst the location and number of resorption events was not recorded in poly-mineralic glomerocryst components, 55% of these glomerocrysts show evidence of resorption.

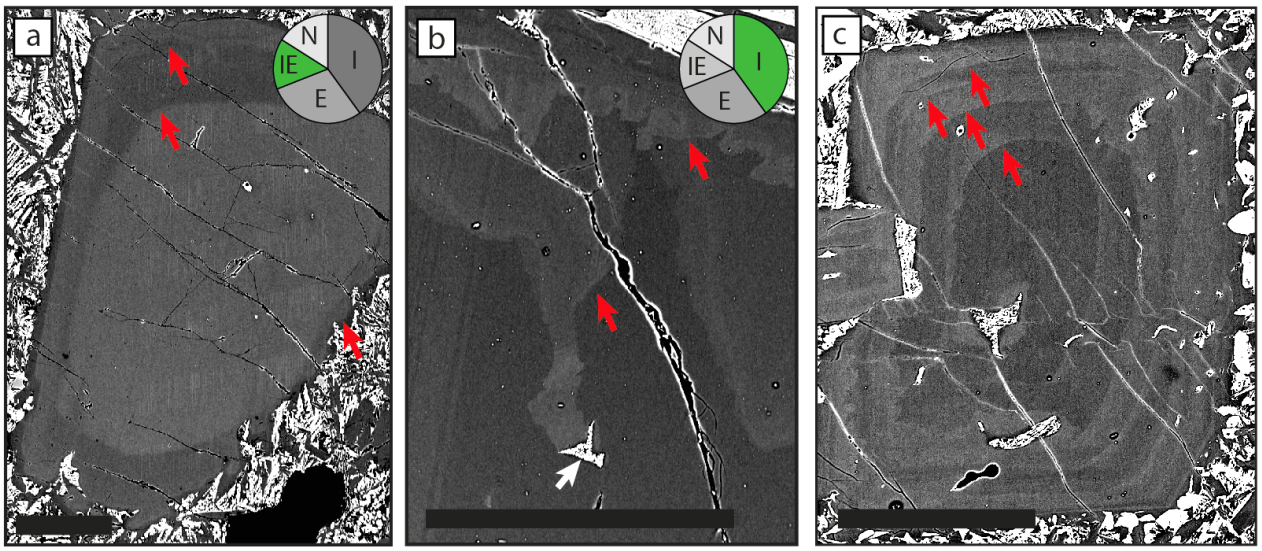

Fig. 5.10: Types of plagioclase resorption. **a** Plagioclase showing both internal and external resorption events. **b** Plagioclase with two internal resorption events. **c** Plagioclase with multiple internal resorption events. Red arrows indicate the position of resorption interfaces within the plagioclase crystals. White arrow in **b** indicates a melt inclusion. Pie charts illustrate the proportions of each type of resorption in all individual plagioclase crystals in the database. Pie chart abbreviations are as follows: E, external; IE, internal and external; N, no resorption; I, internal. All scale bars are 0.25 mm.

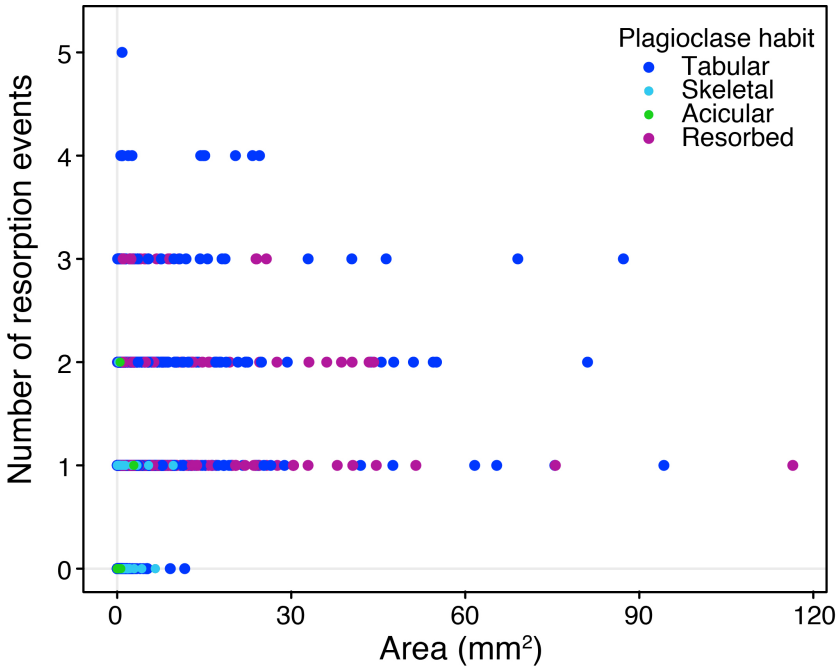

Fig. 5.11: Relationship between crystal area and number of resorption events; there is no relationship between crystal area and number of resorption events. Note: because the crystal area was calculated using the maximum dimensions of the crystal and does not account for resorption, the crystal areas are maximums; the area of resorbed crystals will be less than that calculated.

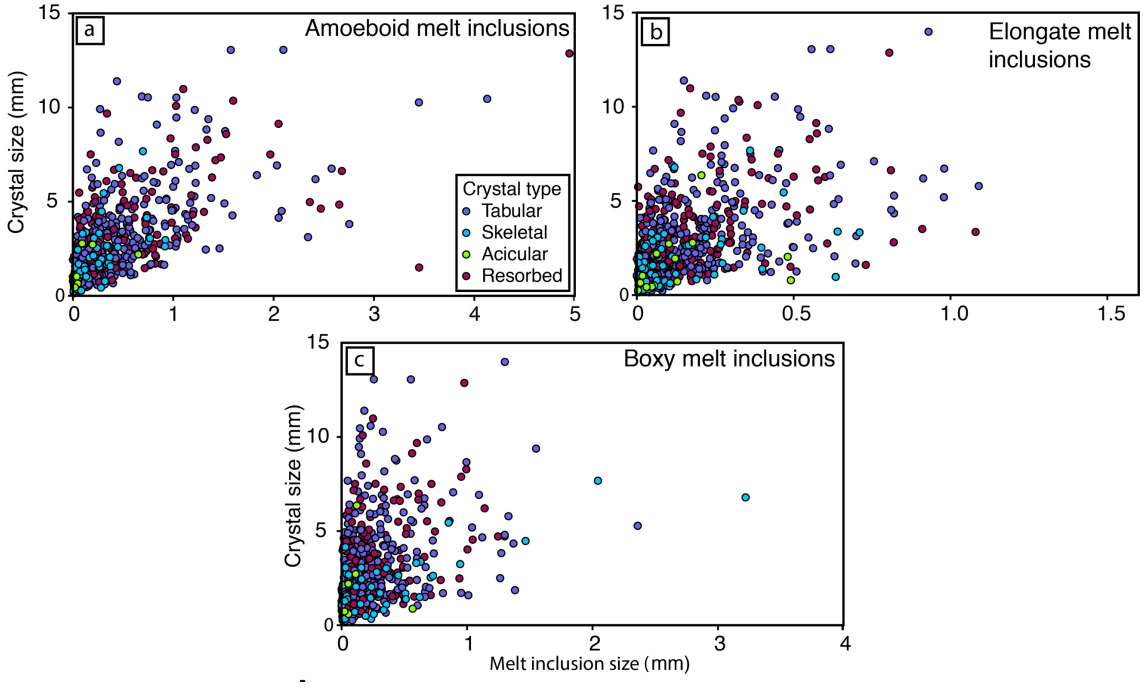

Fig. 5.12: Relationship between crystal size and size of amoeboid (**a**), elongate (**b**) and boxy (**c**) melt inclusions. For the three types of melt inclusions shown, there are weak positive correlations between crystal and melt inclusion size, larger crystals tending to have larger melt inclusions. **a** The largest amoeboid melt inclusions are situated in resorbed and tabular crystals. **b** Elongate melt inclusions are smaller than both amoeboid and boxy melt inclusions, with the largest elongate melt inclusions located in tabular and resorbed crystals. **c** Boxy melt inclusions have a similar size range to amoeboid inclusions, but the largest inclusion are located in skeletal and tabular crystals.

5.3.2.4 Glomerocryst configuration and component contacts

Glomerocrysts are found in both open (Fig. 5.6a,b) and closed configurations (Fig. 5.6c). Closed configurations are more common in mono-mineralic glomerocrysts, whilst both configurations are as common in poly-mineralic glomerocrysts (Table A2.8). Embedded component contacts are the most common in all glomerocrysts, while planar (Fig. 5.6c) and point contacts (Fig. 5.6a,b) are more common in mono- and poly-mineralic glomerocrysts respectively (Table A2.8). Glomerocrysts commonly show more than one component contact type.

5.3.3 Plagioclase major element compositions

Plagioclase major element compositions are presented in Electronic Appendix 2. The An content of plagioclase core (An_{54-87}) and mantle (An_{56-86}) compositions show multimodal distributions with peaks at ~An_{80}, ~An_{68} and ~An_{60}; the two lower An core peaks are shifted toward lower An compared to mantle peaks (Fig. 5.13a). Patches (An_{59-84}) and mottled cores (cores that show diffuse patchy zoning, Fig. 5.9g) (An_{64-83}) show peaks in compositions at ~An_{75} and ~An_{79} respectively (Fig. 5.13b), similar to cores and mantles. Plagioclase rim compositions (An_{50-87}) show at least two broad compositional peaks at ~An_{70} and ~An_{80} (Fig. 5.13c). Quench rim compositions (An_{43-80}) define a multimodal distribution with a main compositional peak located at ~An_{64}; melt inclusion quench rims (An_{48-75}) and skeletal core (An_{60-79}) compositions fall within the range defined by quench rims (Fig. 5.13d). The range of average core An contents of megacrysts (An_{54-87}), microcrysts (An_{54-85}) and mono-mineralic glomerocrysts (An_{58-85}) are similar to one another and differ to the more restricted range of poly-mineralic glomerocrysts (An_{54-79}) (Fig. 5.14).

Crystal habit is correlated with An content: tabular and resorbed plagioclase have higher average core An contents than acicular, skeletal and cores of matured skeletal crystals (Fig. 5.5a). Poly- and mono-mineralic glomerocrysts have similar size ranges, however the core An content of poly-mineralic glomerocryst components is lower than mono-mineralic glomerocryst components (Fig. 5.5b); the latter have core An contents similar to tabular and resorbed crystals.

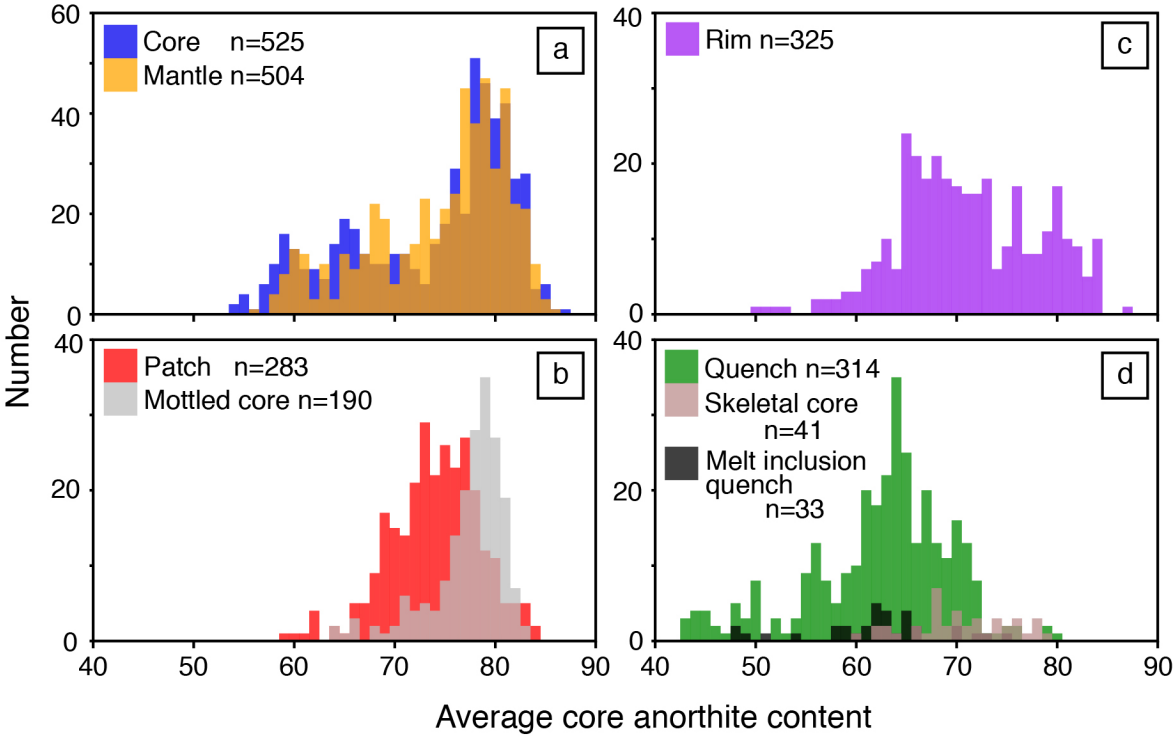

Fig. 5.13: Anorthite (defined as molar Ca/(Ca+Na) x 100) content of all plagioclase analyses separated by analysed crystal location (e.g., core, rim etc.). **a** Plagioclase cores and mantles. **b** Plagioclase mottled cores and patches. **c** Plagioclase rims. **d** Plagioclase skeletal cores, quench and melt inclusion rims. There are few relationships between analysed location and composition. Note: For all crystal locations, other than those in **b,** each value is an average of multiple analyses, values in **b** are not averages due to the heterogeneous nature of both patches and mottled cores therefore the number of analyses does not reflect the number of plagioclase analysed.

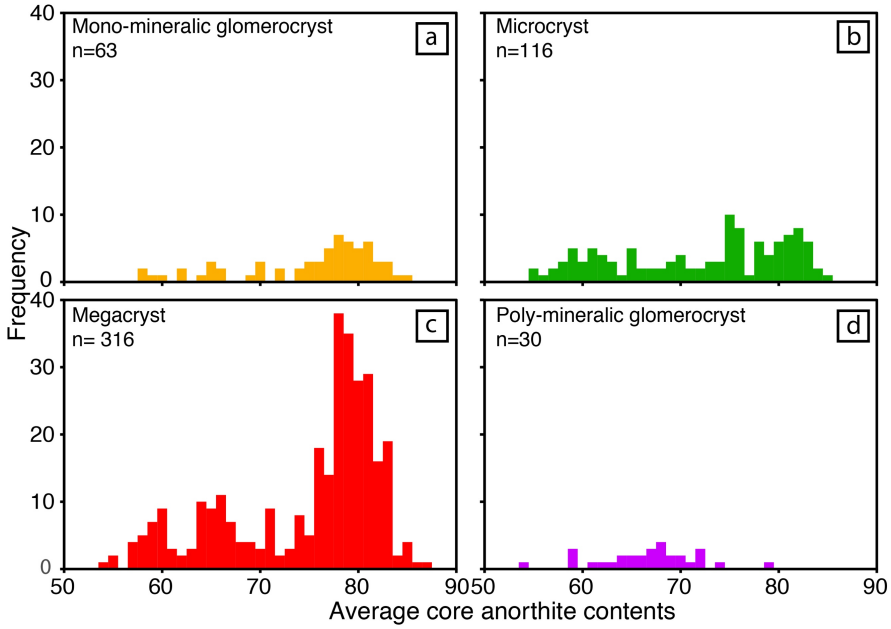

Fig. 5.14: Relationship between average core anorthite and crystal type. The range of average core anorthite for each crystal category overlap; the average core anorthite contents of poly-mineralic glomerocrysts is more restricted.

5.3.4 Plagioclase-melt equilibria

Of the 34 basaltic glasses analysed in Lissenberg et al. (2019) only 18 samples contain both glass and plagioclase, enabling the calculation of plagioclase-melt equilibria. To these, additional glass analyses from van der Zwan et al. (2017) (HLY0102-D12-1 and HLY0102-D21-4) and Gale et al. (2013) (HLY0102-D18-1, HLY0102-D18-6, HLY0102-D22-1, HLY0102-D21-1, HLY0102-D23-36, HLY0102-D26-6, HLY0102-D27-32 and HLY0102-D66-32) were added for which plagioclase data is presented herein. There are several models for calculating plagioclase-melt equilibrium (e.g., Grove et al. 1992; Pajasawatwong et al. 1995; Putirka 2005; and Namur et al. 2012). Here the model of Grove et al. (1992) has been used:

$$An = \frac{A}{(1+A)} \quad (1)$$

where A is defined as:

$$A = \frac{X_{CaAl_2O_4}{}^{Liq}}{X_{NaAlO_2}{}^{Liq} \times X_{SiO_2}{}^{Liq}} \times EXP\left[11.1068 - 0.0338 \times P - 4.4719 \times \left(1 - X_{NaAlO_2}{}^{Liq}\right)^2 - 6.9707 \times \left(1 - X_{KAlO_2}{}^{Liq}\right)^2\right] \quad (2)$$

Where *P* is the pressure in kbar. The model of Grove et al. (1992) was chosen because these equations were calibrated on 171 plagioclase-liquid assemblages produced experimentally at pressures from 0.001-27 kbar and predicts the equilibrium plagioclase composition as a function of both pressure and melt composition (Grove et al. 1992). The model was specifically designed to investigate the composition of plagiocalse crystallising from MORB and recovers all but 6 MORB-experimental data used in the calibration to within ±5%. Whilst more recent calibrations, such as that of Namur et al. (2012), report 50% of plagioclase compositions are predicted to within an error of ± 2% of experimentally derived values, this model by design, which investigates the effect of anhydrous liquid composition on the composition of equilibrium plagioclase, does not include a pressure component in their equations; plagioclase composition has been shown to be influenced by pressures (Yoder 1968; Panjasawatwong et al. 1995; Ustunisik et al. 2014). The equations of Grove et al. (1992) use the liquid albite, anorthite and orthoclase components of selected Gakkel Ridge glasses calculated following the equations of Bottinga and Weill (1972). Equilibrium plagioclase compositions have been calculated assuming a pressure of 2 kbar; because An contents of plagioclase decrease by only ~1% An per kbar, and pressures at the Gakkel Ridge are not expected to be larger than ~3 kbar (Shaw et al. 2010), the assumed pressure has little effect on the overall results. Our calculations show that many of the crystals are not in equilibrium with their host glasses (Fig. 5.15). The degree of disequilibrium is defined as as ΔAn ($An_{measured}$ minus $An_{calculated}$): hence, equilibrium is at ΔAn=0. For example, only 22% of crystal cores are in equilibrium with their host melts, 13% and 65% plotting in equilibrium

with more evolved and primitive melts respectively (Fig. 5.15a). Plagioclase rims (Fig. 5.15c), quench rims and melt inclusion quench rims (Fig. 5.15d) show higher percentages in equilibrium with their host melts; however, 53% of rim analysis still plot in equilibrium with more primitive melts.

Values of ΔAn for each crystal location analysed (e.g., core, rim etc.) overlap (Fig. 5.15). Plagioclase cores, mantles, rims and patches all have similar ΔAn ranging from -14 to +15; mottled cores range from -4 to +15. Cores, mantles, rims and patches and mottled cores show peaks around ΔAn=12 and ΔAn=9 respectively. Skeletal cores straddle equilibrium with more restricted ΔAn values of -6 to +8. Quench and melt inclusion quench rims have the most extreme negative ΔAn (≤-19). Several relationships between ΔAn and crystal type are present in Figure 5.15: (1) macrocrysts and mono-mineralic glomerocrysts show similar distributions; (2) microcrysts show a similar distribution to both macrocrysts and mono-mineralic glomerocrysts but can extend to lower ΔAn; and (3) with the exception of one rim analysis, poly-mineralic glomerocrysts tend to plot within equilibrium or toward lower ΔAn.

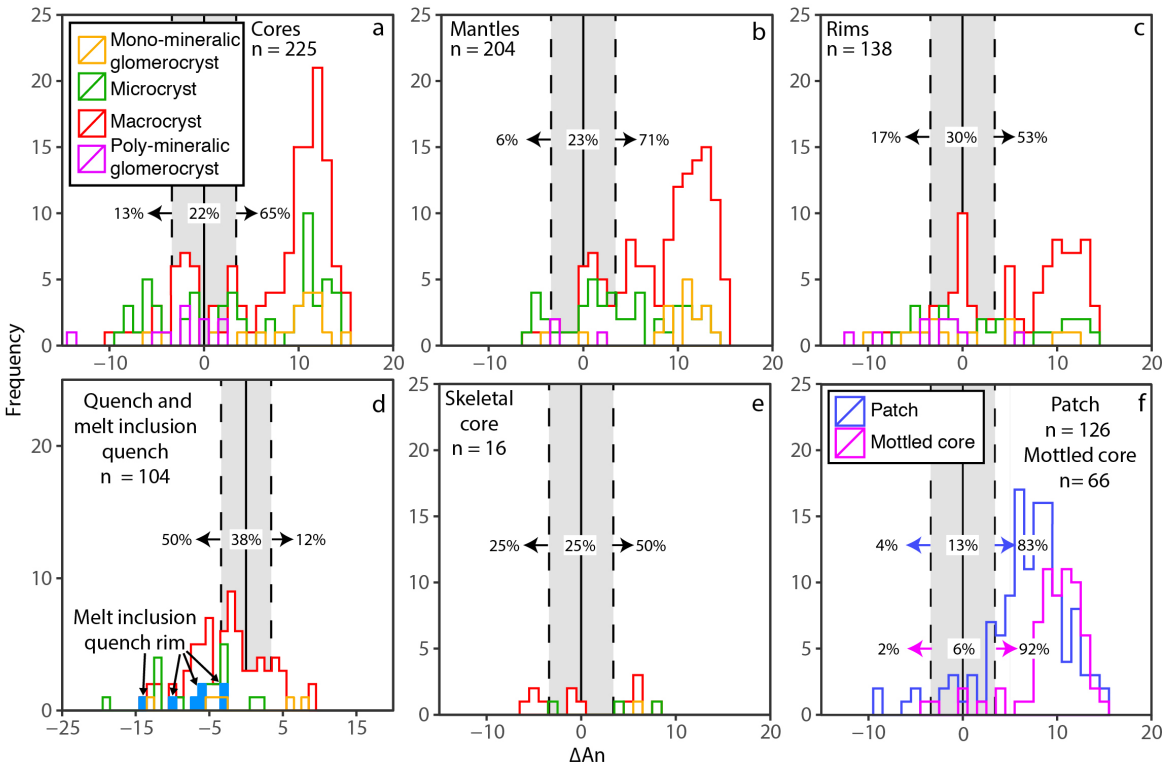

Fig. 5.15: Histograms of ΔAn for each crystal location split by crystal type. **a** Cores. **b** Mantles. **c** Rims. **d** Quench and melt inclusion quench rims. **e** Skeletal cores. **f** Patches and mottled cores. Whilst some analyses plot in equilibrium with their host melts (within the grey area), a vast proportion of analyses plot in equilibrium with more primitive melt compositions. Percentages on each panel represent the percentage of analyses that plot in equilibrium with the melt or with more evolved (left) or primitive (right) melts. Solid black vertical lines represent equilibrium (ΔAn=0); dashed lines represent ±5% error (Grove et al. 1992) on the average plagioclase anorthite content (An_{69}) calculated using equations (1) and (2). ΔAn = $An_{measured}$ minus $An_{calculated}$. $An_{measured}$ is the An content determined from EDS analysis, $An_{calculated}$ is the An content calculated from equations (1) and (2).

5.3.5 Plagioclase TiO_2 contents

Plagioclase TiO_2 contents range from 0.02-0.34 wt.% (Electronic Appendix 4). There are no clear relationships between crystal location and TiO_2; TiO_2 contents of all crystal locations overlap (Fig. 5.16a). However, TiO_2 contents correlate negatively with plagioclase An content (Fig. 5.16a). Two parameters, ΔTiO_2 and ΔAnR, have been calculated here to quantify the change in composition across a resorption interface. These are defined as $TiO_{2inboard}$ minus $TiO_{2outboard}$ and $An_{inboard}$ minus $An_{outboard}$ respectively. Plagioclase plot from + ΔAnR and – ΔTiO_2 to – ΔAnR and + ΔTiO_2 (Fig. 5.16b).

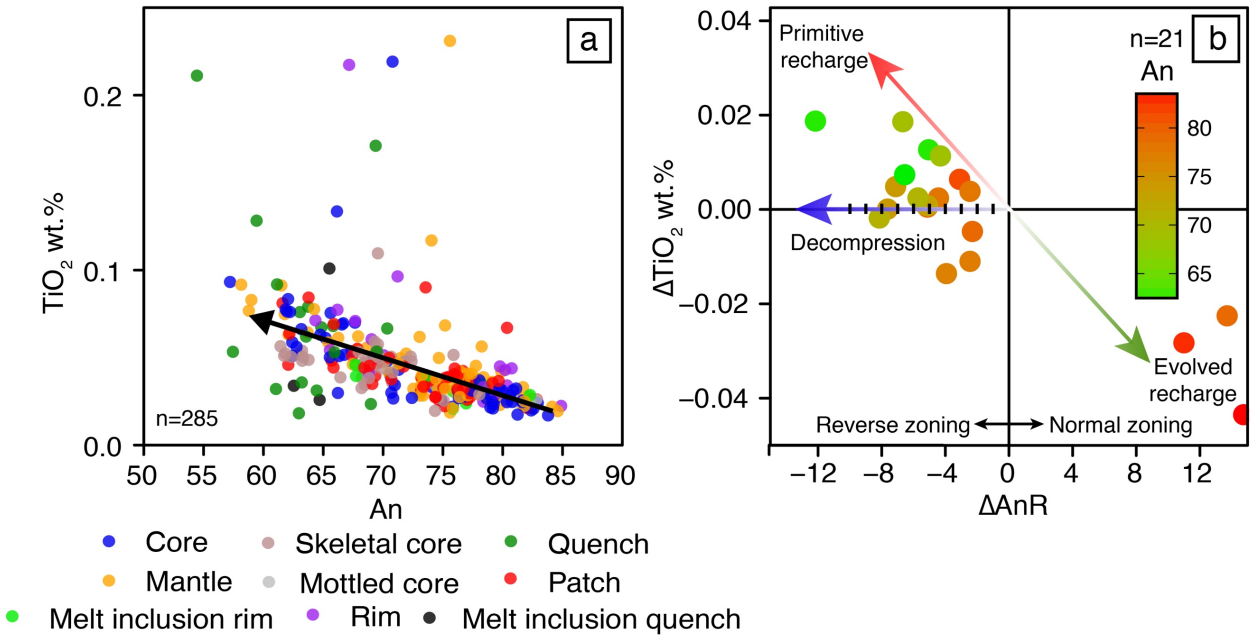

Fig. 5.16: a Plagioclase TiO_2 and An content correlate negatively. There is no correlation between plagioclase TiO_2 content and analysis location (e.g., core, rim etc.). **b** Relationship between ΔAnR and ΔTiO_2. Analyses plot both along the decompression vector and within quadrants for both primitive and evolved recharge, suggesting resorption may occur due to both decompression and magma mixing. Intervals along the decompression vector represent 1%An.

5.3.6 Juxtaposition of chemically and texturally distinct populations

Individual samples contain multiple distinct chemical and textural populations (Fig. 5.17). Considering the maximum An content of cores, 73% of samples show a range equal to or greater than 5% An with an average range of 10% An; the smallest range is 1%. Texturally, zoning complexity within a single sample ranges from 0 to 10, 80% of samples show zoning complexity ranges greater than 3; only three samples possess plagioclase crystals with no variation in zoning complexity. Although the variation in core An content could in part relate to sectioning effects, this variation agrees well with the observed textural variation. For example, plagioclase in Figure 5.17c and d have very similar core anorthite content but exhibit both different zoning patterns and crystal habits (no zoning and skeletal habit (Fig. 5.17c) and oscillatory zoning and tabular habit (Fig. 5.17d)).

Figure 5.18 also illustrates the presence of mixed chemical and textural populations. This modal map shows the presence of large anorthitic (An_{80-83}) macrocrysts overgrown by more evolved plagioclase (An_{65-70}) which is the same composition as poly-mineralic glomerocrysts in the same sample.

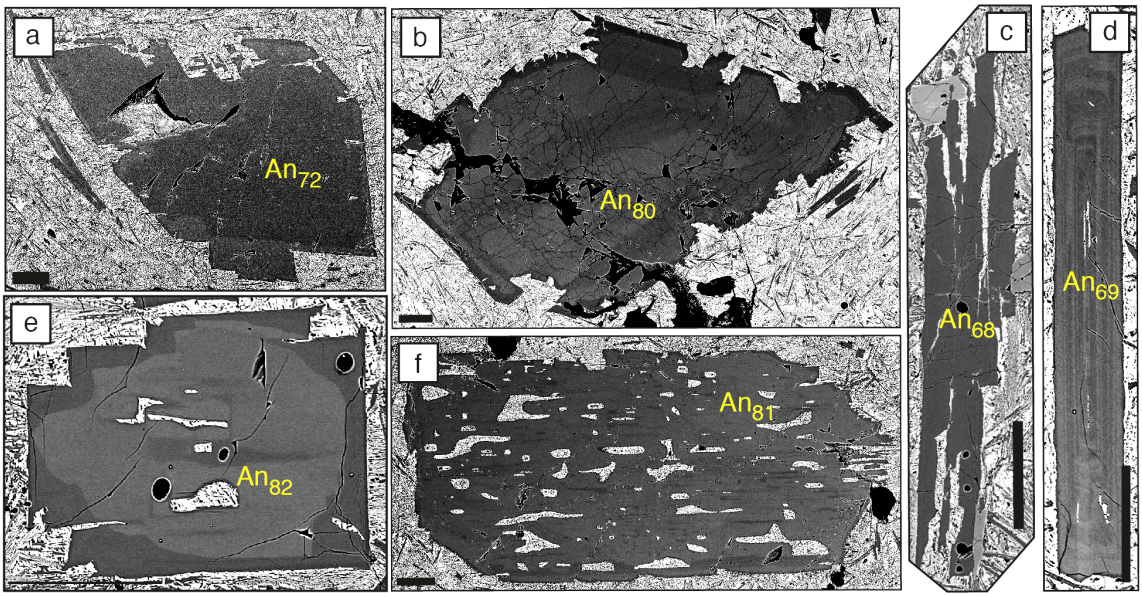

Fig. 5.17: An example of the juxtaposition of chemically and texturally distinct plagioclase crystals within sample HLY0102-D22-1. Crystal habits include resorbed (**a-b, f**), skeletal (**c**) and tabular (**d-e**). Zoning can be simple (oscillatory (**d**)) or show more complex forms (patchy zoning (**e-f**)). Average core anorthite contents in this sample range from An_{68} to An_{82}. All scale bars are 0.25 mm.

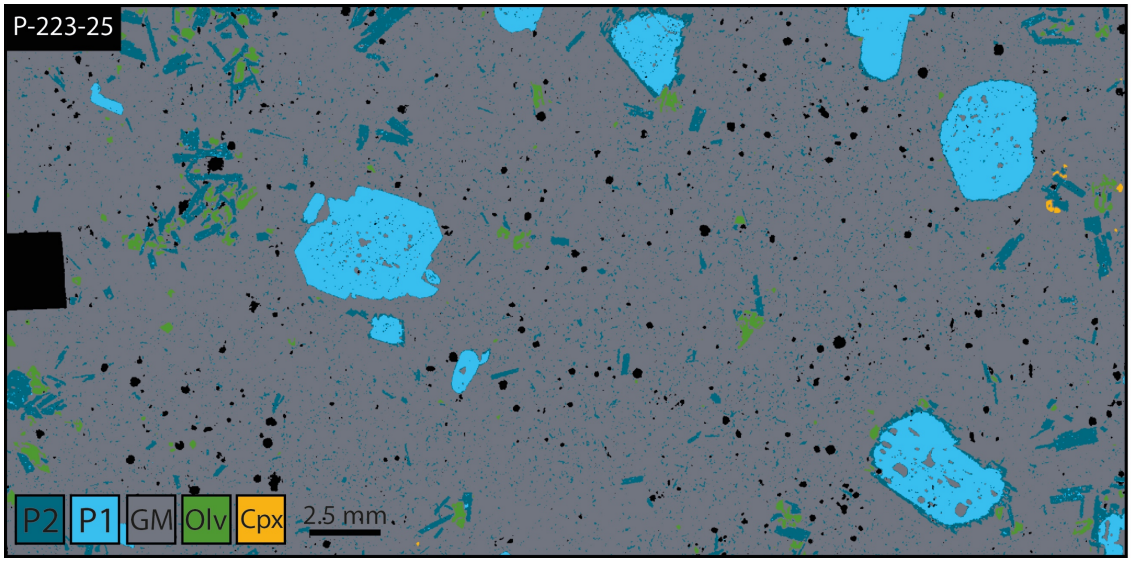

Fig. 5.18: Modal map of sample PS59-223-25 showing the presence of two plagioclase populations, P1 and P2. P1 cores are primitive and have compositions of An_{80-83}. The rims of these P1 plagioclase are overgrown by P2 plagioclase which have a composition of An_{65-70}.

5.4 Discussion

Above, plagioclase crystal cargo from the Gakkel Ridge has been shown to be complex and records a range of textures and compositions. Below, how these textures and compositions relate to magmatic processes will be discussed.

5.4.1 Significance of plagioclase textures

5.4.1.1 Skeletal growth: disequilibrium during undercooling

A first order observation that can be taken from the presented plagioclase compositions is that skeletal crystals and skeletal cores of matured skeletal crystals have lower core An contents compared to tabular and resorbed habits (Fig. 5.5a). Whilst this could be interpreted as the different crystal habits having grown under different pressure or temperature conditions or from melts of different bulk compositions, their morphologies and more sodic compositions are better explained as the result of their growth mechanism. It has been shown experimentally that under strong undercooling, plagioclase growth is diffusion-limited and results in plagioclase crystals that are more sodic than those that would grow under equilibrium conditions (Lofgren 1974). Sodic growth during strong undercooling is demonstrated well by crystal and melt inclusion quench rims which have more sodic compositions (Fig. 5.13d) and negative ΔAn values (Fig. 5.15d). In contrast, when the system is not strongly undercooled, growth from a melt is interface-controlled (Kirkpatrick et al. 1979) resulting in the growth of the remaining non-skeletal crystal cargo.

An important observation is that matured skeletal crystals record periods of undercooling distinct from that occurring during quench crystallisation (e.g., crystallisation of quench rims and some skeletal plagioclase), suggesting multiple periods of disequilibrium and undercooling within the magmatic system. Both magma mixing (e.g., Kuo and Kirkpatrick 1982) and intrusion of melts into cold regions of the plumbing system (e.g., Meyer and Shibata 1990; Hellevang and Pedersen 2008) have been attributed to undercooling and the formation of similar skeletal plagioclase from the Mid-Atlantic, Mohns and Knipovich Ridges. To our knowledge, similar matured skeletal plagioclase has not been reported from fast-spreading ridges. This cannot be due to a lack of magma mixing, as there is abundant evidence suggesting the importance of this process (Dungan et al. 1978; Grove et al. 1992; Pan and Batiza 2003; Ridley et al. 2006). Instead, the thinner and warmer lithosphere at fast spreading ridges may reduce the magnitude of undercooling experienced by magmas as they move through the magmatic system. Alternatively, matured skeletal plagioclase at fast-spreading ridges may simply not be erupted. This is supported by a recent study by Lange et al. (2013) that suggests axial melt lenses act

as density filters. They propose that when melts enter axial melt lenses at fast-spreading ridges the ascent velocity drops sufficiently to cause plagioclase to settle out of its host liquid and remain within the magmatic system. Whilst we cannot definitively say which factor led to the undercooling recorded by matured skeletal plagioclase at the Gakkel Ridge, the presence of a cool lithosphere likely favours the occurrence of undercooling as melts advance through the magmatic system; the absence of a steady-state plumbing system such as that at fast-spreading ridges favours their eruption. The presence of thin normally zoned melt inclusion rich zones within plagioclase may provide additional evidence for this process as suggested by Hellevang and Pederson (2008).

5.4.1.2 Resorption: recharge and decompression

Crystal resorption can occur through multiple processes, as illustrated in Fig. 5.1. Whilst, as indicted by the blue arrow in Figure 5.1a, heating alone can cause resorption, resorption interfaces are often associated with changes in compositions (Figs. 5.4,6,7,9,10) suggesting that the process(s) causing resorption must involve a change in composition of the system. The process(s) must also occur repetitively in order to explain the presence of multiple resorption interfaces within individual plagioclase (e.g., Fig. 5.10). Magma mixing is one mechanism that can cause changes in both the temperature and bulk composition of the system and is often invoked to explain resorption observed in mid-ocean ridge systems (e.g., Hellevang and Pedersen 2008). For example, during magma mixing, pre-existing plagioclase (X_2) is superheated (X_2-X'_2) and becomes resorbed, as the system tends toward equilibrium, and if the plagioclase was not completely dissolved, reverse zoning can form (X'_2-X_4) (Fig. 5.1). Alternatively, Figure 5.1a shows that a reduction in pressure (yellow-green) causes the equilibrium plagioclase composition to become more anorthitic, thus causing pre-existing plagioclase to become unstable; if the plagioclase is not completely dissolved, subsequent crystallisation is more anorthitic and reverse zoning forms.

Both magma mixing and decompression could occur multiple times within the system. However, because both of these processes result in similar textures and changes in major element composition, these cannot be used alone to distinguish the cause of resorption. Here, plagioclase TiO_2 contents has been used to distinguish between magma mixing- and decompression-induced resorption. The underlying rationale is that TiO_2 and An content form a well-defined negative correlation (Fig. 5.16a). In principle, this correlation can be related to (1) an increase in TiO_2 concentration in the melt during magmatic differentiation and (2) an increase in the Ti partition coefficient with both decreasing An content of the crystallising plagioclase and evolution of the melt composition (Bédard 2005). However, over the range of An_{60-85} the Ti partition coefficient

only increases by a factor of 1.5 (eq. 8 of Bédard (2005)) compared to TiO_2 that increases by a factor or 4. The change in partition coefficient is therefore not sufficient to explain the observed negative correlation; hence, the An-TiO_2 correlation (Fig. 5.16a) is interpreted to reflect a liquid line of decent. Assuming crystallisation occurs under equilibrium conditions, crystallisation following mafic recharge would have higher An and lower TiO_2 contents than crystallisation from a more evolved magma. Furthermore, plagioclase TiO_2 contents are relatively insensitive to changes in pressure with the partition coefficient of Ti in plagioclase changing by 0.01/GPa (Bédard 2005). Therefore, decompression-induced resorption would result in subsequent crystallisation of plagioclase that was reversely zoned but that has TiO_2 contents the same as the adjacent compositional zone formed prior to resorption.

Three relationships in Figure 5.16b suggest both decompression- and magma mixing-induced resorption have occurred. Magma mixing, involving evolved and primitive recharge, is supported by normal and reverse zoning outside of the resorption interface that have positive and negative ΔTiO_2 values respectively (Fig. 5.16b). Those resorption interfaces that show reverse zoning in An and no change in TiO_2 suggest that resorption has resulted from decompression (Fig. 5.16b). The ΔAn across these interfaces ranges from ~-4 to -8, which, assuming the pressure dependence of plagioclase is ~1.3% An/kbar, corresponds to decompression over ~9-18 km. The pressure dependence of plagioclase anorthite content was determined using rhyolite-MELTS (Gualda et al. 2012). Six glass samples (HLY0102-050-043, POL0059-228-003, HLY0102-012-013, POL0059-306-026, HLY0102-095-037, HLY0102-091-004, HLY0102-028-HY, HLY0102-060-045, HLY0102-053-018), were run at 1-5 kbar and QFM-1, and the pressure dependence determined from the slopes of the pressure-An relationships. Whilst a single decompression interval over these depths may seem high, the lithosphere at the Gakkel has been estimated to be up to 35 km thick (Schlindwein and Schmid 2016), indicating that there is ample distance over which decompression could occur. In addition, new plagioclase-hosted melt inclusion data extend the melt inclusion crystallisation pressure record to ~16 km (see Chapter 6). Therefore, the depth range inferred from the plagioclase anorthite contents are consistent with independent constraints on the lithospheric thickness and depths of crystallisation.

Whilst normal zoning and negative ΔTiO_2 can indicate evolved recharge, it may also suggest crystallisation under disequilibrium conditions. During disequilibrium, TiO_2 can become concentrated in a chemical boundary layer at the melt-crystal interface (Bottinga et al. 1966). Continued crystal growth may ultimately cause TiO_2 to become incorporated into the plagioclase resulting in both normal zoning and negative ΔTiO_2 values. However,

(1) only one of the three plagioclase crystals in this field (the lowest ΔTiO_2 and highest ΔAnR in Fig. 5.16b) shows morphological evidence of skeletal growth (e.g., outer rim that shows some intergrowth with the groundmass) and (2) the absolute TiO_2 contents of the outboard portions of these crystals are not elevated at low An as expected during skeletal growth; therefore at least two of the analysed crystals are consistent with having experienced resorption associated with evolved recharge.

Regardless of whether normal zoning and negative ΔTiO_2 reflect evolved recharge or disequilibrium growth, reverse zoning is the most common type of zoning following resorption. This suggests that the processes of primitive recharge and/or decompression are more common.

5.4.1.3 Patchy zoning: infilling following skeletal growth and resorption

Patchy zoning is often attributed to two different processes: (1) resorption and subsequent overgrowth (Vance 1965; Maaløe 1976; Ginibre and Wörner 2007; Ridley et al. 2006) and (2) skeletal growth and subsequent infilling (Kuo and Kirkpatrick 1982; Meyer and Shibata 1990). Patchy zoning observed here exhibits two morphologically distinct end-members, geometric (Type 1) and amoeboid (Type 2), that below are proposed to result from two processes.

Type 1 patchy zoning is geometric and present in matured skeletal crystals that have skeletal cores (Fig. 5.9a,b). These crystals are commonly reversely zoned and have high An patches within the skeletal core, or low An patches within the reversely zoned region (Fig. 5.9a,b). To understand the origin of Type 1 zoning, we first need to determine the origin of the reverse zoning. The lack of resorption at the junction between the skeletal core and surrounding high An region suggests the reverse zoning is not related to changes in magma composition or pressure, and instead likely reflects changes in growth kinetics. Crystallisation experiments of Lofgren (1974) have produced reverse zoning in skeletal plagioclase crystals under conditions of strong undercooling as the result of the crystal attempting to re-attain equilibrium growth conditions (Smith and Lofgren 1979); it is through this mechanism that reverse zoning within these crystals is suggested to have formed. A two-stage origin for Type 1 patchy zoning is proposed whereby initial undercooling (ΔT_U) within the magmatic system forms a lower An geometric skeletal core (S_1 in Fig. 5.19a and c). This core-forming stage is followed by a period when the crystal attempts to re-attain equilibrium (S_1 to S) resulting in overgrowth and infilling of the skeletal core with high An plagioclase producing matured skeletal crystals (S_2). The low and high An patches we observe are a result of sectioning of the matured skeletal plagioclase crystal. Isolated patches of low An correspond to the

skeletal core; in 3D these isolated patches would be connected to the remaining skeletal crystal. High An patches are the result of infilling of voids within the original skeletal framework.

Type 2 patchy zoning is characteristically amoeboid in form (Fig. 5.9c-g). The irregular shape of Type 2 patches are interpreted as the result of crystal resorption (Fig. 5.19, X_2-X'_2) that either proceeded along cleavage planes, resulting in a degree of crystallographic alignment and elongation of patches (Fig. 5.9c) or occurred randomly throughout (Fig. 5.9d-g). Patches are often associated with amoeboid melt inclusions that possess zonation about their margins; this zoning can be similar to zoning around the outside of the host crystal (Fig. 5.9f). This suggests that melt inclusions have not been occluded and have remained connected to the matrix following resorption. Any subsequent crystallisation occurs on both the exterior of the crystal and walls of the inclusions (Fig. 5.19, X'_2-X_4). Depending on where the crystal is sectioned, one may observe a patch or a melt inclusion with a rim (Fig. 5.20). The interpretation that voids formed during resorption remained connected to the matrix is supported by the similar compositions of isolated patches (i.e., those not associated with melt inclusions) and other compositional zones of the crystal (Fig. 5.9c). Here zoned patches are not considered to have formed from the crystallisation of trapped melt as suggested by Vance (1965) and Meyer and Shibata (1990), due to the absence of multi-phase inclusions associated with isolated patches.

5.4.1.4 Glomerocrysts: mush fragments and synneusis

Plagioclase crystal cargo contains both poly- and mono-mineralic glomerocrysts (Fig. 5.6a,b). Poly- and mono-mineralic glomerocrysts that have open structures and plagioclase components at high angles to one another (Fig. 5.6a,b) are interpreted here as portions of crystal mush networks that have been entrained into an ascending melt. High-angle, predominantly plagioclase networks have high porosities and have previously been interpreted as pieces of immature crystalline mush (e.g., Holness et al. 2005). Similar crystal networks from the East Pacific Rise are interpreted a pieces of entrained crystal mush (Pan and Batiza 2003; Moore et al. 2014). The presence of olivine within some of the poly-mineralic glomerocrysts (e.g., Fig. 6a) suggests, that in some instances, olivine may remain stuck within the mush zone. In contrast to those with open mush network structures, some glomerocrysts have closed structures with components at low angles to one another (Fig. 5.6c). Whilst the lack of open structures and presence of planar contacts may reflect derivation from a more compacted portion of the mush system, they could equally have formed through synneusis. Synneusis is the drifting together and attachment of like phases during turbulent flow (Vance and Gilreath 1967)

and is likely to occur during melt ascent. It might be that individual glomerocryst components originate from a mush zone, and that following mush zone disaggregation the components come together through synneusis during transport in the melt.

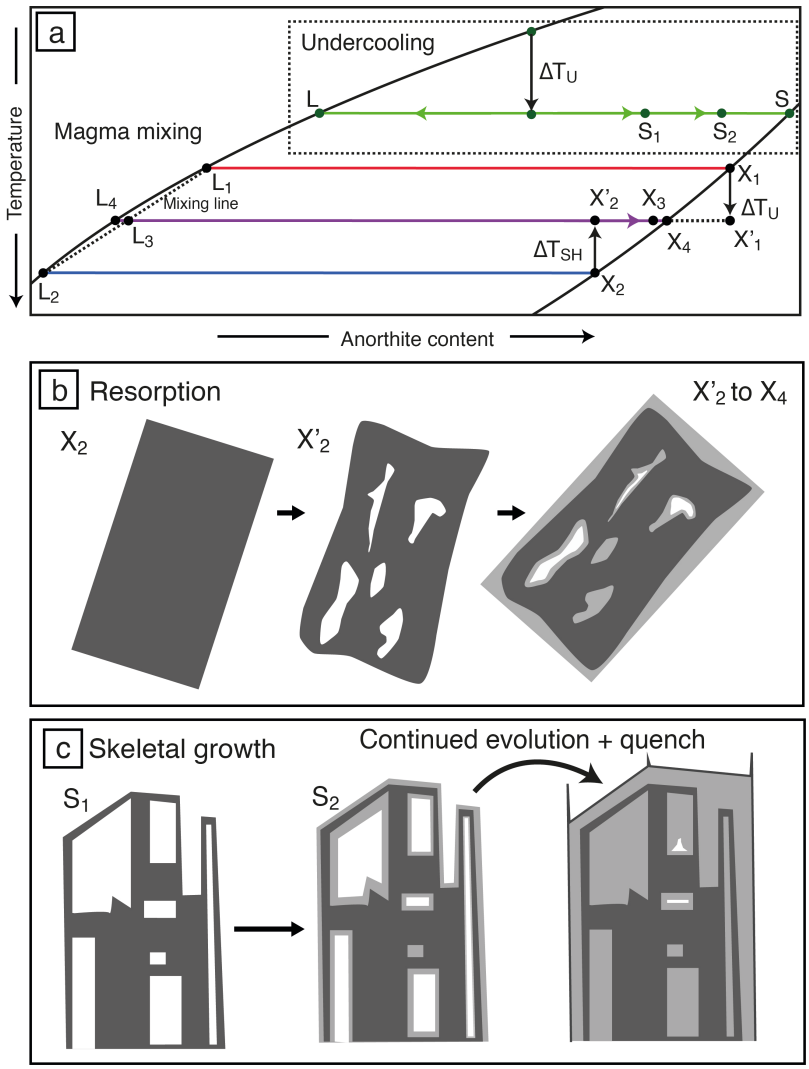

Fig. 5.19: Schematic phase diagram, as shown in Fig. 5.1, in the albite-anorthite system showing the effect of (1) undercooling and (2) mixing between two liquids (L_1 and L_2 to form L_3) on both plagioclase composition and morphology. During magma mixing, pre-existing plagioclase (X_2) experience superheating (ΔT_{SH}) and resorption (X_2-X'_2). If plagioclase is not completely dissolved the resorbed plagioclase become overgrown and infilled with more anorthitic plagioclase (i.e., reverse zoning) as the system moves toward equilibrium; Type 2 patchy zoning is formed (X'_2-X_4) (**b**). Newly formed plagioclase (X_3) also grow from L_3 and become reverse zoned (X_3-X_4). Magma mixing can also result in undercooling (ΔT_u) of pre-exiting plagioclase (X_1-X'_1). Type 1 patchy zoning (**c**) results from initial undercooling (ΔT_u to produce L_*) resulting in the formation of skeletal crystals (S_1) whose composition lies between L_* and S. Both solid and liquid phases will evolve toward equilibrium (L and S respectively). As the system evolves (S_1-S), the skeletal framework becomes infilled through continued crystallisation; the plagioclase become reverse zoned and matured skeletal crystals exhibiting Type 1 patchy zoning are formed. Phase diagrams are re-drawn from Lofgren (1974) (undercooling), and Kuo and Kirkpatrick (1982) (magma mixing).

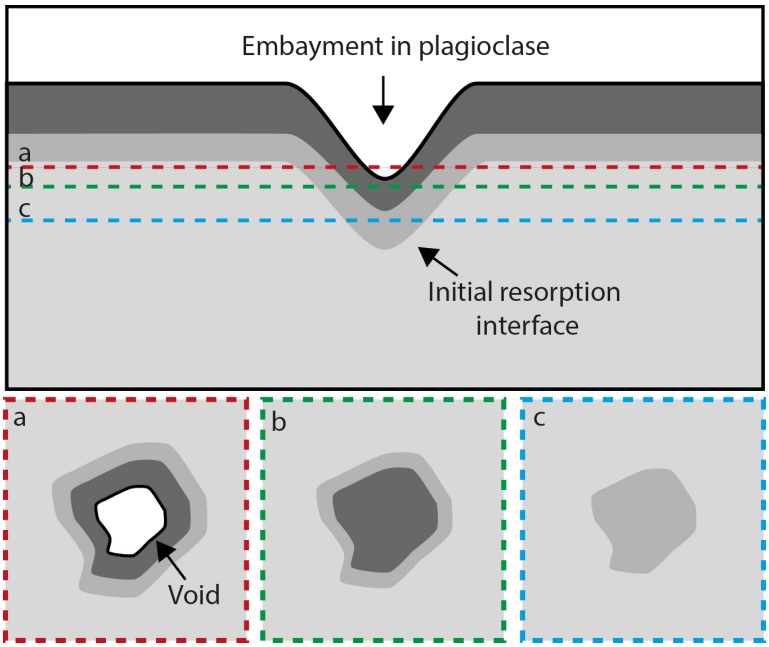

Fig. 5.20: Schematic showing the effect of sectioning on the observed plagioclase zoning pattern. Depending on the level at which plagioclase is sectioned through you may observe an internal void surrounded by compositional zoning (**a**), or a single patch if the crystal is sectioned at a deeper level (**c**).

Whilst poly-mineralic glomerocrysts can exhibit simpler zoning than mono-minerlic glomerocrysts, components in each record evidence of complex crystallisation histories (e.g., resorption, patchy zoning and complex zoning combinations), with the more evolved compositions of some glomerocrysts suggesting they were derived from more evolved regions of the plumbing system. Indeed, the presence of plagioclase rims in both poly- and mono-mineralic glomerocrysts that are too evolved to be in equilibrium with their host melts indicates that the glomerocrysts equilibrated in an evolved mush zone before being picked up by a more primitive host melt (Fig. 5.15c). Reverse zoning in 20% of the 45 mono-mineralic glomerocryst components that had both cores and rims analysed further indicates that mush zones experienced primitive recharge, with some plagioclase growing directly from the recharging melt. In addition to the evidence of primitive recharge, rims of some glomerocrysts that are too primitive to be in equilibrium with their host melts (Fig. 5.15c) indicate that they were entrained by more evolved melts. Taken together, these lines of evidence demonstrate that both primitive and evolved mush zones are present in the Gakkel Ridge and that mush zone components were entrained by both primitive and evolved recharging melts.

5.4.2 Melt inclusion entrapment

The relationship between melt inclusion morphology and host plagioclase textures suggests that different morphologies result from different processes; understanding how these different morphologies form is necessary in order to correctly interpret melt inclusion data (Michael et al., 2002; Faure and Schiano 2005). Within matured skeletal crystals, boxy, often elongated melt inclusions occur in association with both reversely zoned portions of the crystals and geometric high An patches within the low An skeletal core (Fig. 5.9a,b). These melt inclusions are proposed to originate as hollows within the geometric skeletal core. Infilling of the voids by reversely zoned plagioclase suggests that the voids formed during skeletal growth were not immediately isolated from the matrix. Continued connection to the matrix means that any modification to the melt composition caused by the initial skeletal growth (i.e., plagioclase incompatible element enrichment in adjacent boundary layer (Bottinga et al. 1966)) can become dissipated over time if element diffusivities are rapid enough (Danyushevsky et al. 2002). If at a later stage these voids become isolated from the matrix, the composition of the inclusion would not be the same that existed at the time of initial skeletal growth, nor would it record geochemical evidence of skeletal growth. Only if melt inclusions were occluded rapidly would chemical evidence of skeletal growth be observed.

Similarly, resorption causes melt adjacent to resorbed plagioclase to become enriched in plagioclase components (Nakamura and Shimatika 1998; Danyushevsky et al. 2002); melt inclusions will record these modified compositions if melt inclusions are occluded from the matrix soon after the initial resorption event. In the Gakkel samples, Type 2 patchy zoning and marginal zoning around melt inclusions suggest that occlusion did not occur rapidly, and that inclusions remained connected to the matrix. Therefore, as with the melt inclusions in the skeletal crystals, the composition of resorption-related amoeboid melt inclusions may not record the melt composition at the time of resorption or any compositional modification resulting from initial resorption. These amoeboid melt inclusions are found at multiple levels within plagioclase; around the margins, associated with internal resorption interfaces (Fig. 5.4a, 10b) or randomly distributed throughout (Fig. 5.9e). Where melt inclusions are related to resorption interfaces, it may be possible to determine a relative timing for their formation. However, Cashman and Blundy (2013) have highlighted that the three-dimensional nature of melt inclusions and their prolonged connection to the matrix means that there is often no spatial pattern to volatile contents and in turn entrapment pressures; this should be kept in mind when determining the evolutionary stages of a system.

The association of particular melt inclusion morphologies with specific textures in plagioclase demonstrates that their formation may be associated with processes which alter the composition of trapped melts. If boundary layers do become trapped within melt inclusions, compositions of these inclusions will not faithfully represent the true composition of melts within the magmatic system. Equally, if melt inclusions remain connected to the matrix for a period before occlusion, their compositions will not relate to those that existed when the inclusion formed. Therefore, without a thorough understanding of how melt inclusions formed, melt inclusion compositions cannot be reliably used as tools to study the compositional variability of magmatic systems.

5.4.3 The origin of plagioclase crystal cargo

Within mid-ocean ridges, axial melt lenses, dykes, and mush zones are all potential sources of the plagioclase crystal cargo. When considering the origin of plagioclase in the Gakkel ridge, any model needs to account for the following observations: (1) mixed crystal populations; (2) crystal content; (3) open-structured glomerocrysts; (4) plagioclase-melt disequilibrium; (5) plagioclase habits indicative of undercooling; and (6) multiple periods of resorption. Whether these observations are consistent with plagioclase crystal cargo originating from a melt (i.e., axial melt lens or dykes) or crystal (i.e., mush zone) dominated system will be explored below.

The presence of plagioclase with contrasting magmatic histories within individual samples (Fig. 5.17 and 18) requires an efficient mechanism by which these crystals become juxtaposed. Convection within a melt body, such as an axial melt lens, is one mechanism by which this could occur, and would need two criteria to be met: (1) the presence of a magma chamber; and (2) low enough magma crystallinities to facilitate convection. To date, melt lenses at multiple depths have been identified at fast- (e.g., Detrick et al. 1987; Marjanović et al. 2014) and intermediate-spreading (e.g., Canales et al. 2005) ridges, with similar, likely ephemeral lenses identified along limited portions of slow-spreading ridges (e.g., Sinha et al. 1998; Singh et al. 2006). Melt lenses are often segmented into crystal-rich and crystal-poor regions (Singh et al. 1998; Xu et al. 2014; Marjanović et al. 2015); melt within melt-dominated regions has low viscosities and can convect freely (e.g., Sinton and Detrick 1992). Whilst an axial magma reservoir containing 3-10% melt was recently identified beneath the ultraslow-spreading Southwest Indian Ridge (Jian et al. 2017a,b), there is as yet no evidence to support the presence of melt lenses similar to those at fast-spreading ridges beneath ultraslow-spreading ridges, including Gakkel. Additionally, as magma crystallinity reaches 20-25%, magma viscosity increases to the point where the system is essentially a mush (Marsh 1989) and convection is greatly inhibited (Sinton and Detrick 1992). Basalt samples

reported here have crystal contents up to 50% (Fig. 5.2). Therefore, both the lack of melt lenses along the Gakkel Ridge and high crystal content of many basalts are inconsistent with crystal cargo originating from a melt-rich body. Nonetheless, the low crystal content of some basalts (Fig. 5.2) indicates that melt-dominated regions may exist locally within the Gakkel Ridge plumbing system.

As opposed to crystallisation in a melt lens, the plagioclase crystal cargo may have crystallised during dyke injection (e.g., Zellmer et al. 2011). However, multiple observations are at odds with this relatively simple model and instead suggest that crystallisation during magma ascent was limited. Firstly, if crystallisation occurred solely during dyke ascent, one would expect either equilibrium between the host glass and crystals, or disequilibrium growth of low-An crystals if undercooling prevails. However, the data suggests that much of the plagioclase crystal cargo is in equilibrium with melts that are more primitive than the host glasses (Fig. 5.15). Of note is the observation that plagioclase crystals in samples from the same dredge analysed by Zellmer et al. (2011) show some of the most extensive disequilibrium (Fig. 5.21). Furthermore, the zoning complexity of the Gakkel plagioclase is typically high (Fig. 5.7 and 5.8), indicating that multi-stage histories, often including resorption (Fig. 5.10), are the norm. However, lower zoning complexity values and number of resorption events recorded by skeletal and acicular plagioclase (Table A2.1 and A2.6) indicate they experienced simpler histories than resorbed and tabular forms which may relate to the timing of crystallisation (e.g., skeletal and acicular plagioclase have grown during late periods of undercooling). Finally, the juxtaposition of chemically and texturally distinct plagioclase populations within samples (Fig. 5.17 and 18) indicates that individual crystals experienced different magmatic histories and, with the exception of the few true phenocrysts and micro-phenocrysts, were likely entrained into an ascending melt from distinct parts of the plumbing system.

Alternatively, crystal cargo could have originated from a crystal-dominated region within the plumbing system where melt viscosities are low, and crystallinities are high (Sinton and Detrick 1992). The presence of mush zones at mid-ocean ridges is supported by both geophysical (e.g., Singh et al. 1998; Crawford et al. 1999) and petrological (e.g., Pan and Batiza 2003; Ridley et al. 2006) evidence whilst their disaggregation has been identified as a key process occurring in basaltic systems (Sinton and Detrick 1992; Hansen and Grönvold 2000; Pan and Batiza 2003; Costa et al. 2009; Passmore et al. 2012; Lange et al. 2013; Neave et al. 2014; Neave et al. 2017). Multiple observations support that this process plays a vital role in the origin of the plagioclase crystal cargo at the Gakkel Ridge.

Firstly, the high crystal content of some samples is more consistent with an origin from a mush zone as opposed to a convecting melt body. Whilst one might expect other phases that might have formed in the mush zone, such as olivine, to be present in erupted crystal cargo, we observe an enrichment in plagioclase relative to olivine as the total crystal contents increases (Fig. 5.2). This plagioclase enrichment has been identified in other MORB crystal cargo (e.g., Bryan 1983) and is a common feature of plagioclase ultraphyric basalts (PUBs) sampled at intermediate- to ultraslow-spreading ridges (e.g., Lange et al. 2013). This enrichment may reflect the loss of olivine by gravity settling during melt ascent following mush disaggregation or, as suggested by Lange et al. (2013) for the origin of PUBs, the disruption of non-cotectic plagioclase-rich cumulates. Secondly, whilst individual plagioclase crystals might represent parts of disaggregated mush, glomerocrysts, in particular those with open crystal networks interpreted as pieces of entrained crystal mush, support an origin for at least some of the crystal cargo through mush disaggregation. Finally, the amount of disequilibrium (Fig. 5.15) and physical evidence for resorption (Fig. 5.10) supports the idea that plagioclase crystal cargo did not grow from its host melt and was entrained from elsewhere. Instead, as indicated by diffusion studies (Costa et al. 2009; Moore et al. 2014), it is suggested here that pre-existing mush zones become disaggregated following melt replenishment; plagioclase from these mush zones is subsequently out of equilibrium with the host melt. Through disaggregation, plagioclase from different parts of the mush zone that have experienced different magmatic histories becomes juxtaposed resulting in mixed chemical and textural populations (e.g., Fig. 5.17). It is important to highlight that multiple resorption events within single plagioclase crystals indicates that the process of melt replenishment and mush disaggregation may occur multiple times within the magma plumbing system. Alternatively, following disaggregation, melts with their entrained crystal cargo may experience staged decompression resulting in multiple periods of disequilibrium and subsequent resorption.

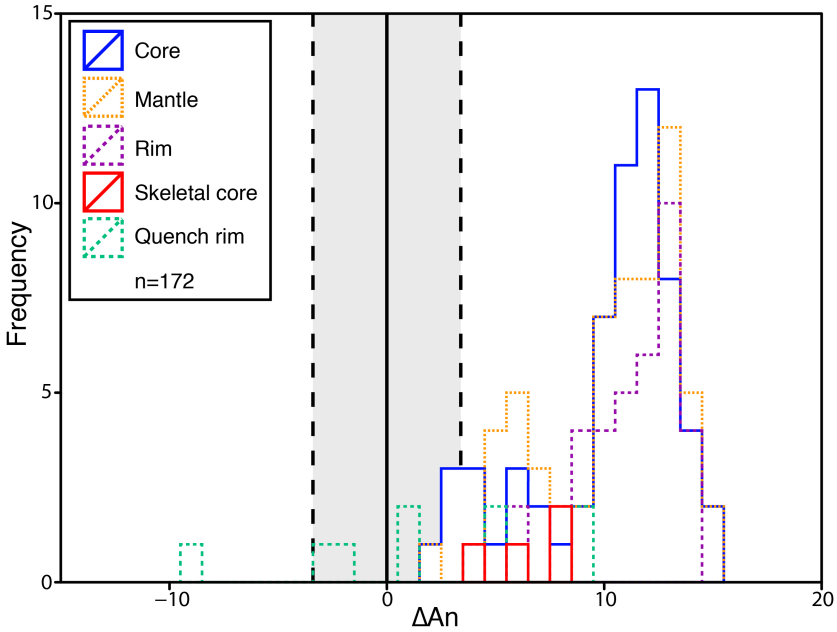

Fig. 5.21: Histogram of ΔAn demonstrating that plagioclase from dredge HLY0102-D27 show extensive disequilibrium regardless of the analysis location (e.g., core, rim etc.). The majority of analyses plot to the right in equilibrium with more primitive melt compositions than host glasses. Solid black vertical lines represent equilibrium (ΔAn=0); dashed lines represent ±5% (Grove et al. 1992) error on the average plagioclase anorthite content (An_{69}) calculated using equations (1) and (2)

5.5 Synthesis

The textural and compositional complexity of the plagioclase crystal cargo presented here allow the processes occurring within the magma plumbing system of the ultraslow-spreading Gakkel Ridge to be reconstructed (Fig. 5.22). Following initial melt focussing (1) and extraction (2) from the asthenosphere, melts are intruded into the lithosphere that comprises a relatively thin basaltic crust directly overlying mantle peridotite. Intrusion into the mantle lithosphere and subsequent crystallisation produces a mushy, crystal dominated plumbing system within which variable degrees of fractionation can occur. Within these zones there may be localised melt-rich regions as suggested by the low crystal contents of some samples. Multiple lines of evidence suggest that later melt replenishment, with both primitive and evolved melts, causes mush zones to become disaggregated (3), with mush components becoming incorporated into the ascending melt in the form of both individual crystals and networks. Disaggregation of different parts of the mush zone results in the juxtaposition of texturally and chemically distinct plagioclase populations. The simpler zoning complexities of skeletal and acicular plagioclase indicate they had simpler crystallisation histories compared to tabular and resorbed forms and may have formed during later periods of undercooling. Repeated episodes of melt decompression (4) and magma mixing (5) generate periods of disequilibrium and resorption. Periods of crystallisation following initial resorption generate Type 2 patchy zoning. Evidence for periods of disequilibrium growth is also

present in the form of skeletal and matured skeletal crystals. Matured skeletal crystals result from periods of undercooling that are distinct to that occurring upon quench crystallisation and could result from both magma mixing (5) and intrusion into cool regions of the lithosphere (6). Subsequent re-attainment of equilibrium growth mechanisms results in the generation of Type 1 patchy zoning and matured skeletal crystals. The presence of repeated reverse zones separated by thin normal zones that may or may not be melt inclusion rich support the occurrence of magma intrusion into cool regions of the lithosphere. Finally, turbulent flow during the movement of melts within the system, potentially during final ascent and eruption, may result in synneusis (7) and the formation of mono-mineralic glomerocrysts and attachment of plagioclase crystals. Eventual eruption (8) results in basalts that contain complex plagioclase crystal cargo, the textures of which can be related to both protracted growth histories and occurrence of specific processes within the plumbing system of the Gakkel Ridge.

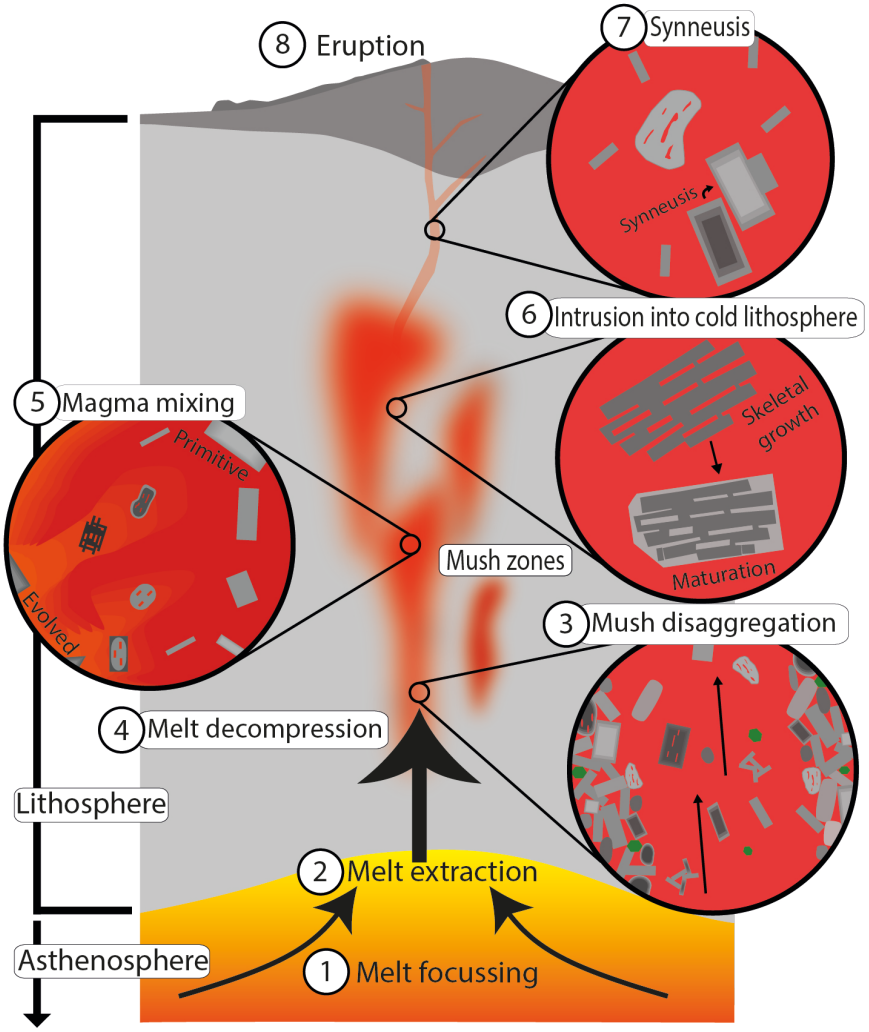

Fig. 5.22: Schematic model for the processes occurring within the Gakkel Ridge magma plumbing system. Here the asthenosphere is overlain by lithosphere that comprises a basaltic cap directly overlying mantle peridotite. Processes within the Gakkel Ridge are as follows: **1**, melt focussing; **2**, melt extraction; **3**, mush disaggregation; **4**, melt decompression; **5**, magma mixing; **6**, intrusion into cold lithosphere; **7**, synneusis; **8**, eruption. See text for discussion. Note: all processes other than **1**, **2** and **8** can occur in any order.

Chapter 6

Deep roots for mid-ocean ridge volcanoes revealed by plagioclase-hosted melt inclusions

This chapter is based upon the following published paper:

Bennett, E.N., Jenner, F.E., Millet, M.A., Cashman, K.V. and Lissenberg, C.J. 2019. Deep roots for mid-ocean-ridge volcanoes revealed by plagioclase-hosted melt inclusions. Nature, *572*; 235-239.

Author contribution and declaration:

E.N.B. and C.J.L. conceived of the study. E.N.B. collected all data, except melt inclusion trace element data collected by F.E.J. E.N.B. wrote the manuscript and chapter under supervision of C.J.L. and K.V.C.; M-A.A. and F.E.J contributed to critical discussions and commented on the manuscript. Note: Melt inclusion trace element data presented in the manuscript are not presented as part of this thesis.

Chapter 6

6.1 Introduction

Direct constraints on the depth of crystallisation beneath mid-ocean ridge volcanoes, the most productive magmatic system on Earth, come from melt inclusions (Shaw et al. 2010; Wanless and Shaw 2012; Wanless et al. 2014a, b; Colman et al. 2015; Wanless and Behn 2017). Crystallisation pressures determined from melt inclusion volatile contents typically correspond to the depth of seismically imaged melt lenses (Wanless and Shaw 2012) and reveal that much of the crystallisation is restricted to crustal depths (Wanless and Shaw 2012; Wanless et al. 2014b; Colman et al. 2015) (nominally 6 km), with limited crystallisation up to 9.9 km (Wanless et al. 2014b). These pressures suggest that mid-ocean ridge volcanoes have shallow magmatic roots that are largely restricted to the lower oceanic crust, with limited sourcing of eruptions from the lithospheric mantle (Phipps-Morgan and Chen 1993a; Chen and Lin 2004; Wanless and Shaw 2012; Wanless et al. 2014b; Jian et al. 2017). However, lithospheric thickness (Schlindwein and Schmid 2016) and crystallisation pressures determined from basalt major element barometers (Wanless and Behn 2017) are greater than that suggested by olivine-hosted melt inclusions, particularly at ultraslow-spreading ridges. A case in point is the Gakkel Ridge, where melt inclusion vapour saturation pressures (40-309 MPa or 0-9 km below seafloor (Shaw et al. 2010; Wanless et al. 2014a)) are substantially less than the proposed lithospheric thickness (≤30 km (Schlindwein and Schmid 2016)) and petrological estimates of crystallisation pressures from basalt major elements (≤600 MPa or ~20 km) (Wanless and Behn 2017). These contradictory records raise the question as to whether, using current constraints, we can confidently constrain the true vertical extent of mid-ocean ridge magmatic systems.

There are currently several approaches to constraining crystallisation pressures beneath mid-ocean ridges: 1) major element thermobarometery and 2) melt inclusion volatile contents. Major element thermobarometers (e.g., Grove et al. 1992; Yang et al. 1996; Herzberg 2004; Villiger et al. 2007) are calibrated from experiments run at different pressures that map the saturation surfaces of olivine, plagioclase and clinopyroxene (e.g., Grove et al. 1992). Through their application to mid-ocean ridge basalts, crystallisation pressures have been shown to increase with decreasing spreading rate (Grove et al. 1992; Michael and Cornell, 1998; Herzberg, 2004; Wanless and Behn 2017), consistent with more efficient conductive cooling with decreasing spreading rate (Reid and Jackson 1992; Bown and White 1994). The barometer of Herzberg (2004)

provides constraints on the pressure at which partial melting is replaced by partial crystallisation and has been used by Standish et al. (2008) to investigate how the depth of the lithosphere varies along the Southwest Indian Ridge. In contrast, OPAM barometry, which relies on plagioclase-olivine-augite-melt equilibrium, provides information on the final pressures of melt equilibration prior to eruption (e.g., Neave et al. 2013). There are several limitations to using major element barometers. First, the major element barometers can only be applied to magmas which are multiply saturated with olivine + plagioclase + clinopyroxene, which is not always the case for mid-ocean ridge basalts (MORBs). Second, whilst these barometers provide single pressures, mid-ocean ridge basalts experience polybaric crystallisation, hence the pressures only represent a single stage in the crystallisation history of mid-ocean ridge basalts. For example, as discussed by Neave et al. (2013), because equilibrium is only present between glass and the outer rims of olivine, plagioclase and clinopyroxene, results of OPAM barometry here only provides constraints on the final pressures of melt equilibration prior to eruption; to constrain the physical conditions of earlier crystallisation, they suggest that additional approaches such as clinopyroxene thermobarometry are needed.

An alternative to major element barometers is petrological modelling (e.g., Michael and Cornell 1998). In this approach, crystallisation pressures are determined by comparing suits of basalts to fractional crystallisation models run at a range of pressures (Michael and Cornell 1998; Wanless and Behn 2017). The pressure of crystallisation is assigned to a suit of basalts by identifying the best-fit fractional crystallisation line. Like major element barometers, petrological modelling provides a single pressure. However, because the single pressure relates to the range of erupted basalt compositions, it does not provide information on, or account for, polybaric crystallisation. A benefit of petrological modelling over major element barometry is that it does not require 3-phase saturation. A further limitation of both major element barometers and petrological modelling is that neither accounts for the modification of basalt major element compositions through processes other than fractionation, such as melt-crystal reactions within the magmatic plumbing system–a process for which there is abundant evidence (e.g., Lissenberg and Dick 2008; Lissenberg et al. 2013; Lissenberg and MacLeod 2016).

An alternative approach to determining crystallisation pressures is the use of melt inclusion vapour-saturation pressures which capitalizes on the pressure dependence of CO_2 solubility (Dixon and Stolper 1995). These melt inclusions, small volumes of trapped melt, have the potential to record an accurate, fine-scale, polybaric pressure record if they are trapped within host minerals at different depths during melt transport through

the magmatic plumbing system. Olivine-hosted melt inclusions are often preferred because: (1) olivine is a primitive, early-formed mineral (Kent 2008), and hence should, in principle, track the earliest stages of magmatic differentiation; and (2) olivine is viewed as a tighter "vessel" compared to plagioclase, which possesses cleavage planes along which volatiles may escape (Kress and Ghiorso 2004; Neave et al. 2017). However, the low vapour saturation pressures recorded by olivine-hosted melt inclusions, not only from mid-ocean ridges, but also from a range of low-H_2O basaltic settings including ocean islands, continental rifts and arcs, poses a significant question as to their ability to capture the full depth range of the magmatic plumbing systems from which they are sourced (Maclennan 2017).

To date there are three mid-ocean ridge plagioclase-hosted melt inclusion studies. However, because these plagioclase-hosted inclusions have come from atypical tectonic settings (e.g., off-axis seamounts (Helo et al. 2011; Coumans et al. 2016) and a transform fault (Drignon et al. 2018)), their compositions are not considered indicative of the depths of plumbing systems directly beneath active mid-ocean ridge axes and thus are not included for further comparison. In addition, the plagioclase-hosted melt inclusions of Helo et al. (2011) are CO_2 oversaturated and thus cannot be used to constrain crystallisation pressures. Furthermore, these studies provide no comparison to pressures derived from olivine-hosted melt inclusions and hence, as will be argued later on, are unlikely to provide a full picture of the depths of crystallisation within these systems.

Here detailed textural analysis of host olivine and plagioclase crystals are combined with measurements of the volatile (H_2O and CO_2) content of 29 olivine-hosted and 72 plagioclase-hosted melt inclusions from the Gakkel Ridge to compare their respective records of crystallisation. The 15 samples studied were retrieved from nine locations that cover the full extent of the Gakkel Ridge (Fig. 6.1). These data are supplemented by existing data from olivine-hosted melt inclusions from this region (Shaw et al. 2010; Wanless et al. 2014a).

6.2 Methods

6.2.1 Post-entrapment crystallisation correction

The major and volatile element compositions of both olivine- and plagioclase-hosted melt inclusions were corrected for the effects of post-entrapment crystallisation (PEC). Raw and corrected melt inclusion compositions (major and volatile elements) are reported in Electron Appendix 5.

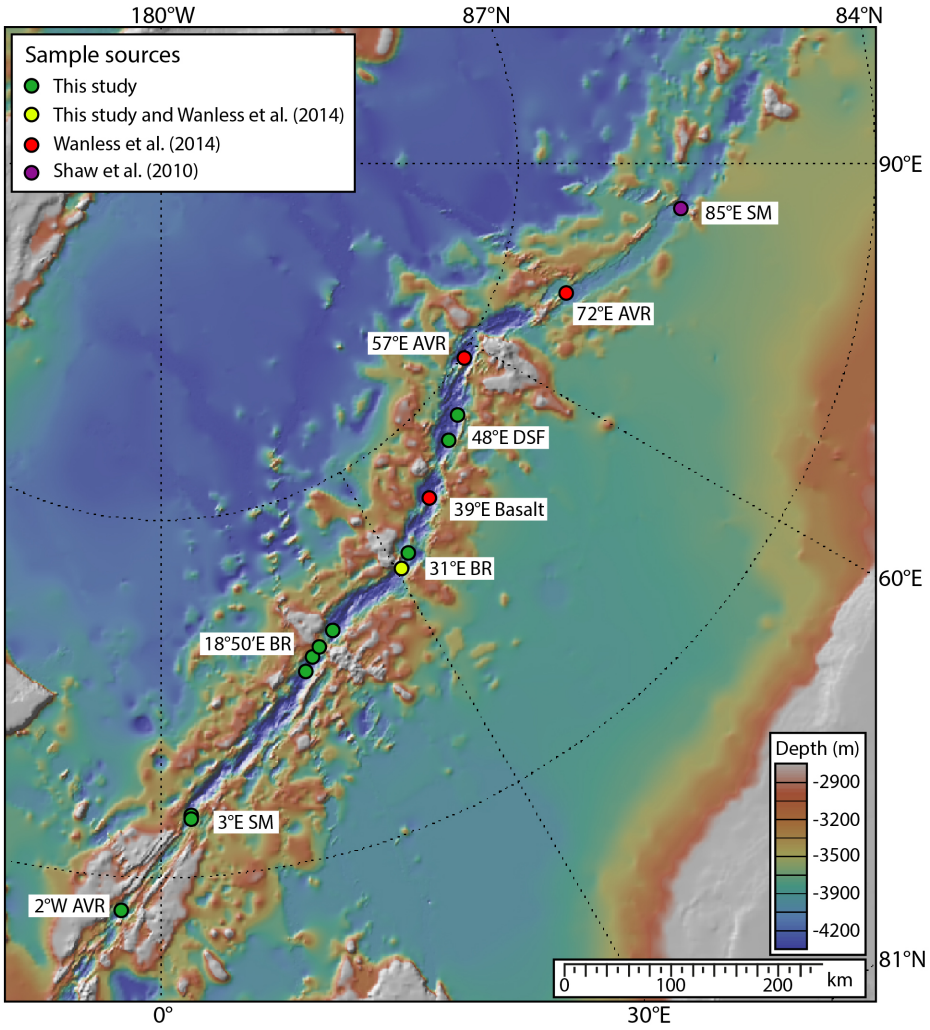

Fig. 6.1: Sample locations along the Gakkel Ridge. Symbol colours are as follows: green, new plagioclase- and olivine-hosted melt inclusion analyses; yellow, new plagioclase-hosted melt inclusion data supplemented by olivine-hosted melt inclusion data from Wanless et al. (2014a); red and purple points indicate data from Shaw et al. (2010) and Wanless et al. (2014a). Location name abbreviations are as follows: AVR, Axial Volcanic Ridge; SM, Seamount; BR, Basement Ridge; DSF, Deep Seafloor. IBCAO bathymetric data from Jakobsson et al (2012). The Global Multi-Resolution Topography (GMRT) synthesis (Ryan et al. 2009) base map underlies IBCAO bathymetry. Map made using GeoMapApp (http://www.geomapapp.org).

6.2.1.1 Olivine PEC correction

Two olivine PEC correction schemes have been investigated. First, olivine compositions were corrected by iteratively adding equilibrium olivine back into the melt until the melt and host olivine were in equilibrium with one another (Sobolev and Shimizu 1993). This assumed an equilibrium Fe-Mg distribution coefficient (K_D) of 0.3 (Roeder and Emslie 1970) and $Fe^{3+}/\Sigma Fe$ of 0.1 (Berry et al. 2018). Olivine PEC corrections range from 2-22% (median 13.0%). For comparison, the composition of six olivine-hosted melt inclusions, spanning the full range of measured CO_2 contents, have been reconstructed using Petrolog3 (Danyushevsky and Plechov, 2011) which accounts for Fe-loss caused by diffusive re-equilibration between the melt inclusion and olivine host; Fe-loss results in melt inclusions with low FeO content. Olivine PEC corrections using Petrolog3 are

slightly lower than the previous method and range from -1.31-19.50%. Both PEC correction methods result in similar melt inclusion CO_2 contents and Mg# (Fig. 6.2), except in the case of some melt inclusions where Petrolog3 predicts lower Mg# than the first method; the first method results in higher MgO contents, FeO is similar. In order to correct for Fe-loss using Petrolog3, the initial FeOt content of the inclusion at the time of entrapment is required. Here, FeOt was determined by examining the FeOt-TiO_2 systematics of Gakkel glasses. The rationale behind this is that TiO_2, which is incompatible in olivine, should not be modified extensively during olivine crystallisation (i.e., PEC). Therefore, using the TiO_2 contents of the melt inclusions, FeOt of the original melt inclusion can be estimated from a regression through the Gakkel glass array. However, because FeOt can vary significantly at a given TiO_2 content there is significant uncertainty in this estimation of FeOt. For example, FeOt content, based on the Gakkel glass array, for a TiO_2 content of 1.21 (corresponding to O3b in Fig. 6.2) ranges from 7.5-11.04. This results in a range of pressures from 812-1278 bar. Similarly, at a TiO_2 contents of 1.13 wt%, FeOt of 8.2±1 wt.% results in a range of pressures from 1977-2539 bar. Therefore because of the uncertainty in the initial FeOt the following discussion will use olivine compositions calculated using the first method described.

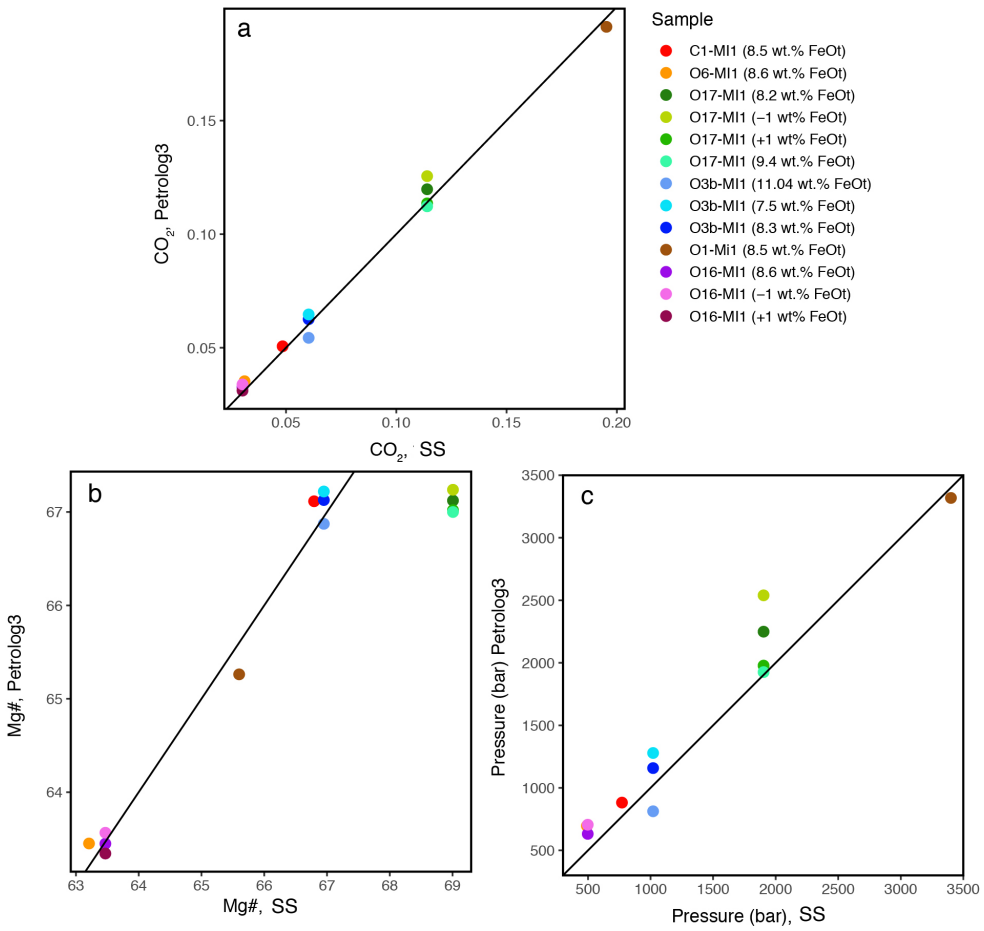

Fig. 6.2: CO_2 (**a**), Mg# (**b**) and saturation pressures (MPa) (**c**) resulting from olivine PEC correction using Petrolog3 and the approach of Sobolev and Shimizu (1993) (SS) described in the text.

6.2.1.2 Plagioclase PEC correction

To date there is no widely accepted method of correcting PEC in plagioclase-hosted melt inclusions. Previously, PEC corrections have been undertaken by adding plagioclase (equilibrium plagioclase or host plagioclase) to the melt inclusion until its MgO-Al_2O_3 (Neave et al. 2017) or TiO_2-Al_2O_3 (Hartley et al. 2018) systematics are consistent with regressions through Icelandic glass arrays. However, these corrections are unconstrained in that the melt inclusion compositions can move in both MgO or TiO_2 and Al_2O_3 space toward these regressions. An alternative approach developed here is an empirical correction which assumes that during plagioclase crystallisation, Al_2O_3 is the most modified melt component, whilst Mg# remains unchanged because both Mg and Fe are incompatible in plagioclase. Plagioclase was therefore added to the melt inclusion composition until the melt inclusions met the Al_2O_3 content (at a given Mg#) of the combined Gakkel glass (Lehnert et al. 2000; Lissenberg et al. 2019) (Fig. 6.5) and olivine-hosted melt inclusion (Shaw et al. 2010; Wanless et al. 2014a) datasets. In practice a pseudo-liquid line of descent was created (Fig. 6.5 caption for details) and then host plagioclase compositions were iteratively added to the melt inclusions until the liquid line of descent was intersected. From here onwards, the three above approaches will be referred to as Hartley, Neave and Bennett (this study) corrections.

In Fig. 6.3 the major element compositions of melt inclusions corrected using each approach outlined above are compared to Gakkel glasses and olivine-hosted melt inclusions. In general, corrected plagioclase-hosted melt inclusion compositions are similar regardless of the correction scheme used and fall within the field of Gakkel glasses. However, the correction scheme of Hartley, which relies on adding host plagioclase to the melt inclusion composition until it is consistent with TiO_2-Al_2O_3 of the Gakkel glasses, results in melt inclusion compositions with unrealistically high Al_2O_3 contents (Fig. 6.3e,f). An additional combined correction scheme is also shown and involves adjusting the amount of plagioclase added to the melt inclusion so that its composition is consistent with MgO-Al_2O_3, TiO_2-Al_2O_3 and Mg#-Al_2O_3 systematics of Gakkel glasses. Major element compositions resulting from this combined correction are similar to other approaches.

Plagioclase-hosted melt inclusion PEC corrections using the Bennett correction range from 0-41.5% (median 14.8%) (Electronic Appendix 5) and are similar to PEC corrections of other approaches (Fig. 6.4); PEC corrections are lower using the Neave correction (Fig. 6.4b). There is a strong positive correlation between the combined and Bennett PEC correction approaches. The corrected CO_2 contents of melt inclusions is similar

regardless of PEC corrections scheme used (Fig. 6.4d). Lower PEC corrections from the Neave correction result in moderately higher corrected CO_2 contents (Fig. Fig. 6.4d).

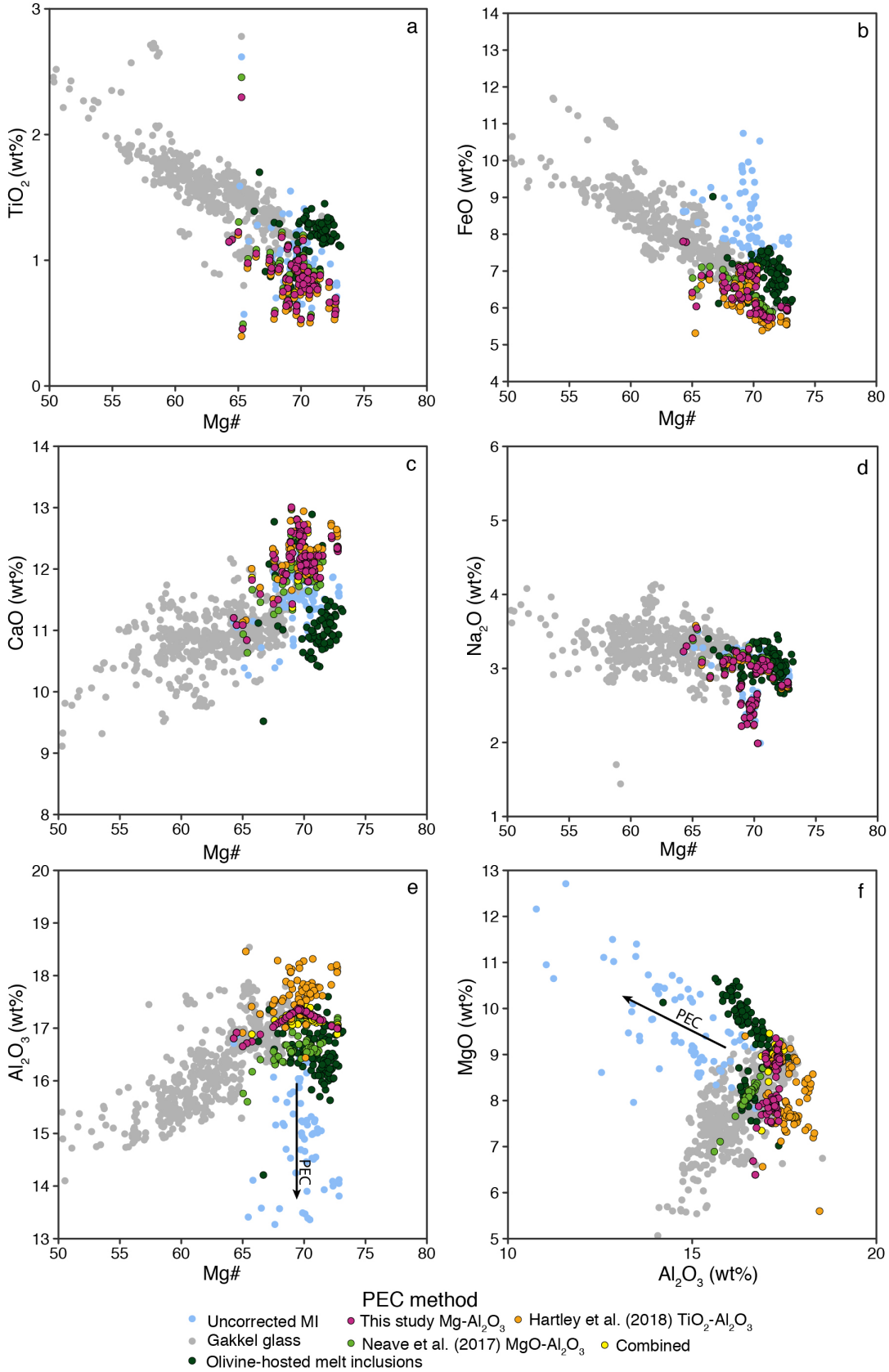

Fig. 6.3: Major element composition of plagioclase-hosted melt inclusions following correction for PEC using different correction schemes. Olivine-hosted melt inclusions (Shaw et al. 2010; Wanless et al. 2014a) Gakkel glass data were downloaded from the PetDB (Lehnert et al. 2000) Database (www.earthchem.org/petdb) on 15 July 2016. Black arrow labelled indicates compositions effected by PEC.

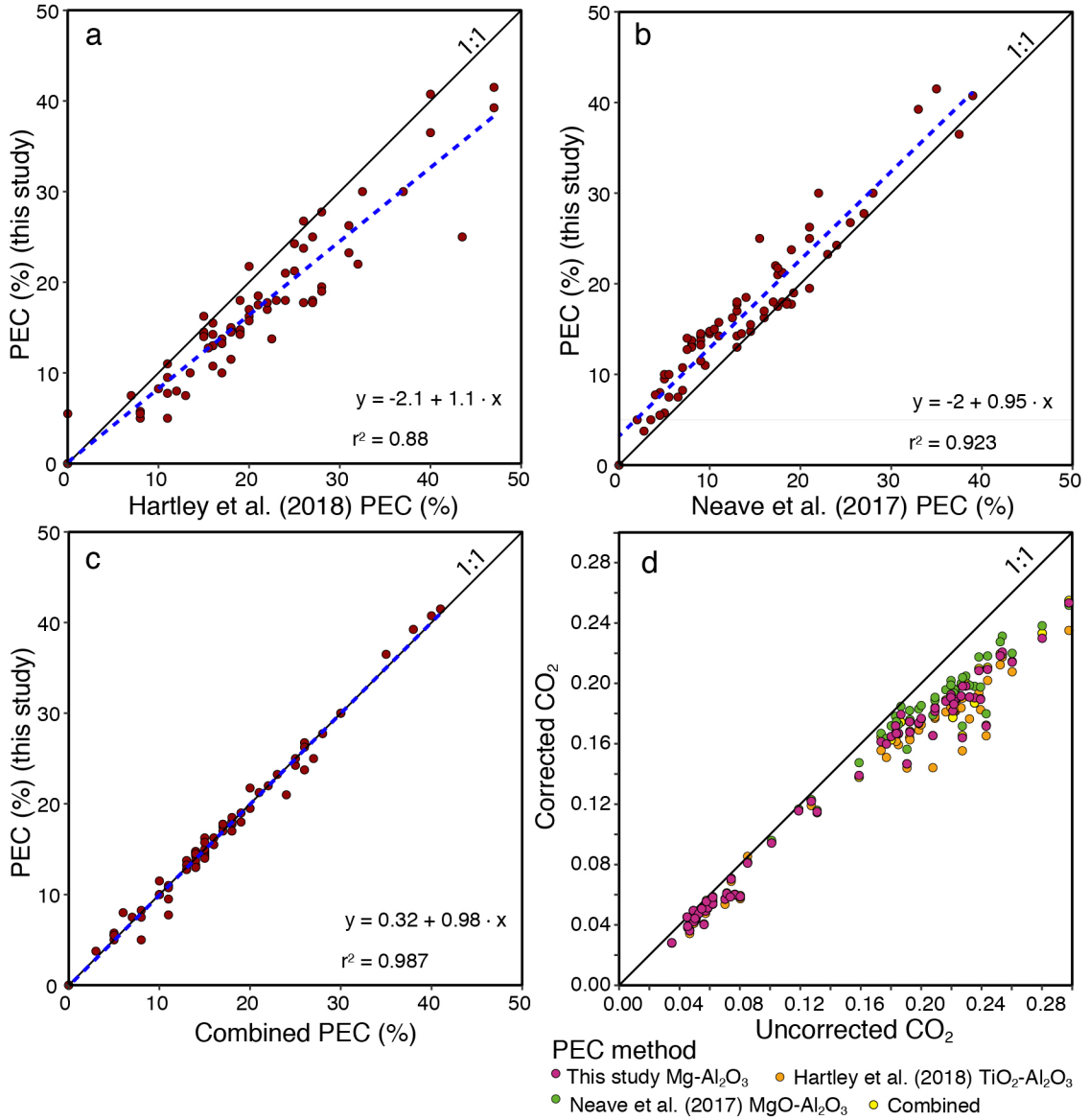

Fig. 6.4: Comparison of the amount of PEC correction (%) required in each correction scheme (**a**-**c**) and the effect this has on melt inclusion CO_2 content (**d**). The Hartley approach has the highest PEC corrections (**a**), whilst the Neave approach has the lowest (**b**). The combined and Bennett schemes show a strong positive correlation (**c**). There is negligible difference between the CO_2 contents calculated using the difference approaches.

The Bennett correction scheme has two benefits over that of Hartley and Neave: (1) Mg# does not change during the correction and therefore the melt inclusion composition only changes vertically in Al_2O_3 space; and (2) the addition of the line drawn through the olivine-hosted melt inclusion data to create the pseudo-liquid line of descent prevents corrections that would result in melt inclusion compositions with unrealistically high Al_2O_3 contents compared to the Gakkel glass and olivine-hosted melt inclusion arrays. Because of this, melt inclusion composition corrected using the approach of Hartley will not be considered further because the correction results in melt inclusion compositions with unrealistically high Al_2O_3 contents.

To test the effect of the choice of pseudo-liquid line of descent used in the Bennett correction, a second pseudo-liquid line of descent passing through the olivine-hosted melt inclusion data was used for a second correction; new PEC corrections range from 0-37.5% (median 11.5%). It can be seen from Figure 6.5d that pressures calculated from this second PEC correction show negligible change from those calculated following the first PEC correction. There is no correlation between the percentage correction and calculated depth of crystallisation (Fig. 6.6). Below the choice of barometer used to calculate the pressures, as well as the effect the choice of PEC correction scheme has on calculated pressures, is discussed in greater depth.

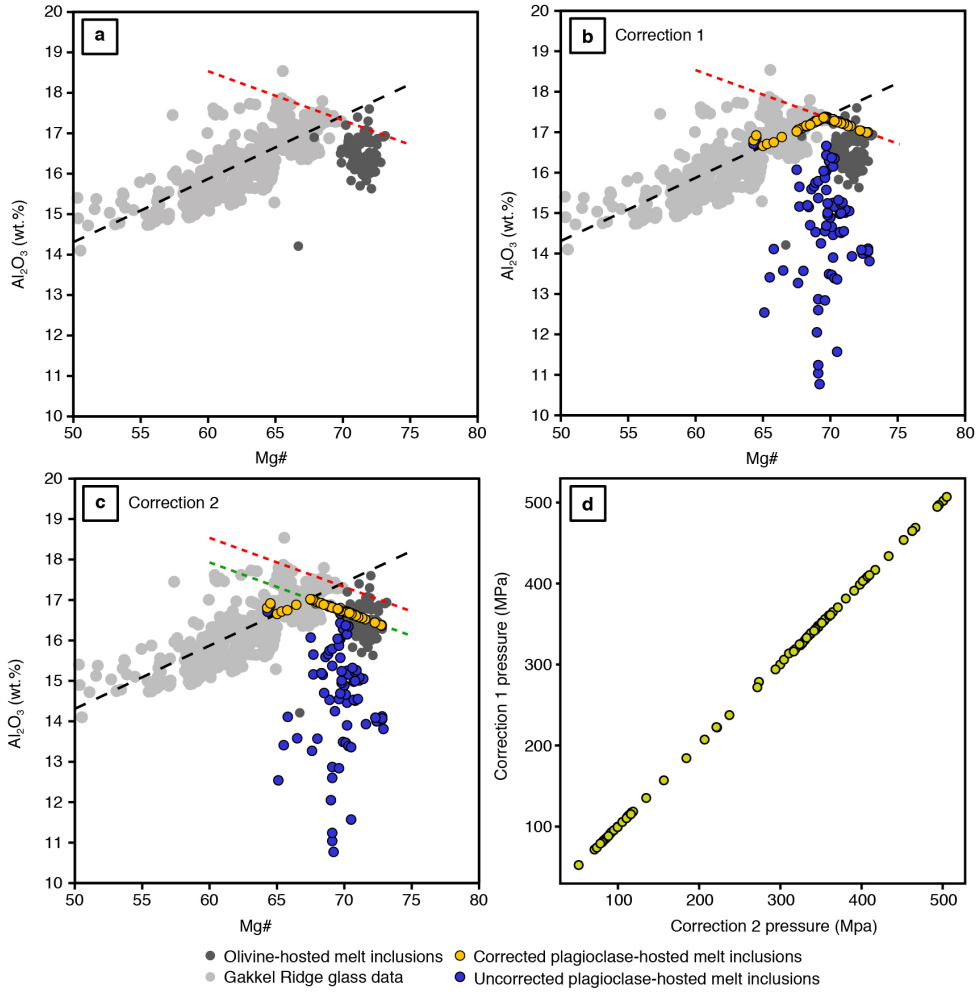

Fig. 6.5: Plagioclase-hosted melt inclusion post-entrapment crystallisation (PEC) correction. Plagioclase-hosted melt inclusion compositions were empirically corrected for PEC. Host plagioclase compositions were added to the melt inclusions iteratively until the melt inclusions met the Al_2O_3 content (at a given Mg#) of the pseudo-liquid line of descent. The pseudo-liquid line of descent comprises two parts. Firstly a regression through Gakkel glass data (Lehnert et al. 2000; Lissenberg et al. 2019) (grey line), and secondly a hand-picked line that runs along the top of olivine-hosted melt inclusions (Shaw et al. 2010; Wanless et al. 2014a) and Gakkel glass data (red line) (**a**). A second PEC correction was undertaken using a different pseudo-liquid line of descent (green line) (**c**) that resulted in lower corrections. A comparison of pressures calculated using MagmaSat (Ghiorso and Gualda 2015) following each of these PEC corrections shows there is negligible difference in pressures calculated from the resulting melt compositions (**d**). Gakkel glass data were downloaded from the PetDB (Lehnert et al. 2000) Database (www.earthchem.org/petdb) on 15 July 2016.

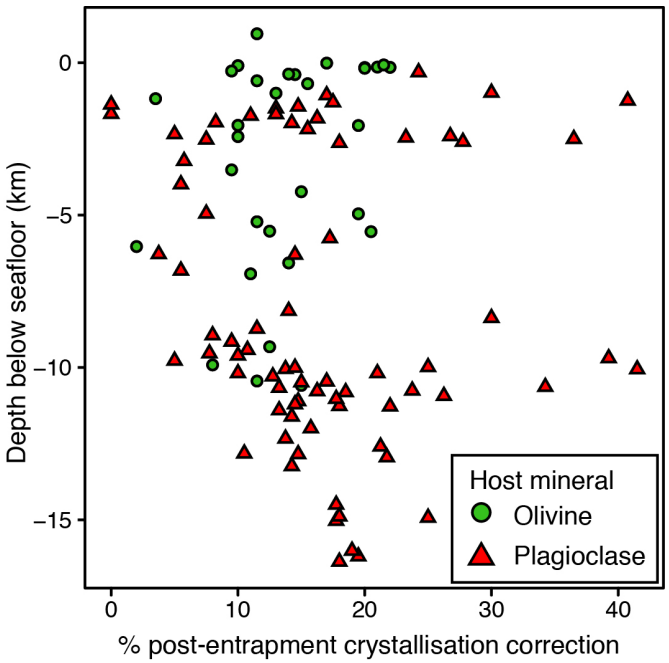

Fig. 6.6: Relationship between post-entrapment crystallisation (PEC) correction and crystallisation depths. Melt inclusion major element and volatile contents have been corrected for the effects of PEC.

6.2.2 Pressure calculation

Following correction for PEC of major and volatile elements, vapour saturation pressures can be calculated. Because volatile solubility in magmas is dependent on melt composition as well as pressure, numerous parameterisations and barometers have been developed that examine their effect on CO_2 solubility (e.g., VolatileCalc (Newman and Lowenstern 2002); Papale et al. 2006; Iocono-Marziano et al. 2012; MagmaSat (Ghiorso and Gualda 2015); Eguchi and Dasgupta 2018; Allison et al. 2019). To determine the most suitable parameterisation to calculate vapour saturation pressures of Gakkel Ridge melt inclusions, experimental compositions have been run in each of the different models to assess how well the parameterisations recover the experimental pressures. Experimental compositions used include MORBs and low-k tholeiites from Dixon et al. (1995) and Shishkina et al. (2012, 2014). In Fig. 6.7 the parameterisations of VolatileCalc (Newman and Lowenstern 2002), MagmaSat (Ghiorso and Gualda 2015), Allison et al. (2019), Eguchi and Dasgupta (2018), Shishkina et al. (2014) and Iocono-Marziano et al. (2012) are assessed. Saturation pressures for the last four parameterisation have been calculated using a python script written by, and available from, Simon Matthews (Johns Hopkins University).

Accounting for error on CO_2 measurements, the parameterisations of MagmaSat and Iacono-Marziano et al. (2012) recover experimental pressures best (Fig. 6.7b and f). Whilst both VolatileCalc and the parameterisation of Shishkina et al. (2014) recover

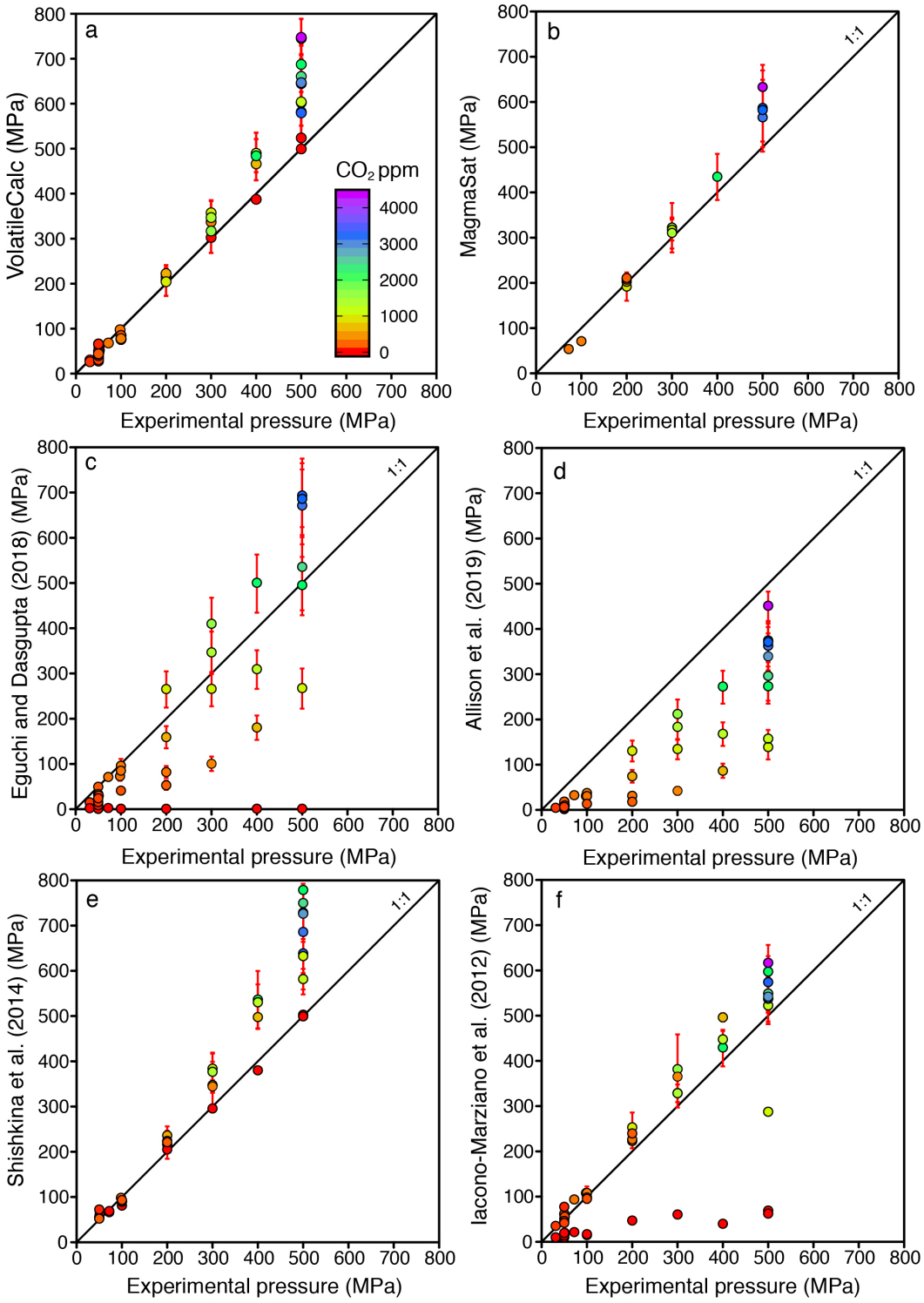

Fig. 6.7: Comparison of experimental pressures to pressures determined using different parameterisation for calculating saturation pressures. Saturation pressures determined using: **a** VolatileCalc (Newman and Lowenstern 2012); **b** MagmaSat (Ghiorso and Gualda 2015); **c** Eguchi and Dasgupta (2018); **d** Allison et al. (2019); **e** Shishkina et al. (2014); **f** Iocono-Marziano et al. (2012). Error bars represent maximum and minimum pressures calculated accounting for error on CO_2 measurements (2σ). VolatileCalc pressures calculated using default 49 wt.% SiO_2.

pressures ≤300 MPa , they both overestimate higher pressures (Fig. 6.7a and e). Furthermore, VolatileCalc, a mixed H_2O-CO_2 solubility model based on the parameterisation of Dixon and Stolper (1995), only allows SiO_2 contents between 40-49 wt.% SiO_2 and thus does not account for compositional variability present at a given

SiO_2. Whilst pressures calculated using the parameterisation of Eguchi and Dasgupta (2018) show a broad positive correlation with experimental pressures (Fig. 6.7c) results are scattered compared to other models. Similarly, whilst there is a broad positive correlation between model and experimental pressures using the parameterisation of Allison et al. (2019), which is calibrated on alkali-rich mafic magmas, fails to recover experimental pressures (Fig. 6.7d), the model pressures are systematically lower than experimental pressures. The alkali contents of compositions used to calibrate this model range from 4-9 wt.%; this contrasts to experimental composition plotted in Fig. 6.7 which have lower median total alkali contents of 2.8 wt%, similar to plagioclase- and olivine-hosted melt inclusions in this study (3.2 and 2.9 wt.% respectively). Therefore, because this parameterisation is not calibrated for the compositions of interest here, it is not considered further. Of the six models examined in Fig 6.7, the parameterisations of MagmaSat (Ghiorso and Gualda 2015) and Iocono-Marziano et al. (2012) are preferred. Saturation pressures determined using these two models are directly compared in Fig. 6.8a; the models are in good agreement with one another.

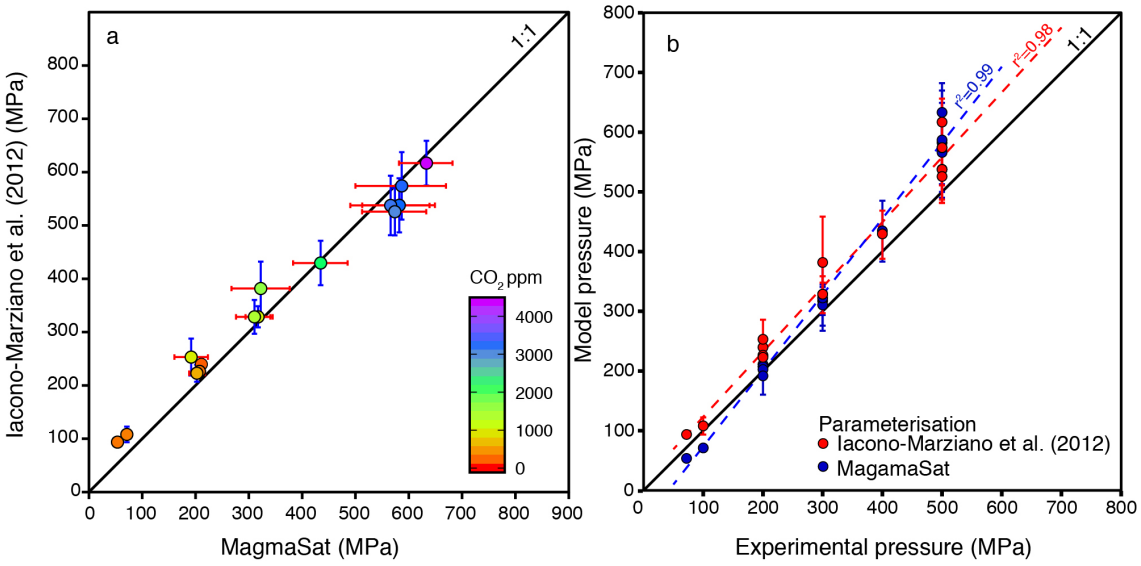

Fig. 6.8: Comparison of pressures calculated using the parameterisations of MagmaSat (Ghiorso and Gualda 2015) and Iocono-Marziano et al. (2012) for experimental compositions (**a**). Both models show strong correlations with experimental pressures (**b**). Error bars represent maximum and minimum pressures calculated accounting for error on CO_2 measurements (2σ).

Melt inclusion saturation pressures have subsequently been calculated using parameterisations of both MagmaSat (Ghiorso and Gualda 2015) and Iocono-Marziano et al. (2012) and are shown in Fig. 6.9. Saturation pressures are higher using the parameterisation of of Iocono-Marziano et al. (2012) than MagmaSat. Importantly, pressures of plagioclase-hosted melt inclusions, calculated using each parameterisation (Bennett, Fig. 6.9a and Neave, Fig 6.9b), are not significantly different using different correction schemes; this shall be discussed further in section 6.3.3.

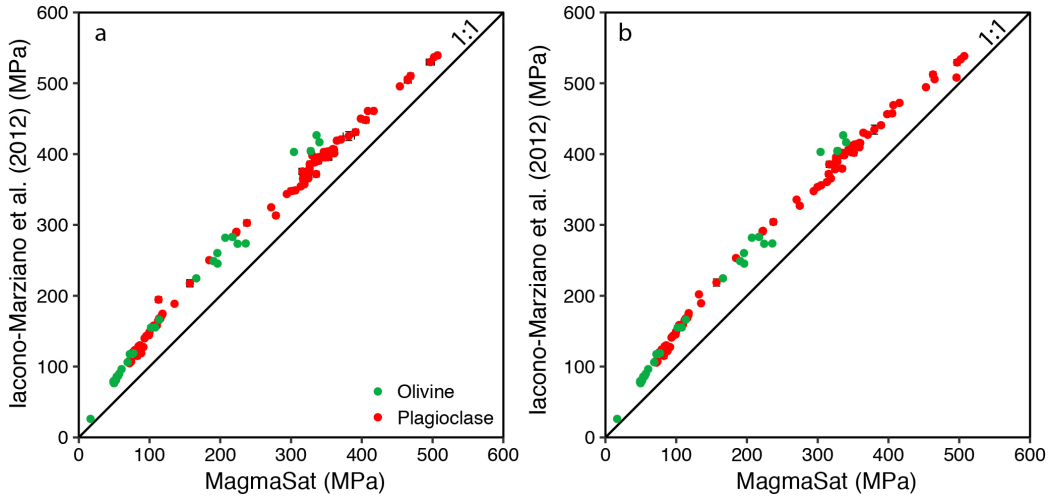

Fig. 6.9: Comparison of plagioclase- (red) and olivine-hosted (red) melt inclusion saturation pressures calculated using the parameterisations of MagmaSat (Ghiorso and Gualda 2015) and Iocono-Marziano et al. (2012). Plagioclase-hosted melt inclusions in **a** and **b** are corrected using the Bennett and Neave correction schemes, respectively, discussed in section 6.2.1.2. Olivine-hosted melt inclusions in both panels are calculated using the correction scheme of Sobolev and Schimizu (1993). Black error bars, when not visible, are smaller than the points and account for error on the CO_2 analysis.

Magmas which become trapped as melt inclusions are assumed to be vapour saturated (see section 6.3.2 for further discussion). Both olivine- and plagioclase-hosted melt inclusions present in Gakkel Ridge crystal cargo can contain bubbles, with 62% of all melt inclusion-bearing individual plagioclase having bubbles. Because studies show that bubbles in both plagioclase- (Drignon et al. 2018) and olivine-hosted melt inclusions (Hartley et al. 2014; Maclennan 2017) can sequester large amounts of CO_2 (Anderson and Brown 1993; Wallace et al. 2015), pressures determined from melt inclusions here are minima. In order to compare like-to-like, melt inclusions with visible bubbles were avoided, however, because polished blocks were used during ion microprobe analysis, the presence or absence of vapour bubbles deeper inside the inclusions could not be determined. Pressures were converted to crystallisation depths accounting for the pressure of the overlying water and crust, assuming a crustal density of 2.9 g/cm^3.

6.3 Results

6.3.1 Textural analysis

The contrasting textural complexity of olivine and plagioclase is illustrated in Figure 6.10. Whilst both phases exhibit a range of crystal habits, plagioclase shows more evidence of resorption (Fig.6.10a compared to d-f,h-l) and more complex zoning, although both phases may also lack zoning (olivine, Fig. 6.10b,c,o; plagioclase, Fig. 6.10h,l). Zoning patterns in plagioclase include, but are not restricted to, reverse zoning (Fig. 6.10e,g,k), concentric zoning punctuated by undulose resorption interfaces (Fig. 6.10f,k) and complex combinations of patchy (Fig. 6.10j) and concentric zoning (Fig. 6.10i). Complex zoning patterns (Fig. 6.10d,e,f,i-j), and large amoeboid melt inclusions interpreted as the

product of resorption (Fig. 6.10h,i), indicate that plagioclase crystals have experienced protracted growth (±resorption) histories within open magmatic systems.

Olivine-hosted melt inclusions are found in host crystals with both skeletal (37%; Fig. 6.10 b,o) and non-skeletal morphologies (63%; Fig. 6.10c,n). In euhedral and subhedral olivine, inclusions are randomly distributed (Fig. 6.10c,n) whilst those in skeletal olivine are found in hour-glass arrangements (Fig. 6.10b) or located close to the host margins (Fig. 6.10o). The inclusions in olivine are not associated with observable zonation, although whilst not mapped, trace elements (i.e., P) may preserve zoning (Welsch et al. 2014). Melt inclusions in plagioclase may be randomly distributed throughout the host crystal (Fig. 6.10h,i,j,l), restricted to cores (Fig. 6.10g,k), or associated with resorption interfaces (Fig. 6.10f); only 4% are directly associated with resorption interfaces.

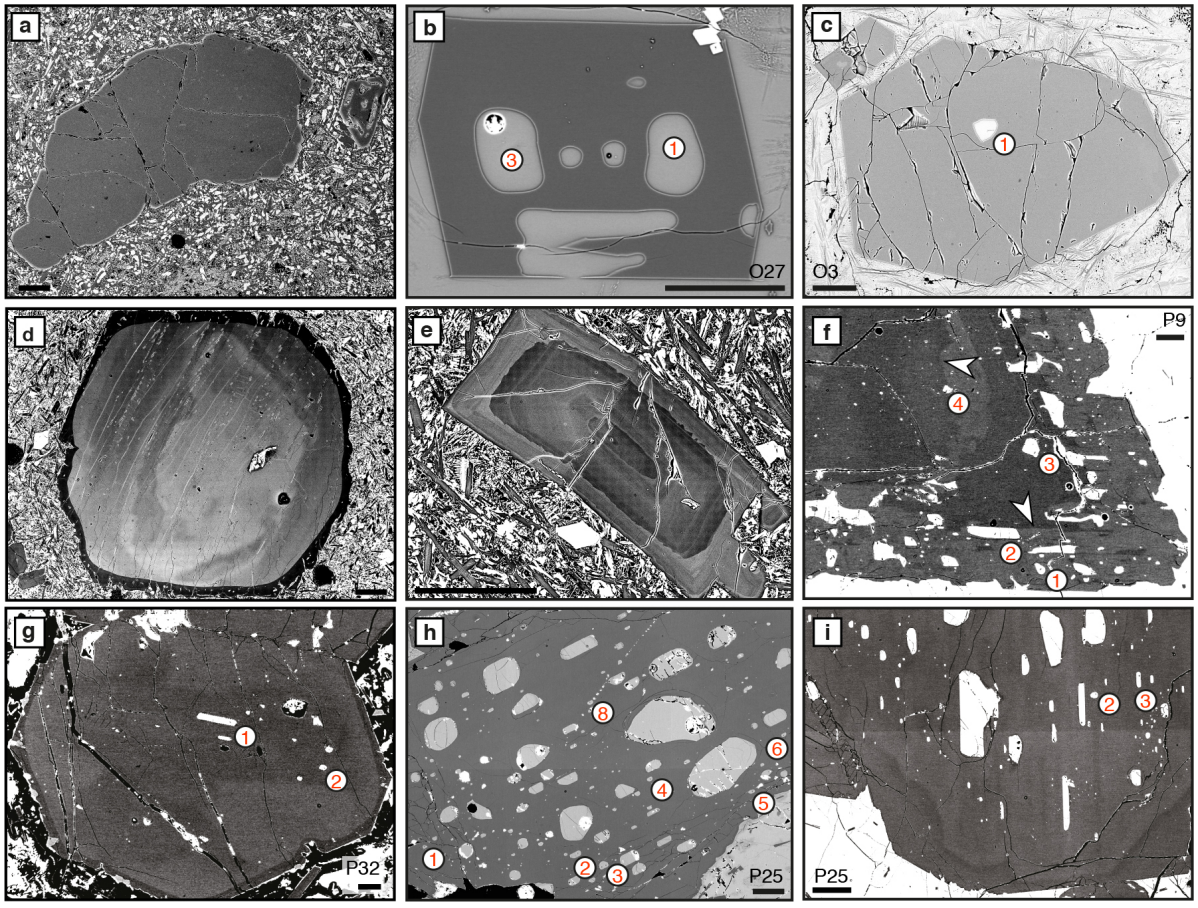

Fig. 6.10: Textural complexity of olivine and plagioclase and melt inclusion distribution and associations. Backscattered electron images of olivine (**a**-**c**) and plagioclase (**d**-**i**). **a** Resorbed olivine with weak normal zoning. **b** Skeletal olivine with hourglass melt inclusion arrangement and no visible zoning. **c** Euhedral olivine with no visible zoning. **d** Complexly zoned plagioclase (e.g., reverse, normal and patchy) with both internal and external resorption. **e** Complexly zoned plagioclase (e.g., oscillatory and reverse) with multiple internal resorption interfaces. **f** Complexly zoned plagioclase (e.g., reverse and normal zoning) with internal resorption interfaces associated with melt inclusions. **g** Reverse zoned plagioclase in which melt inclusions are restricted to the core. **h** Unzoned plagioclase with large amoeboid melt inclusion. **i** Complexly zoned plagioclase (e.g., patchy, normal and reverse) with internal resorption; melt inclusion are restricted to the core. Scale bars are 100 μm (**b**,**c**,**f**,**g**) and 250 μm (**a**,**d**,**e**,**h**,**i**). Small numbers show the locations of analysed melt inclusions; numbers correspond to highlighted analyses in Electronic Appendix 5.

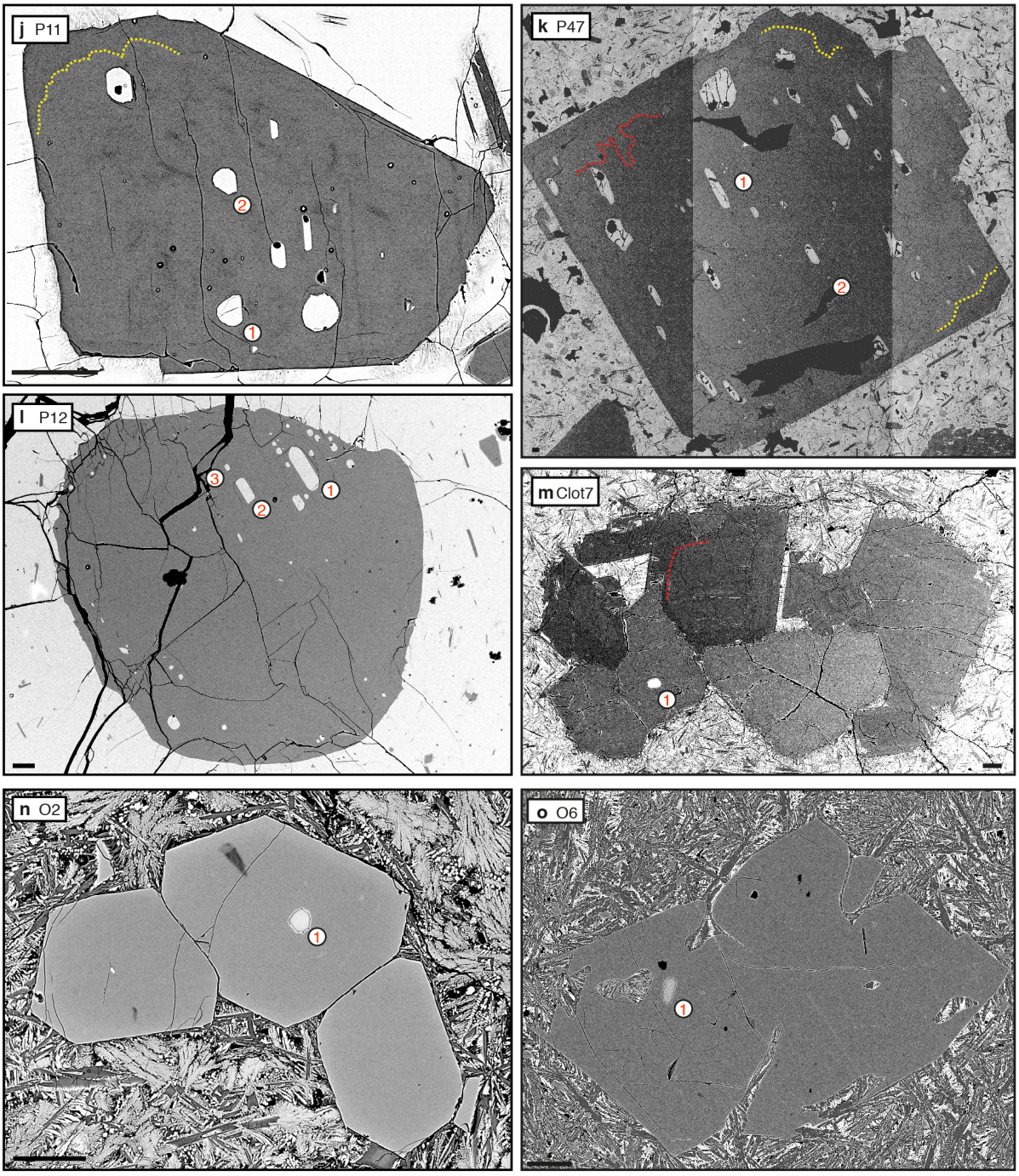

Fig. 6.10 continued. Backscattered electron images of plagioclase (**j-l**) and olivine (**m-o**). **j** Plagioclase with patchy zoning and internal resorption. **k** Plagioclase with normal and reverse zoning and two (red and yellow dashed lines) internal resorption events. **l** Unzoned plagioclase with external resorption. **m** Poly-mineralic glomerocryst containing olivine and plagioclase. Plagioclase shows oscillatory zoning and internal resorption events; olivine is reverse zoned. **n** Mono-mineralic glomerocryst of olivine which shows weak normal zoning. **o** Skeletal olivine with no evidence of zoning. Scale bars are all 100 μm. Dashed red and yellow lines in **j, k** and **m** show the locations of resorption.

6.3.2 Melt inclusion volatile content and crystallisation pressures

The Gakkel Ridge volatile data are presented in Figure 6.11, along with other olivine-hosted melt inclusion data for which saturation pressures have been calculated. Melt inclusion volatile contents can be found in Electron Appendix 5. H_2O concentrations of

both olivine- and plagioclase-hosted melt inclusions are similar and range from 0.12-0.56 wt.% H_2O. However, plagioclase-hosted melt inclusions record a larger range of CO_2 (282-2857 ppm) than olivine-hosted melt inclusions (94-1984 ppm). Furthermore, plagioclase-hosted melt inclusions have significantly higher median CO_2 contents (1668 ppm) compared to olivine-hosted melt inclusions (603 ppm). Hence, the CO_2 record of Gakkel plagioclase-hosted melt inclusions is unlike that of olivine from either the Gakkel Ridge or from mid-ocean ridges elsewhere, being offset to higher values (Fig. 6.11). There is no correlation between melt inclusion size or location and CO_2 content (Fig. 6.12 and 6.13b respectively). The positive correlation between Mg# and CO_2 of Gakkel Ridge melt inclusions from the locations where the highest CO_2 contents were measured (Fig. 6.13) indicates that Gakkel Ridge melt inclusions preserve evidence for the occurrence of simultaneous degassing and crystallisation, suggesting that melts were saturated at the time of entrapment.

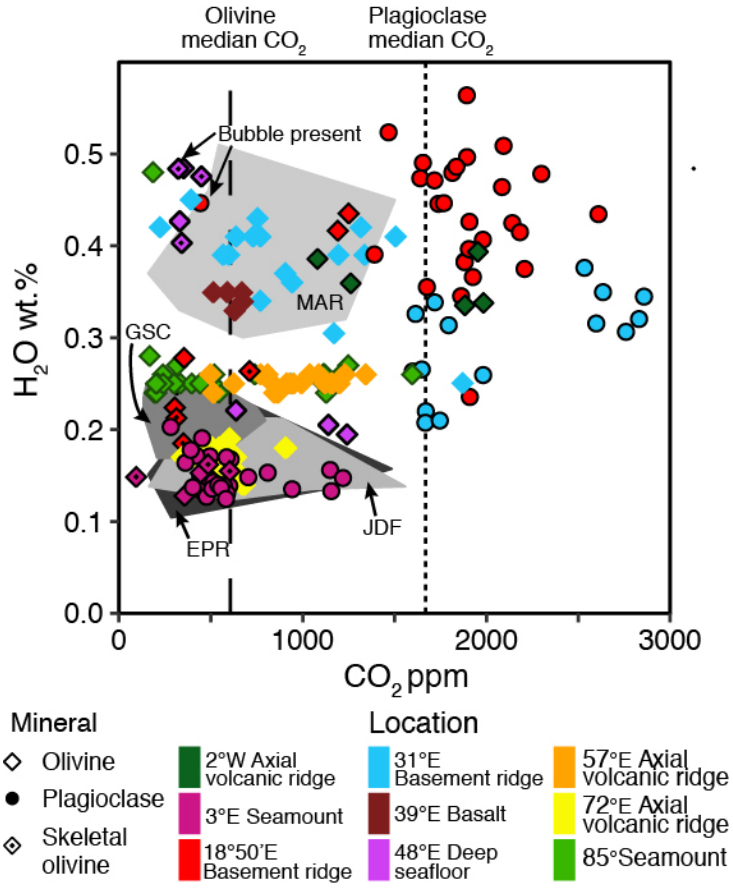

Fig. 6.11: Volatile contents of Gakkel Ridge olivine- and plagioclase-hosted melt inclusions. CO_2 versus H_2O for Gakkel Ridge plagioclase- (circles) and olivine- (diamonds) hosted melt inclusions. Black outlines points are from this study; those from 85°E Seamounts are from Shaw et al. (2010), points with no outlines are from Wanless et al. (2014a). Grey fields include the following data: Lucky Strike volcano on the Mid-Atlantic Ridge (MAR) (Wanless et al. 2014b); Galapagos Spreading Centre (GSC) (Colman et al. 2015); Juan de Fuca Ridge (JDF) and East pacific Rise (EPR) (Wanless and Shaw 2012). Comparative datasets have all used volatiles to investigate crystallisation pressures and are from on-axis locations.

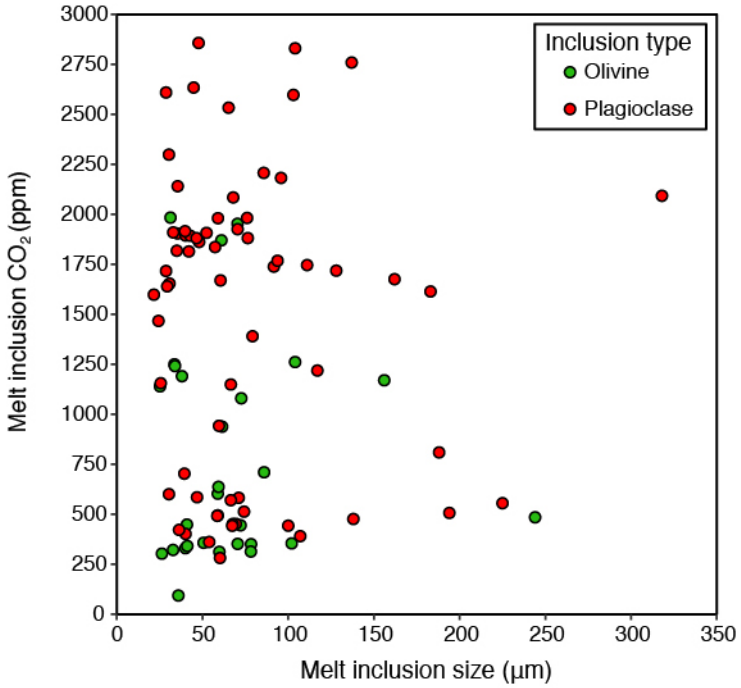

Fig. 6.12: Relationship between melt inclusion size and CO_2 content. Both plagioclase- and olivine-hosted melt inclusions show no relationship between melt inclusion size and CO_2 content.

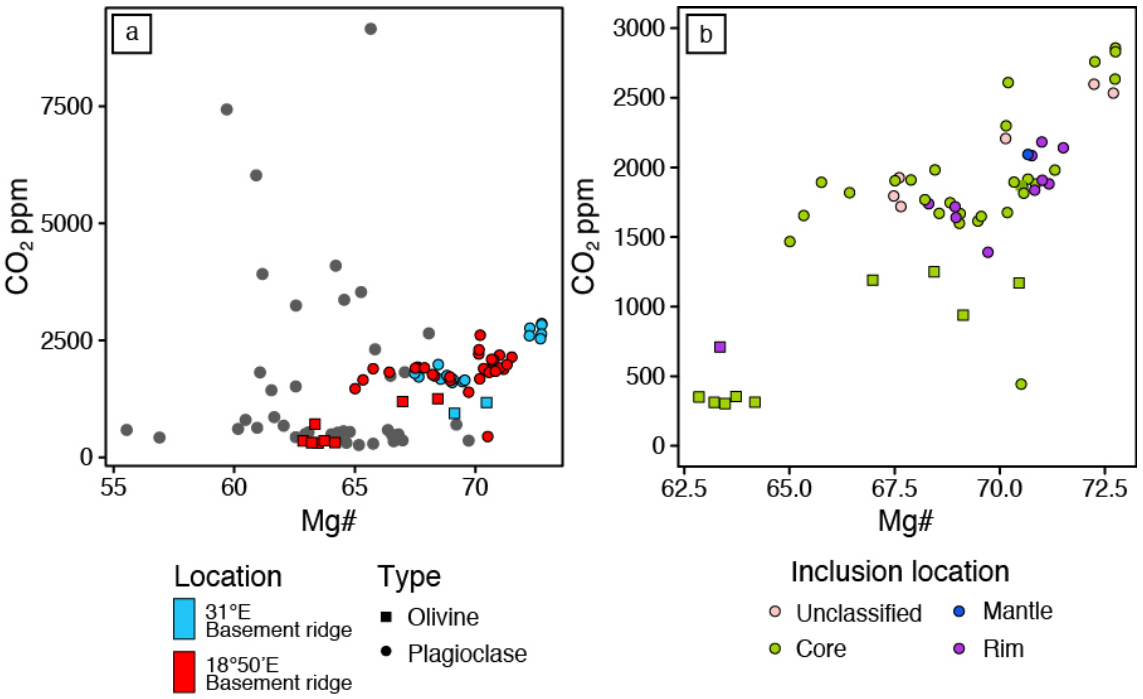

Fig. 6.13: Relationship between melt inclusion Mg# and CO_2 content. a Plagioclase- and olivine-hosted melt inclusions from the two locations where the highest CO2 content are found show a positive correlation between Mg# and CO_2 contents indicating the occurrence of concomitant crystallisation and degassing; plagioclase-hosted melt inclusion data from Helo et al. (2011), plotted for comparison, show no such correlation. There is no systematic relationship between melt inclusion location and CO_2 content (b). Note: Inclusion locations are unclassified if melt inclusions come from either a broken host crystal where the entire crystal is not observed, or from a host crystal where no back-scattered electron image exists to allow the locations to be assigned based on compositional zoning.

6.3.3 Crystallisation pressures

The volatile contents of Gakkel Ridge melt inclusions correspond to entrapment pressures of ≤ 506 MPa (equivalent to 16.4 km below the seafloor) andz ≤ 340 MPa (10.6 km) for plagioclase- and olivine- hosted melt inclusions respectively (Fig. 6.14a). In olivine, entrapment pressures correlate with host crystal morphology (Fig. 6.14b), such that inclusions hosted within skeletal crystals (Fig. 6.10b) have lower CO_2 contents (<710 ppm; Fig. 6.11), and correspondingly lower pressures (<~113 MPa , or <2.4 km below the seafloor) than non-skeletal olivines, which preserve a range in entrapment pressures of 49-340 MPa (0.2-10.6 km below the seafloor).

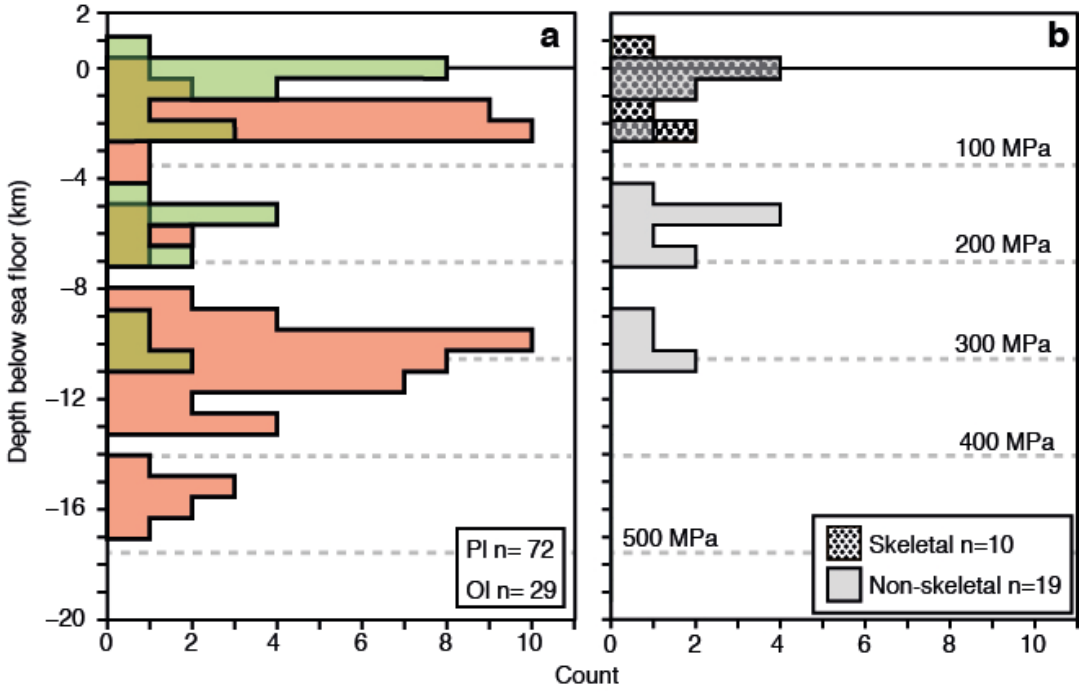

Fig. 6.14: Crystallisation depth and pressures recorded in both plagioclase- and olivine-hosted melt inclusions. **a** Depth histogram showing the difference in the distributions of crystallisation depths recorded in olivine- (green) and plagioclase-hosted (red) melt inclusions. **b** Depth histogram comparing skeletal (spotted) and non-skeletal (grey) olivine. The one bubble-bearing melt inclusion analysed plots at 0 km. Pressures correspond to the pressures below the seafloor. Here melt inclusion pressures, converted to depths, were calculated using MagmaSat.

From Fig. 6.15 it can be seen that plagioclase- and olivine-hosted melt inclusion crystallisation pressures are higher when calculated using the parameterisation of Iacono-Marziano et al. (2012) compared to MagmaSat. However, an important result is that the difference in entrapment pressures between olivine- and plagioclase-hosted melt inclusions, recognised in Fig. 6.14a, persists regardless of which parameterisation is used to calculate entrapment pressures (Fig. 6.15a compared to b and c compared to d). Further to this, the method of plagioclase-hosted melt inclusion PEC correction used makes negligible difference to the plagioclase-hosted melt inclusion pressure record or the difference between olivine and plagioclase. For the following discussion, and use

elsewhere in this thesis, compositions corrected using the Bennett correction scheme developed here, and pressures calculated using MagmaSat are used.

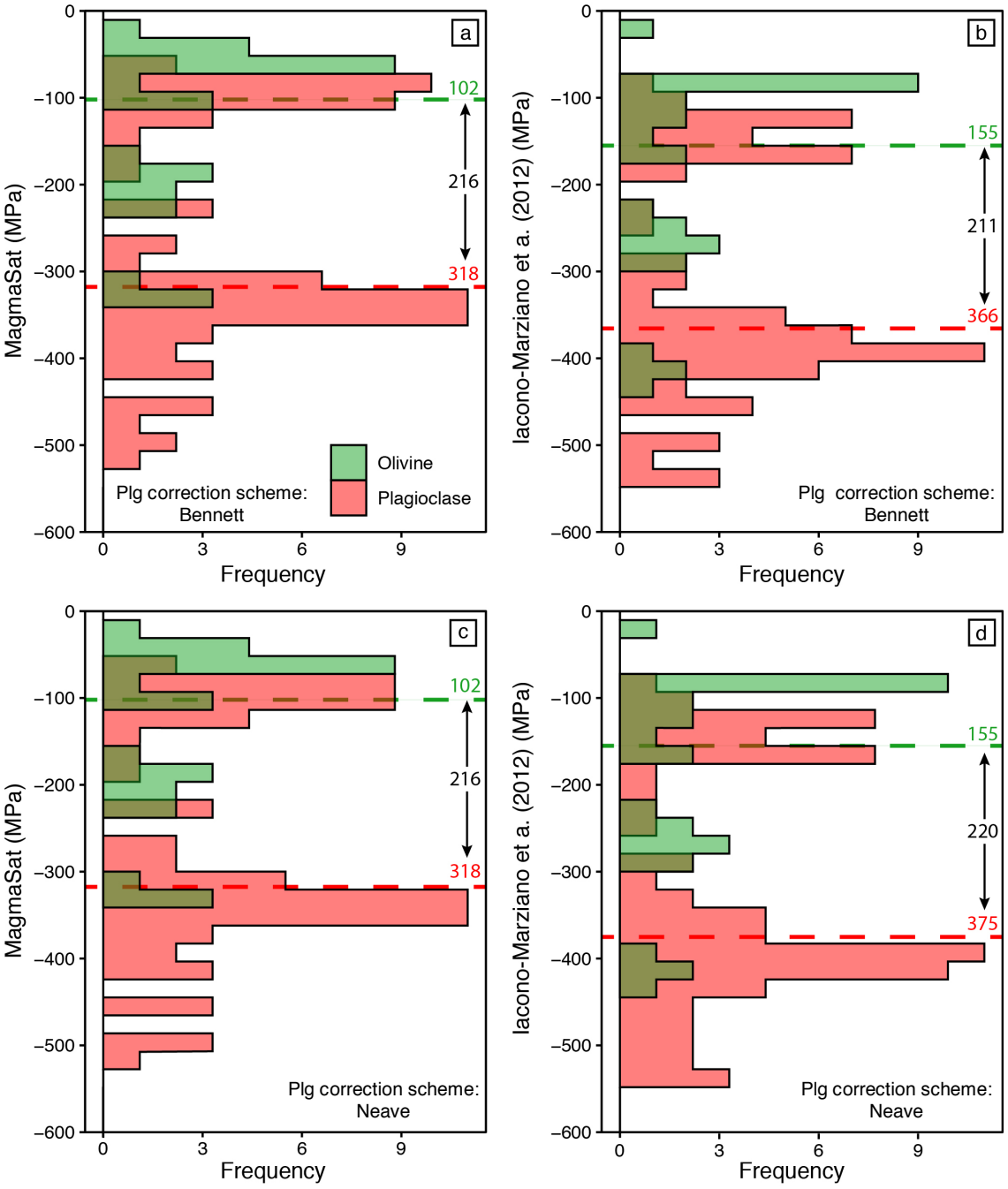

Fig. 6.15: Comparison of melt inclusion saturation pressures calculated using parameterisations of MagmaSat (Ghiorso and Gualda 2015) (**a**,**c**) and Iocono-Marziano et al. (2012) (**b**,**d**). Olivine-hosted melt inclusions data in all panels is calculated using the approach of Sobolev and Shimizu (1993). Plagioclase-hosted melt inclusions in panels **a** and **b** have been corrected using the scheme developed here of Bennett, those in **c** and **d** have been corrected using the scheme of Neave. Red and green text in each of the panels shows the median pressures of plagioclase- and olivine-hosted melt inclusions respectively. Text in black is the difference between the two records. Median plagioclase-hosted melt inclusion pressures are higher following calculation with the Iacono-Marziano et al. (2012) parameterisation (**b** and **d**). Median pressures are similar using both PEC correction schemes. Importantly, regardless of pressure calculation or correction method, the different between the two records is consistent; plagioclase crystallisation pressures are higher than olivine. Note: pressures are not corrected for pressure below the seafloor. Plg, plagioclase.

6.3.4 Olivine- vs. plagioclase-hosted melt inclusion record

For a direct comparison of the crystallisation depths recorded by olivine- and plagioclase-hosted melt inclusions, data can be examined from three locations along the Gakkel Ridge where both olivine- and plagioclase-hosted melt inclusions have been analysed (31°E Basement Ridge, 18°50' E Basement Ridge and 3°E Seamounts; Fig. 6.16a-c). The data show a systematic offset in pressures, such that mean pressures are 215, 247 and 51 MPa higher in plagioclase-hosted melt inclusions than those recorded by olivine-hosted melt inclusions at the same location. This translates into mean depths of crystallisation that are 7, 9 and 2 km higher in plagioclase-hosted melt inclusions compared to olivine-hosted melt inclusions, with only limited overlap between the two records. Critically, the difference between the melt inclusion pressures in the two phases is present in the dataset as a whole (Fig. 6.14a), in particular locations (Fig. 6.16a-c), and within individual samples (Fig. 6.16d and Fig. 6.17); from this it can be concluded that the volatile contents are not reflecting specific ascent and quenching conditions. Instead they are suggested to reflect a fundamental difference in the pressure record of olivine- and plagioclase-hosted melt inclusions, with olivine being biased towards low pressures.

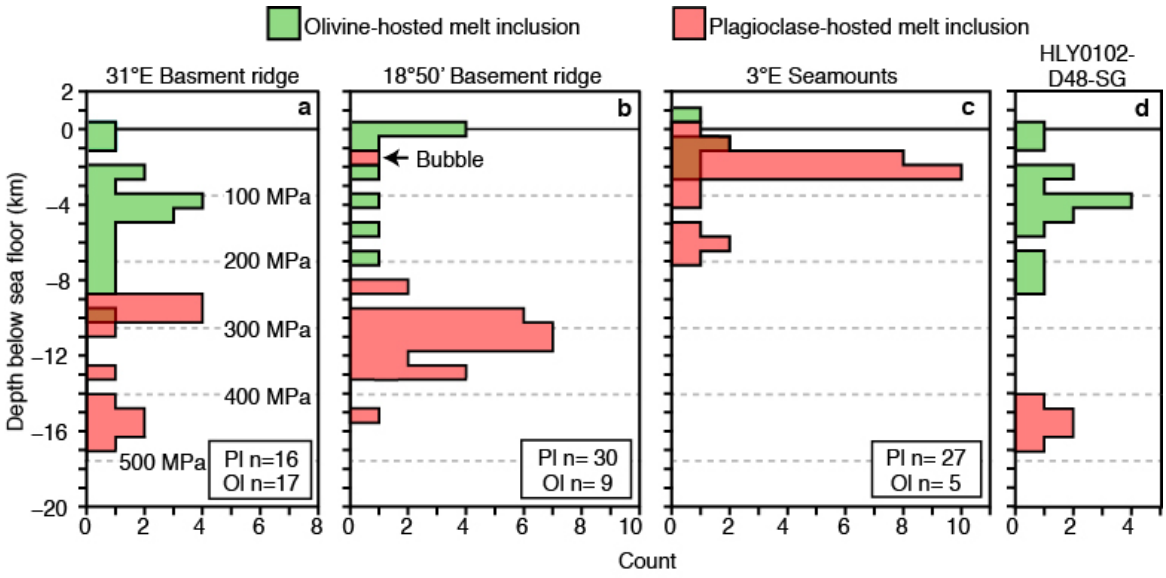

Fig. 6.16: Comparison of crystallisation depths recorded in melt inclusions. Histograms showing the distribution of crystallisation depths recorded in olivine- and plagioclase-hosted melt inclusions at three locations along the Gakkel Ridge (31°E Basement Ridge, **a**; 18°50'E Basement Ridge, **b**; and 3°E Seamounts, **c**). **d** Comparison of pressures recorded by olivine- and plagioclase-hosted melt inclusions in a single sample (HLY0102-D48-SG) from 31°E Basement Ridge; olivine data here are from Wanless et al. (2014a). Pressures correspond to the pressure below the seafloor.

6.4 Origin of the plagioclase-olivine crystallisation depth dichotomy

There are three potential explanations for the observed difference between olivine- and plagioclase-hosted melt inclusion pressure records. First, the entrapment pressures may

be geologically significant and record crystallisation conditions within the magmatic system. Alternatively, the olivine data may be compromised by either decrepitation (Lowenstern 1995; Maclennan 2017) or volatile loss into bubbles (Anderson and Brown 1993; Wallace et al. 2015). In the following section these explanations will be explored.

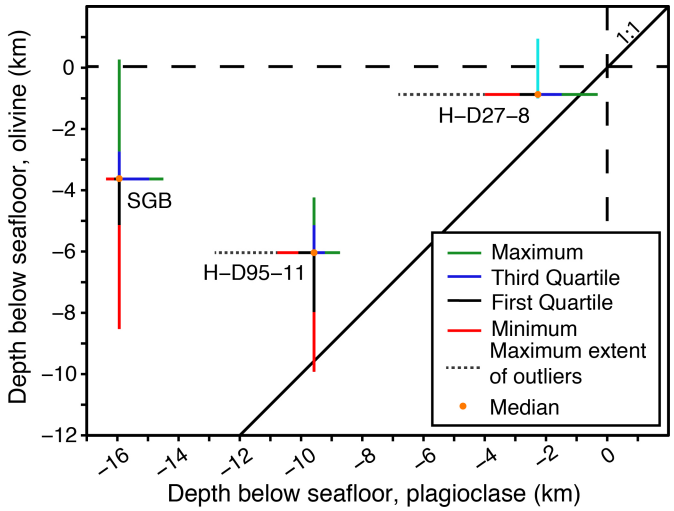

Fig. 6.17: Crystallisation depths recorded by melt inclusions from individual samples. Within each sample, plagioclase records greater crystallisation depths than olivine. The three individual samples are from the 31°E Basement Ridge (HLY0102-D95-11 and HLY0102-D48-SGB), and 3°E Seamounts (HLY0102-D27-8). Dashed line = seafloor.

First, we examine the possibility of secondary volatile loss. If olivine and plagioclase are, respectively, tight and leaky vessels, one might expect olivine-hosted inclusions to record higher CO_2 contents, and in turn greater entrapment pressures, than plagioclase. However, Figures 6.11 and 6.16 demonstrate the opposite. Loss of CO_2 by decrepitation, or breaking of inclusions, is the more common explanation, and has been used to explain why 95% of olivine-hosted melt inclusions from a range of low-H_2O basaltic settings record similar, low entrapment pressures (≤200 MPa) (Maclennan 2017). Whilst this might explain the shallow pressures recorded by olivine-hosted melt inclusions, no physical evidence of decrepitation is observed (e.g., melt filled fractures (Roedder 1965) and melt inclusion halos around larger melt inclusions (Portnyagin et al. 2005)). Finally, CO_2 may be sequestered into bubbles (Anderson and Brown 1993; Wallace et al. 2015) formed as result of post-entrapment crystallisation (Roedder 1984) or thermal contraction of the melt inclusion (Lowenstern 1995). Multiple studies have shown that significant amounts of CO_2 can be sequestered into bubbles in both plagioclase- (Drignon et al. 2018) and olivine-hosted melt inclusions (Hartley et al. 2014; Maclennan 2017). Therefore, pressure estimates determined from the CO_2 content of bubble-bearing melt inclusion are minimas. This is demonstrated well in Figure 6.16b, which shows that the only analysed bubble-bearing plagioclase-hosted melt inclusion yields significantly lower pressures (88 MPa) than the remainder of inclusions in that host

plagioclase (339-391 MPa). Similarly, the only analysed bubble-bearing olivine-hosted melt inclusion records slightly lower pressure (~52 MPa) than an inclusion in the same host with no visible bubble (~57 MPa; Fig. 6.16b). These observations, along with the absence of observed bubbles in most measured melt inclusions, suggests that bubble formation does not control the melt inclusion pressure record. Therefore, that the lack of physical evidence of either decrepitation or bubbles, in combination with the preservation of high crystallisation pressures in plagioclase-hosted melt inclusions despite the assumed "leaky" nature of plagioclase, is inconsistent with a secondary cause for the difference in pressure between olivine- and plagioclase-hosted melt inclusions.

Observations of the host crystals suggest that the data are recording geologic processes. Firstly, complex zoning patterns and abundant evidence of resorption in plagioclase attests to protracted growth histories within an open magmatic system. Whilst similar textures in the olivine hosts may have been erased by fast major element diffusion (Chakraborty 1997), the observation remains that there is a correlation between textural complexity and crystallisation pressures. In fact 58% of olivine crystals hosting melt inclusions with <1000 ppm CO_2 have skeletal morphologies and record shallower mean crystallisation pressures (63 MPa) compared to host crystals with non-skeletal morphologies (178 MPa). This suggests that skeletal olivines formed in the shallow portion of the plumbing system, consistent with their inferred origin via rapid, late-stage growth. Interestingly, the olivine crystal with the highest melt inclusion crystallisation pressure (340 MPa; 10.6 km) forms part of a poly-mineralic glomerocryst that also contains complexly zoned plagioclase crystals (Fig. 6.18).

The volatile data can be reconciled in a model where olivine and plagioclase experience different crystallisation histories, with plagioclase capturing multi-stage processes in a deep-seated crystal mush, and olivine forming predominantly during late stage crystallisation in shallower portions of the plumbing system. Whilst phase relationships show that olivine is the first phase to crystallise from MORBs, and therefore should record crystallisation at elevated pressures, the high density of olivine (3.2 gcm^{-3}) compared to that of plagioclase (~2.7 gcm^{-3}) and basaltic melt (~2.6 gcm^{-3}) may prevent its eruption from deeper within the plumbing system. This would account for the sparsity of olivine-hosted melt inclusions that record pressures as high as those recorded by plagioclase-hosted melt inclusions. The poly-mineralic glomerocryst of high-pressure olivine intergrown with complexly zoned, resorbed plagioclase (Fig. 6.18) provides a direct snapshot of this olivine-plagioclase mush. Moreover, plagioclase crystallisation at depths as shallow as olivine is absent in the melt inclusion dataset at two of the three locations (Fig. 6.16a,b). Here, this is suggested to reflect an absence of analysable melt

inclusions in plagioclase that crystallised shallowly. Indeed, whilst skeletal plagioclase in samples from both locations may represent shallow level crystallisation analogous to that recorded by skeletal olivine, these crystals do not contain analysable melt inclusions, as inclusions are either absent, too small or microcrystalline. Thus, textural observations of olivine and plagioclase host crystals suggest that the disparity between recorded crystallisation pressures is primary.

6.5 Conclusions

The data presented here provide important insights into the physical nature of magmatic systems at mid-ocean ridges and reveal, contrary to current constraints, that magmatic roots are vertically extensive, at least at ultraslow-spreading ridges. More specifically, the Gakkel Ridge magmatic system extends from the seafloor to at least 16.4 km. Moreover, the depth distribution revealed by plagioclase-hosted inclusions (Fig. 6.16) places most crystallisation in the lithospheric mantle. Finally, it has been demonstrated that plagioclase-hosted melt inclusions preserve reliable vapour saturation pressures, and that plagioclase provides a comprehensive record of the deeper levels of crystallisation in magmatic systems. In contrast, olivine captures predominantly shallower levels. Hence, combined studies of olivine- and plagioclase-hosted melt inclusions will enable significantly improved reconstructions of the true extent of magma plumbing systems.

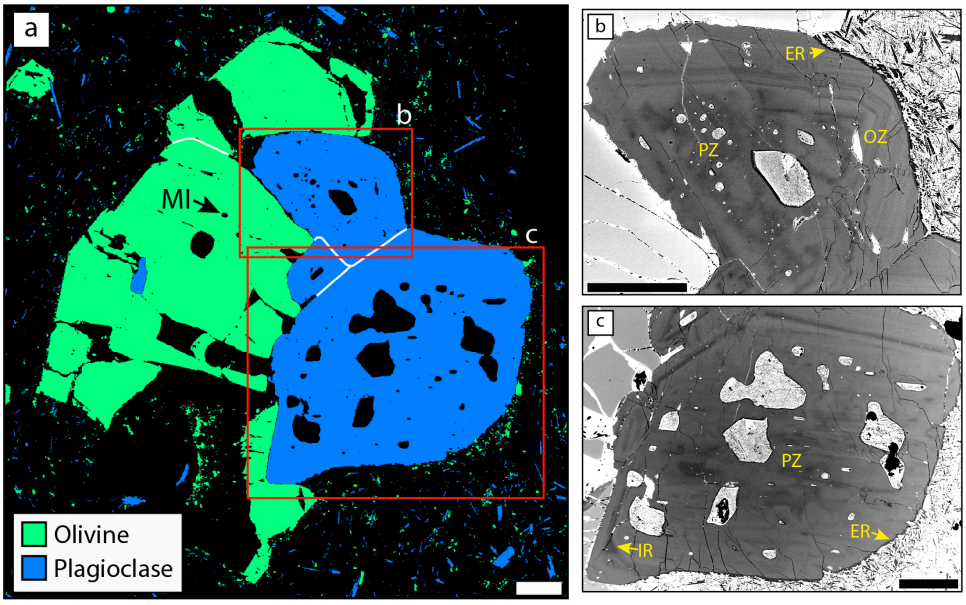

Fig. 6.18: Textural relationship of high-pressure olivine-hosted melt inclusion**. a** Phase map showing the association of the high-pressure olivine-hosted melt inclusion with plagioclase. White lines delineate grain boundaries. Plagioclase exhibits complex zoning including oscillatory (OZ) and patchy zoning (PZ) (**b, c**). Both internal and external resorption (IR and ER respectively) are present in the plagioclase (**b, c**). Large amoeboid melt inclusions (**c**) also suggest the occurrence of resorption. Scale bars are 500 μm.

Chapter 7

Regional along-axis variations in the nature of the Gakkel Ridge magma plumbing system

Chapter 7

7.1 Introduction

Variations in the nature of sub-volcanic magma plumbing systems—in terms of their size, extent, crystal content, connectivity and how frequently they are replenished—all act to control volcanic outputs. Early on, using geophysical constraints, it was suggested that magma plumbing systems at slow-spreading ridges are likely to be dominated by crystal mush and to erupt more crystalline magmas compared to fast-spreading ridges where high melt supply can sustain a melt-filled axial magma chamber (Sinton and Detrick 1992); however, it has since been shown that the axial melt lens is generally filled with crystal mush, with only short (km-scale) sections containing high melt proportions (Carbotte et al. 2013; Marjanovic et al. 2014; Xu et al. 2014). Nonetheless, higher crystal content basalts tend to be erupted at slower spreading rates (Stewart et al. 2003). Axial melt lenses at fast-spreading ridges are steady-state systems that can extend several kilometres along axis (e.g., Detrick et al. 1987; Carbotte et al. 2013); in contrast, the few melt lenses identified at slow-spreading ridges are short-lived, transient features (e.g., Sinha et al. 1998) which will likely cool within several thousands of years if not replenished (Macgregor et al. 1998). Despite the different melt supply at these ridges, geophysical data indicate that mush zones, characterised by low seismic velocities (i.e., low velocity zones or LVZs), are present in plumbing systems across the full spectrum of spreading rates from slow to fast (e.g., Sinton and Detrick 1992; Singh et al. 1998; Sinha et al. 1998; Dunn et al. 2005). Despite the common interpretation of LVZs as mush zones, it has been argued that the spatial resolution of geophysical imaging is not sufficient to distinguish whether melt is distributed within a mush zone or concentrated in sills within solid host rock (e.g., Maclennan 2019). Instead, using Iceland as a template, Maclennan (2019) argued that plumbing systems are characterised by stacked melt-dominated sills that are encased by envelopes of transient, spatially restricted mush zones.

Both geophysical and geochemical data have shown that the depth of axial melt lenses correlates with spreading rate and melt supply; axial melts lenses are shallower at fast-spreading ridges where melt supply is high compared to slow-spreading ridges where melt supply is reduced (Purdy et al. 1992; Carbotte et al. 1998; Rubin and Sinton 2007; Wanless and Behn 2017). This increase in magma chamber depth with decreasing spreading rate results from more efficient conductive cooling at slow-spreading rates as a result of reduced melt supply (Bown and White 1994; Coakley and Cochran 1998). In support of deepening magmatic systems with spreading rate, major element systematics

of basalts and melt inclusion volatile saturation pressures show that crystallisation pressures increase and become more variable with decreasing spreading rate (Wanless and Behn 2017).

Whilst we know a substantial amount about the magma plumbing systems at both fast- and slow-spreading ridges, we know comparatively little about the nature of magma plumbing systems beneath ultraslow-spreading ridges, despite the fact that these ridges make up ~36% of the global ridge system (Solomon 1989; Michael et al. 2003). This in part reflects the absence of detailed seismic studies—due to their locations under permanent pack ice cover or deep seas—that would provide constraints on the physical nature of the plumbing system. Prior to this study, the only constraints on the Gakkel Ridge plumbing system have come from olivine-hosted melt inclusion studies (Shaw et al. 2010; Wanless et al. 2014a); however, in Chapter 6 it was argued that pressures derived from olivine-hosted melt inclusions alone are unlikely to represent the full record of crystallisation within the plumbing system. In addition, despite the existence of an extensive basalt geochemistry dataset, much of the research done on the Gakkel Ridge has focussed on the recovery of abyssal peridotites (e.g., Mühe et al. 1993; Mühe et al. 1997; Goldstein et al. 2008; Liu et al. 2008; D'Errico et al. 2016). Information recorded by basalt crystal cargo has been neglected, and few constraints have been placed on the plumbing system of the Gakkel Ridge as a result.

In this chapter, an integrated dataset of glass and mineral geochemistry, melt inclusion crystallisation pressures and mineral textures at both the ridge- and segment-scale is examined with the aim of: (i) reconstructing the Gakkel magma plumbing system; (ii) determining how the magma plumbing system changes along the Gakkel Ridge axis, and how this relates to regional changes in melt supply and lithospheric thickness; and (iii) establishing global correlations between spreading rate and the nature of the magma plumbing systems.

7.2 Data and approach

Along axis variations in magma plumbing system characteristics (e.g., melt vs crystal content and vertical extent) have been constrained using a range of parameters including:

- Glass temperatures and Mg#
- Basalt crystal content
- Mineral chemistry and textures
- Plagioclase- and olivine-melt equilibrium

- Melt inclusion geochemistry and crystallisation pressures

Mantle melting characteristics (e.g., source compositions and melting extent) were determined using the following parameters:

- Glass $Na_{8.0}$ and K/Ti
- Melt flux parameter (discussed below)

New glass and mineral chemistry, modal mineralogy and textural data presented in this chapter are supplemented by data compiled from the literature (Table 7.1). Because mineral chemistry, modal and textural analysis were limited to dredges which were sampled, not all locations along the Gakkel Ridge have all variables constrained.

Table 7.1 Supplementary data sources

Data	Data source	Reference		Location
Ridge bathymetry	Gakkel Bathymetry	Michael et al. (2003)		
	GMRT data	Ryan et al. (2009)		
	IBCAO data	Jakobsson et al. (2012)		
Gakkel glass data		New Gakkel glass analyses	Lissenberg et al. (2019)	
	PetDB	Existing Gakkel glass analyses	Lehnert et al. (2000)	
Gakkel Ridge olivine-hosted melt inclusion crystallisation pressures		Shaw et al. (2010)		85°E Gakkel Ridge
		Wanless et al. (2014a)		Gakkel Ridge EVZ
Global modal mineralogy data		Stewart et al. (2005)		EPR and MAR compilation
		Pan and Batiza (2003)		EPR compilation
Global mineral chemistry data		Batiza and Niu (1992)		EPR (plagioclase + olivine)
		Batiza et al. (1995)		EPR (plagioclase + olivine)
		Pan and Batiza (2002)		EPR (Ol)
		Ridley et al (2006)		EPR (Pl + Ol)
		Bryan et al. (1979)		MAR (Pl + Ol)
		Meyer and Shibata (1990)		MAR (Pl)
		Ciazella et al. (2017)		MAR (Pl + Ol)
		Kirkpatrick et al. (1979)		MAR (Pl)
		Kuo and Kirkpatrick (1982)		MAR (Pl)
		Wanless et al. (2012)		EPR (Ol)
		Laubier et al. (2012, 2007)		MAR (Ol)
		Laubier et al (2007)		MAR (Ol)
Global Mid-ocean Ridge Basalt (MORB) data		Gale et al. (2013)		

In this chapter a new parameter—melt flux—has been created, which is a qualitative estimate of the vigour of the magmatic system in any given location. This melt flux parameter ranges from 1-10, with 1 being low melt flux and 10 high. It is designated by evaluating a range of observables, each of which relates to magmatic vigour: the axial depth of the ridge, the size and shape of morphological features, the along-axis extent of the magmatic system, the abundance of basalt in the vicinity of the system and the magnitude of magnetic anomalies; the relation of each of these to magmatic vigour is outlined in Table 7.2. Melt flux values were assigned to locations where both glass and crystal cargo data exists. First, melt flux values were assigned to dredges based on considerations of each of the parameters outline in Table 7.2 at the segment scale; at this stage there was no consideration of differences between the three segments. Melt flux values were subsequently adjusted to account for local-scale variations within individual magmatic systems and for differences between each of the three segments (e.g., ridge depth).

Table 7.2: Melt flux parameters

Parameter	Relation to magmatic vigour
Axial Depth of the ridge	Traditionally, the axial depth of mid-ocean ridge has been interpreted to reflect the extent of melting; shallower ridges experience higher extents of melting and melt supply compared to deeper ridges. Note: there has been some recent debate whether mantle potential temperature (Klein and Langmuir 1987; White and Klein 2014), or mantle fertility (Niu and O'Hara 2008; Niu 2016) control axial depth.
Size and shape of axial morphology and axial extent	At a basic level, larger volcanic features are formed when: 1) more material is erupted; and 2) repeated eruptions occur in that location. For example, large volcanic features such as axial volcanic ridges (WVZ) and large circular seamounts (EVZ) require larger volumes of erupted material compared to smaller seamounts scattered throughout the ridge axis. The formation of large features also requires that magmatism is focussed and sustained.
Magnitude of magnetic anomalies	Magnetic anomalies are interpreted to indicate the presence of magnetized rocks in the upper lithosphere. Along the Gakkel Ridge they are interpreted as evidence for the presence of basaltic crust (Jokat and Schmid-Aursch 2007). Jokat and Schmid-Aursch (2007) note that whilst the magnetic signal could be from gabbros, seismic velocities typical of layer 3 are absent. Furthermore, the shape of magnetic anomalies provide information about the extent of melt focussing (Jokat et al. 2003; Jokat and Schmidt-Aursch 2007); bullseye patterns indicate more focussed magmatism than elongate patterns.
Abundance of basalt	The presence of basalt on the ridge axis is taken to indicate that that region of the ridge is volcanically active relative to regions of peridotite exposure.

At the segment-scale, dredges from the WVZ have the highest melt flux values (5-10) which reflects the shallower axial ridge depth (Fig. 7.1a), abundant basalt and continuous high amplitude magnetic anomaly present in this segment (7.1b). In contrast, melt flux values in the SMZ and EVZ are both lower and more variable (Fig. 7.1c-f). This results from deeper axial valleys, discontinuous and variable magnetic anomalies and the recovery of more variable lithologies, especially in the SMZ where peridotite is abundant on the seafloor. It should be noted that this parameter is preliminary and qualitative and in order to apply it more broadly in the future (i.e., to other ridge segments) it requires further refinement through rigorous and quantitative assessment of all parameters influencing melt flux; such assessment was beyond the scope of this thesis.

To better illustrate the melt flux parameter used here, consider two end-member magmatic systems: the 2°W Axial Volcanic Ridge (Fig. 7.1g-h) and 48°E Deep Seafloor (Fig. 7.1i-j). Bathymetrically, these two locations are markedly different. The 2°W Axial Volcanic Ridge is a large volcanic construct that extends for 46 km along-axis and shoals from 3800 to 2770 mbsl. In contrast, the ridge axis at 48°E Deep Seafloor is deeper (~5095-4853 mbsl) and is characterised by seamounts, but no peridotite. Samples from 48°E Deep Seafloor region were dredged from fault scarps and seamounts (~106-265 m high). Whilst basalt was recovered in dredges from both locations (Michael et al. 2003), 2°W Axial Volcanic Ridge is characterised by a continuous high amplitude magnetic anomaly whilst 48°E Deep Seafloor is underlain by a lower amplitude magnetic anomaly that wanes towards the east; such magnetic anomalies have been used by Jokat and Schmid-Aursh (2007) to suggest that magma supply is more robust in the Western Volcanic Zone (WVZ). In combination these characteristics indicate melt flux values that are higher (7-10) at 2°W Axial Volcanic Ridge than at 48°E Deep Seafloor (1-3: Fig. 7.1).

On a local scale, melt flux values will vary depending on variations in bathymetry, volcanic morphology and magnetic character. At 48°E Deep Seafloor, melt flux values decrease towards the northeast as the amplitude of the magnetic anomaly decreases (Fig. 7.1i,j). In the southeast the magnetic anomaly is higher and the two locations here have been assigned melt flux values of 3; melt flux values of 1 correspond to the locations of the lowest magnetic anomaly values. At 2°W Axial Volcanic Ridge the highest melt flux values are situated at the centre of the axial volcanic ridge, not in locations corresponding to the highest amplitude magnetic anomalies (Fig. 7.1g,h); in contrast, the lowest melt flux values are situated at the flanks of the axial volcanic ridge despite them having comparable, or even higher, amplitude magnetic anomalies.

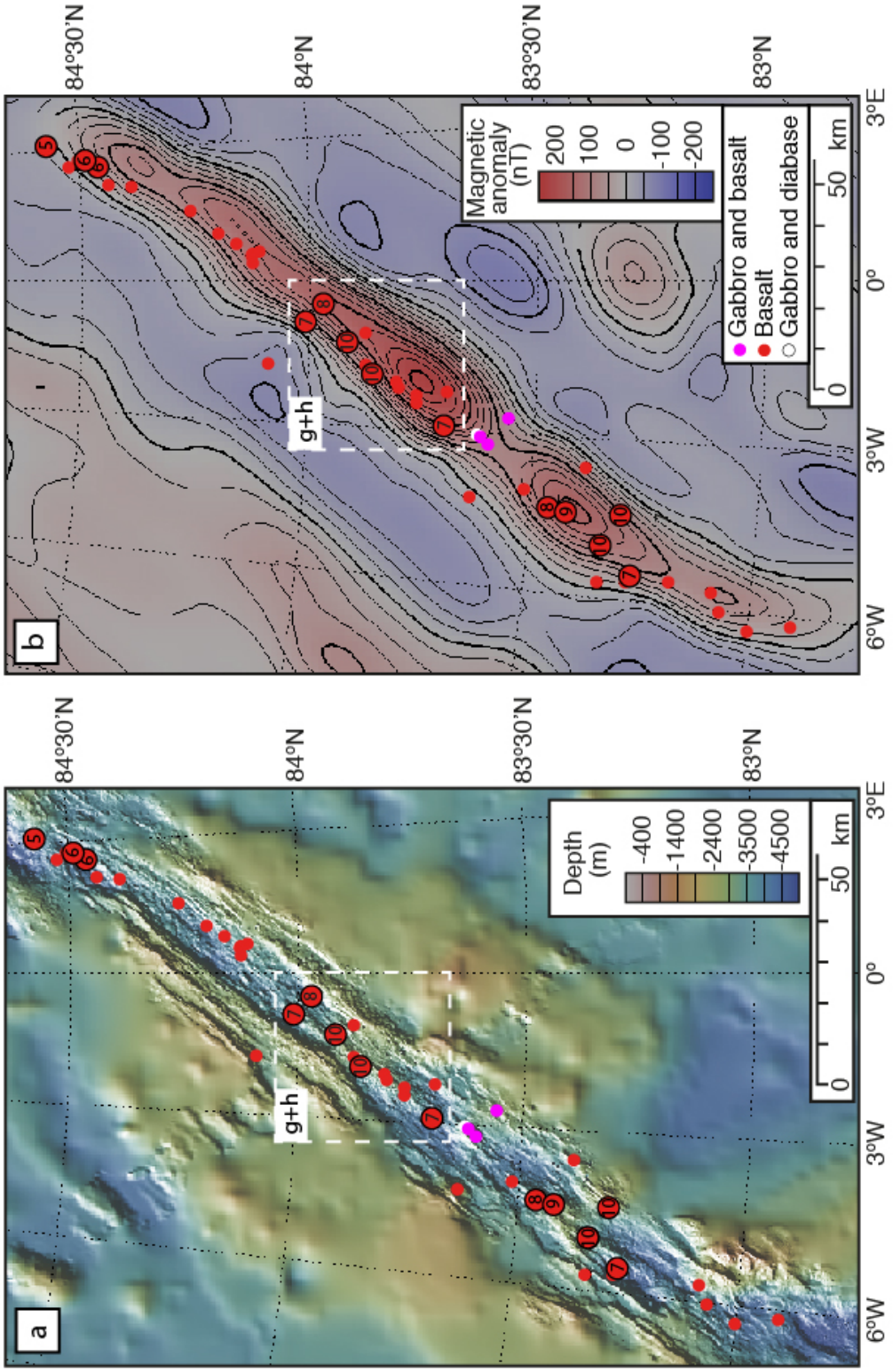

Fig. 7.1: Melt flux parameter determination for the Western Volcanic Zone (WVZ). Bathymetric (**a**) and magnetic anomaly (**b**) maps of the WVZ are shown. Melt flux values were only determined for samples with both glass and crystal cargo analysis data; points with no numbers do not have both types of data. Points indicate the location of dredges; their colour relates to the lithology types recovered. Detailed images of 2°W Axial Volcanic Ridge are outlined in white (**g+h**). Maps were made in GeoMapApp (http://www.geomapapp.org). Bathymetry data includes the GMRT dataset (Ryan et al. 2009) and bathymetry collected during the AMORE expedition (e.g., Michael et al. 2003). EMAG 2 magnetics data is from Meyer et al. (2017). White circles in **b** are seamounts. Contour intervals: bathymetric maps, fine line 200 m, bolding line 600 m; magnetic maps, fine line 10 nT, bolding line 50 nT.

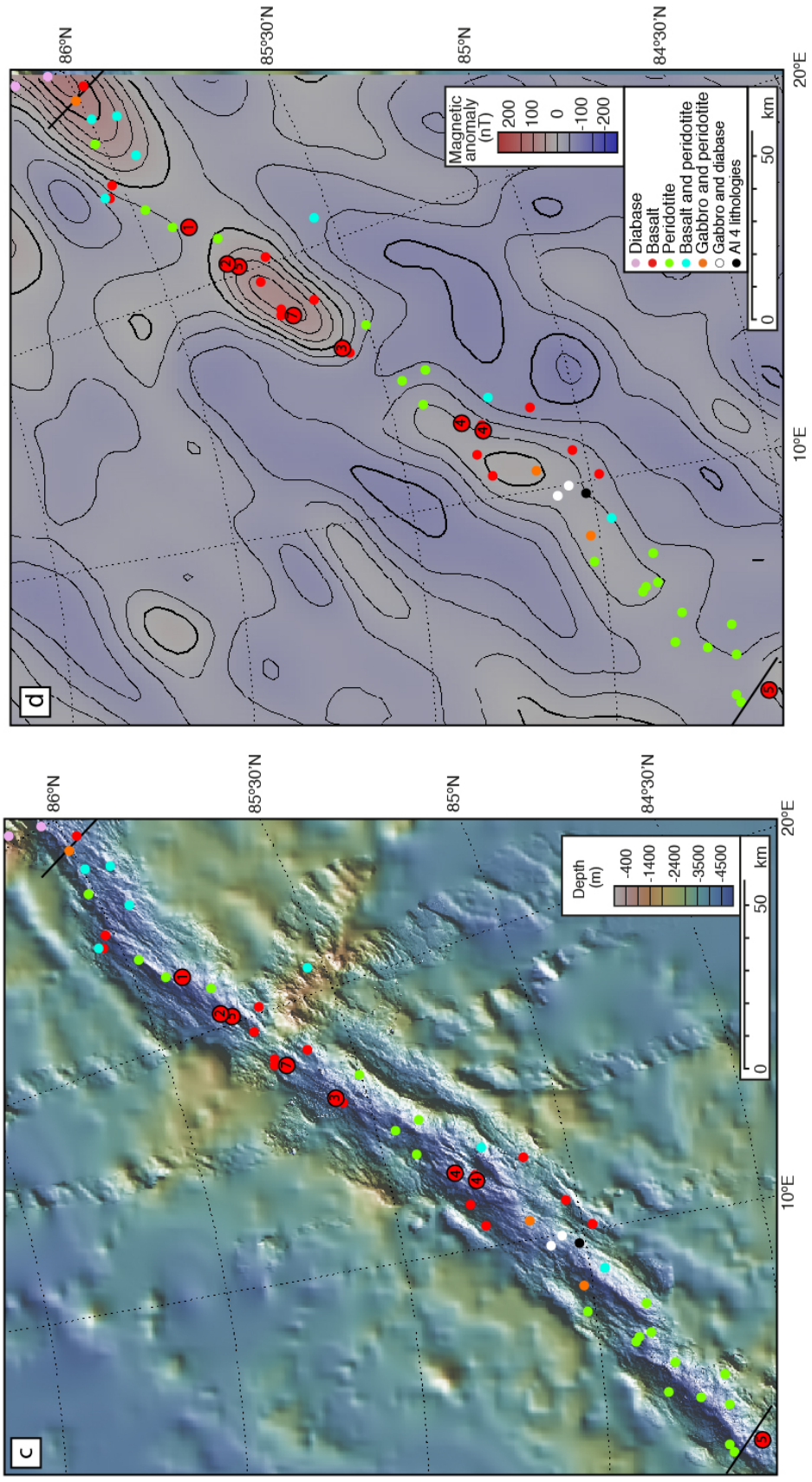

Fig. 7.1 continued: Melt flux parameter determination for the Sparsely Magmatic Zone (SMZ). Lithologies are more variable that in the WVZ and magnetic anomalies are lower amplitude and discontinuous. Bathymetric (**c**) and magnetic anomaly (**d**) maps of the SMZ are shown.

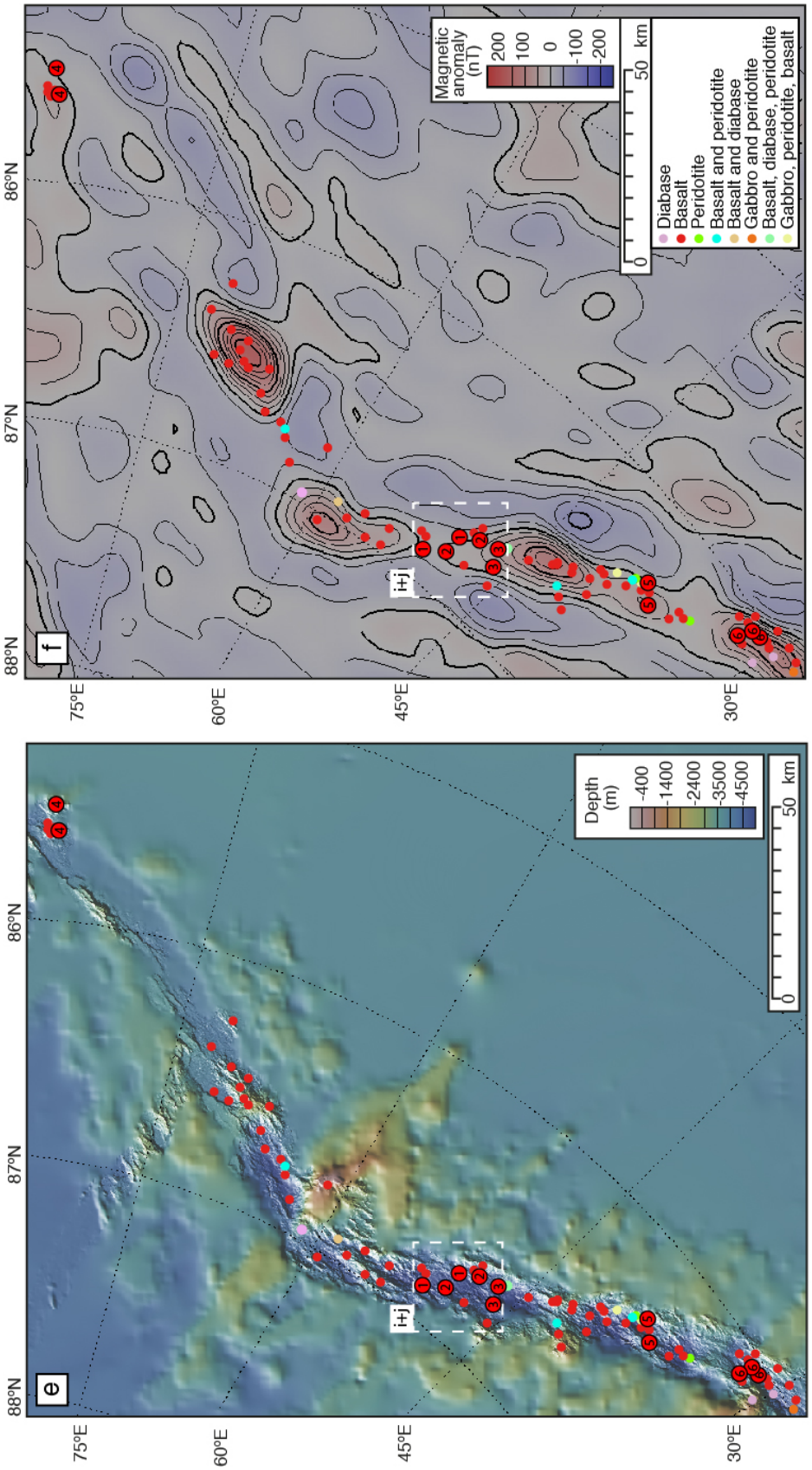

Fig. 7.1 continued: Melt flux parameter determination for the Sparsely Magmatic Zone (EVZ). Bathymetric (**e**) and magnetic anomaly (**f**) maps of the EVZ are shown. Lithologies are more variable than in the WVZ. Magnetic anomalies have bullseye shapes. Detailed images of 48°E Deep Seafloor outlined in white (**i+j**) are shown below.

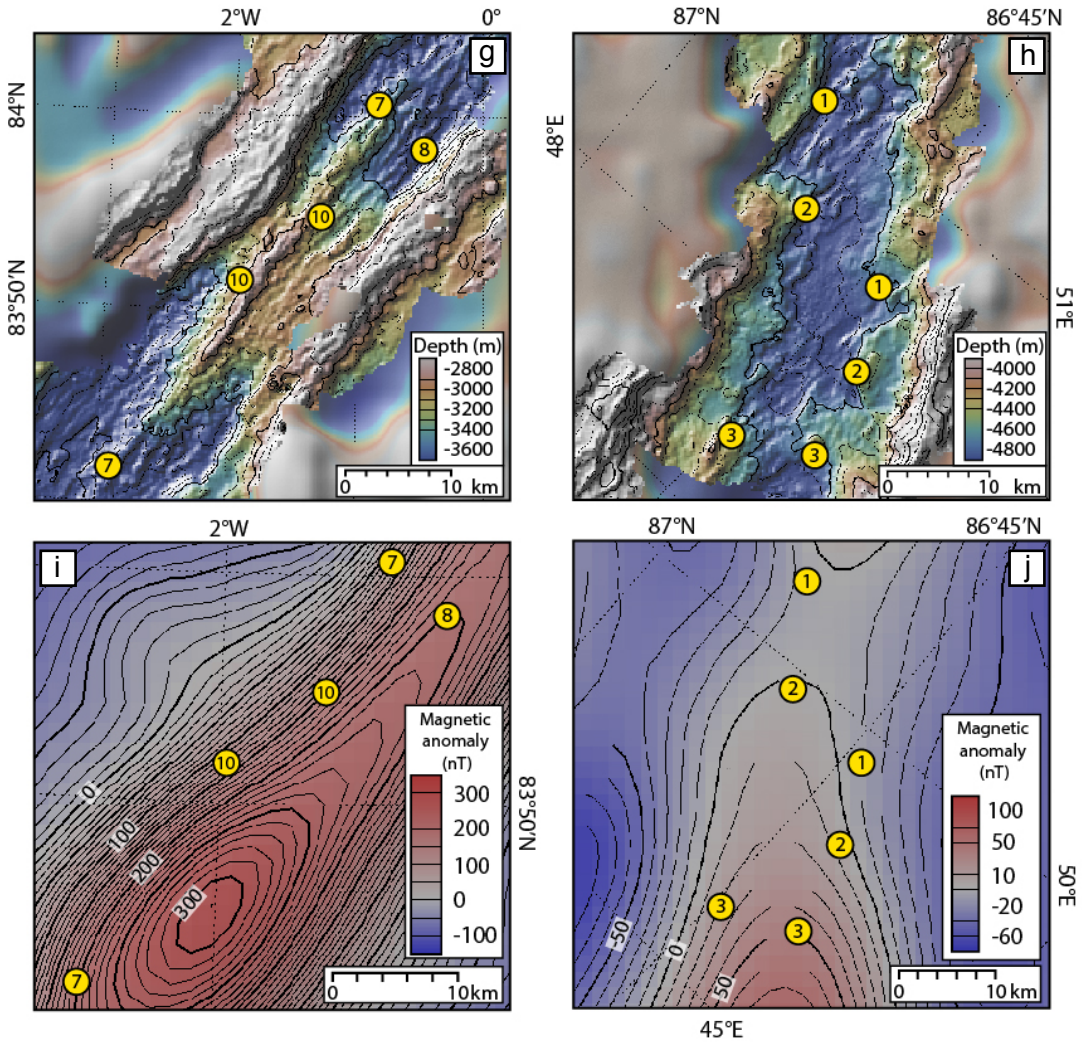

Fig. 7.1: Melt flux parameter determination: a comparison between 2°W Axial Volcanic Ridge and 48°E Deep Seafloor. **g,h** Bathymetric maps show that melt flux values (in yellow) are higher at 2°W Axial Volcanic Ridge (**g**) where the seafloor is shallower and significant volcanic relief is present compared to 48°E Deep Seafloor where the seafloor is deep and volcanic relief is reduced. **i,j** Magnetic anomaly maps of both regions showing that the high melt flux region (**g**,**j**) are characterised by a continuous high amplitude magnetic anomaly compared to the lower amplitude waning anomaly in **h**,**j**. Contour intervals: bathymetric maps, fine line 200 m, bolding line 600 m; magnetic maps, fine line 10 nT, bolding line 50 nT.

7.3 Results

7.3.1 Basalt crystal cargo

All three tectono-magmatic segments (WVZ; Sparsely Magmatic Zone, SMZ; and Eastern Volcanic Zone, EVZ) are characterised by olivine only and olivine + plagioclase crystal assemblages (Fig. 7.2). Although clinopyroxene is present in all segments, it is present in only ~14% of dredges and never makes up more than 2% of the crystal assemblage (Fig. 7.2d). All ridge segments contain both aphyric and highly phyric (up to 50%) basalts (Fig. 7.2a); however, basalts from the SMZ and EVZ have more variable total crystal contents than the WVZ basalts (Table 7.3). Basalt plagioclase content closely mirrors the total crystal content (Fig. 7.2b); plagioclase and total crystal content

correlate positively with one another (Fig.7.3a). Figure 7.2 shows that plagioclase content remains relatively high and stable throughout the WVZ (Fig. 7.2b), with peaks in plagioclase and total crystal content occurring in the middle of the SMZ and start of the EVZ. High plagioclase:olivine ratios demonstrate that samples in all segments are enriched in plagioclase relative to olivine (Fig. 7.2d). Plagioclase occurs both as individual crystals and as components of poly- and mono-mineralic glomerocrysts (Fig. 7.4). Individual plagioclase crystals make up the greatest proportion of the crystal cargo, followed by poly-mineralic glomerocrysts and then mono-mineralic glomerocrysts. This relationship is observed along the entire ridge, as are poly-mineralic glomerocrysts, characterised by plagioclase + olivine ± pyroxene.

Olivine content remains low (average 2%) along the entire ridge (Fig. 7.2c) but increases moderately at the start of the EVZ; olivine and total crystal content do not correlate other than in some samples from the EVZ (Fig. 7.3b). These samples originate from a region at ~50°E where plagioclase is essentially absent. Here, crystal content is relatively low (0.5-6.5%) but is dominated by olivine (0.5-4.1%); five dredges from this region (H-D80, P-271, P-270, H-D79 and H-D77) contain only olivine and have relatively high glass Mg# of 64-67 (Fig. 7.5b).

Spinel is present in all tectono-magmatic segments of the ridge. In the six samples where spinel was identified during modal analysis, spinel contents range from 0.01-0.13% (average 0.05%). It should be noted that although spinel is present in a total of 58 samples it was not identified in all samples during modal analysis because of the thresholding level used. Whilst spinel is more commonly found in samples that contain olivine only, it can occur in plagioclase-rich samples.

Table 7.3: Total crystal content variations of Gakkel Ridge basalts

	Sample	Total crystal content (%)				
Segment	number	Minimum	Median	Maximum	Range	Standard deviation
WVZ	39	0.79	8.11	34.94	34.15	8.13
SMZ	28	0.00	5.86	50.28	50.28	14.54
EVZ	29	0.53	3.46	45.22	44.69	12.65

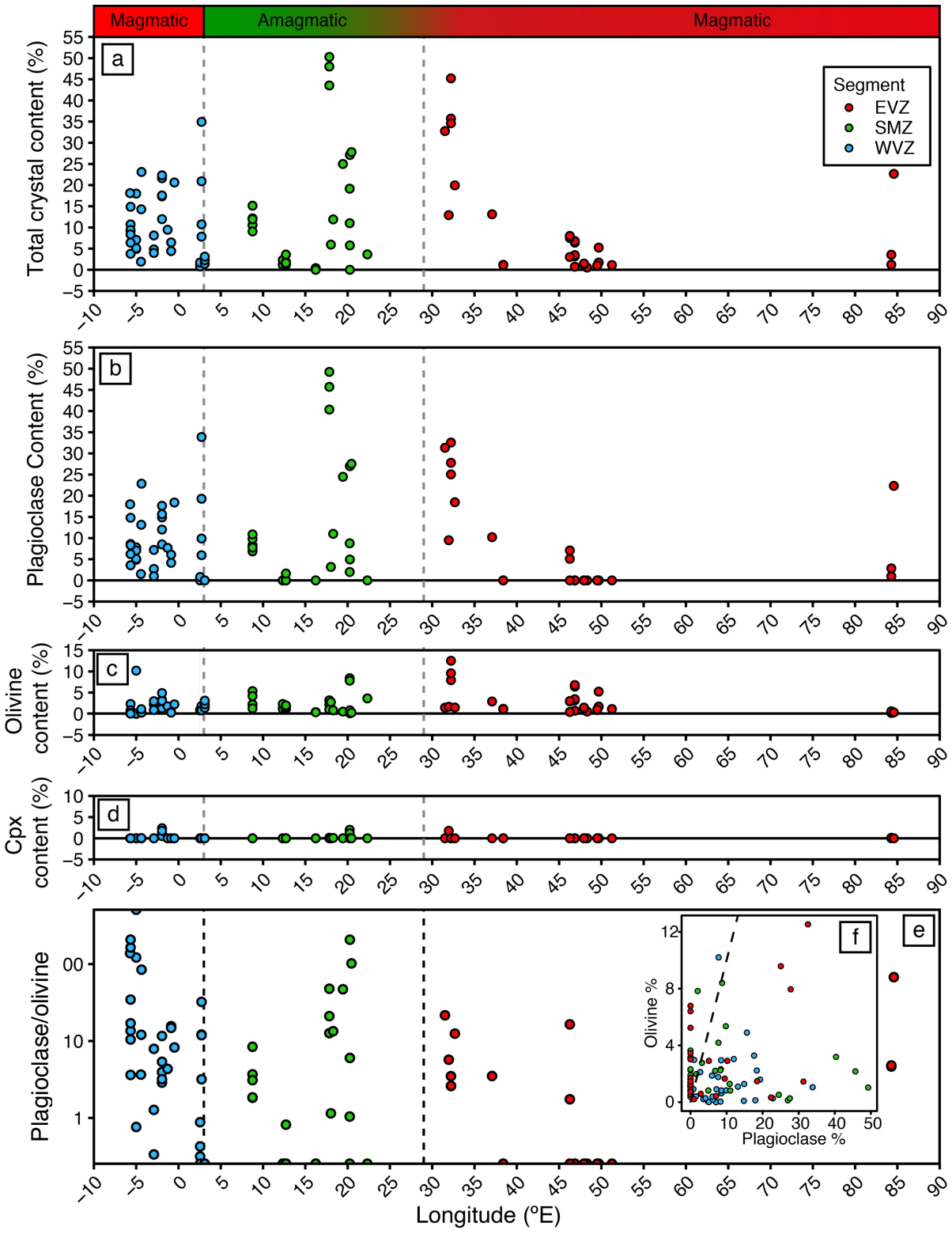

Fig. 7.2: Along-axis variation in basalt modal mineralogy. **a** Variation in total crystal content along axis. **b** Variation in plagioclase content along axis. Plagioclase content closely mirrors total crystal content along most of the ridge. **c** Variation in olivine content along the ridge. **d** Variation in clinopyroxene (Cpx) content along axis. **e** Along-axis variation in plagioclase:olivine ratios. Samples in all three segments show enrichment in plagioclase relative to olivine. Inset **i** shows there is no correlation between plagioclase and olivine content; the dashed line is 1:1.

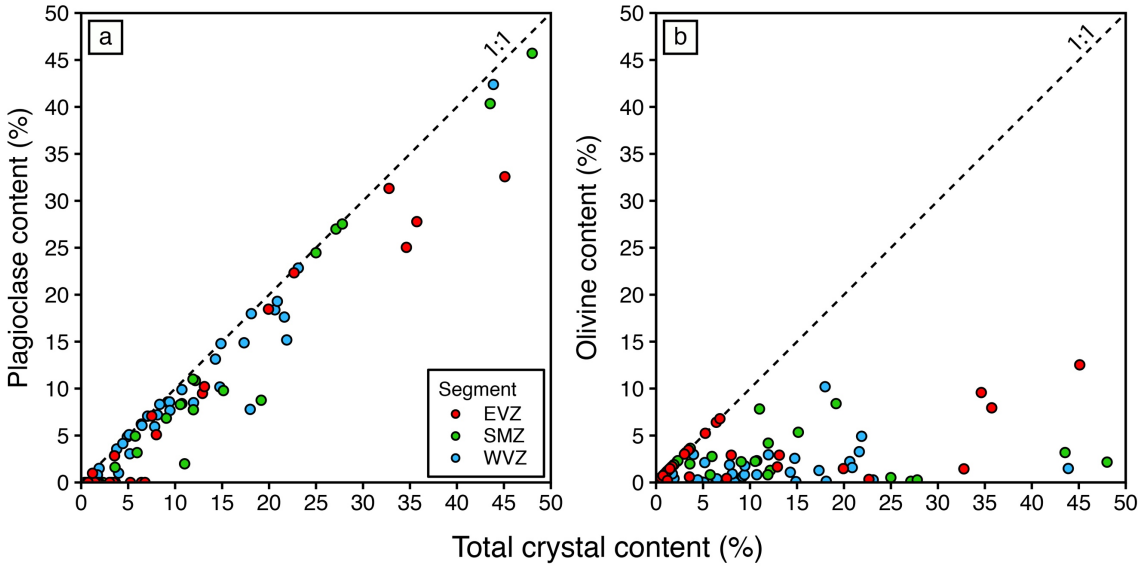

Fig. 7.3: Plagioclase (**a**) and olivine (**b**) content as a function of total crystal content. The positive correlation between total crystal content and plagioclase content demonstrates that crystal content is dominated by plagioclase; this relationship is present in samples from all segments. In contrast, only samples from the EVZ and several from the SMZ show a correlation between total crystal content and olivine content; these samples contain no plagioclase.

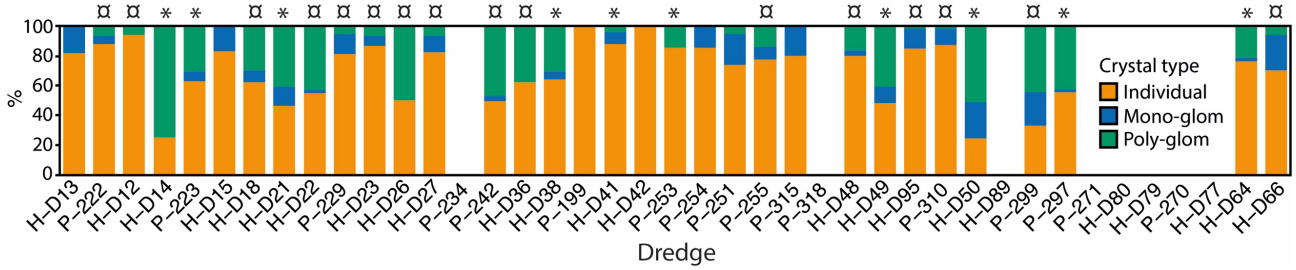

Fig. 7.4: Discrete along-axis plot displaying the proportions of individual plagioclase and poly- and mono-mineralic glomerocrysts. ∗ Denotes poly-mineralic glomerocrysts with plagioclase + olivine + pyroxene or plagioclase + olivine, ¤ denotes those containing plagioclase + olivine only. There is no systematic change in the proportions of different types of glomerocryst along the ridge axis, or within individual segments.

7.3.2 Basalt glass geochemistry

Basalt glasses do not show systematic geochemical variations in SiO_2, Mg# and $Na_{8.0}$ from west to east along the entire length of the Gakkel Ridge (Fig. 7.5a-c). Instead, trends are present on the scale of the three tectono-magmatic segments.

7.3.2.1 SiO_2

Basalt glass SiO_2 contents are variable along the length of the ridge, ranging from 46.43-52.20 wt.% (Fig. 7.5a). Whilst the SiO_2 content does not change systematically along the full length of the ridge, the range in SiO_2 content decreases from the WVZ to the EVZ

(Table 7.4 And Fig. 7.5a). Each segment displays regional trends in SiO_2 content (Fig. 7.5a). In the western WVZ, basalts show relatively restricted SiO_2 values that decrease toward the east and the junction with the SMZ. Here, SiO_2 becomes highly variable and reaches the lowest values seen along the entire ridge. Within the SMZ, SiO_2 content shows the greatest variability of any segment (Table 7.4) with no systematic along-axis pattern. The SiO_2 variability of EVZ basalts is the lowest of any segment (Table 7.4) and, like the WVZ, shows a well-defined along-axis pattern of initially relatively high SiO_2 contents that decrease toward, and then increase away from, ~50°E.

7.3.2.2 Mg#

In contrast to SiO_2, the range of glass Mg# increases and becomes more variable from west to east (Table 7.4, Fig 7.5b). Throughout the western portion of the WVZ, the range of Mg# appears relatively constant until the junction with the SMZ is reached. Here, as with SiO_2 content, the range increases and extends to more primitive compositions than seen in the west of the segment. In the SMZ, barring a few more evolved samples, glass compositions are more primitive than most of those in the WVZ. Basalts in the WVZ and SMZ show similar variability (Table 7.4). At the transition to the EVZ, basalt Mg# shows the greatest range and variability (SD = 4.43). Moving east through the EVZ Mg# increases and variability decreases until ~85°E, where basalts again show increased variability. Basalt Mg# in the EVZ extends to higher values than in the WVZ and SMZ.

7.3.2.3 $Na_{8.0}$

To infer the conditions of mantle melting, mid-ocean ridge basalt compositions need to be corrected for the effects of shallow fractionation. Klein and Langmuir (1987) derived a series of parameters by correcting oxide abundances to a specified value of MgO (e.g., 8 wt.%). One such fractionation corrected parameter, $Na_{8.0}$, is commonly used to describe the extent of partial melting, with higher values of $Na_{8.0}$ indicating lower degrees of partial melting (Klein and Langmuir 1987). Figure 7.6 shows three binary plots of glass Na_2O vs MgO for each segment of the Gakkel Ridge. Regressions through these datasets deviate from lines of constant $Na_{8.0}$ calculated using the equation of Klein and Langmuir (1987). Regression slopes are both higher (SMZ) and lower (WVZ and EVZ) than the Klein & Langmuir (1987) parameterisation, suggesting that this parameterisation is not appropriate for the Gakkel Ridge data. Hence, regressions through the data for each segment are used to calculate $Na_{8.0}$. Figure 7.6d shows that this approach results in significant deviations from the $Na_{8.0}$ values calculated using the Klein and Langmuir (1987) parameterisation, with values becoming both higher and lower.

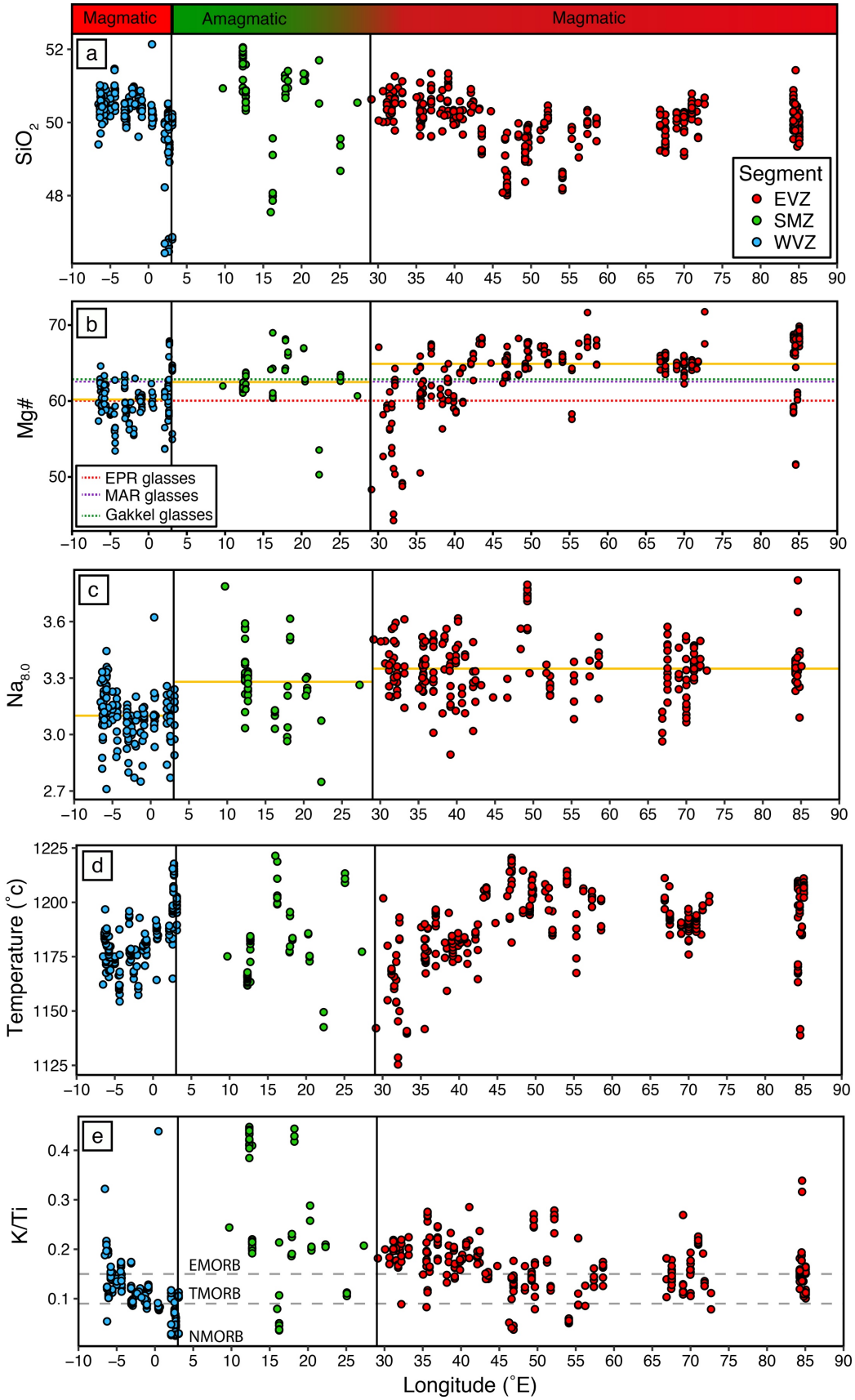

Fig. 7.5: Along axis variations in Gakkel glass SiO_2 (**a**), Mg# (**b**), $Na_{8.0}$ (**c**), temperature (**d**) and K/Ti ratios (**e**). Horizontal yellow lines in **b** and **c** are segment medians. Red, green and purple lines in **b** are median Mg# of the EPR, Gakkel and MAR ridges respectively. MORB classification in **e** is as follows: NMORB, <0.09 K/Ti; TMORB, 0.09-0.15 K/Ti ; EMORB, >0.15 K/Ti (Standish et al. 2008). Mg# were calculated assuming an $Fe^{3+}/\Sigma Fe$ of 0.1 (Berry et al. 2018).

At the scale of the Gakkel Ridge, glass $Na_{8.0}$ values become progressively higher towards the east (Fig. 7.5c). $Na_{8.0}$ of basalts in the WVZ are both more restricted (SD = 0.13) and shifted to lower values (median = 3.10) than those typical of the segments to the east; the SMZ in particular is more variable (SD = 0.18). Within the WVZ itself, $Na_{8.0}$ decreases toward, and then increases away, from ~2°W toward the SMZ. Basalts in the SMZ are characterised by higher $Na_{8.0}$ values (median = 3.28) than those in the WVZ with $Na_{8.0}$ decreasing from ~10°E towards the EVZ. Basalt $Na_{8.0}$ values at the start of the SMZ (~10°E) are some of the highest found along the entire ridge (Table 7.4 and Fig. 7.5c). The EVZ is similar to the SMZ in that basalt $Na_{8.0}$ values are shifted to higher values than those typical of the WVZ (median of 3.35 compared to 3.10). At the start of the EVZ, $Na_{8.0}$ values straddle those found in the WVZ and SMZ before increasing towards and then decreasing away from ~50°E where $Na_{8.0}$ values reach similarly high values to those in the SMZ.

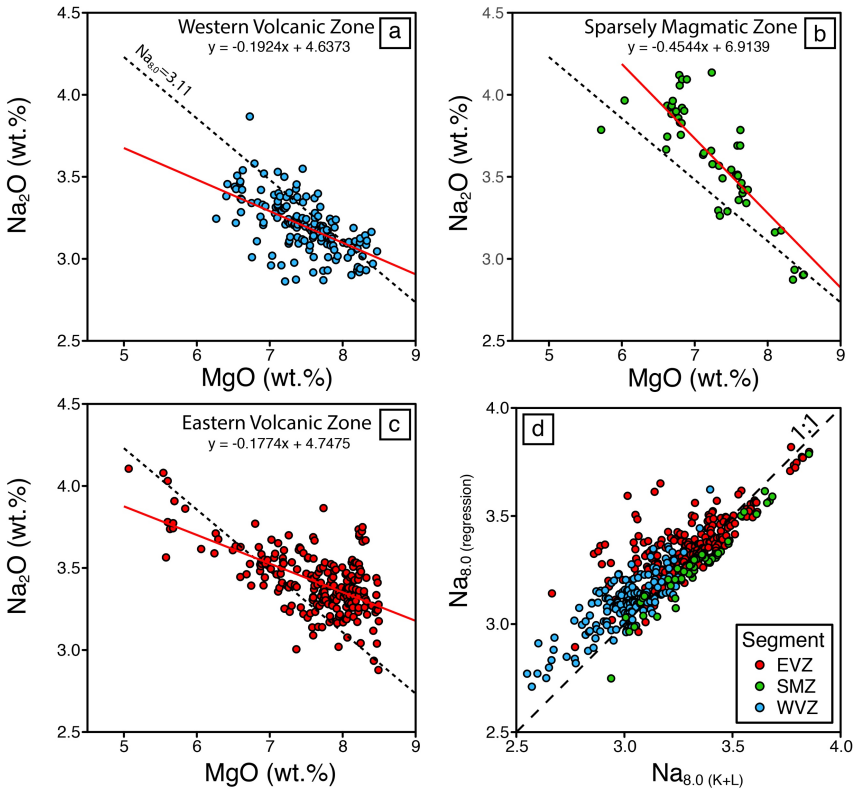

Fig. 7.6: Binary plots of Na_2O vs. MgO for Gakkel Ridge basalt glass data; Western Volcanic Zone, **a**; Sparsely Magmatic Zone, **b;** and Western Magmatic Zone, **c**. A line of constant $Na_{8.0,}$ calculated using the equations of Klein and Langmuir (1987) is shown in the three panels (dashed line). The red line is a regression through each of the datasets shown; corresponding regression equations are shown at the top of each panel. Using the slopes of these regressions, $Na_{8.0(regression)}$ is calculated for each segment and compared to $Na_{8.0(K+L)}$ calculated with the Klein and Langmuir (1987) equation (**d**). Panel **d** shows that $Na_{8.0(regression)}$ values are higher than $Na_{8.0(K+L)}$ values in the WVZ and EVZ, and lower in the SMZ.

Table 7.4 Compositional variations of Gakkel Ridge glasses

Variable	Segment	Minimum	Maximum	Median	Range	Standard deviation
SiO_2 (wt.%)	WVZ	46.43	52.14	50.36	5.71	0.99
	SMZ	47.55	52.06	50.93	4.51	1.24
	EVZ	48.01	51.43	50.07	3.42	0.67
Mg#	WVZ	53.43	67.89	60.26	14.46	2.95
	SMZ	50.30	68.99	62.47	18.69	2.91
	EVZ	44.25	71.76	64.94	27.51	4.43
$Na_{8.0}$	WVZ	2.71	3.62	3.10	0.91	0.13
	SMZ	2.75	3.79	3.28	1.04	0.18
	EVZ	2.89	3.82	3.35	0.93	0.15
K/Ti	WVZ	0.03	0.44	0.11	0.41	0.05
	SMZ	0.04	0.45	0.22	0.41	0.13
	EVZ	0.04	0.34	0.16	0.30	0.05

7.3.2.4 Glass K/TI

Glass K/Ti ratios show significant variation at the segment-scale but no systematic along-axis changes at the ridge-scale (Fig. 7.5e). Median K/Ti is highest in the SMZ and lowest in the WVZ (Table 7.4). Within the WVZ, K/Ti values decrease systematically from west to east (Fig. 7.5e) and show low variability (SD=0.05) (Table 7.4); there is a gradual change from EMORB in the west to NMORB in the east. Glasses in the SMZ are distinctly different: K/Ti values are highly variable (SD=0.41) (Table 7.4), there is no systematic change along-axis within the segment, and most samples are EMORBs (Fig. 7.5e). EVZ glasses show the same variability (SD=0.05) as samples from the WVZ, but here the range of K/Ti is reduced. Within the EVZ, K/Ti is initially high and then decreases toward, and then increases away, from ~45-55°E (Fig. 7.5e).

7.3.3 Glass geochemistry correlations

Glass geochemistry shows several weak correlations, both in the dataset as a whole and at the segment scale (Fig. 7.7). There are no clear correlations between $Na_{8.0}$ and SiO_2 in the entire dataset or within individual segments (Fi. 7.7a). However, samples from each segment plot in distinct regions, with the WVZ shifted towards lower $Na_{8.0}$ and higher SiO_2 compared to samples from the EVZ, whilst samples from the SMZ are shifted toward higher SiO_2 (Fig. 7.8). A distinct group of samples from the WVZ and SMZ plots at lower $Na_{8.0}$ and SiO_2. In the dataset as a whole, there is a weak positive correlation between glass $Na_{8.0}$ and K/Ti; samples from the WVZ are shifted to lower values of K/Ti and $Na_{8.0}$ compared to the EVZ, and some samples from the SMZ plot at higher K/Ti values at a given $Na_{8.0}$ (Fig. 7.7b). There is no correlation between Mg# and both $Na_{8.0}$ (Fig. 7.7c) or K/Ti (Fig. 7.7d).

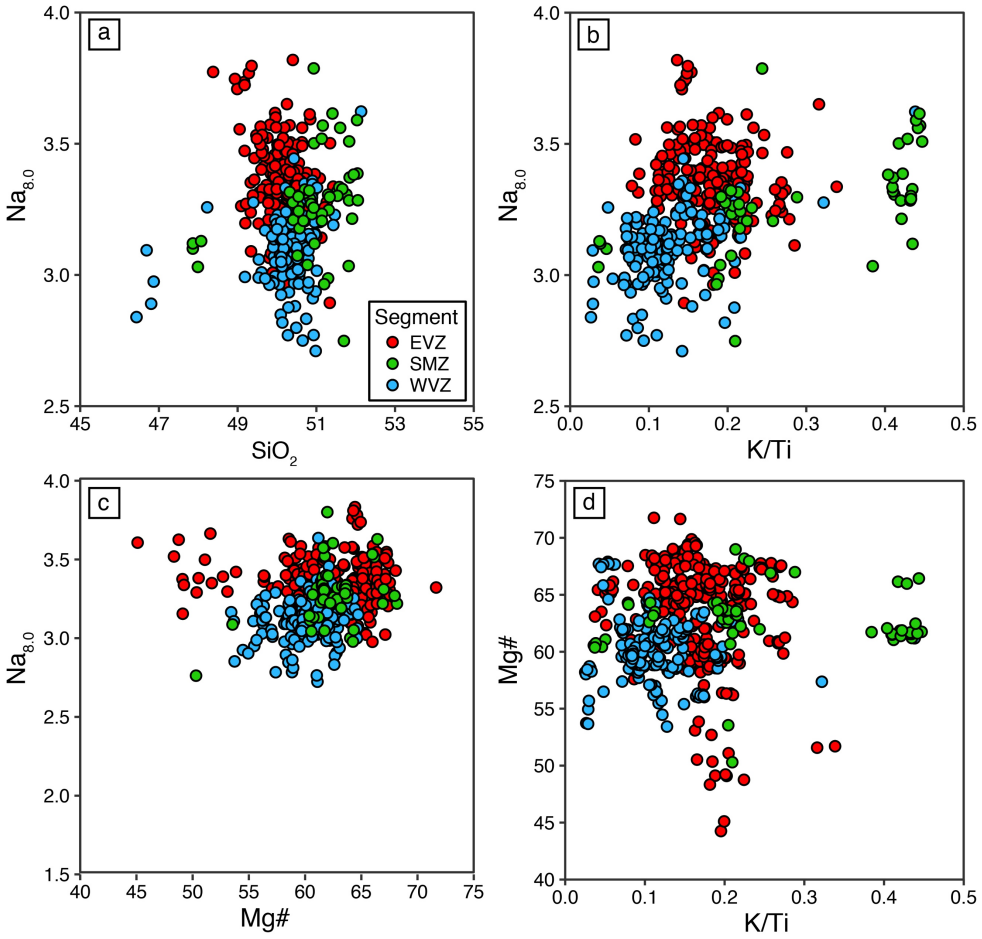

Fig. 7.7: Glass geochemistry correlations between $Na_{8.0}$ and SiO_2 (**a**), K/Ti (**b**) and Mg# (**c**) and between Mg# and K/Ti (**d**). There is no correlation between $Na_{8.0}$ and SiO_2 (**a**); glasses from the SMZ, and some from the WVZ, plot at both higher and lower $Na_{8.0}$ and SiO_2 than the bulk of the samples. A positive correlation is present between $Na_{8.0}$ and K/Ti (**b**). There is no correlation between either $Na_{8.0}$ and Mg# or Mg# and K/Ti; note that samples from the SMZ show a greater range in K/Ti values .

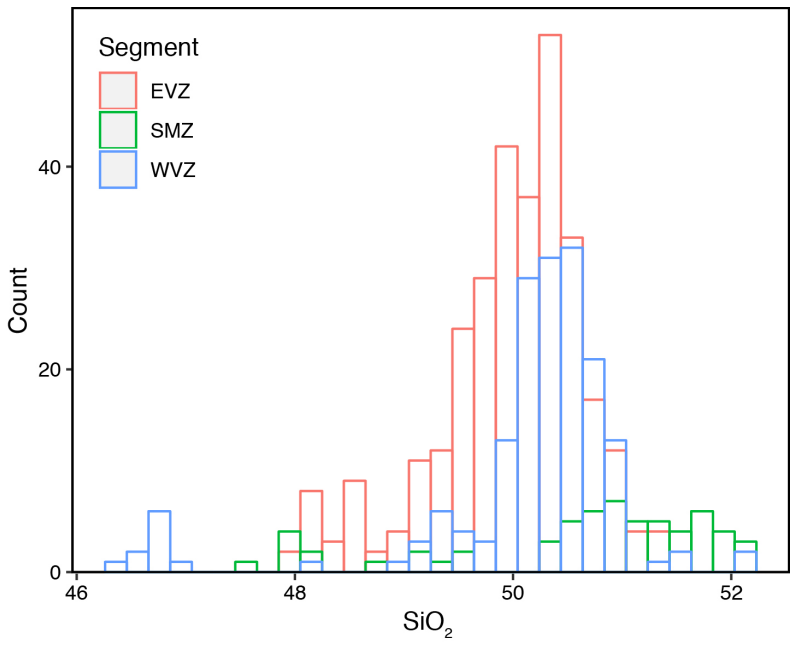

Fig. 7.8: Histogram illustrating the distribution of glass SiO_2 (wt.%) content. Glasses from the Western Volcanic Zone (WVZ) show the greatest range in SiO_2 content with a small group of samples plotting at distinctly lower SiO_2 content. Glasses from the Eastern Volcanic Zone (EVZ) do not show as great a range of values as the WVZ glasses, but SiO_2 contents are shifted toward lower values compared to the WVZ. Glasses from the Sparsely Magmatic Zone (SMZ) show a similar range to other segments.

7.3.4 Basalt glass temperatures

Basalt glass temperatures have been calculated using equations 1 and 2 of Sugawara (2000) which predict a linear relationship between temperature and the mole % MgO of a basaltic glass:

$$X_{MgO}^{Liq}(wt.\%) = 0.68X_{MgO}^{Liq}\ (mol\%) \quad (1)$$

and

$$T(K) = A + BX_{MgO}^{Liq}\ (mol\%) + CP(0.1\ MPa) \quad (2)$$

Here A, B and C are empirical constants of 1293 (±24), 14.60 (±0.26) and 0.0055(±0.0001), respectively, derived from experimental datasets. Trends in glass Mg# (Fig. 7.5b) and temperature (Fig. 7.5d) are similar because they are both a function of glass MgO. Glass temperatures vary both between and within segments (Fig. 7.5d). Whilst the maximum glass temperatures in each segment are similar (Table 7.5), the minimum glass temperature and temperature range decrease and increase respectively from west to east along the ridge (Table 7.5 and Fig. 7.5d). Glass temperatures are more variable in the SMZ and EVZ compared to the WVZ (Table 7.5); in the WVZ temperatures are similar along much of the segment and increase towards the SMZ, much like Mg#. Temperatures in the SMZ show the greatest variability and do not change systematically along the ridge. At the start of the EVZ, glass temperatures reach some of the lowest found along the entire ridge and are highly variable. Glass temperatures increase gradually toward and then decrease away from ~50°E; high temperatures at ~50°E correlate with high $Na_{8.0}$ (Fig. 7.5c). There are no correlations between glass temperature and either total crystal content (Fig. 7.9a) or $Na_{8.0}$ (Fig. 7.9b).

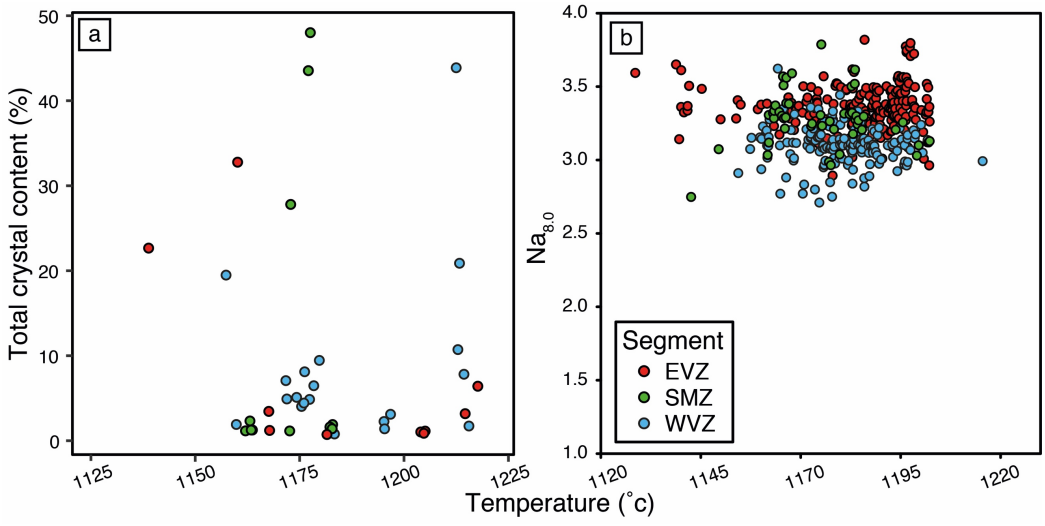

Fig. 7.9: Relationship between glass temperature and both total crystal content (**a**) and glass $Na_{8.0}$ (**b**). Glass temperature does not correlate with crystal content or $Na_{8.0}$.

Table 7.5 Temperature variations of Gakkel Ridge glasses

	Temperature (°c)				
Segment	Minimum	Median	Maximum	Range	Standard deviation
WVZ	1154	1180	1218	64	14
SMZ	1143	1176	1221	78	18
EVZ	1125	1194	1221	96	17

7.3.5 Melt flux

A broad negative correlation exists between melt flux and $Na_{8.0}$ with WVZ samples having higher melt flux and lower $Na_{8.0}$ compared to samples from the SMZ and EVZ (Fig. 7.10a). Samples from the SMZ have the greatest range in melt flux values (1-7), compared to those from the WVZ (5-10) and EVZ (1-6), which overlap. Melt flux does not correlate with olivine or plagioclase content or plagioclase:olivine ratios (Fig. 7.10b-d). Similar to $Na_{8.0}$, melt flux shows a broad negative correlation with Mg#; in general, lower melt flux values correlate to higher Mg# (Fig. 7.11). Relationships between melt flux and mineral chemistry are covered in section 7.3.7.

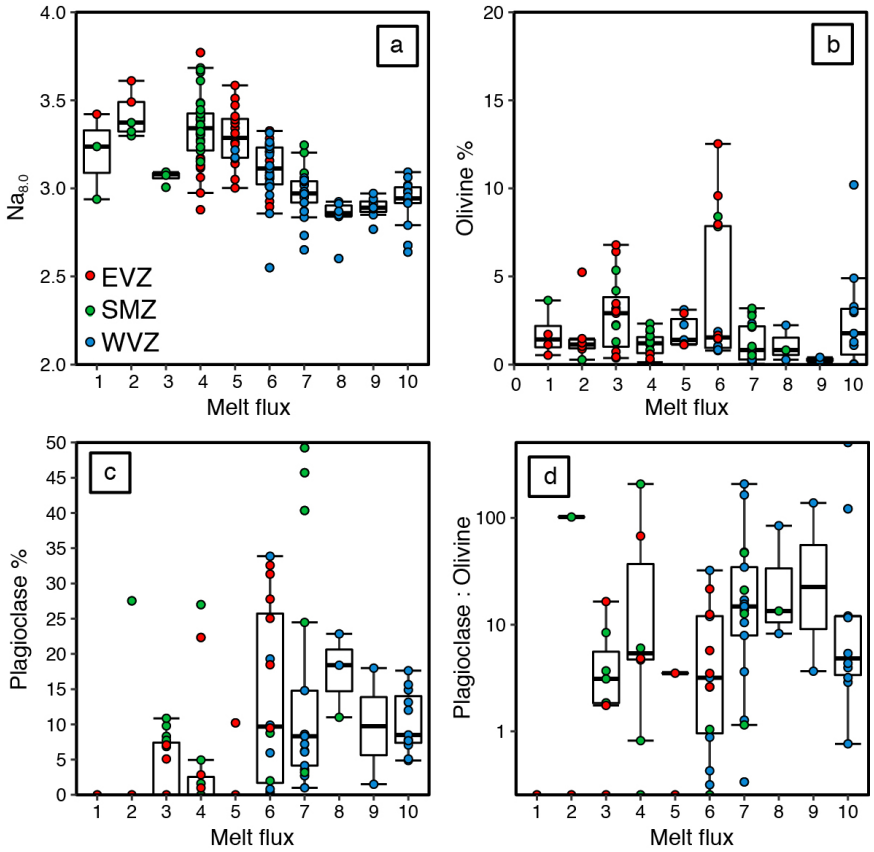

Fig. 7.10: Relationship between melt flux and $Na_{8.0}$ (**a**), olivine content (%) (**b**), plagioclase content (%) (**c**) and plagioclase:olivine ratio (**d**). Melt flux correlates negatively with glass $Na_{8.0}$ but shows no correlation with crystal content. Boxplot whiskers = 1.5 x IQR.

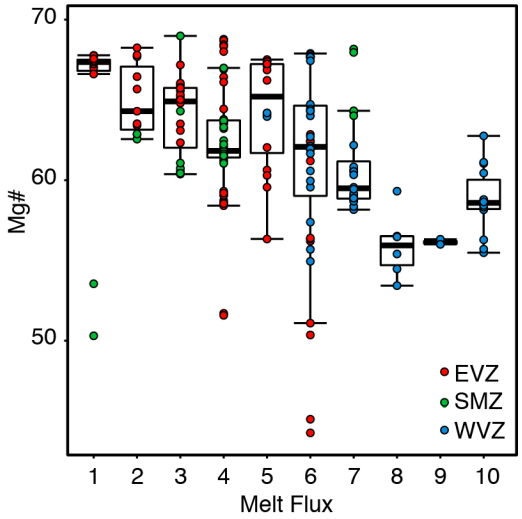

Fig. 7.11: Relationship between melt flux and glass Mg#. Except for a few deviations, samples in general shown a broad negative correlation between melt flux and Mg. Samples with lower melt flux values have higher Mg#.

7.3.6 Crystal cargo geochemistry

The major element contents of plagioclase (anorthite; An), olivine (forsterite; Fo) and clinopyroxene (Mg#) crystal cargo of samples from along the full length of the Gakkel Ridge are presented below.

7.3.6.1 Plagioclase

The only systematic pattern shown by plagioclase anorthite content is a gradual reduction in maximum anorthite content from west to east (Table 7.6 and Fig. 7.12a). The median core anorthite content is highest in the WVZ where compositions tend to be restricted to An_{60-85}. Whilst plagioclase compositions do not change systematically eastwards along the WVZ, plagioclase compositions do become more restricted at the junction with the SMZ. In contrast, plagioclase compositions in the SMZ change systematically along the segment, becoming more anorthitic towards the east (Fig. 7.12a). At the western end of the SMZ plagioclase compositions are restricted and overlap with the most evolved samples from the WVZ; at ~20°E plagioclase is similar in compositions to the bulk of the samples in the WVZ. Plagioclase in the EVZ have the greatest compositional range, with the most evolved plagioclase from along the entire ridge located at its western end. The reduced and then increased variability in anorthite content moving east toward 85°E mirrors the pattern shown by glass Mg# (Fig. 7.5b and Fig. 7.12a). Crystal and core types show no systematic differences (Fig. 7.12a).

Table 7.6 Anorthite content of Gakkel Ridge basalt plagioclase crystal cargo

		Average plagioclase core anorthite content*				
Segment	Number of crystals analysed	Minimum	Median	Maximum	Range	Standard deviation
WVZ	353	54.12	77.44	87.19	33.07	6.97
SMZ	193	54.36	75.56	83.71	29.35	9.28
EVZ	296	48.59	76.32	82.22	33.63	7.85

* Statistics include all core types in Fig. 7.12

To assess whether mixed chemical populations are present in samples from the Gakkel Ridge, the parameter ΔAnV ($An_{Crystal\ maximum}$ minus $An_{Crystal\ minimum}$) can be used; this parameter expresses the range, or variation (V), of compositions present within a single plagioclase crystal independent of the location of these data within the crystal; hence, it is not a measure of core-rim zonation. The plagioclase crystal maximum and minimum are the maximum and minimum An values analysed from any one of the following crystal locations: plagioclase cores, mottled cores, skeletal cores, mantles, rims and patches (where analysed). Quench and melt inclusion quench rims have not been included because they formed during disequilibrium growth (see Chapter 5); skeletal cores also formed under similar conditions but form the core of these crystals. If ΔAnV varies within individual samples, it suggests that individual crystals may have experienced different crystallisation histories. Whilst the variation observed could in part relate to sectioning effects, the variation in ΔAnV, as discussed in Chapter 5, agrees well with observed textural variation.

At the ridge- and dredge-scale, plagioclase shows a wide range in ΔAnV values. However, there is no inter-segment ΔAnV variation, and, as observed for many other parameters, ΔAnV does not vary systematically from west to east (Fig. 7.13). Within the WVZ, except for a few high ΔAnV values, the range in ΔAnV appears to become more restricted towards the boundary with the SMZ (Fig. 7.13a). Within the SMZ, ΔAnV values become more variable towards the east and extend to higher values (Fig. 7.13). Finally, plagioclase show the greatest range in ΔAnV at the start of the EVZ, become more restricted at the centre of the segment, and increase again at 85°E (Fig. 7.13). All three tectono-magmatic segments show patterns in ΔAnV that are similar to patterns defined by average plagioclase core compositions (Fig. 7.12a).

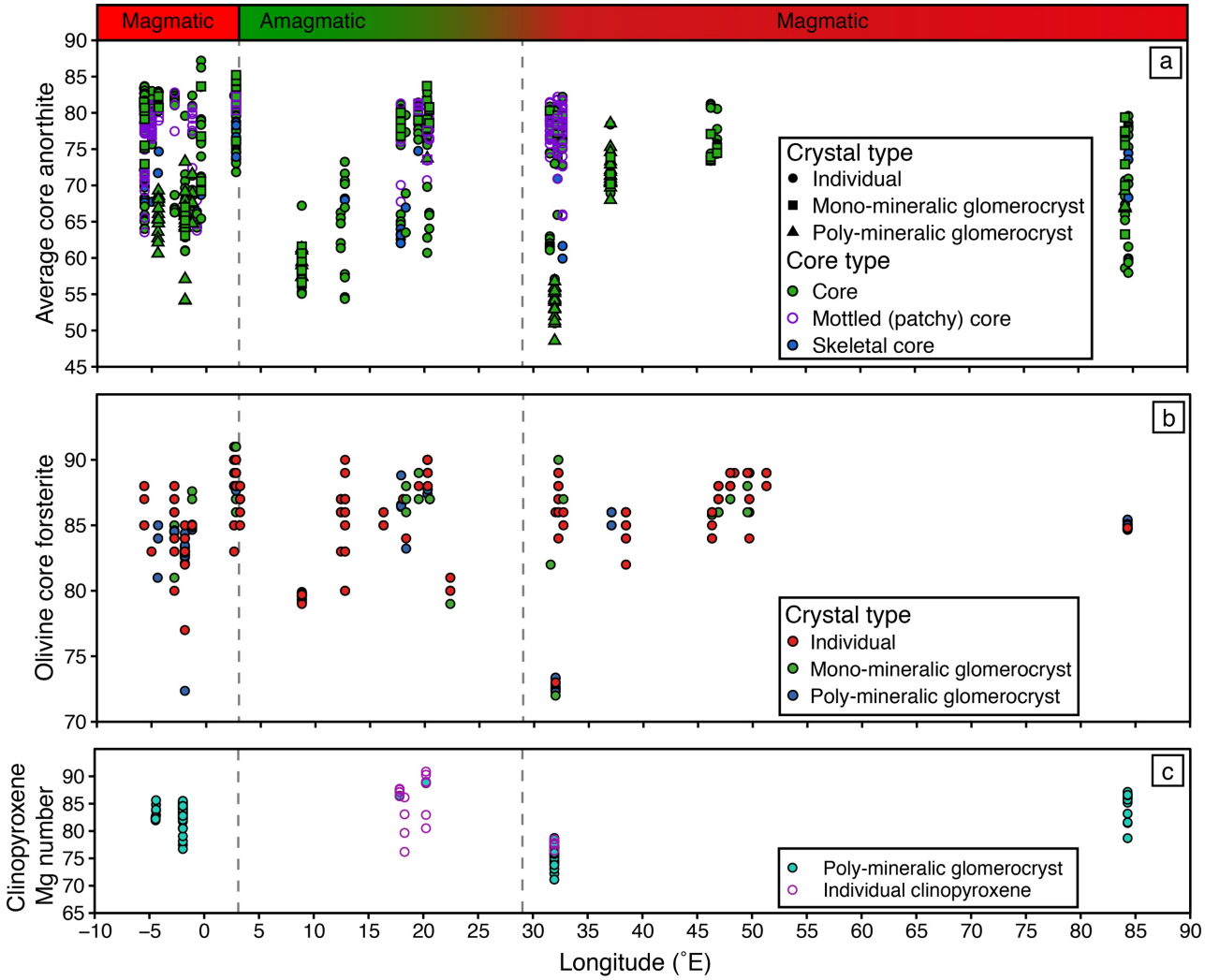

Fig. 7.12: Along-axis change in plagioclase (**a**), olivine (**b**) and clinopyroxene (**c**) mineral chemistry. **a** At the ridge-scale, only the maximum plagioclase core anorthite content decreases. Only within the SMZ do plagioclase core anorthite contents change systematically, becoming more primitive and variable towards the east. The most evolved samples are found at the start of the EVZ; within this segment plagioclase compositions become more primitive and restricted towards 50°E where olivine is the dominant phase (Fig.7.2), compositions then become more variable at the eastern end of the EVZ. **b** As with plagioclase, olivine compositions do not change systematically at the ridge-scale. The most primitive and evolved olivine is found at the end of the WVZ and start of the EVZ respectively. **c** The restricted occurrence of clinopyroxene makes it difficult to constrain any ridge- or segment-scale variations, however the most evolved clinopyroxene coincides with occurrences of the most evolved plagioclase and olivine.

Along-axis variations in plagioclase-melt equilibria are shown in Figure 7.14. Plagioclase-melt equilibria have been calculated in the same way as discussed in Chapter 5. Figure 7.14 shows that plagioclase-melt disequilibrium is present in samples from the full length of the ridge, and that the extent of disequilibrium does not change systematically along axis. Whilst some samples appear to be in equilibrium with their host melts (e.g., H-D21), both cores and rims can show extensive plagioclase-melt disequilibrium.

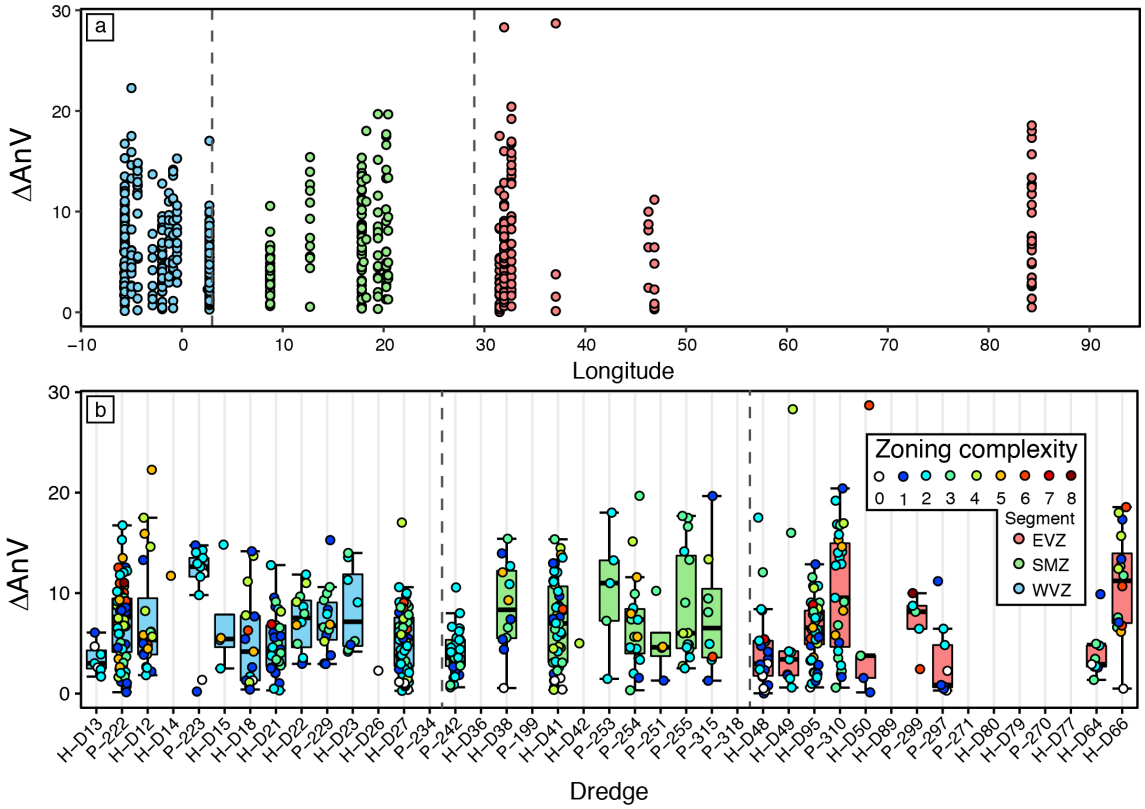

Fig. 7.13: Along-axis variations in ΔAnV for each plagioclase crystal plotted against longitude (**a**) and for each individual dredge arranged by longitude (**b**). There is no inter-segment, or segment-scale variation in ΔAnV. However, individual segments show systematic changes. Within the WVZ, ΔAnV values become more restricted towards the boundary with the SMZ, and ΔAnV can be seen to increase from west to east within the SMZ. The greatest range in ΔAnV occurs at the start of the EVZ and decreases towards ~50°E before increasing towards the end of the EVZ.

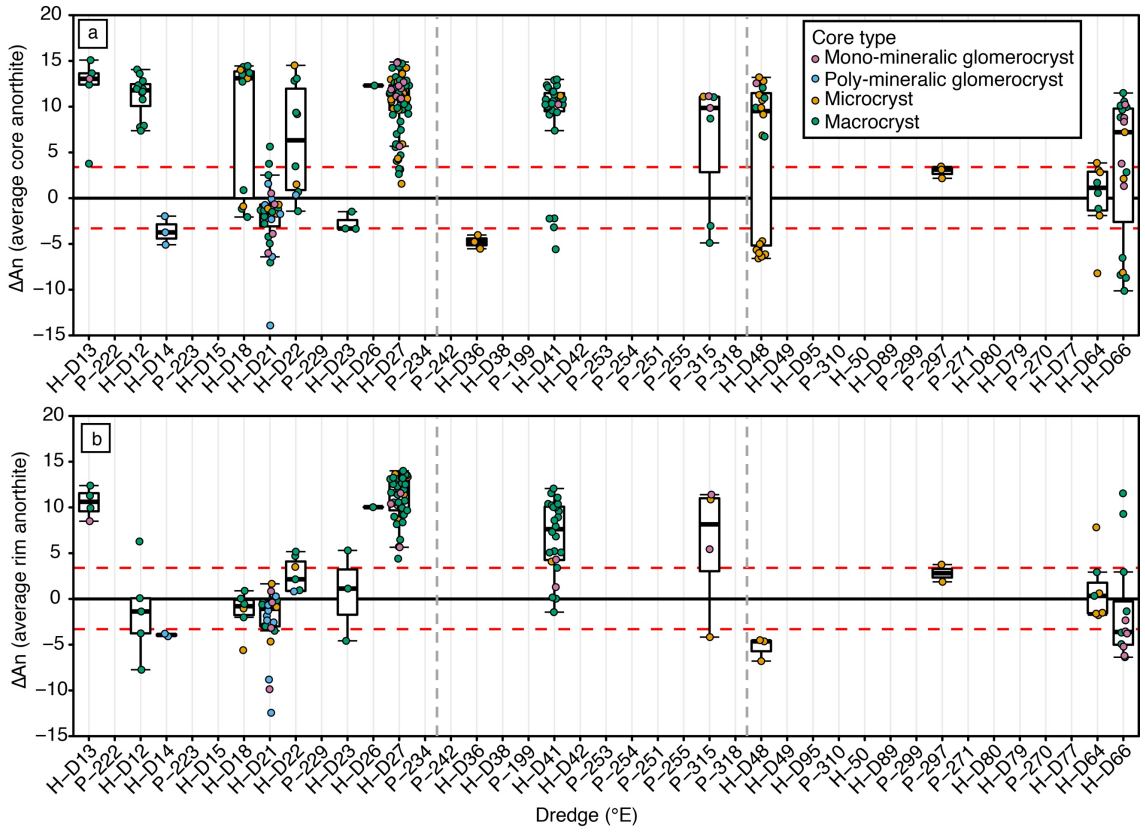

Fig. 7.14: Longitudinal variations in plagioclase-melt equilibrium for plagioclase cores and rims. Whilst some core and rims plot in equilibrium with melt compositions (within the red dashed lines), many are either too evolved or primitive to be in equilibrium with their host melts. Solid black horizontal lines represent equilibrium (ΔAn=0); dashed red lines represent ±5% error (Grove et al. 1992) on the average plagioclase anorthite content (An_{69}) calculated using equations (1) and (2) (see Chapter 5).

7.3.6.2 Olivine

Olivine core Fo contents show few systematic changes along the ridge. Whilst the variability of olivine compositions and median Fo contents increase from the WVZ to the EVZ (Table. 7.5), there is no systematic change in compositions moving along the ridge (Fig. 7.12b); minimum forsterite values do not change systematically. Within the WVZ olivine forsterite contents increase toward the SMZ (Fig. 7.12b), similar to glass Mg# (Fig. 7.5b); olivine at the eastern end of the WVZ is the most primitive found along the ridge, exceeding Fo_{90} (Fo_{83-91}). Olivine in the SMZ has the lowest compositional range (Fo_{79-90}; Table 7.6), however more locations in the SMZ have compositions closer to the upper limit of those in the WVZ (Fig. 7.12b). Compositions in the SMZ do not vary systematically along the segment. At the western end of the EVZ olivine compositions are highly variable (Fo_{72-90}) and become more restricted towards the east (Fig. 7.12b); this mirrors glass Mg# (Fig. 7.5b). At the eastern extent of the EVZ, olivine compositions are restricted ($Fo_{84.6-85.4}$). There is no systematic difference between the compositions of different crystal types (Fig. 7.12b). Olivine forsterite content of cores and rims correlate poorly with their host melt compositions (Fig. 7.15a); there is no systematic change in the degree of melt-olivine equilibrium along-axis (Fig. 7.15b). Olivine zonation, shown by ΔFo in Figure 7.16, is variable along axis. ΔFo ranges from +10.8 to -5.6 and shows no systematic variation along axis. Olivine from the SMZ and EVZ show the greatest magnitudes in zonation.

Table 7.7 Forsterite content of Gakkel Ridge basalt olivine crystal cargo

		Olivine forsterite content				
Segment	Number of olivine	Minimum	Median	Maximum	Range	Standard deviation
WVZ	151	72.36	85.02	91.00	18.64	2.68
SMZ	140	79.00	86.00	90.00	11.00	3.44
EVZ	248	72.00	87.00	90.00	18.00	3.72

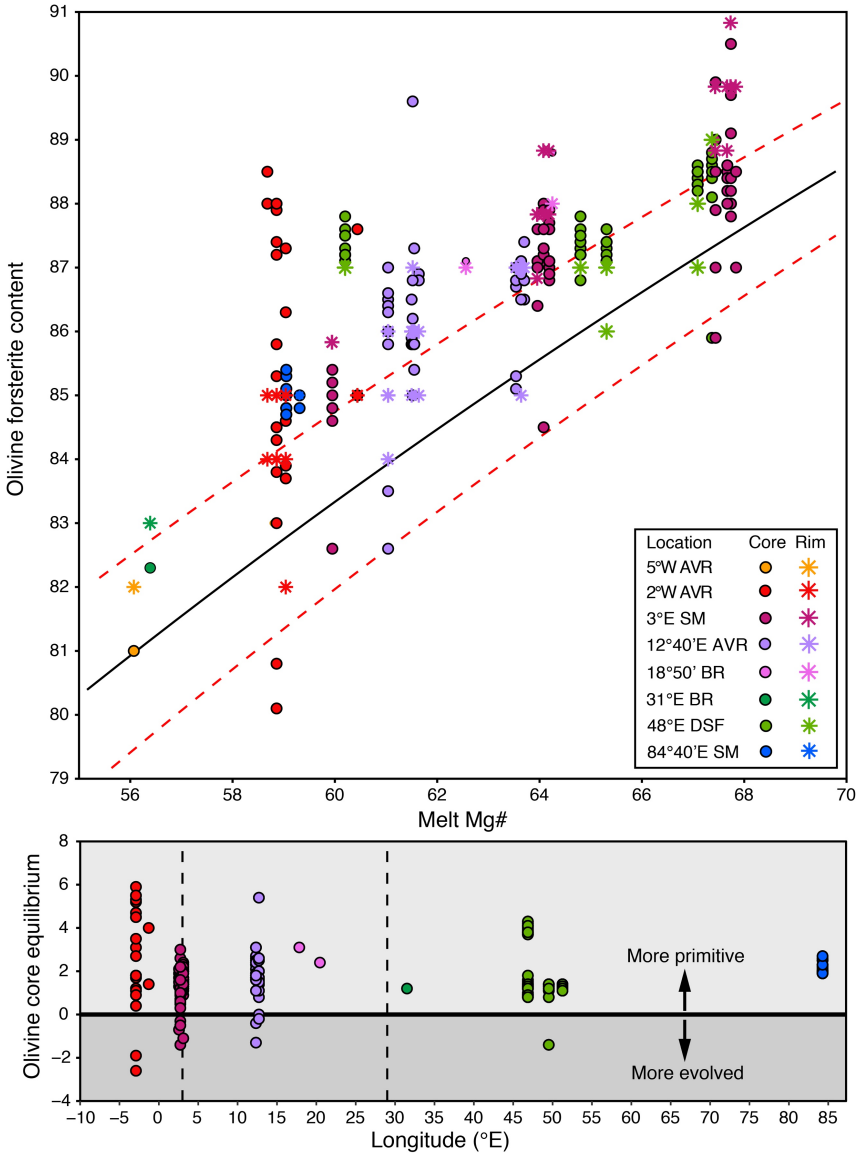

Fig. 7.15: a Rhodes diagram of olivine forsterite against host melt Mg#. Both olivine cores and rims tend to be in disequilibrium with their host melt. **b** Olivine-melt equilibrium plotted as a function of longitude along the ridge. There is no significant change in the amount or degrees of disequilibrium along-axis. Equilibrium calculated assuming Fe-Mg exchange coefficient of 0.30± 0.03 (Roeder and Emslie 1970).

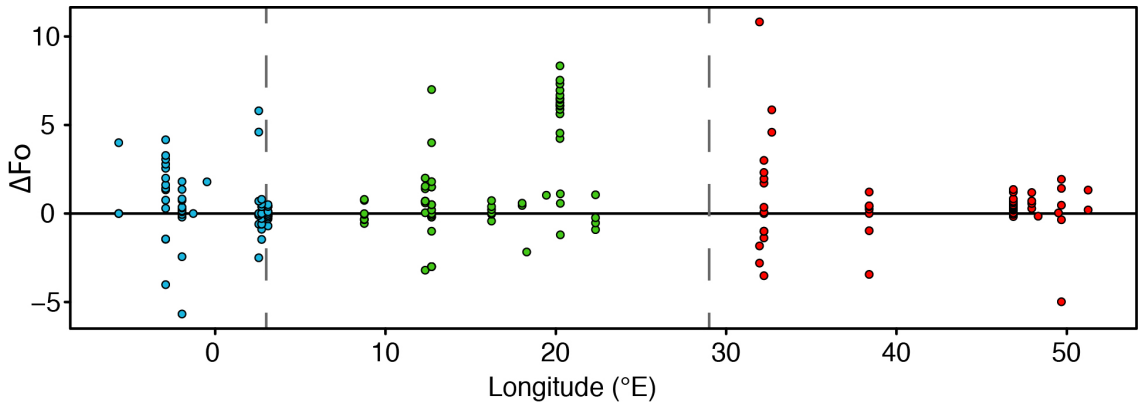

Fig. 7.16: Along-axis variation in olivine zonation (ΔFo = core - rim). Olivine in each segment show both normal and reverse zoning. The magnitude of zoning does not change systematically along axis or within individual segments. Point colours are as follows: blue, WVZ; green, SMZ; red, EVZ.

7.3.6.3 Clinopyroxene

Clinopyroxene compositions range from Mg# 71-91 and do not change systematically along the ridge (Fig. 7.12). The most evolved compositions coincide with the locations of the most evolved glass (Fig. 7.5), plagioclase and olivine compositions (Fig. 7.12). In comparison, the most primitive clinopyroxene compositions are found at ~20°E. The clinopyroxene is present as individual crystals or, more commonly, as components in poly-mineralic glomerocrysts. Locations along the ridge tend to be characterised by one of these types, with most individual clinopyroxene present at ~20°E. Whilst the compositions of plagioclase and olivine in poly-mineralic glomerocrysts with and without clinopyroxene show some overlap, mineral compositions in clinopyroxene-bearing glomerocrysts extend to more evolved compositions than non-clinopyroxene bearing glomerocrysts (Fig. 7.17a); lower Mg# clinopyroxene crystallised from more evolved, cooler melts (Fig. 7.17b).

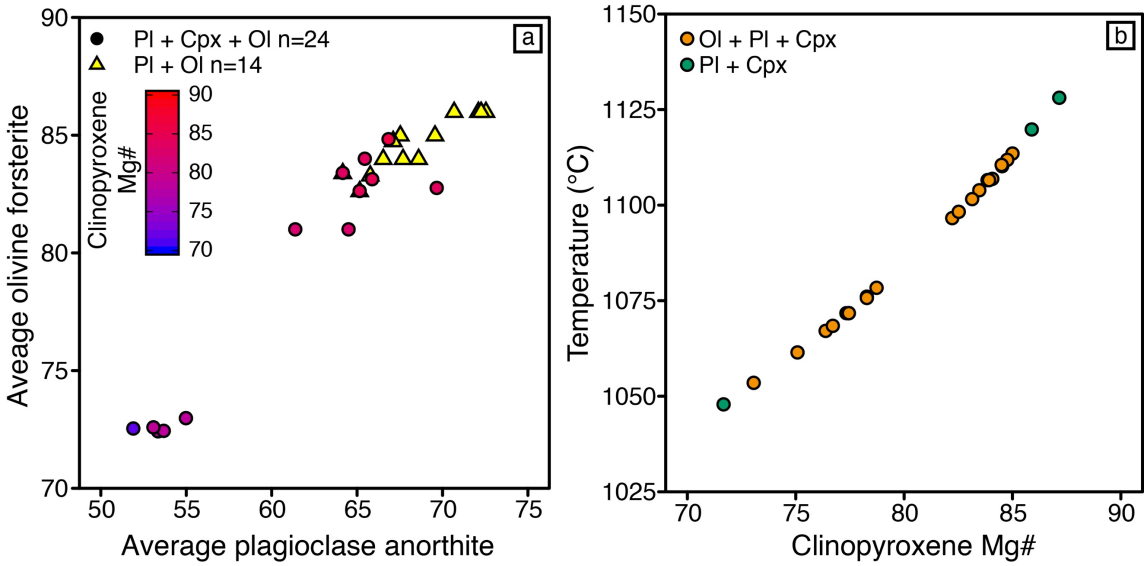

Fig. 7.17: a Composition of plagioclase and olivine in poly-mineralic glomerocrysts with and without clinopyroxene. Glomerocrysts with clinopyroxene in extend to more evolved compositions than those without. The values potted are averages of multiple analyses from a single glomerocrysts. **b** Temperature of melts in equilibrium with clinopyroxene. Assuming a clinopyroxene-melt Fe-Mg distribution coefficient of 0.23 ±0.2, the Mg# of melts in equilibrium with clinopyroxene were calculated. Using the MgO-Mg# relationship of Gakkel glasses, MgO content of melts in equilibrium with clinopyroxene were determined; melt temperatures were subsequently calculated using equations of Sugawara (2000).

7.3.7 Mineral chemistry correlations

When superimposed on a global compilation of plagioclase and clinopyroxene compositions, Gakkel Ridge samples show a positive correlation between plagioclase An content and clinopyroxene Mg# (Fig. 7.18). Here the slopes of the lines of constant $Na_{8.0}$ increase with decreasing partial melting (i.e., higher $Na_{8.0}$). In general, the $Na_{8.0}$ values that mineral compositions correspond to (2.5-3.9) agree with the range of $Na_{8.0}$

values of Gakkel Ridge glasses (2.7-3.8; Fig. 7.5); however a point plotting at 3.9 (Fig. 7.18) is above that seen in glasses. Olivine and plagioclase compositions show no systematic variations with either melt flux or glass Mg# (Fig. 7.19), and average plagioclase core compositions and median values do not change systematically with changing melt flux (Fig. 7.19a). Similarly, there is no relationship between average plagioclase core anorthite content and host glass Mg#; both primitive and evolved glasses contain plagioclase of similar anorthite content and there is no difference between different ridge segments (Fig. 7.19c). As with plagioclase anorthite content, olivine core forsterite shows no relationship with melt flux (Fig. 7.19b).

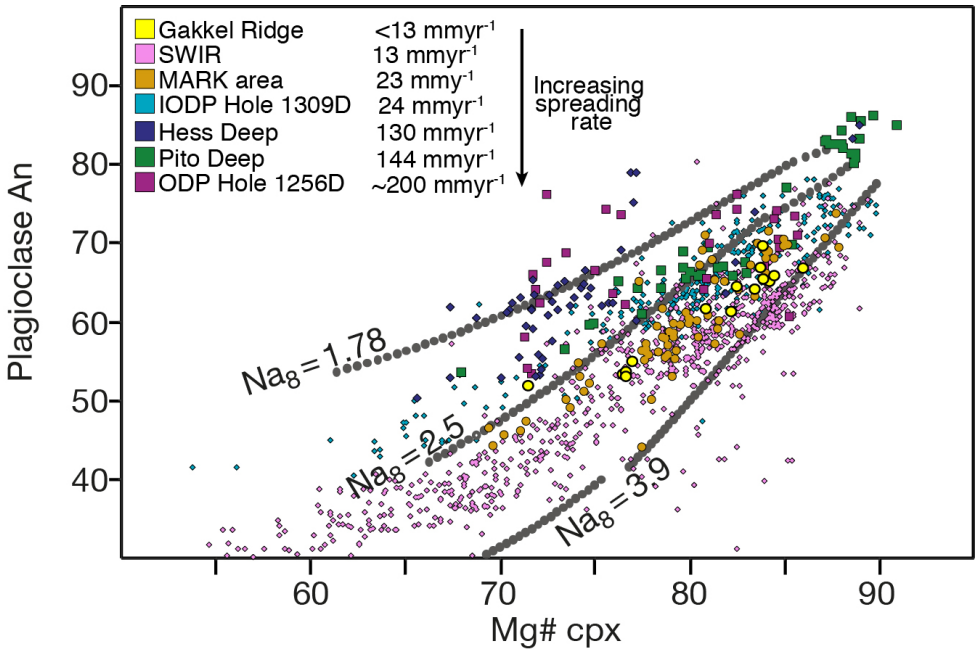

Fig. 7.18: Composition of plagioclase and clinopyroxene from the Gakkel Ridge superimposed on a global compilation of plagioclase and clinopyroxene compositions from oceanic gabbros. Each data point from the Gakkel Ridge represents the average core composition of plagioclase and clinopyroxene from individual glomerocrysts. Figure adapted from Coogan (2014). The extent of partial melting decreases with increasing $Na_{8.0}$.

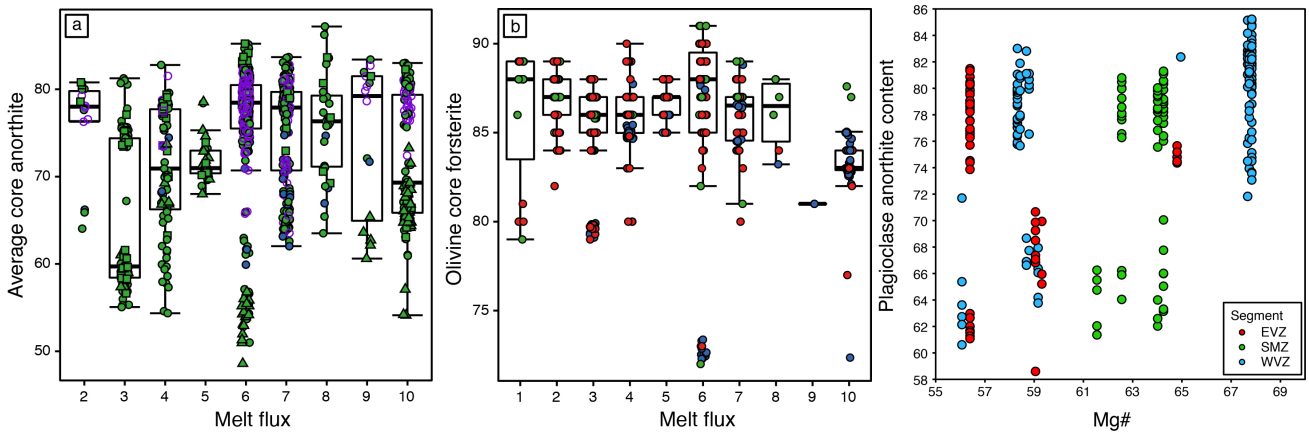

Fig. 7.19: Correlations between melt flux and plagioclase anorthite content (**a**) and olivine forsterite content (**b**); and plagioclase anorthite content and glass Mg# (**c**). There are no correlations between mineral chemistry and either melt flux of glass Mg#.

7.3.8 Plagioclase crystal cargo textural analysis

7.3.8.1 Zoning complexity

Zoning complexity values are highly variable both at the ridge scale (Fig. 77.20a) and within individual dredges (Fig. 7.20b) from within each of the tectono-magmatic segments. At the ridge-scale, the range in zoning complexity values does not change systematically (Fig. 7.20a) and there is no systematic inter-segment variation. Figure 7.20b highlights the lack of zoning complexity variation between and within each of the segments. Zoning complexity shows no correlation with melt flux (Fig. 7.21).

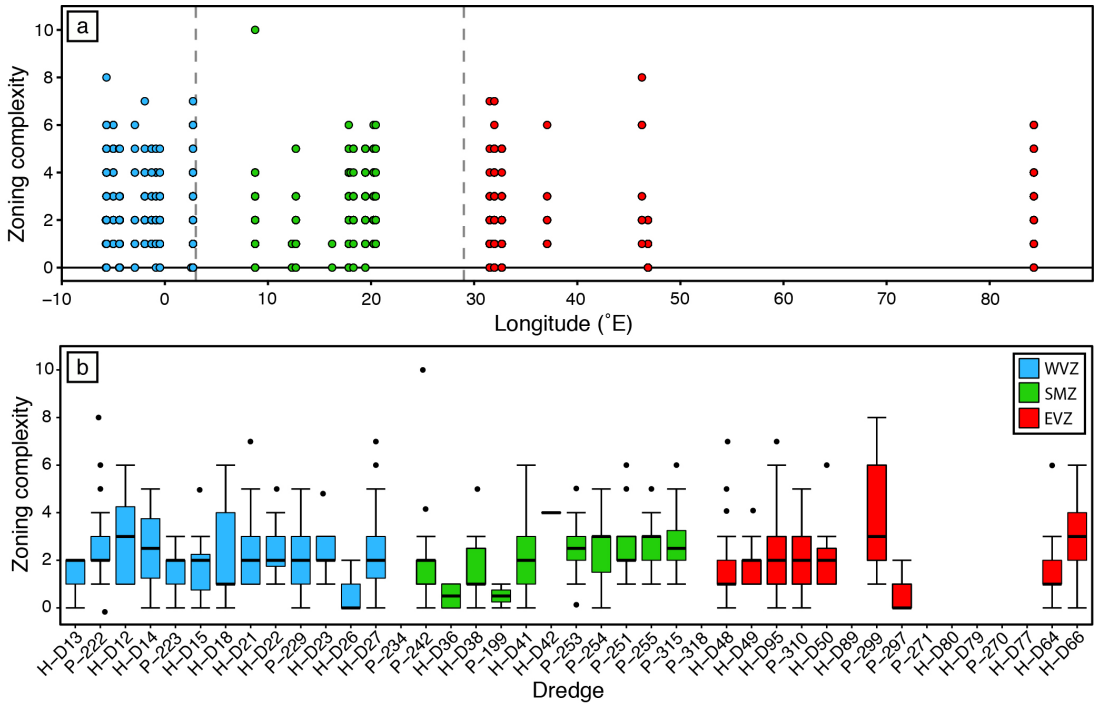

Fig. 7.20: Along-axis variations in plagioclase zoning complexity plotted against longitude (**a**) and for each individual dredge arranged by longitude (**b**). There are no systematic changes in zoning complexity from west to east along the ridge.

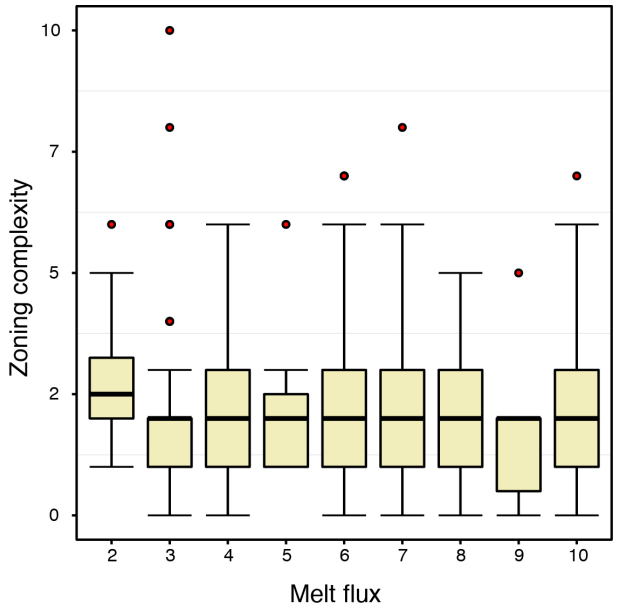

Fig. 7.21: Relationship between melt flux and zoning complexity for plagioclase crystal cargo. Red points are outliers. There is no systematic change in plagioclase zoning complexity with changing melt flux.

7.3.8.2 Resorption

Resorption characteristics (i.e., location, magnitude and number of stages) show little variation between and within the three tectono-magmatic segments (Table 7.8). Additionally, there is no systematic variation in the number of resorption stages recorded by individual plagioclase crystals along the axis (Fig. 7.22a). Resorption location shows the most intra-segment scale variation with the percentage of plagioclase with no resorption being highest in the WVZ and EVZ (Table 7.8a). The WVZ shows the highest percentage of plagioclase with both internal and external resorption, while plagioclase from the SMZ exhibits predominantly internal resorption. Plagioclase from the EVZ has almost equal proportions of internal and external resorption. Plagioclase from the WVZ also show lower average resorption magnitude and lower maximum number of resorption events (Table 7.8b,c). Whilst both reverse and normal zoning follow internal resorption events, reverse zoning is the most common type in all segments; there is no systematic variation in zoning type along the axis (Fig. 7.22c). Both resorption magnitude and number of resorption stages show no correlation with melt flux; ranges and median values remain relatively uniform as melt flux increases (Fig. 7.23). Resorbed and tabular crystal habits both record higher magnitude resorption events (Fig. 7.23a) and evidence of more resorption events (Fig. 7.23b) as shown and discussed previously in Chapter 5.

Table 7.8 Plagioclase resorption statistics

a	**Resorption location**				
Segment	Internal (%)*	External (%)*	Both (%)	No resorption (%)	Number of crystals
WVZ	9	26	48	17	413
SMZ	53	23	11	13	385
EVZ	32	29	16	23	340

b	**Resorption Magnitude**				
Segment	Minimum	Median	Maximum	Range	Standard deviation
WVZ	0	3	5	6	1
SMZ	0	3	5	6	1
EVZ	0	2	5	6	1

c	**Resorption stages**				
Segment	Minimum	Median	Maximum	Range	Standard deviation
WVZ	0	1	4	5	1
SMZ	0	1	5	6	1
EVZ	0	1	5	6	1

*** Plagioclase that shows evidence of only internal or external resorption**

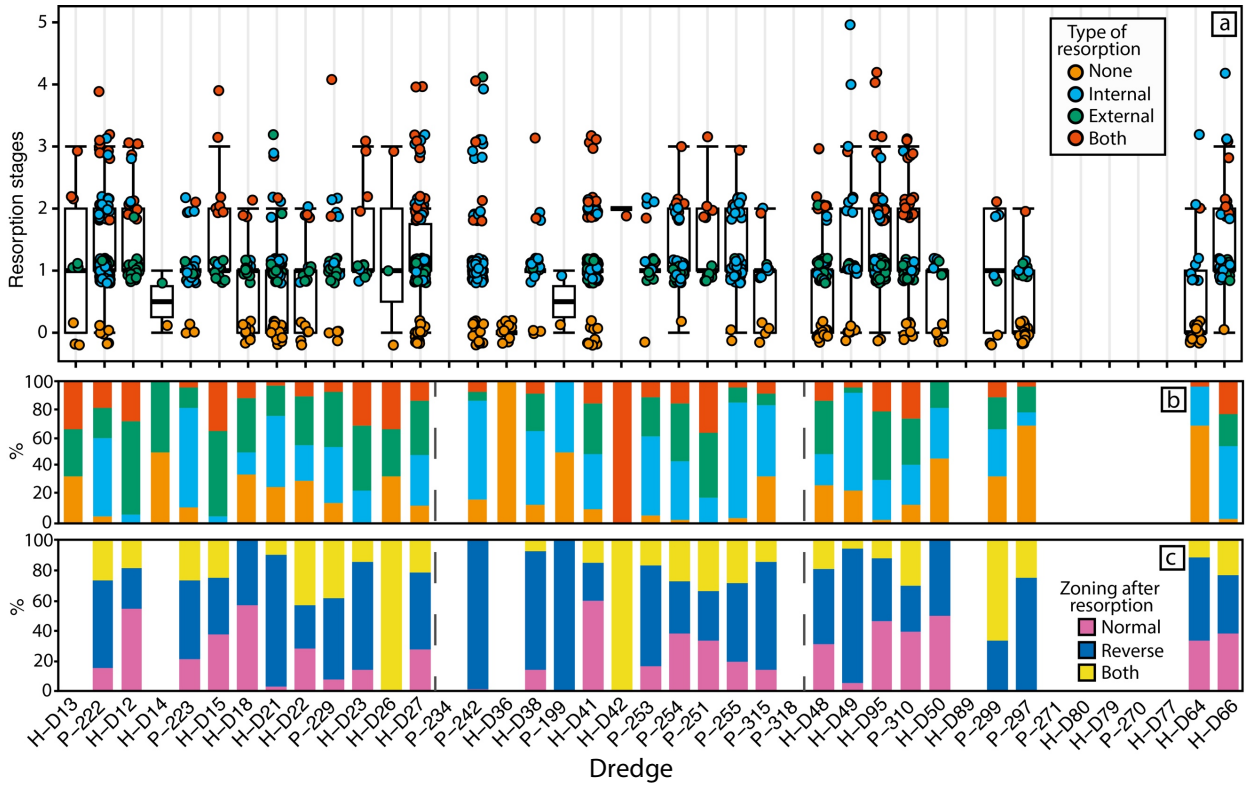

Fig. 7.22: Discrete plots of the number of resorption stages recorded in individual plagioclase from each dredge (**a**) and the proportions of plagioclase showing different resorption types (i.e., internal or external) (**b**) and zoning following the resorption interface (**c**). There are no systematic changes in the number of resorption stages or characteristics of the resorption events at either the ridge- or segment-scale. Where boxplots are not visible in **a**, the boxplots are smaller than the points shown. Points do not plot at integer values because they have been plotted to cluster around the integer within a given circumference; this allows the distribution of the type of resorption to be illustrated.

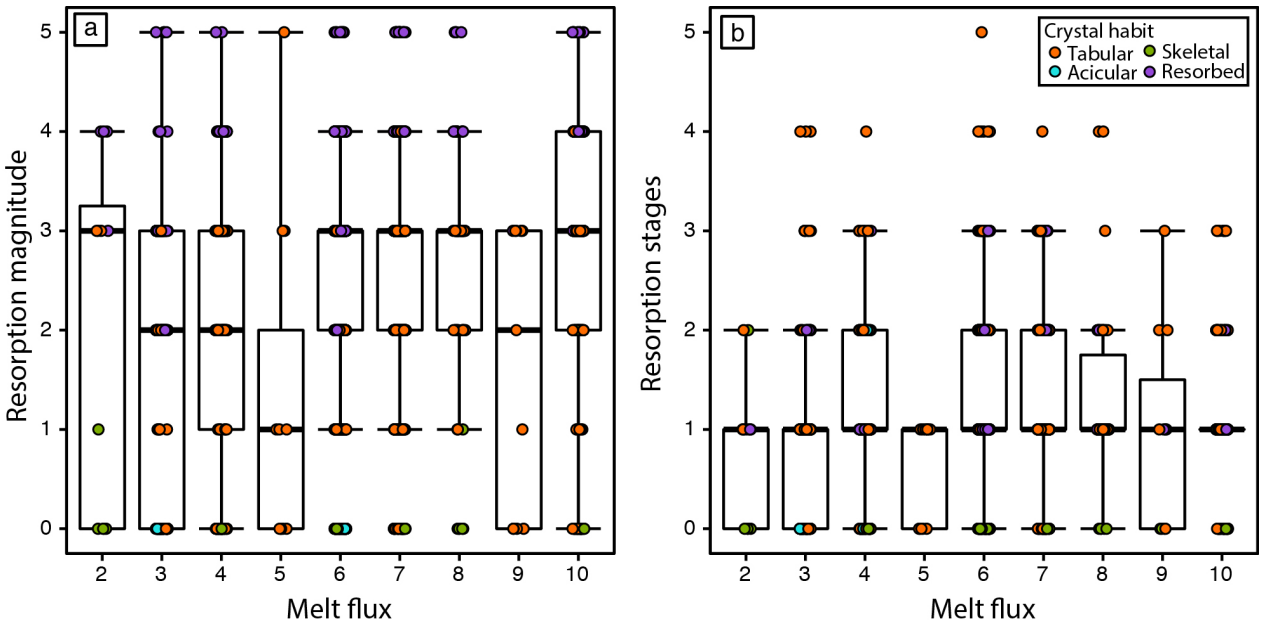

Fig. 7.23: Relationship between melt flux and both resorption magnitude (**a**) and number of resorption stages (**b**). **a** There is no correlation between melt flux and resorption magnitude. Both the range of values and median values remain relatively stable with increasing melt flux. Resorbed and tabular crystal habits have higher resorption magnitudes than acicular and skeletal habits. **b** The number of resorption stages recorded by plagioclase does not change systematically with melt flux. Skeletal and acicular habits recorded fewer stages of resorption then resorbed and tabular crystals.

7.3.9 Melt inclusion crystallisation pressures and geochemistry

7.3.9.1 Melt inclusion crystallisation pressures

Using new plagioclase- and olivine hosted melt inclusion data in combination with existing olivine-hosted melt inclusions data (Shaw et al. 2010; Wanless et al. 2014a), crystallisation depths within the Gakkel Ridge plumbing system are shown to range from the seafloor to 16.4 km below (Chapter 6; Fig. 7.24). The dataset as a whole shows little systematic change along axis. Olivine-hosted melt inclusions record restricted, relatively shallow crystallisation depths ≤10.6 km below the seafloor regardless of the location along the ridge, whilst plagioclase-hosted melt inclusions record depths ≤16.4 km. Whilst there is no systematic trend along axis, crystallisation depths recorded by plagioclase-hosted melt inclusions are shallower at the end of the WVZ compared to the SMZ and EVZ (Fig. 7.24). Individual dredges record a wide range in melt inclusion crystallisation pressures (Fig. 7.25).

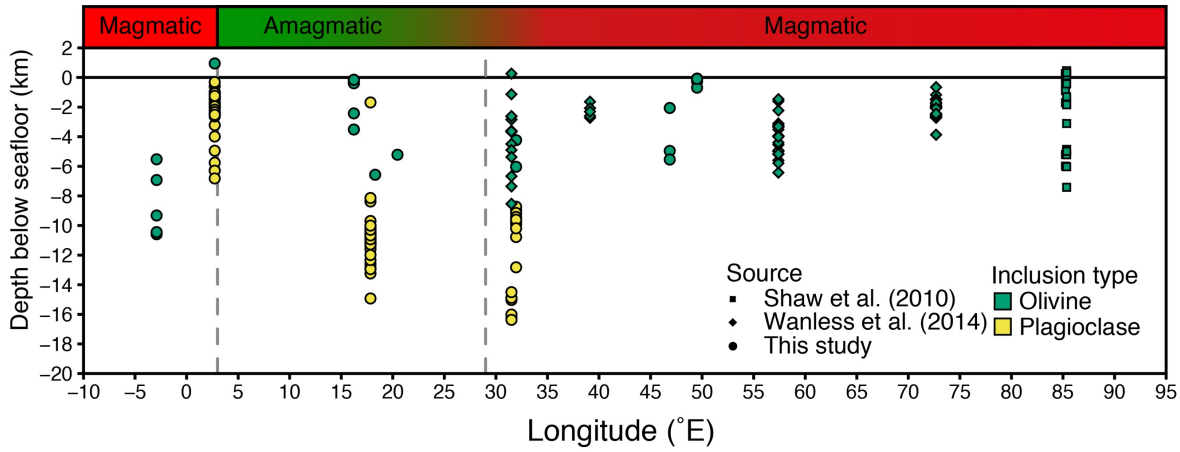

Fig. 7.24: Along axis variation in melt-inclusion crystallisation pressures. Crystallisation depths do not show any systematic variations at the scale of the entire ridge. Depths of crystallisation in olivine-hosted melt inclusions are all <10.6 km, whilst those in plagioclase extend up to 16.4 km. Considering plagioclase-hosted melt inclusions alone, crystallisation depths in the WVZ are shallower than those in the SMZ and EVZ.

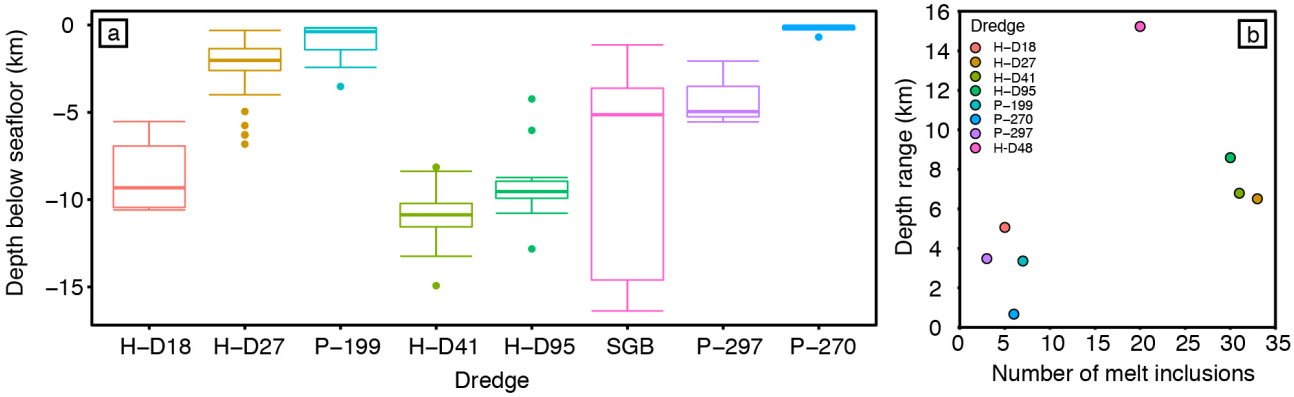

Fig. 7.25: **a** Range of crystallisation pressures recorded in individual dredges. Crystallisation pressures are from both olivine- and plagioclase-hosted melt inclusions. Melt inclusions in all dredges, other than P-270, record crystallisation occurring over several kilometres. **b** There is no relationship between the range of crystallisation pressures recorded in each dredge and the number of melt inclusions analysed.

7.3.9.2 Melt inclusion geochemistry

Variations in Mg# with depth can be constrained by melt inclusion compositions from three on-axis locations along the Gakkel Ridge; these locations include samples from 3°E (WVZ), 18°50'E (SMZ) and 31°E (EVZ). Whilst both olivine- and plagioclase-hosted melt inclusions are shown, it should be noted that there may be uncertainties in the Mg# of PEC-corrected olivine-hosted melt inclusions.

Despite recording different crystallisation depths, melt inclusions from each location show a similar range in Mg# (3°E, ~64-70; 18°50'E, 65-72; and 31°E, 66-73) and inter-sample variation (Fig. 7.26). At 3°E Seamounts melt inclusion Mg# ranges from ~64-70 (H-D27). Whilst Mg# changes little over 4 km between 7 and 3 km below the seafloor, at ~1-3km both olivine- and plagioclase-hosted melt inclusion Mg# become more evolved (Fig. 7.26a). Excluding two plagioclase crystals at depth with more evolved host compositions, in general host plagioclase compositions follow the same pattern defined by the melt inclusion Mg# (Fig. 7.27a). Similarly, plagioclase-hosted melt inclusions in sample H-D41 from 18°50'E Basement Ridge become more evolved with decreasing depth: from ~13-8 km Mg# decreases from ~72 to 65 (Fig. 7.26b) and host plagioclase anorthite contents become more variable with reduced depth (Fig. 7.27b). The most notable intra-sample variation is shown by H-D48 where plagioclase- and olivine-hosted melt inclusions record a change in Mg# from ~66-73 over a depth range of ~16 km (Fig. 7.26c). There is no clear change in plagioclase host compositions with depth at this location (Fig. 7.27c).

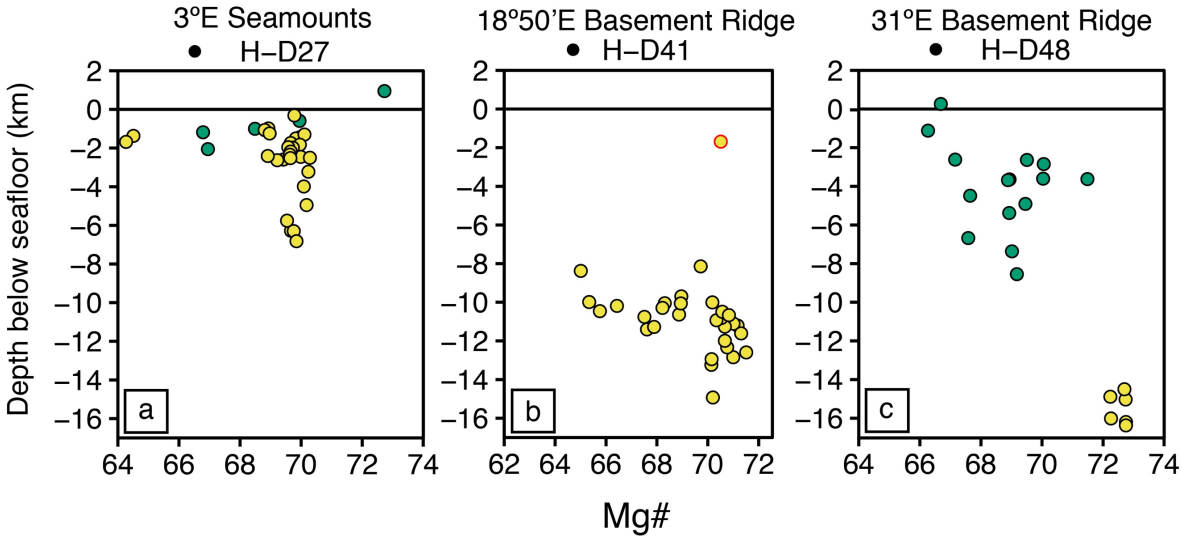

Fig. 7.26: Variations in olivine- and plagioclase- hosted melt inclusion Mg# with depth below the seafloor at 3°E Seamounts (**a**), 18°50'E Basement Ridge (**b**) and 31°E Basement Ridge (**c**). Dredge numbers are shown below. Yellow and green points are plagioclase- and olivine-hosted melt inclusions respectively. Olivine-hosted melt inclusions in **c** are from Wanless et al. (2014a). The red outlined plagioclase-hosted melt inclusion in **b** contains a bubble.

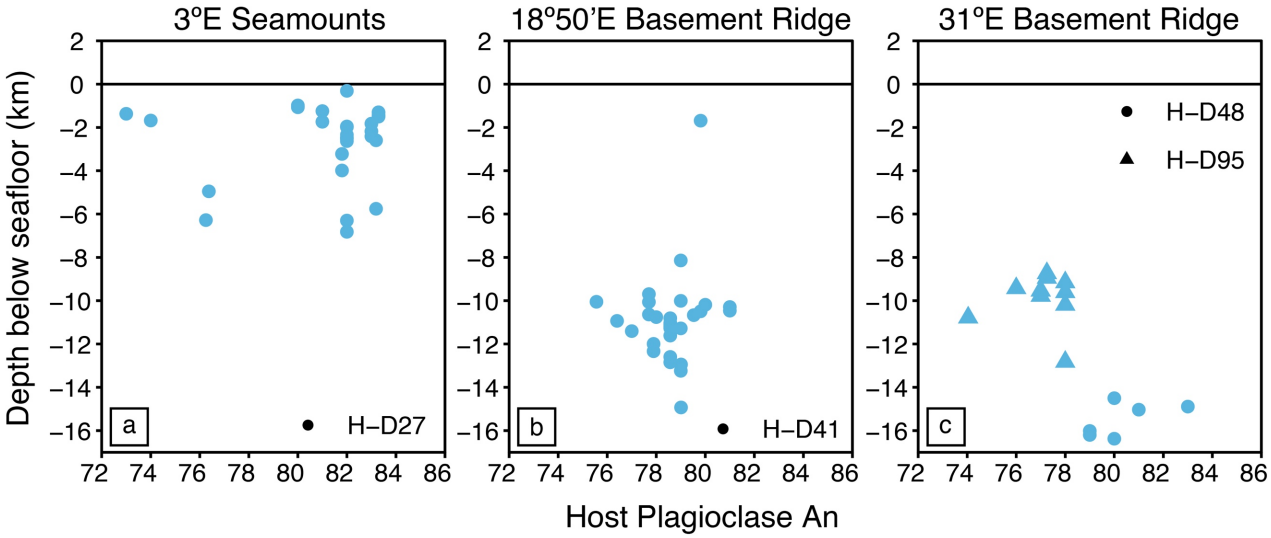

Fig. 7.27: Variations in plagioclase-hosted melt inclusion host anorthite compositions with depth at 3°E Seamounts (**a**), 18°50'E Basement Ridge (**b**), 31°E Basement Ridge**.**

7.4 Discussion

Above, glass chemistry, mineral geochemistry and textures and melt inclusion crystallisation pressures have been shown to be variable at the ridge-scale. In the following discussion, these variations will be used to constrain the nature of the Gakkel ridge plumbing system in terms of its physical state (i.e., crystal vs. melt content), stage of maturity, vertical extent as well as how and if it changes along-axis. Following this, controls on the nature of the magma plumbing system will be explored. Finally, modal data and glass and mineral chemistry from the Gakkel Ridge will be compared to the same data from the fast-spreading East Pacific Rise and slow-spreading Mid-Atlantic Ridge to explore spreading rate controls on the nature of mid-ocean ridge plumbing systems.

7.4.1 Physical nature of the Gakkel Ridge magma plumbing system

7.4.1.1 Melt vs. crystal mush

Over the last ~50 years, our understanding of mid-ocean ridge plumbing systems has shifted from the view that mid-ocean ridge magma chambers are large melt-filled bodies (e.g., Cann 1974), to the view that the plumbing system comprises regions of both mush and melt (e.g., Sinton and Detrick 1992; Singh et al. 1998; Sinha et al. 1998; Carbotte et al. 2013; Xu et al. 2014; Marjanović et al. 2015; Lissenberg et al. 2019).

Whilst it was argued in Chapter 5 that samples with high crystal content, mixed chemical and textural populations and glomerocrysts are evidence for mush disaggregation, and

despite the general shift towards a mush-dominated view of magma plumbing systems at mid-ocean ridges, a recent paper (Maclennan 2019) uses several lines of petrological evidence to argue that vertically extensive pervasive mush systems are not present beneath Iceland. The two main pieces of petrological evidence used to argue against their presence are: (1) a well-defined relationship between crystal cargo and host melts (e.g., melt inclusion trace elements are similar to trace elements of their host liquid); and (2) crystal cargo from separate eruptions show little compositional overlap, suggesting eruptions are sourced from distinct regions. Whilst these lines of evidence may support the absence of pervasive mush zones in Iceland, they do not hold at the Gakkel Ridge. First, extensive plagioclase- and olivine-melt disequilibrium at multiple locations along the Gakkel Ridge (Fig. 7.14 and 15) argues that the crystal cargo did not grow from the melts in which they now reside. Second, whilst there are no temporal constraints on eruptions, samples collected from adjacent locations commonly exhibit overlap in both plagioclase compositions and zoning characteristics (i.e., zoning complexity and resorption), suggesting that eruptions are not sampling distinct separated regions of the plumbing system but are instead sampling a range of storage regions. Therefore, the petrological evidence used by Maclennan (2019) to rule out the presence of pervasive mush zones in Iceland is not observed at the Gakkel Ridge. Furthermore, the range in melt inclusion crystallisation pressures both within individual dredges (Fig. 7.25) and crystals (e.g., plagioclase in Fig. 6.5f records crystallisation over ~3 km) is inconsistent with the crystal cargo originating from restricted regions, instead it indicates reservoirs at the Gakkel Ridge are vertically extensive. The complexity of host crystals also attests to the occurrence of complex crystallisation histories within these systems. Moreover, the presence of mush zones along the full length of the Gakkel Ridge, and their subsequent disaggregation, is supported by the presence of samples from the full length of the ridge that have high crystal content (≤50%), mixed chemical and textural populations and contain glomerocrysts. The high degree of textural complexity (e.g., resorption characteristics and zoning complexity) also argues against crystallisation within a single reservoir. Taken together, petrological evidence supports the presence of mush zones at the Gakkel Ridge with crystal cargo within individual samples having been scavenged by ascending melts from distinct regions of the magma plumbing system (e.g., petrological cannibalism (Cashman and Blundy 2013)).

Whilst the presence of mush zones along much of the Gakkel Ridge is consistent with the idea that magma plumbing systems are increasingly mush dominated at slower spreading rates (e.g., Sinton and Detrick 1992), there are regions of the Gakkel Ridge that are distinctly different. One such region is between 45-50°E, which is characterised

by a low amplitude magnetic anomaly (Fig. 7.1) and small seamounts; samples here have low crystal contents (Fig. 7.2) and contain predominantly olivine that is relatively primitive (Fo 84-89; Fig. 7.12b). Glass compositions are also primitive, with low SiO_2 and high Mg# (60-68; median 65), temperatures (1182-1221°C) and $Na_{8.0}$ (3.2-3.8). Taken together these features indicate these are low degree partial melts that have experienced minimal fractionation. Hence, this part of the Gakkel Ridge appears to be underlain by a melt-dominated plumbing system.

According to Rubin and Sinton (2007), less fractionated melts are erupted at slower-spreading ridges because they originate from deep thermally insulated reservoirs that preclude extensive fractionation. Alternatively, the eruption of primitive melt compositions may simply reflect short residence times in immature melt-dominated plumbing systems. The idea that melts reside within the plumbing system for short times is consistent with observations made during the RAMESSES experiments at 57°45'N on the Mid-Atlantic Ridge (Macgregor et al. 1998; Sinha et al. 1998) where a magma chamber comprising a melt lens and underlying mush zone containing 20% melt was identified. Melt residing within this magma body represents 20 kyr worth of crustal accretion; if it is not replenished, it would freeze within 1.5 kyr (Macgregor et al. 1998; Sinha et al. 1998). Therefore, because melt supply is episodic, melts erupted from this magma body would have resided for short periods in the system; such episodic melt supply is likely in the region of 45-50°E of the Gakkel Ridge, with short residence times being necessary to erupt primitive melt compositions. Some magmatic systems such as those at 15-25°E (18°50' Basement Ridge) and 3°E (3°E seamounts), erupt both aphyric and phyric samples thus indicating that regions of mush and melt co-exist. As discussed by Sinha et al. (1998) in relation to the Reykjanes Ridge, this may be the result of non-uniform crystallisation and the formation of pockets of melt in the plumbing system. Alternatively, melt-rich domains can result from replenishment of crystal mush or the self-organisation of crystal mush into crystal-rich and melt-rich portions (Solano et al., 2012, 2014; Lissenberg et al., 2019; Jackson et al., 2018). Subsequent eruptions from different regions of the magma plumbing system will include both aphyric and phyric basalts.

7.4.1.2 Mush zone melt content

Mush zones at fast- and slow-spreading ridges have been estimated, using geophysical techniques, to contain several to tens of percent melt (Sinha et al. 1998; Crawford et al. 1999; Crawford et al. 2002; Dunn et al. 2005). Despite there being no geophysical constraints on the magma plumbing system of the Gakkel Ridge, glomerocrysts with open crystal structures or melt films can provide constraints on the amount of melt

present in the environment they were derived from. Melt trapped within glomerocrysts can be preserved as a matrix phase (i.e., solidified basalt) and thus used as a proxy for the amount of melt present (Holness et al. 2007, 2019). To assess the amount of melt present within mush zones, a small subset (n = 17) of glomerocrysts with open crystal structures (Fig. 7.28a-e) or thin melt films (Fig. 7.28f) from along the full length of the Gakkel Ridge have been analysed; analysed glomerocrysts are characterised by olivine and plagioclase ±clinopyroxene. Melt content was determined by calculating the total number of pixels in both the glomerocrysts as a whole (framework + trapped melt) and in the trapped melt. Using this approach, the melt content of the glomerocrysts can be seen to range from 0.26-13.51% (median 4.77%). This demonstrates that glomerocrysts originate from environments within the magma plumbing system characterised by relatively high crystallinity and variable melt content. For comparison, intergranular glass within a cumulate xenolith from the EPR suggests that ~17% melt was present within the region the xenolith was sourced from (Ridley et al. 2006).

7.4.1.3 Mush zone maturity: hot vs. cold mush zones

Mush zone maturity, the extent of crystallisation, can be assessed from the mineralogy of glomerocrysts and compositions of their individual components. The mineralogy of poly-mineralic glomerocrysts is dominated by plagioclase + olivine ±clinopyroxene (Fig. 7.4). At mid-ocean ridges, the first mush networks formed are dominated by plagioclase and olivine and clinopyroxene frequently crystallises as a late interstitial phase within these early frameworks (Lissenberg et al. 2019). The implication is that glomerocrysts containing clinopyroxene likely represent fragments of more mature mush zones than glomerocrysts characterised by plagioclase ±olivine only. Indeed, Figure 7.17 shows that clinopyroxene-bearing glomerocrysts extend to more evolved mineral compositions than glomerocrysts without. This suggests that these glomerocrysts have originated from evolved “cold” mush zones, consistent with Figure 7.17b. Crystallisation of clinopyroxene as an interstitial phase will result in highly sutured mush zones that may be harder to disaggregate than “hotter” mush zones characterised by plagioclase ±olivine. Difficulty in disrupting these “cold” mush zones may in part explain the paucity of clinopyroxene as a phase in the Gakkel Ridge basalts. In contrast, “hot” and relatively poorly sutured plagioclase ± olivine mush zones may be easier to disaggregate, thus explaining the abundance of plagioclase and olivine relative to clinopyroxene (Fig. 7.2).

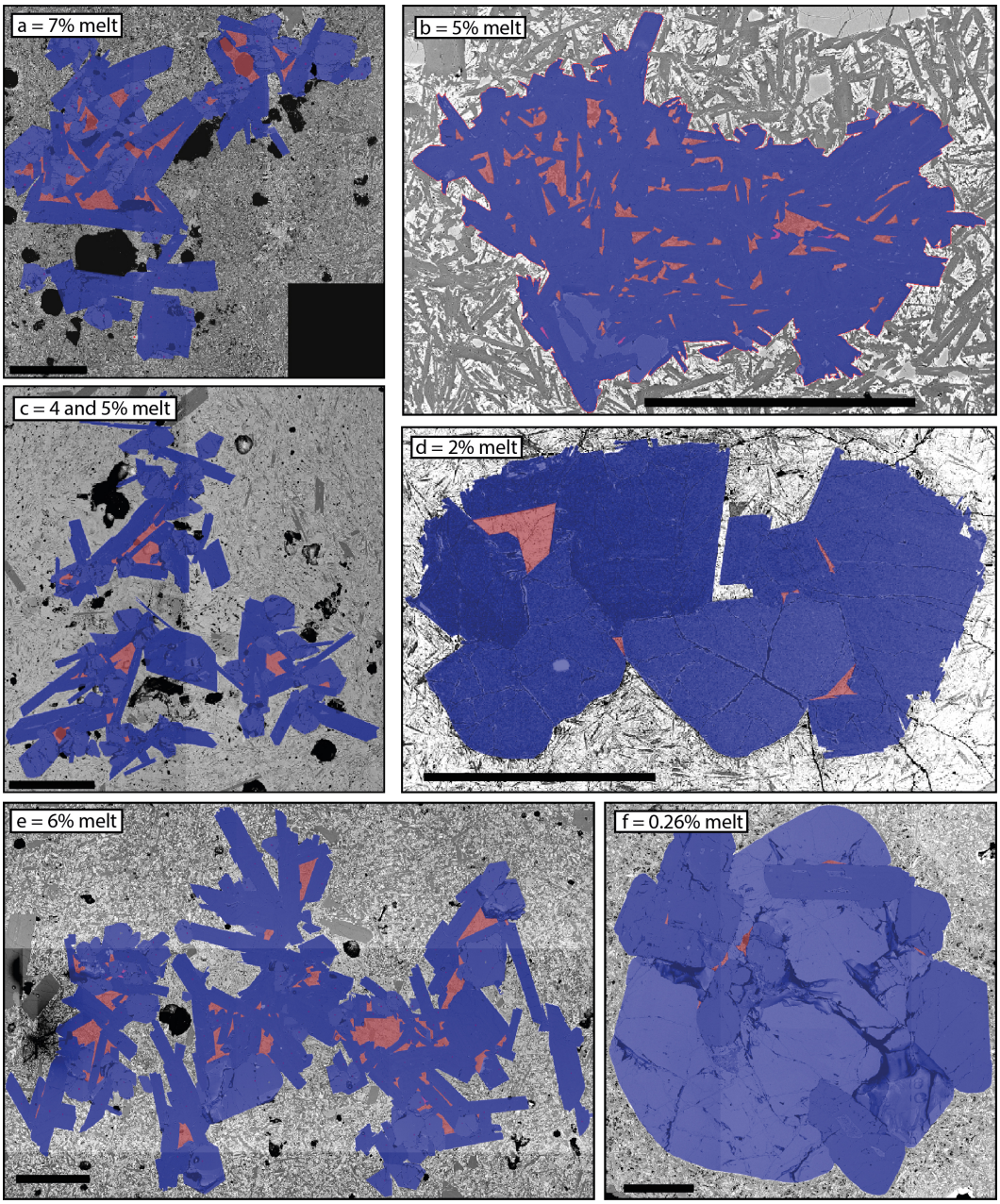

Fig. 7.28: Glomerocryst melt content. Glomerocrysts may contain melt preserved as a trapped matrix phase either within complex interstitial spaces (**a**-**e**) or as thin melt films between glomerocryst components (**f**). The blue and orange in each panel represent the crystal framework and trapped melt respectively. Scale bars are 1 cm.

7.4.1.4 Variations in magma plumbing system maturity

Fast-spreading ridges are often thought of as mature magmatic systems where high melt supply results in homogenised steady-state systems that erupt uniformly more fractionated and cooler lavas; in comparison, slow-spreading mid-ocean ridges erupt lavas with higher temperatures and glass Mg# (Rubin and Sinton 2007). Nonetheless there are regions of faster spreading ridges that exhibit extreme variations in plumbing system maturity manifested by spatial variations in lava composition. One example is the

Galapagos spreading centre (Christie and Sinton, 1981) where the Galapagos Ridge propagates westwards at 65 $mmyr^{-1}$ (Francheteau et al. 1990) into ± 1.3 Myr old oceanic crust formed at the East Pacific Rise (Rioux et al. 2012). Here, primitive, unfractionated basalts erupted close to the propagating rift tip are followed first by a bimodal distribution of basalt compositions (primitive and evolved FeTi basalts) and then by basalts with the greatest range in degree of fractionation. Further behind the ridge tip the compositional variability is reduced and becomes more homogeneous. Christie and Sinton (1981) attribute these spatial changes to the evolutionary stage of the magmatic plumbing system which is related to magma supply. Where the Galapagos ridge is propagating through cold crust formed at the East Pacific Rise, magma supply is low, and lithosphere is thick, hence erupted lavas undergo little differentiation. As magma supply increases behind the rift tip, magma plumbing systems form small, interconnected magma bodies within which variable degrees of fractionation occur. Only when magma supply is high does an interconnected, steady-state, chemically buffered magma plumbing system form. Here, the plumbing system is clearly related to changes in melt supply that can be linked to the extent of partial melting and lithospheric thickness. Therefore, glass geochemistry (e.g., temperature, Mg# and $Na_{8.0}$) in combination with bathymetric and geophysical observations can be used to assess the maturity of Gakkel Ridge magma plumbing systems. Here, both the composition of erupted lavas and the degree of chemical variability is used to infer the evolutionary stage of the magma plumbing system and its maturity/level of development.

The presence of a relatively mature plumbing system that is both thermally and chemically buffered is indicated by glass Mg# (59.74±2.27) and temperatures (1178±9.31°C) that show little variation and appear relatively homogeneous along much of the WVZ (excluding 3°E Seamounts). Interestingly, the median glass Mg# of the WVZ is remarkably similar to the East Pacific Rise, which is characterised by higher melt supply (Fig. 7.5b). Mineral compositions also show little variation along this stretch of the WVZ (Fig. 7.12a), which is characterised by a continuous high amplitude magnetic anomaly, significant volcanic relief (i.e., axial volcanic ridges) (e.g., Fig. 7.1) and relatively thick crust (~6.6 km; Schmid-Aursch and Jokat 2016). All features argue for the presence of robust magmatism in this region. The plumbing system along this section of the ridge can therefore be thought of as relatively mature.

In contrast, samples from ~3°E at the eastern extent of the WVZ exhibit features that argue for the presence of an immature magma plumbing system. Samples here are relatively primitive (Mg# 62.77±3.71) and hot (1200±11.42°C) and have been dredged

from a seamount region situated on the outer margin of the WVZ magnetic anomaly; both plagioclase and olivine have primitive compositions (Fig. 7.12). The transition from a mature to immature plumbing system along the WVZ can be attributed to the increased proximity, moving eastwards, to the peridotite-dominated SMZ where colder thicker lithosphere likely reduces the amount of partial melting occurring in the mantle beneath ~3°E, thus preventing a more mature system from developing. Thickening lithosphere toward the boundary with the SMZ is supported by a reduction in crustal thickness (e.g., Schmid-Aursch and Jokat 2016). Whilst there is no ridge propagation occurring, the increase in system maturity with increased melt supply westward along the WVZ is analogous to that observed at propagating rift tips (Christie and Sinton 1981).

Similar to ~3°E, multiple observations indicate that the portion of the ridge from 45-55°E is characterised by an immature plumbing system. This portion of the ridge, situated between two focussed magnetic anomalies (Fig. 7.1d), is devoid of significant volcanic relief such as that observed along the WVZ and is instead characterised by abundant seamounts often closely associated with fault scarps (Fig. 7.1b). Samples here are both primitive (Mg# 65.31±1.86) and hot (1205±11.42°C) (Fig. 7.5) and are dominated by olivine crystal cargo (Fig. 7.2). These observations suggest an immature plumbing system is present, with melts ascending from their storage region relatively quickly without undergoing significant modification. The association of seamounts with fault scarps suggests that faults here may act as magma conduits (e.g., Cochran 2008); similar relationships between faulting and eruptions have been observed in the northern Red Sea (Cochran 2005), with the eruption of near-primary melts at the Siqueiros and Garrett Transform faults attributed to transport through transform-related conduits (Perfit et al. (1996) and Hekinian et al. (1995) respectively) .

The region between 30-33°E, in contrast, exhibits extreme variations in glass and mineral compositions (Fig. 7.5 and 12). Indeed, whilst there is some overlap in glass compositions between the three locations (Fig. 7.5b), glasses here extend to lower Mg# (44.25) and temperatures and are more variable (Mg# 57.62±5.85 and 1165±19.09°C); both plagioclase and olivine show similar degrees of compositional variability (Fig. 7.12). This extreme compositional variability is akin to that observed at propagating rifts, where highly differentiated melts are proposed to develop in immature non-steady state systems located within thicker lithosphere where melt supply is intermittent and reduced (Christie and Sinton 1981; Sinton et al 1983). Whilst the lithosphere should be thick in the regions of both 30-33°E and 45-55°E, the extreme fractionation at 30-33°E may result from the highly focussed nature of melt supply in these region; this shall be expanded upon in Section 7.4.3.2.

To summaries, lavas from the most immature (e.g. 3°E and 45-55°E) and mature (e.g., WVZ) magma plumbing systems show low compositional variability but primitive and relatively evolved compositions respectively. In contrast, magma plumbing systems transitional between the two end-members show high degrees of compositional variability (e.g., 30-33°E). Therefore, using a combination of glass and mineral chemistry with bathymetric and geophysical observations, the Gakkel Ridge can be seen to contain plumbing systems that span the full spectrum of plumbing system maturity, from the mature homogeneous WVZ, through to the immature plumbing systems at 3°E, 30-33°E and 45-55°E. The maturity of these systems reflects the robustness of magmatism in the region, with melt supply and lithospheric thickness controlling the extent to which fractionation occurs.

7.4.1.5 The vertical extent of plumbing systems: Presence of trans-lithospheric magmatic systems?

In Chapter 6 the crystallisation pressure records of both plagioclase- and olivine-hosted melt inclusions from the Gakkel Ridge were discussed. Examination of melt inclusion crystallisation pressures from individual samples at 3°E Seamounts and 18°50'E and 31°E Basement Ridges (H-D27, H-D41 and H-D48 respectively) reveals that magma plumbing systems at the Gakkel Ridge are vertically extensive; shallower crystallisation pressures at ~3°E are consistent with the more magmatically robust nature of the WVZ. Importantly, at 3°E Seamounts and 18°50'E Basement Ridge, plagioclase-hosted melt inclusions record crystallisation occurring over ~7 km intervals (Fig. 7.26a,b) whilst plagioclase- and olivine-hosted melt inclusions from 31°E Basement Ridge record crystallisation occurring over ~16 km (Fig. 7.26c). Such vertically extensive crystallisation could record crystallisation occurring during ascent in dykes or within vertically extensive magma reservoirs. When considering which scenario has occurred, any model needs to account for the following observations: (1) host crystal zoning complexity; (2) melt inclusion Mg# variability; and (3) plagioclase- and olivine-melt disequilibrium. Whether these observations are consistent with crystallisation during dyke ascent or within vertically extensive magma reservoirs is explored below.

First, if crystallisation accompanied dyke ascent, minimal textural variation of the host crystals would be expected. However, host crystals, particularly plagioclase, are more-often-than-not complexly zoned. In Chapter 5 such complex zoning patterns were interpreted as evidence for complex magmatic processes within the magma plumbing system. Furthermore, evidence of skeletal growth in plagioclase, which might be

expected to occur during crystallisation in ascending dykes, is only present in one host plagioclase (Fig. 6.5g). In this crystal melt inclusions are restricted to the skeletal core. Second, if inclusions were trapped during dyke ascent, melt inclusion compositions should show minimal variation with depth because the extent of fractionation during dyking would be limited. Whilst minimal variation in melt inclusion Mg# over 4 km at 3°E Seamounts supports limited crystallisation, melt inclusions at 31°E Basement Ridge show variable Mg# and fractionation inconsistent with crystallisation during dyking (Fig. 7.26). Indeed, if olivine-hosted melt inclusions at 31°E Basement Ridge had crystallised during dyke ascent, the Mg# of melt inclusions would be expected to show minimal variation, instead the observed variation is consistent with fractionation within a vertically extensive magma reservoir. Similarly, melt inclusions from 18°50'E Basement Ridge have variable Mg# over a greater depth range. Finally, if crystallisation occurred during dyking, the crystals should be in equilibrium with their carrier melts, and the inclusions would all reflect the carrier basalt composition. However as discussed in Chapter 5 and shown in Figures 7.14 and 7.15, crystal-melt disequilibrium is the norm. Together, these data indicate that only limited crystallisation occurred during dyking, and instead crystallisation occurred within vertically extensive magmatic reservoirs.

Vertically extensive magmatic systems, commonly termed trans-crustal magmatic systems (TCMS), are being recognised in many magmatic environments using a range of both geophysical and petrological techniques (e.g., see Cashman et al. (2017) for a review). However, the term trans-crustal is not strictly applicable to the Gakkel Ridge. Whilst the crust in these locations has been suggested to be ~2.5-4.5 km thick (3°E Seamounts, 2.5 km; 18°50'E Basement Ridge, 2.5 km; and 31°E Basement Ridge, 4.5 km: Schmidt-Aursch and Jokat (2016)), plagioclase-hosted melt inclusions indicate crystallisation at depths of ≤7-16 km in these locations. Therefore, magmatic systems at the Gakkel Ridge are not restricted to the crust but are instead trans-lithospheric, spanning both the upper mantle and crust.

By combining crystallisation pressures with the trends in differentiation recorded by the Mg# of both plagioclase- and olivine-hosted melt inclusions, the vertical distribution and organisation of magma reservoirs within the Gakkel Ridge magma plumbing system can be reconstructed. At 3°E seamounts, melt inclusions show that whilst crystallisation occurs from the seafloor to 7 km depth, melt inclusion Mg# are primitive (>68) and show little variation until a horizon at ~1-3 km is reached; here melt inclusion Mg# become more variable and extend to more evolved compositions. Taken together this suggests that melts experience minimal fractionation during ascent in a dyke until melts stagnate

in a reservoir at ~1-3 km depth; within this magma reservoir, fractionation causes the observed Mg# variability. High crystal content of this sample suggests that the reservoir is a crystal mush zone. It should be noted that whilst melt inclusion crystallisation pressures suggest only one level of melt stagnation and crystallisation, the presence of mixed chemical and textural populations and wide range in zoning complexity values argue for multiple regions within the plumbing system where crystallisation can occur.

At 18°50'E Basement Ridge, melt inclusions Mg# variability is not restricted to a single horizon; instead it occurs over a depth range of 7 km. Samples from the centre of this magmatic system have high crystal contents whilst eruptions at its flanks are aphyric (Fig. 7.2a). These observations provide evidence for crystallisation at a range of depths within a vertically extensive mush zone, or series of closely nested mushes. As discussed in section 7.4.1.1, there may be melt-rich pockets within this mush from which aphyric basalts are erupted. The high zoning complexity of plagioclase (Fig. 7.20) in combination with the large range in mineral core compositions (Fig. 7.12) and extensive plagioclase-melt disequilibria (Fig. 7.14) further suggest that plagioclase crystal cargo were entrained from distinct regions of this mush zone prior to eruption.

The greatest range in crystallisation pressure is recorded at 31°E Basement Ridge (Fig. 7.26c). Here, melt inclusions from a single sample show up-system fractionation from ~16 km below the seafloor to seafloor depths. A 5 km gap in the crystallisation record (Fig. 7.26c) suggests that there are at least two regions of crystallisation. Deep and primitive melt inclusions hosted within complexly zoned plagioclase (Fig. 6.5i) indicate that melts were initially intruded into a mush zone and that subsequent crystallisation was limited. Subsequently, upward transport into a higher reservoir (1-9 km below the seafloor) occurred. As argued above, Mg# variability of these olivine-hosted melt inclusions argues against them representing crystallisation that occurred during melt ascent in dykes. The high crystal contents of samples, in combination with plagioclase-melt disequilibrium (Fig. Fig. 7.2a) and high zoning complexity (Fig. 7.20) of plagioclase erupted from this magmatic system are interpreted here to support that this upper reservoir was a crystal-dominated mush zone.

In addition to using melt inclusion crystallisation pressures to constrain the vertical extent of magma plumbing systems, partial crystallisation pressures (the depth of initial Ol-Pl-Cpx saturation) can be calculated using the approach of Herzberg (2004), which is calibrated on experimental data. If these pressures reflect the early crystallisation history of melts, they may provide an estimate of the base of the lithosphere (e.g., Standish et

al. 2008). Partial crystallisation pressures of primitive (Mg# >67) three-phase (Ol + Pl + Cpx) saturated MORB glasses from 45-55°E were identified by selecting melts that fall on a trend of decreasing CaO and MgO. Using the equation CaO = -0.3MgO + 14.5 basalts with excess CaO that are saturated in Ol + Pl only can be identified (Herzberg 2004). Only crystallisation pressures of the most primitive melts were determined because subsequent fractionation at shallower pressures will modify the melt composition and likely destroy signals of high pressure partial crystallisation. Calculated pressures of 0.54-0.66 GPa (median 0.61 GPa) correspond to depths of 16-20 km; these pressures are consistent both with pressures determined from melt inclusions, and the elevated partial crystallisation pressures identified at the slow-spreading Mid-Atlantic Ridge (Herzberg 2004) and ultraslow-spreading Southwest Indian Ridge (Standish et al. 2008). These partial crystallisation depths suggest that in the vicinity of 45-55°E the base of the lithosphere may be situated at ~16-20 km depth. The primarily aphyric nature of basalts erupted in this region further suggests that melts erupt directly from a melt-rich sill at the base of the lithosphere.

7.4.2 Along axis variation in the Gakkel Ridge plumbing system

In the previous sections the plumbing systems of the Gakkel Ridge have been shown to be characterised by crystal- and melt-rich regions, are vertically extensive and display differing degrees of maturity. To visualise how the magma plumbing system of the Gakkel Ridge varies along axis, a ridge-scale schematic has been created (Fig. 7.29). This schematic has been drawn to account for variations in crustal (Schmidt-Aursch and Jokat 2016) and lithospheric thickness (Schlindwein and Schmid 2016) and differences in the degree of melt focussing between the three tectono-magmatic segments (Jokat and Schmidt-Aursch 2007; Schmidt-Aursch and Jokat 2016). Seismic studies have shown that the base of the lithosphere at ultraslow-spreading ridges shallows significantly beneath volcanic centres and thickens in regions of peridotite exposure, where the lithosphere may be ≤35km thick (Schlindwein and Schmid 2016). Accordingly, the thinnest lithosphere in Figure 7.29 is present beneath the magmatically robust WVZ, whilst the thickest lithosphere occurs beneath the SMZ where magmatism is reduced, and peridotite is abundant. Lithosphere thickness increases in the order of WVZ>EVZ>SMZ. Topography at the base of the lithosphere has been drawn to account for: (1) differences in lithospheric thickness between each segment; and (2) the observations that earthquake hypocentres shallow significantly beneath magmatic centres (Schlindwein and Schmid 2016). Similarly, 3D gravity models have shown that crustal thickness is highly variable along-axis and can be related to melt supply (Schmidt-Aursch and Jokat 2016). Crustal thickness values are determined from this 3D gravity

model; regions of elevated crustal thickness generally correlate with regions with more robust magmatism or highly focussed melt supply.

Whilst much of the magma plumbing system of the Gakkel Ridge is crystal-rich and comprises multiple mush zones, isolated portions within each of these plumbing systems may be melt rich. Eruptions from melt- and crystal-rich regions will result in the eruption of low and high crystal content basalts respectively. In addition, relatively unfractionated, aphyric basalts are erupted from depth where well-developed magma plumbing systems are absent (e.g., 48°E Deep seafloor). In some instances, such as within the SMZ, the presence of thick lithosphere may prevent the eruption of melts that instead intrude into, and freeze within, the lithosphere.

Crystallisation pressures derived from melt inclusions indicate that magma plumbing systems are vertically extensive along the full length of the ridge (e.g., crystallisation up to 10.4 km at 2°W Axial Volcanic Ridge and 16.4 km at 31°E Basement Ridge), and that the most vertically extensive plumbing systems coincide with locations of melt focussing. Whilst in some instances these pressures may suggest only one region of melt storage and fractionation (e.g., 3°E Seamounts), textural complexity recorded by plagioclase attests to complex crystallisation histories within multiple regions of the magma plumbing system. In contrast, melt inclusion crystallisation pressures from 31°E Basement Ridge indicate the presence of two magma reservoirs, with melts becoming fractionated as they move upwards. This suggests that more primitive melts may be erupted from greater depth as is suggested in Hawaii (Helz et al. 2015). It must be highlighted that whilst melt supply in the WVZ may be robust and melt focussing may sustain vertically extensive magma plumbing systems (section 7.4.3.2), the low melt supply at ultraslow-spreading ridges, relative to faster spreading ridges, and the cool thermal structure of the lithosphere, may mean that these plumbing systems are ephemeral features. Despite this, basement ridges that extend up to 25 Myr off-axis demonstrate magmatic systems at the Gakkel Ridge can be long-lived (Jokat et al. 2003).

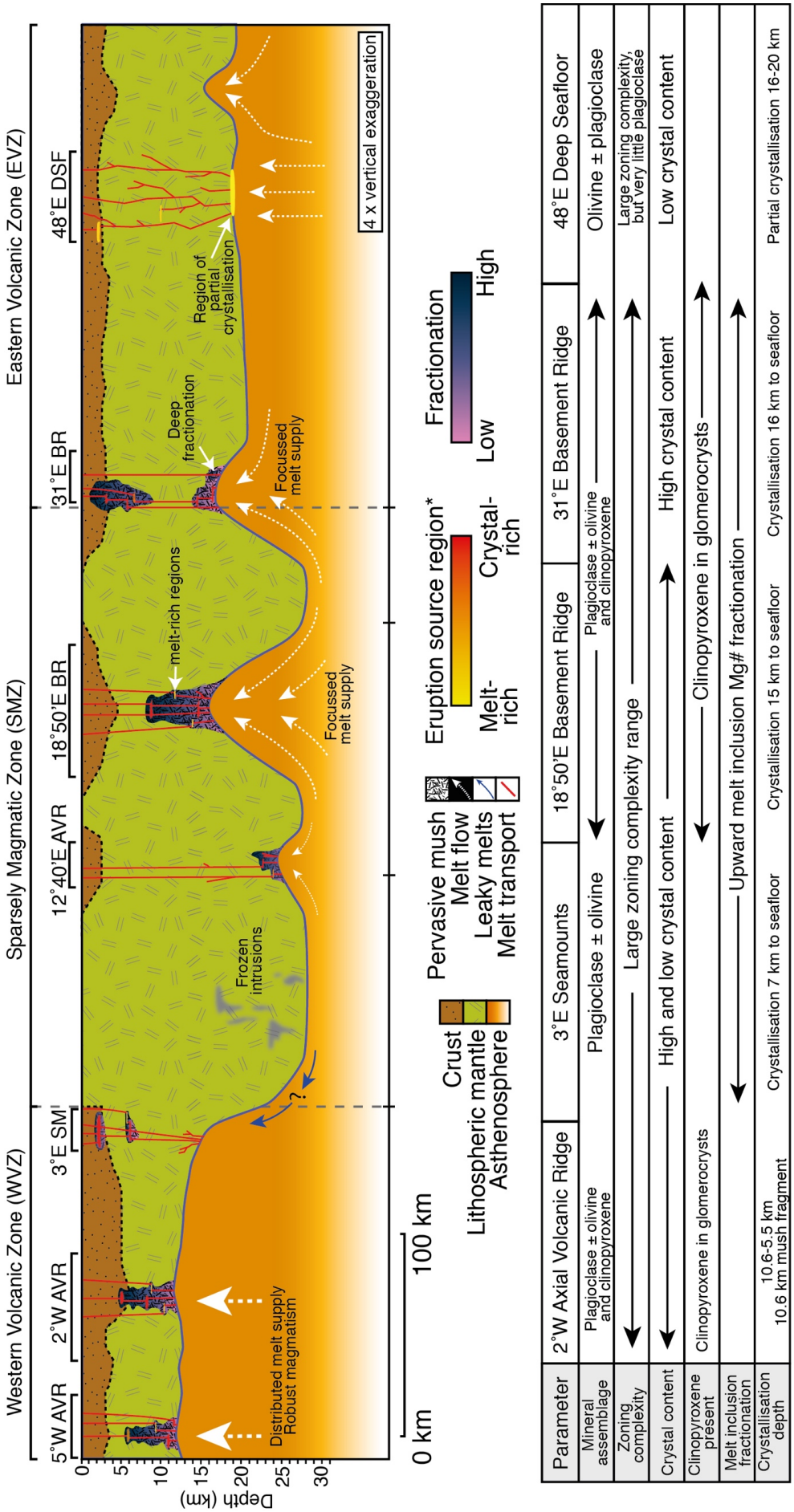

Parameter	2°W Axial Volcanic Ridge	3°E Seamounts	18°50'E Basement Ridge	31°E Basement Ridge	48°E Deep Seafloor
Mineral assemblage	Plagioclase ± olivine and clinopyroxene	Plagioclase ± olivine	Plagioclase ± olivine and clinopyroxene		Olivine ± plagioclase
Zoning complexity		Large zoning complexity range			Large zoning complexity, but very little plagioclase
Crystal content		High and low crystal content		High crystal content	Low crystal content
Clinopyroxene present	Clinopyroxene in glomerocrysts		Clinopyroxene in glomerocrysts		
Melt inclusion fractionation		Upward melt inclusion Mg# fractionation			
Crystallisation depth	10.6-5.5 km 10.6 km mush fragment	Crystallisation 7 km to seafloor	Crystallisation 15 km to seafloor	Crystallisation 16 km to seafloor	Partial crystallisation 16-20 km

← **Fig. 7.29:** Schematic of the Gakkel Ridge showing the along-axis variations in the magma plumbing system. More robust melt supply in the WVZ results in thinner crust and lithosphere and less vertically extensive magma plumbing systems than those typical of the SMZ and EVZ; the formation of vertically extensive plumbing systems here is aided by enhanced melt focussing. Magma plumbing systems in all segments are characterised by both mush- and melt-dominated regions; aphyric samples may be erupted from melt-rich pockets within mush zones. Spatial variability in melt and crystal content may result from non-uniform evolution and crystallisation of magma reservoirs. Some regions lack well-developed magma plumbing systems and instead erupt melts from depth with little modification during ascent. Along axis variations in crustal and lithospheric thickness are taken from Schmidt-Aursch and Jokat (2016) and Schlindwein and Schmidt (2016), respectively. * Note: Eruptions may be sourced from both melt- and crystal-rich regions of pervasive mush zones. Abbreviations are as follows: AVR, Axial Volcanic Ridge; SM, Seamounts; BR, Basement Ridge; DSF, Deep Seafloor.

7.4.3 Controls on the Gakkel Ridge magma plumbing system

Above, the magma plumbing system of the Gakkel Ridge has been reconstructed. Below the factors that control the nature of the Gakkel Ridge magma plumbing system will be examined.

7.4.3.1 Extent of melting

Initial studies of Gakkel Ridge basalts identified ridge-scale variations in $Na_{8.0}$, a parameter commonly used as a geochemical proxy for the extent of partial melting (e.g., Klein and Langmuir 1987). Michael et al. (2003) recognised that the WVZ has lower average $Na_{8.0}$ values than basalts from the SMZ and EVZ suggesting greater extents of melting occur in this segment; this relationship persists with the addition of more recent analyses and using recalculated $Na_{8.0}$ values more appropriate for individual ridge segments (Fig. 7.5c). Michael et al. (2003) remark that the magmatism observed in the WVZ is more akin to that found along the Mid-Atlantic Ridge and is greater than expected at its ultraslow-spreading rate. Increased partial melting in this segment has been attributed to the influx of North Atlantic mantle following the separation of Greenland from Svalbard (Goldstein et al. 2008; Schmidt-Aursch and Jokat 2016). This model is supported by Sr-Nb-Pb isotope systematics that suggest an abrupt isotopic mantle boundary at ~20°E within the SMZ (Goldstein et al. 2008), with samples to the west having a 'Southern Hemisphere" like mantle. This influx may have altered mantle convection, allowing robust magmatism that manifests in the form of a continuous high amplitude magnetic anomaly (Fig. 7.1a), magmatic crust that is up to 6.6 km thick (Schmid-Aursch and Jokat 2016), and numerous axial volcanic ridges and seamounts. In addition, the magma plumbing system here is shallow (Fig. 7.24 and 7.26) and mature and erupted basalts are more evolved and homogeneous than other ridge segments (Fig. 7.5). Lower degrees of partial melting in the SMZ and EVZ form less mature magma plumbing systems that can be vertically extensive. The inverse correlations between melt flux and both glass $Na_{8.0}$ (Fig. 7.10a) and Mg# (Fig. 7.11) indicate that increased degrees of partial melting produce elevated magmatic vigour and the eruption of more evolved

glass compositions and more significant volcanic relief (i.e., axial volcanic ridges in the WVZ). In contrast, regions of low degrees of partial melting and melt flux (i.e., ~50°E, Fig. 7.5c) are characterised by subdued or absent volcanic relief (Fig. 7.1b). Therefore, the extent of partial melting plays an important role in controlling the type of volcanic morphology formed as well as the depth and maturity of magma plumbing systems.

Having determined, from $Na_{8.0}$, that the extent of partial melting varies along the Gakkel Ridge, it is worth examining in more detail relationships between $Na_{8.0}$ and both glass K/Ti and SiO_2 observed in Fig. 7.7. From Fig. 7.7b it can be seen that the WVZ is characterised by both low $Na_{8.0}$ and K/Ti, whilst the EVZ is characterised by higher $Na_{8.0}$ and K/Ti. Variations in K/Ti ratios are commonly interpreted as reflecting distinct mantle sources (e.g., Standish et al. 2008; Colman et al. 2012). Following this rationale, one would interpret the WVZ as having undergone higher degrees of melting (low $Na_{8.0}$) of a depleted source and the EVZ experiencing lower degrees of melting (high $Na_{8.0}$) of an enriched source. This seems contradictory because, all else being equal, one would expect a more enriched source to undergo more melting than a depleted one. Alternatively, the elevated $Na_{8.0}$ values of the EVZ likely reflect lower degrees of melting due to the presence of thicker lithosphere; the elevated $Na_{8.0}$ values are therefore controlled by the vertical extent of the mantle melting column more than the composition of the mantle source. Additionally, whilst K/Ti ratios in the EVZ are shifted to higher values than the WVZ, small variations in K/Ti could reflect variations in the extent of melting due to Ti and K being variably incompatible at low degrees of melting (Hirschmann et al. 1999). Therefore, accounting for the above, the observed difference between K/Ti and $Na_{8.0}$ values of the WVZ and EVZ likely results from a combination of variations in mantle source composition and extent of melting that is controlled, at the segment-scale, by lithospheric thickness.

Basalts from the EVZ have not only elevated $Na_{8.0}$, but also lower SiO_2 compared to most samples from the WVZ (except a small group of WVZ basalts which have significantly lower SiO_2) (Fig. 7.7a and 7.8). Basalts with both low SiO_2 and elevated FeO contents are often interpreted as a result of high melt segregation pressures (e.g., Langmuir et al. 1992). Therefore, if the lower SiO_2 of the EVZ was due to elevated segregation pressures consistent with the thicker lithosphere, basalts should show elevated FeO contents, which they do not. The difference between the two segments may simply reflect the overall lower degrees of fractionation in the EVZ compared to the WVZ which is consistent with the higher segment median glass Mg#. Alternatively, the two segments may be underlain by mantle sources of different compositions, as suggested by an isotopic discontinuity in the middle of the SMZ (e.g., Goldstein et al. 2008).

It has previously been argued that basalts from the WVZ with both low SiO_2 and elevated FeO are the product of melt segregation at elevated pressures, “consistent with thicker lithosphere from this region compared to fast-spreading ridges” (Michael et al. 2003). However, if such geochemical signatures indicate elevated melt segregation pressures, similar basalts should be erupted from other segments of the Gakkel Ridge, especially the SMZ. Indeed, robust magmatism in the WVZ will have produced thinner lithosphere relative to that in the SMZ; thick lithosphere in the SMZ is supported by the abundance of peridotite and paucity of basalt. Therefore, if these basalts do indeed represent melts that have segregated at high pressures, it is unlikely that segregation occurred beneath the WVZ. Instead they may represent leaky melts that segregated at high pressures beneath the SMZ, where the lithosphere is thicker, and migrated laterally (Fig. 7.29). The absence of similar melts in the SMZ might result from melts being intruded into the lithosphere and not erupted.

Alternatively, the low SiO_2 and high FeO of these basalts may reflect a heterogeneous mantle source beneath the WVZ that contains a pyroxenite component (Lambart et al. 2009, 2013). Indeed, partial melts from a source containing pyroxenite have lower SiO_2 and higher FeO than partial melts derived from peridotitic mantle (e.g., Lambart et al. 2013). Glasses from all three segments carry geochemical signatures (low SiO_2 and high FeO) of silica deficient pyroxenite and fall within the field of px-MORBs defined by Lambart et al. (2013) (Fig. 7.30). Despite the potential contribution of a pyroxenite component in in the genesis of these basalts, Wanless et al. (2014) argue that the trace element composition of olivine-hosted melt inclusions from the EVZ cannot be explained by partial melting of a mantle source containing pyroxenite veins because the resultant melts are too enriched. However, this conclusion is highly dependent on the starting pyroxenite composition used in the modelling. Taken together, the above demonstrates that the mantle beneath the Gakkel Ridge is heterogeneous and that low SiO_2 and elevated FeO of basalts does not necessarily indicate melt segregation at high pressures.

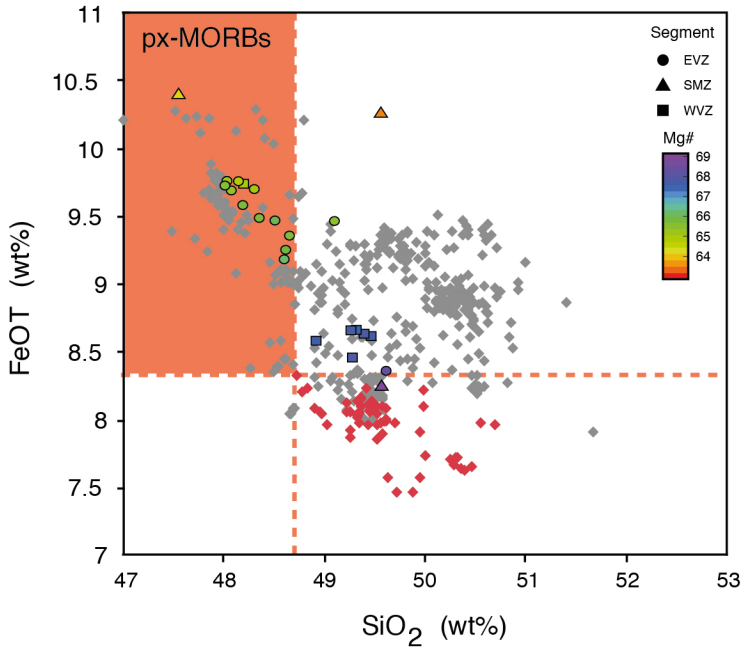

Fig. 7.30: Total iron contents vs. SiO_2 contents for MORB glasses with >9.0 wt.% MgO. Black outlined points are basalt glasses from the Gakkel Ridge, a subset of which fall within the orange field that represents the compositional area of px-MORBs. These px-MORBs have SiO_2 and FeO^T contents lower and higher than glasses with Mg# ≥67 (pink diamonds). Grey and pink points are MORB glasses from Melson and O'Hearn (2003). Figure re-drawn from Lambart et al. (2013).

7.4.3.2 Melt focussing

Melt focussing, whereby melts produced in a broad region in the mantle become focused into a narrow zone beneath the ridge axis, is an important process at all mid-ocean ridges; as spreading rate decreases, melt focussing becomes more efficient (Cochran 2008). Indeed, the change in volcanic morphology from axial volcanic ridges in the WVZ to large circular seamounts in the EVZ has been attributed to more efficient melt focussing eastwards along the Gakkel Ridge (Dick et al. 2003; Jokat et al. 2003; Michael et al. 2003; Cochran 2008; Wanless et al. 2014a). Furthermore, the association of regions of melt focussing with basement perpendicular ridges that extend off-axis for 20-25 Myr has been interpreted as evidence that magma production and transport systems here have been active and stable over this prolonged timescale (Jokat et al. 2003). Therefore, melt focussing at the Gakkel Ridge not only controls the localisation of magma plumbing systems, but also influences their longevity. Furthermore, the occurrence of melt focussing in both the SMZ and EVZ may be responsible for two features of the magma plumbing systems: (1) the formation of vertically extensive magmatic systems; and (2) the production of conditions favourable to the formation of evolved glass and mineral compositions.

Magma plumbing systems located at 18°50'E and 31°E Basement Ridges are vertically extensive, extending to ~15 km and ~16 km below the seafloor respectively (Fig. 7.26

and 7.29). Simple mass balance considerations indicate that efficient melt focussing along these portions of the ridge can facilitate the formation of vertically extensive plumbing systems. For example, to form a 16 km high magma plumbing system at 31°E, where the crust is ~ 4 km thick (Schmid-Aursch and Jokat 2016), requires a fourfold increase in the area over which melts are focussed. Therefore focussing over a region of ~64 km would be required. This is consistent with geophysical studies of ultraslow-spreading ridges that show melts are commonly focussed along-axis from regions between 60-120 km in length (Schlindwein and Schmidt 2016). Similar mass balance considerations are applicable to the magma plumbing system at 18°50'E Basement Ridge.

Whilst melt inclusions provide evidence for melt evolution during upward movement through the system, the eruption of the most evolved basalts and crystal cargo at 31°E Basement Ridge (Fig. 7.5 and 12) provides evidence for extensive fractionation at depth within mush zones. At ultraslow-spreading ridges where melt supply is low and episodic, most melt bodies will have short lifespans, hence the system needs to stay above the solidus for prolonged periods in order for extensive fractionation to occur. In the vicinity of 31°E Basement Ridge, efficient focussing of low volume melts along the base of the lithosphere from a broad region (e.g., Cannat et al. 2003; Standish et al. 2008; Montési et al. 2011; Schlindwein and Schmid 2016) will result in less episodic melt supply (i.e., higher time averaged melt supply). Focussed melt supply and related heat input from melt intrusion (both specific heat and latent heat of crystallisation) may raise the local temperature of the deep part of the lithosphere sufficiently to allow enhanced degrees of fractionation to occur within long-lived mush zones. The presence of evolved mush zones is supported by the eruption of numerous poly-mineralic glomerocrysts with evolved mineral compositions (plagioclase + olivine + clinopyroxene; Fig. 7.4 and 12). In contrast, whilst the long-term melt supply in the WVZ is higher, and the lithosphere thinner, it is less focussed resulting in a lower time averaged melt supply from any one point in the mantle into the system (Fig. 7.29).

7.4.4 Comparison to fast- and slow-spreading mid-ocean ridges

Several models suggest global relationships between spreading rate and both glass chemistry (e.g., Rubin and Sinton 2007) and crystal content (e.g., Flower 1980; Stewart et al. 2003; Lange et al. 2013). However, until now there has been no crystal content data from ultraslow-spreading ridges, hence this relationship has not been examined across the full spreading spectrum. In addition, whilst studies have shown that fast-spreading ridges erupt more fractionated lava compositions than slow-spreading ridges,

no studies have determined whether mineral compositions show similar relationships with spreading rate. To investigate relationships between spreading rate and both mineral chemistry and crystal content, mineral compositions and crystal contents from the Gakkel Ridge (ultraslow-spreading ridge) are compared to those from the East Pacific Rise and Mid-Atlantic Ridge.

7.4.4.1 Relationship between spreading rate and mineral and glass chemistry

Using a global compilation of >11,000 MORB compositions, Rubin and Sinton (2007) show an inverse correlation between spreading rate and basalt Mg#. Whilst this explores how basalt Mg# changes across the full spreading-rate spectrum, they use only a single data point from the Gakkel Ridge whose Mg# was estimated from data presented in Michael et al. (2003). Here, using new and existing Gakkel Ridge glass data, the inverse correlation present between spreading rate and glass Mg# can be seen to extend to ultraslow-spreading rates; glass Mg# becomes more primitive and less variable at progressively slower spreading rates (East Pacific Rise→Gakkel Ridge) (Fig. 7.31a). A similar relationship might be expected between mineral chemistry and spreading rate with more primitive and less variable mineral compositions being erupted at slower spreading rates. However, Figure 7.31b and c shows that there is no systematic change in plagioclase and olivine compositions with changing spreading rate; mineral chemistry appears decoupled from both spreading rate and glass chemistry. Decoupling between mineral and glass chemistry for Gakkel Ridge samples was previously shown in Figure 7.19c and is not surprising if, as interpreted for the origin of much of the Gakkel Ridge crystal cargo in Chapter 5, the crystal cargo is not purely phenocrystic in origin and ascending melts entrain a diverse crystal cargo from a range of storage regions at various depths. Furthermore, whilst there has been some suggestion (Fig. 7.18) that the extent of partial melting may influence mineral chemistry, there is considerable scatter in this dataset, with similar mineral chemistries present at both fast- and ultraslow-spreading ridges. For example, in Figure 7.18, samples from ODP Hole 1256D, a fast-spreading ridge, have similar mineral compositions to samples from the Southwest Indian Ridge, and again mineral compositions from IODP Hole 1309D, a slow-spreading ridge, overlap mineral compositions from both faster and slower spreading ridge segments. This demonstrates that variations in spreading rate and the extent of partial melting cannot alone explain the observed variations in mineral chemistry. Instead it suggests that localised conditions and processes occurring within the magma plumbing system influence the composition of minerals.

Whilst the available data indicate that mineral chemistry and spreading rate are decoupled, further insights into this relationship are limited by the restricted number of locations basalt crystal cargo mineral data is available for (i.e., sampling bias) (Table 7.9) and the number of analyses available for comparison (Table 7.10). For example, not only are there comparatively few plagioclase analyses available from the East Pacific Rise, but the available analyses are restricted to a handful of locations; for comparison, plagioclase from the Gakkel Ridge has been analysed from the full length of the ridge. In addition, in order to compare like-to-like, when possible, only plagioclase core analyses have been used. However, because mineral analysis locations are rarely provided, large quantities of data have had to be excluded (e.g., plagioclase analyses from Pan and Batiza (2003)).

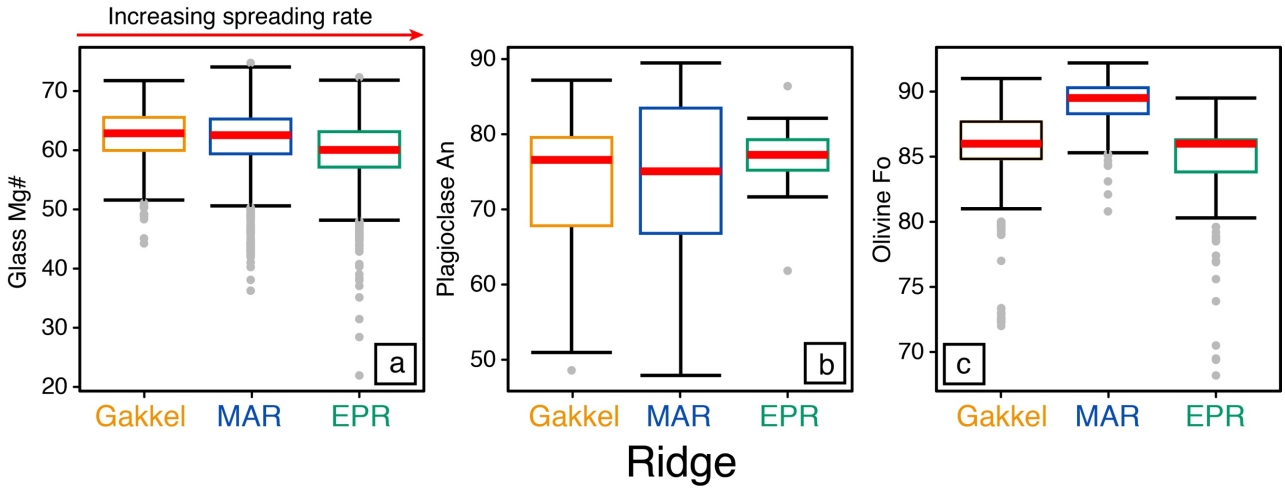

Fig. 7.31: Comparison of glass Mg# (**a**), plagioclase An (**b**) and olivine Fo (**c**) content of samples from the fast-spreading East Pacific Rise (EPR), slow-spreading Mid-Atlantic Ridge (MAR) and the ultraslow-spreading Gakkel Ridge. Data sources and statistics can be found in Table 7.9 and 7.10 respectively.

7.4.4.2 Relationship between spreading rate and crystal content

Previous studies have identified an inverse relationship between spreading rate and total crystal content; faster spreading ridges tend to erupt lavas with lower crystal content than slower spreading ridges (e.g., Stewart et al. 2003). These observations are consistent with the idea that magma plumbing systems at slow-spreading ridges are crystal-rich (e.g., Sinton and Detrick 1992). Until now, relationships between crystal content and spreading rate have been documented at fast- to slow-spreading ridges and have not extended to ultraslow-spreading ridges. Using Gakkel Ridge basalt crystal content data, Figure 7.32a shows that the inverse correlation between spreading rate and total crystal content persists at ultraslow-spreading rates and that crystal content in Gakkel Ridge basalts extends well beyond that typical of both the East Pacific Rise and Mid-Atlantic Ridge; the total crystal content is controlled by plagioclase content. The same inverse relationship is shown by plagioclase and olivine crystal content (Fig 7.32b,c). The high

crystal content of Gakkel Ridge basalts therefore supports the increasingly crystal-rich nature of magma plumbing systems at reduced spreading rates.

Table 7.9 Plagioclase and olivine literature analyses data source

Ridge	Location	Reference	Plagioclase and/or olivine
MAR	36°47'N and 36°8372'N (FAMOUS)	Laubier et al. (2012) Laubier et al. (2007)	O O
	23°38'N (Kane Megamullion)	Ciazela et al (2017)	O + P
	36°N (FAMOUS)	Bryan (1979)	O + P
	23°-25°N (Kane Fracture Zone)	Bryan et al. (1981)	O + P
	Seroki volcano (south of Kane Fracture Zone)	Meyer and Shibata (1990)	P
	22°59.14'N (Kane Fracture Zone)	Kirkpatrick (1978)	P
EPR	~9°30'N	Batiza and Niu (1992)	O + P
	13°N	Zhang et al. (2008)	O
	9°30'N, 10°30'N and 11°20'N	Pan and Batiza (2002, 2003)	O
	9°50'N	Ridley et al (2006)	O + P
	9°46'N-9°56'N, 9°46'N-9°51'N and 12°48'N	Wanless et al. (2012)	O

Table 7.10 Comparative glass and mineral chemistry statistics

	Ridge	Number	Minimum (%)	Maximum (%)	Median (%)	Standard deviation
Glass Mg#	Gakkel	532	44	72	63	4
	MAR	3354	36	75	63	5
	EPR	3216	22	72	60	5
Plagioclase	Gakkel	827	49	87	77	8
	MAR	71	48	90	75	10
	EPR	20	62	86	77	5
Olivine	Gakkel	539	72	91	86	3
	MAR	318	79	92	90	2
	EPR	310	68	90	86	3

Two models have been proposed to account for the plagioclase-rich nature of some MORBs, and plagioclase-ultraphyric basalts (PUBs) at (ultra)slow-spreading ridges in particular: (1) plagioclase accumulation through flotation (e.g., Flower 1980; Cullen et al. 1989; Hansen and Grönvold 2000); and (2) disruption of pre-existing crystal cumulates and absence of magma chambers (Lange et al. 2013). Models proposing accumulation and flotation assume that plagioclase is positively buoyant in MORB host melts. However, Lange et al. (2013) demonstrated that because plagioclase in PUBs is often anorthitic (>An_{80}), it would in fact be negatively buoyant in its host melt, thus precluding accumulation through flotation. Alternatively, the eruption of crystal-rich samples at the Gakkel Ridge may be favoured by the absence of melt-rich magma chambers which have been proposed to act as density filters at fast-spreading ridges (Lange et al. 2013); to date, magma chambers such as those at fast-spreading ridges have not been

identified beneath the Gakkel Ridge. Support for this model comes from the compositions and textures of the crystal cargo, which indicate that the Gakkel crystal cargo is predominantly derived from crystal mush (Chapter 5).

In contrast to plagioclase and olivine content, clinopyroxene content shows a positive correlation with spreading rate. This result was somewhat unexpected. Due to the thicker lithosphere at Gakkel (up to 35 km; Schlindwein and Schmid 2016), it is likely that at least some melt evolution occurs at elevated pressures. This favours clinopyroxene crystallisation; as pressure increases the clinopyroxene stability field expands at the expense of olivine (Grove et al. 1992). Therefore, it follows that clinopyroxene might be more common at ultraslow-spreading ridges. However, Figure 7.32d demonstrates that samples from the East Pacific Rise can contain more clinopyroxene than the Gakkel Ridge, hence the pressure of melt evolution does not necessarily control the abundance of clinopyroxene in erupted MORB. Clinopyroxene is a rare phenocryst phase in MORB because it crystallises as an interstitial phase within mush zones (e.g., Lissenberg et al. 2019), however, Figures 7.31a and 7.32d provide an additional explanation for the increased clinopyroxene abundance in fast-spreading ridge basalts relative to slow- and ultraslow-spreading ridges; that is, the extent of fractionation trumps the pressure of crystallisation. Indeed, glasses from the East Pacific Rise not only have moderately lower Mg# than Gakkel Ridge glasses (Fig. 7.31a), and moderately higher variation (Table 7.10), they also contain more clinopyroxene (Fig. 7.32d). Therefore, it is possible that the relative abundance of clinopyroxene at fast-spreading ridges compared to ultraslow-spreading ridges is a result of the more extensive fractionation occurring here, which causes more clinopyroxene to crystallise. Again, it must be noted that as with the global mineral chemistry data, modal mineralogy datasets have been compiled from a limited number of locations, hence the dataset may be biased geographically (Table 7.11).

Table 7.11 Modal mineralogy data sources

Ridge	Location	Reference
EPR		Pan and Batiza (2003)
	10°N	Allan et al. (1989)*
	9°N	Dmitriev (1980) *
	28°S	Michael and Chase (1987) *
MAR	28-73°N	Schilling et al. (1983) *
	22-25°N	Bryan et al. (1981)*
	25-30N	O'Donnell and Presnall (1980) *
	23°N	Hodges (1978) *
	23°N	Flower et al. (1979) *

* References from Stewart et al. (2003)

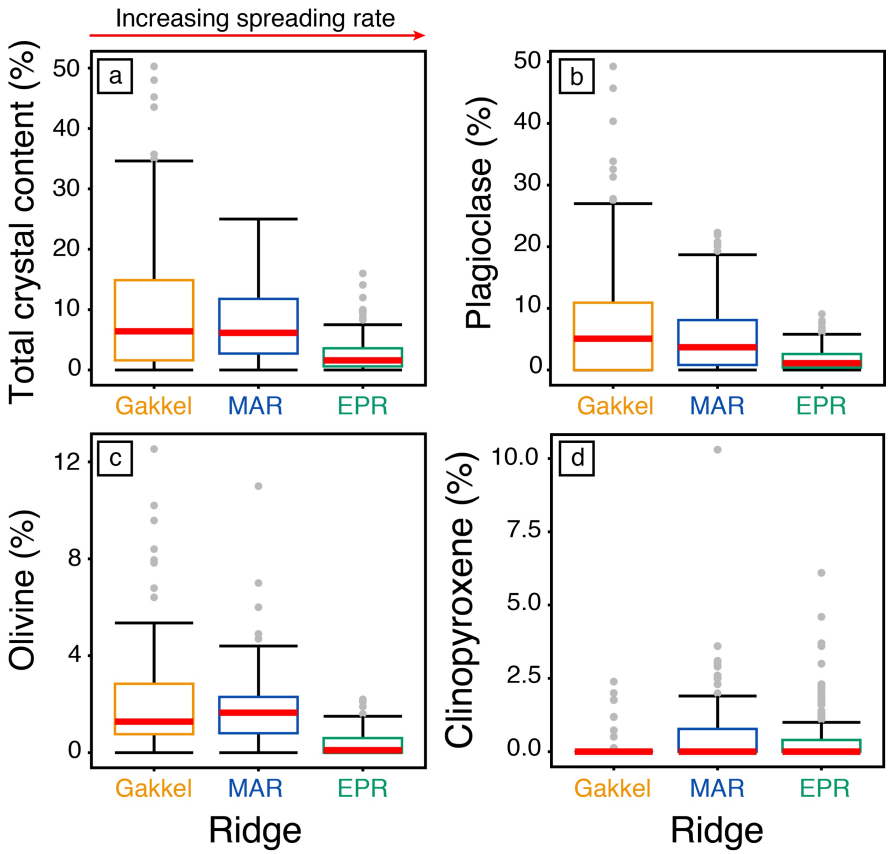

Fig. 7.32: Comparison of the total crystal (**a**), plagioclase (**b**), olivine (**c**) and clinopyroxene **(d)** content in MORB erupted at the East Pacific Rise (EPR), Mid-Atlantic Ridge (MAR) and Gakkel Ridge. Total crystal, plagioclase and olivine content all show an inverse correlation with spreading rate, whilst clinopyroxene content (including outliers) shows a positive correlation. Modal data from the EPR and MAR have been compiled from data sources in Table 7.11. Statistics are in Table 7.12.

Table 7.12 Comparative crystal cargo statistics

	Ridge	Number	Minimum (%)	Maximum (%)	Median (%)	Standard deviation
Total crystal content	Gakkel	95	0	50	6	12
	MAR	82	0	25	6	7
	EPR	177	0	16	2	3
Plagioclase	Gakkel	95	0	49	5	11.3
	MAR	82	0	22	4	6
	EPR	177	0	9	1	2
Olivine	Gakkel	95	0	13	1	2.4
	MAR	82	0	11	2	1.7
	EPR	177	0	2	0	0.5
Clinopyroxene	Gakkel	95	0	2	0	0.4
	MAR	82	0	10	0	1.4
	EPR	177	0	6	0	0.9

7.5 Conclusions

- The physical nature of the Gakkel Ridge varies along axis. Measures of magma plumbing system maturity (e.g., basalt Mg#, temperature), in combination with bathymetric and geophysical observations, reveal that the Gakkel Ridge is characterised by both mature and immature magma plumbing systems. The most mature magma plumbing systems are found in the western WVZ, where higher degrees of partial melting produce both more abundant magmatism and shallower magma plumbing systems than in other segments of the Gakkel Ridge. More immature magma plumbing systems are located in both the SMZ and EVZ, where the degree of melting is lower.
- The eruption of basalts with high crystal contents along the full length of the Gakkel Ridge indicates that magma reservoirs from which eruptions were sourced were crystal-rich. In some instance, the eruption of aphyric, primitive basalts from localised regions suggests that plumbing systems may be entirely absent in some regions of the Gakkel Ridge.
- Mineral textures and melt inclusions plus basalt partial crystallisation pressures indicate that magma plumbing systems are vertically extensive and trans-lithospheric crystal mush systems. Within these trans-lithospheric systems, melt inclusion compositions indicate that melts undergo upward-fractionation, either concentrated in single horizons or over greater depth intervals; multiple storage regions, most likely at different depths, are required to explain the observed textural complexity of crystal cargo.
- Glomerocryst mineralogy shows that mush zones represent variable stages of maturity and that both primitive “hot” and evolved “cold” mush zones exist within the system. Crystallisation of clinopyroxene within mush zones may act to suture the crystal framework, thus producing mush zones which are harder to disaggregate; this may explain the paucity of clinopyroxene as a free phase in many MORBs.
- The proportion of melt trapped with glomerocrysts and melt films indicates that mush zones within the Gakkel Ridge contain 0.26-13.51% melt (median 4.77%).
- Along-axis focussing of melt along the base of the lithosphere plays an important role in generating conditions within the magma plumbing system that facilitate the formation of vertically extensive plumbing systems and extensive degrees of fractionation.
- Glass Mg# becomes systematically more primitive with decreasing spreading rate from the East Pacific Rise to the Gakkel Ridge in accordance with global

models (e.g., Rubin and Sinton 2007) of increased Mg# with decreasing spreading rate.

- Ultraslow-spreading ridges, such as the Gakkel Ridge, erupt basalts with more variable and higher crystal contents than basalts erupted at faster spreading ridges such as the Mid-Atlantic Ridge and East Pacific Rise. This is in part attributed to the absence (or scarcity) of melt-dominated regions such as melt lenses identified beneath the East Pacific Rise that act as density filters. The more common occurrence of clinopyroxene in basalts erupted at the East Pacific Rise compared to the Gakkel Ridge is related to the more extensive fractionation that occurs at the East Pacific Rise and not differences in pressures of melt evolution.
- Mineral chemistry is decoupled from both spreading rate and glass chemistry. This indicates that not only is crystal cargo not purely phenocrystic in origin, but that variations in spreading rate and the extent of partial melting cannot alone explain the observed variations in mineral chemistry. Instead localised conditions and processes occurring within magma plumbing systems are likely to influence the composition of minerals.

Chapter 8

Melt transport at the Gakkel Ridge

Chapter 8

8.1 Introduction

Decades of study have shown that mid-ocean ridges experience both vertical and lateral melt transport. The occurrence of lateral melt transport in mid-ocean ridges has been identified using both geophysical (e.g., Dziak et al. 1995) and petrological (e.g., Thompson et al. 1985) observations. For example, along-axis propagation of an earthquake swam for ~60 km has been interpreted as the lateral propagation of a dyke from a single reservoir at the CoAxial segment of the Juan de Fuca Ridge (Dziak et al. 1995); lateral dyke injection at mid-ocean ridges has also been observed at Axial Volcano (Dziak and Fox 1999) and the North Gorda Ridge (Fox and Dziak 1998). Similar lateral dyke propagation has been recognised using geophysics in Hawaii (e.g., Ryan 1988), Iceland (e.g., Krafla (Einarsson and Brandsdottir 1978); and Bárdðarbunga to Holuhraun (White et al. 2019)) and the Afar Volcanic Province (e.g., Grandin et al. 2012). To complement geophysical studies, using both basalt chemistry and crystal cargo, Thompson et al. (1985) interpreted the presence of evolved crystal-rich basalts at the flank of the 180 km magmatic system between 10°-12°N on the East Pacific Rise as the result of lateral melt intrusion away from a centralised melt source. They suggest that this results from lateral intrusion through cold crust and simultaneous magmatic fractionation. Lateral melt transport in dykes away from volcanic centres at the Southwest Indian Ridge has been proposed to account for lateral melt redistribution (Cannat et al. 2006, 2008; Jian et al. 2017b); diabase dykes in the Kane Megamullion (Mid-Atlantic Ridge) have similarly been interpreted as evidence for lateral melt transport in dykes that fed eruptions away from magmatic centres (Dick et al. 2008).

There are some of observations, however, which suggest that mid-ocean ridge volcanic systems have an important component of vertical melt transport. First, whilst a negative correlation between the distance from volcanic centres and melt MgO content, a predicted consequence of along-axis melt transport, is present at some mid-ocean ridges (Thompson et al. 1985; Fialko and Rubin 1998), it is not observed at all ridge segments. Instead, the presence of multiple lava types in individual dredges (Sinton et al. 1991) and large variations in Mg# in closely spaced samples (Perfit et al. 1994) has been used to suggest that magma chambers beneath these ridges are either continuous and experience limited along-axis mixing (Langmuir et al. 1986; Sinton et al. 1991) and are therefore compositionally zoned, or that magma chambers are small and discontinuous along axis (Langmuir et al. 1986; Perfit et al. 1994; Sinton et al. 2002; Colman et al.

2012) and that melt is injected from the mantle at multiple locations (Reynolds et al. 1992). If so, melt transport from magma reservoirs is vertical (Sinton et al. 2002; Bergmanis et al. 2007) and along-axis spatial variations in erupted basalts can be used to track variations in the sub-volcanic system (Sinton et al. 2002). In addition to Mg#, K/Ti ratios can be used to infer the presence of adjacent magmatic systems fed by melt influxes from mantle sources with different compositions. For example, adjacent flow fields (i.e., basalts erupted during a single eruptive episode) along the Galapagos spreading centre commonly exhibit distinctly different K/Ti ratios (e.g., Altares and Tortuga flow fields) which are attributed to the presence of multiple parent magmas (Colman et al. 2012). Furthermore, the eruption of isotopically distinct basalts at small spatial scales that coincide with ridge discontinuities indicate that along-axis melt migration is limited and that instead vertical melt transport from isotopically distinct mantle regions occurs along 5.5°N to 19°N of the East Pacific Rise (Mallick et al. 2019).

Whilst the numerous studies above examine melt transport at fast- and slow-spreading ridges, comparatively little is known about melt transport at ultraslow-spreading ridges, such as the Gakkel Ridge. The only current insight into melt transport within the Gakkel Ridge lithosphere comes from studies of the 1999 earthquake at 85°E. This magnitude 3.2-5.8 earthquake is the largest mid-ocean ridge earthquake recorded to date and comprised >200 events that occurred over >7 months (Müller and Jokat 2000; Sohn et al. 2008); the earthquake is generally accepted as volcano-tectonic in origin (e.g., Müller and Jokat 2000; Sohn et al. 2008; Rieidel and Schlindwein 2010). Despite multiple studies of this earthquake event, different treatments of the data results in different interpretations. For example, Tolstoy et al. (2001) interpret the earthquake swarm as evidence for lateral migration of magmatic pulses, whilst others argue that there is no evidence of classical along-axis earthquake migration and that extended seismicity over a broad region reflects segment-scale fault reactivation in response to intrusion at its centre (Korger and Schlindwein 2012). Regardless of whether any lateral migration of melts occurred here, it is clear that swarm characteristics are unlike those that typify fissure eruptions (Reidel and Schlindwein 2010; Korger and Schlindwein 2012) such as those in Iceland (e.g., Bárdðarbunga to Holuhraun (White et al. 2019)), Hawaii (e.g., Ryan 1988; Parfitt and Wilson 1994; Smith and Cann 1999; Parfitt et al. 2002) and along faster spreading mid-ocean ridges such as the Juan de Fuca Ridge (e.g., CoAxial segment (Dziak et al. 1995)).

It is worth noting that melt transport need not be exclusively vertical or lateral. Indeed, flow lineation's on the surfaces of dykes in the Troodos ophiolite (Cyprus) indicate that within these dykes, both vertical and sub-horizontal melt flow can occur (Varga et al.

1998); magmatic flow may also evolve from horizontal to vertical during dyke propagation (Eriksson et al. 2011). It may be that individual dykes formed during the same eruptive episode exhibit different flow directions (e.g., vertical and lateral flow in radial dykes, Komochi Volcano, Japan (Geshi 2008)). In the following chapter, using a combination of detailed bathymetric descriptions, glass geochemistry, crystal content and mineral chemistry and textures, melt transport at the ultraslow-spreading Gakkel Ridge will be investigated.

8.2 Magmatic systems of the Gakkel Ridge

Two magmatic systems, the 2°W Axial Volcanic Ridge (AVR) in the WVZ and 18°50'E Basement Ridge in the SMZ, inform melt transport at the Gakkel Ridge. For each of these magmatic systems, local-scale variations in crystal content, glass chemistry and mineral geochemistry and textures are presented. Local-scale variations for magmatic systems not discussed here can be found in Appendix 3. For each magmatic system, bathymetric profiles have been generated with GeoMapApp, using the 100 m scale bathymetric data obtained during the AMORE cruise (Michael et al. 2003). These profiles represent the bathymetry of zero-age crust, along which most of the dredges for which data is presented were located. However, not all dredge locations were on axis, and hence have been projected onto the axial profile orthogonally (see P-229 in Figure 8.1a for an example).

8.2.1 2°W Axial Volcanic Ridge (Fig. 8.1)

Extending for 46 km along axis, the 2°W AVR (Fig. 8.1) rises from from 3800 to 2770 mbsl at its shallowest point. The AVR tapers at both ends but does not appear to be cut by significant normal faults. Normal fault scarps are located to the northwest and southeast of the axial ridge. From west to east samples H-D18, H-D21, H-D22 and H-D23 have been dredged from the AVR. Dredge H-D21 approximates the centre of the AVR whilst H-D18 and H-D23 are situated toward the flanks of the AVR. In contrast, P-299 has been dredged from the south-eastern valley wall. The number of samples studied from each dredge is shown in Table 8.1.

Table 8.1 Number of sample analysed from each dredge at 2°W Axial Volcanic Ridge

	Dredge				
	H-D18	H-D21	H-D22	P-229	H-D23
Number of samples	3	5	1	1	2

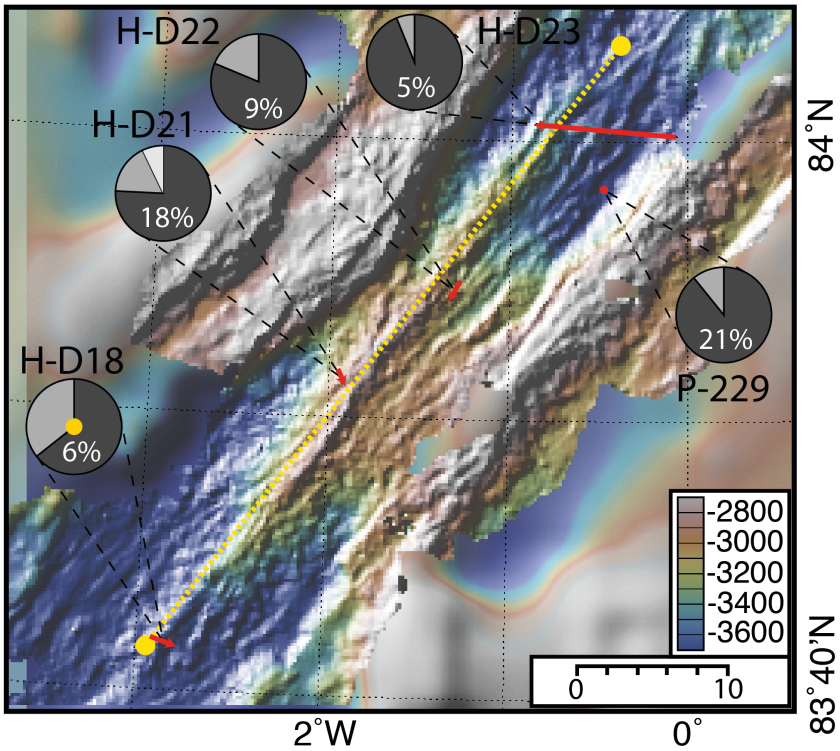

Fig. 8.1: Bathymetric map of 2°W Axial Volcanic Ridge. Pie charts represent the average proportions of plagioclase (dark grey), olivine (middle grey) and clinopyroxene (light grey) present in samples analysed from the dredges. Orange circles indicate the presence of spinel. White numbers show the total crystal content (this is an average if >1 sample was analysed from each dredge). Red dots indicate the on-bottom depth of each dredge; red arrows indicate the directions of dredges from on- to off-bottom depths. The yellow dashed line indicates the bathymetric profile line used for Fig. 8.2a. The bathymetric map was made using GeoMapApp and uses a combination of bathymetric data from the Global Multi-Resolution Topography (Ryan et al. 2009) and data from the AMORE 2001 expedition (e.g., Michael et al. 2003).

8.2.1.1 Local-scale geochemical and textural variation

Multiple geochemical and textural parameters show systematic variations from the centre to flanks of this AVR (Fig. 8.2). A decrease in total crystal content from 17.5% at the centre to ~6% at both flank locations (Fig. 8.2b) correlates with increases in median glass Mg# and temperature (Fig. 8.2c,d); $Na_{8.0}$ and K/Ti show no systematic change along the AVR (Fig. 8.2e,f). Similarly, both median plagioclase core anorthite (excepting H-D23) and olivine core forsterite content increase from H-D21 towards the flanks (Fig. 8.2g,h). The only textural parameter that changes systematically towards the flanks is resorption location with external resorption becoming more common (Fig. 8.2l); the number of skeletal olivine crystals (Fig. 8.2j), zoning complexity (Fig. 8.2k) and the type of zoning after resorption events (Fig. 8.2m) do not change systematically away from the centre. Plagioclase core compositions, zoning complexity and types of resorption (both location and zoning) in the valley wall sample (P-229) are similar to on-axis samples. Crystal contents of this dredge are most similar to H-D21 at the centre.

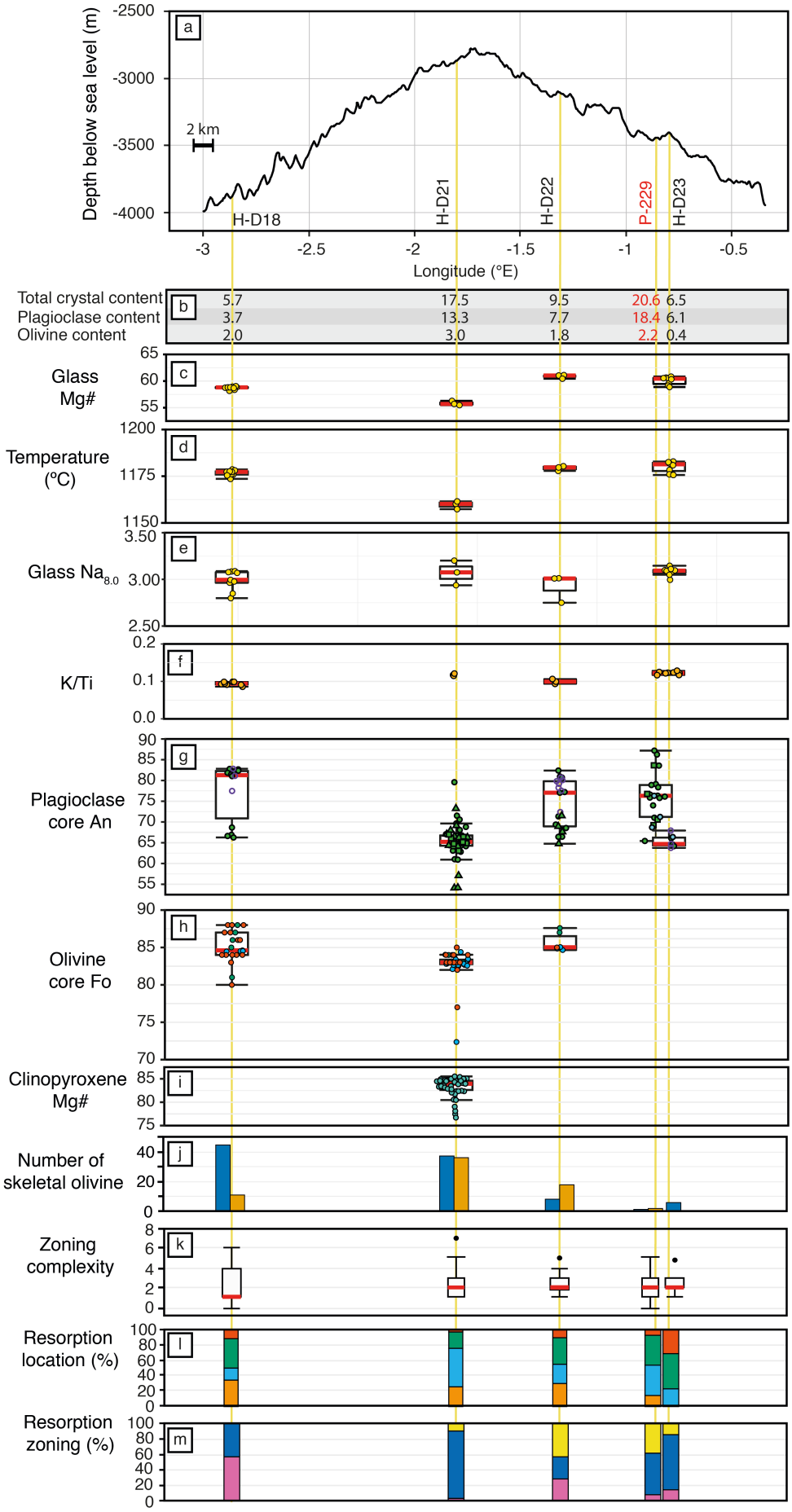
a
Depth below sea level (m)
-2500
-3000
-3500
-4000
2 km
H-D18
H-D21
H-D22
P-229
H-D23
-3
-2.5
-2
-1.5
-1
-0.5
Longitude (°E)
b
Total crystal content 5.7 17.5 9.5 20.6 6.5
Plagioclase content 3.7 13.3 7.7 18.4 6.1
Olivine content 2.0 3.0 1.8 2.2 0.4
c
Glass Mg#
d
Temperature (°C)
e
Glass Na8.0
f
K/Ti
g
Plagioclase core An
h
Olivine core Fo
i
Clinopyroxene Mg#
j
Number of skeletal olivine
k
Zoning complexity
l
Resorption location (%)
m
Resorption zoning (%)

← **Fig. 8.2:** Local-scale variation at 2°W Axial Volcanic Ridge. **a** Bathymetric profile of 2°W Axial Volcanic Ridge; on-axis and valley wall samples are shown in black and red respectively. **b** Variations in average total crystal, olivine and plagioclase content. Glass geochemistry: Mg# (**c**); temperature (**d**)**;** $Na_{8.0}$ (**e**); and K/Ti (**f**). Mineral chemistry: plagioclase core anorthite (**g**); olivine core forsterite (**h**); and clinopyroxene Mg# (**i**). **j** Absolute number of both individual skeletal olivine and skeletal olivine in poly-mineralic glomerocrysts. Plagioclase textures: zoning complexity (**k**); resorption location (**l**); and type of zoning following resorption events (**m**)**.** Symbols in **g-i** are the same as in Figure 7.12.

8.2.2 18°50'E Basement Ridge (Fig. 8.3)

The 18°50'E Basement Ridge is by far the most conspicuous volcanic feature in the SMZ (Fig. 2.5; Fig. 8.3). From its on-axis high to its flank, it has a relief of ~2.3 km, and it extends as a significant off-axis topographic feature for 98 km to the southeast and 80 km to the northwest. Dredges have been collected from within the axial valley and from the valley walls; the westernmost dredge (P-199) samples a seamount. The transect runs from 5188 to 3432 mbsl. The centre of the magmatic system is located between dredges P-253 and P254, with dredges P-318 and P-199 located at the flanks. A single sample, P-251, has been dredged from the southern valley wall. The number of samples studied from each dredge is shown in Table 8.2.

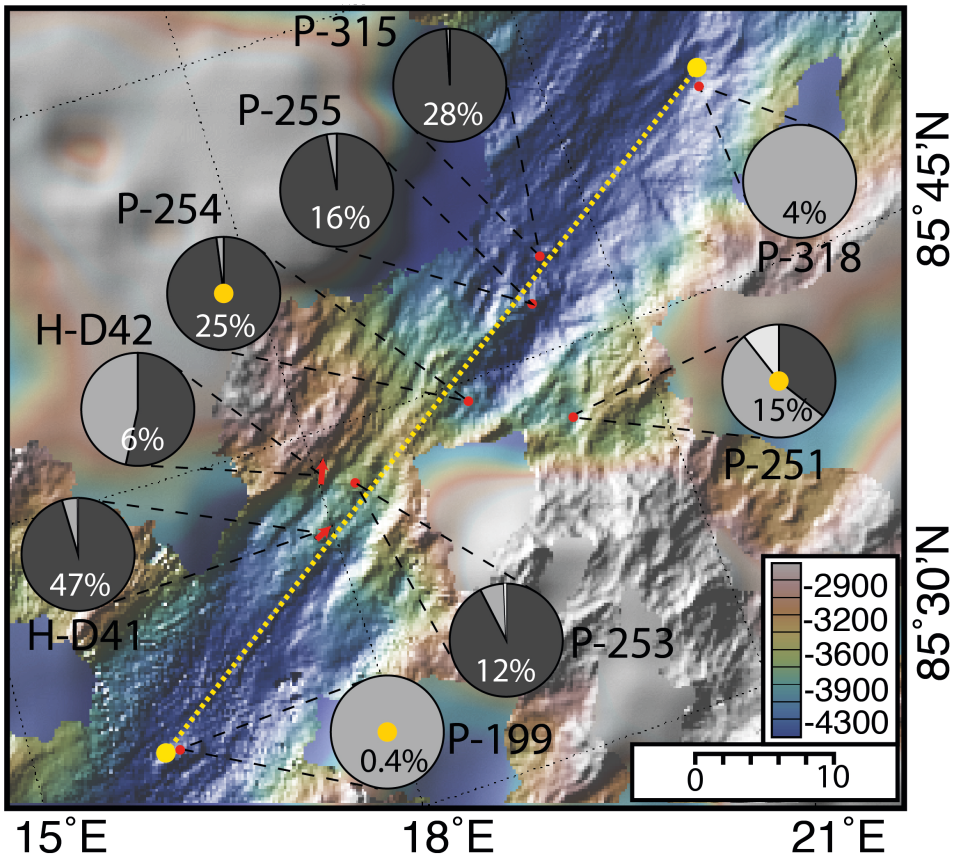

Fig. 8.3: Bathymetric map of 18°50'E Basement Ridge. Pie charts and all symbols shown are the same as in Fig. 8.1. Yellow dashed line corresponds to the bathymetric profile line in Fig. 8.4a**.**

Table 8.2 Number of sample analysed from each dredge at 18°50'E Basement Ridge

	Dredge								
	P-199	H-D41	P-253	H-D42	P-254	P-251	P-255	P-315	P-318
Number of samples	3	4	1	1	1	3	4	1	3

8.2.2.1 Local-scale geochemical and textural variation

Dredges located in the central ~27 km of the magmatic system (H-D41 to P-315) do not show any systematic changes in crystal content; samples are plagioclase-rich and have total crystal contents of 6-47% (Fig. 8.4b). Similarly, plagioclase compositions do not change systematically and show similar median values (excepting P-253) and ranges regardless of their position on the axis or valley wall (P-251) (Fig. 8.4g). In comparison, flank locations are olivine-rich and have total crystal contents <4% (Fig. 8.4b). The core forsterite contents of olivine at the flanks, especially olivine from dredge P-318, are more evolved than those at the centre of the system; olivine in P-251 (i.e., valley wall) is moderately more primitive than olivine at the ridge axis (Fig. 8.4h). The decrease in olivine core forsterite correlates with the decrease in median glass Mg# towards the flanks (Fig. 8.4c). Whilst median glass temperatures generally mirror glass Mg# and decreases towards the flanks (Fig. 8.4d), glasses from P-199 show elevated temperatures contrary to that shown by glass Mg#. Both $Na_{8.0}$ and K/Ti are variable along the ridge, especially the latter, however they do not vary systematically along the ridge (Fig. 8.4e,f); K/Ti is the lowest and most variable at P-199, whilst $Na_{8.0}$ is the lowest at P-318. There is also no systematic relationship between K/Ti and $Na_{8.0}$.

The only textural parameter that changes from the centre to the flanks (P-199) is zoning complexity (Fig. 8.4k). At P-199 the median zoning complexity is lower, and the range is smaller than in dredges located between H-D41 and P-315.

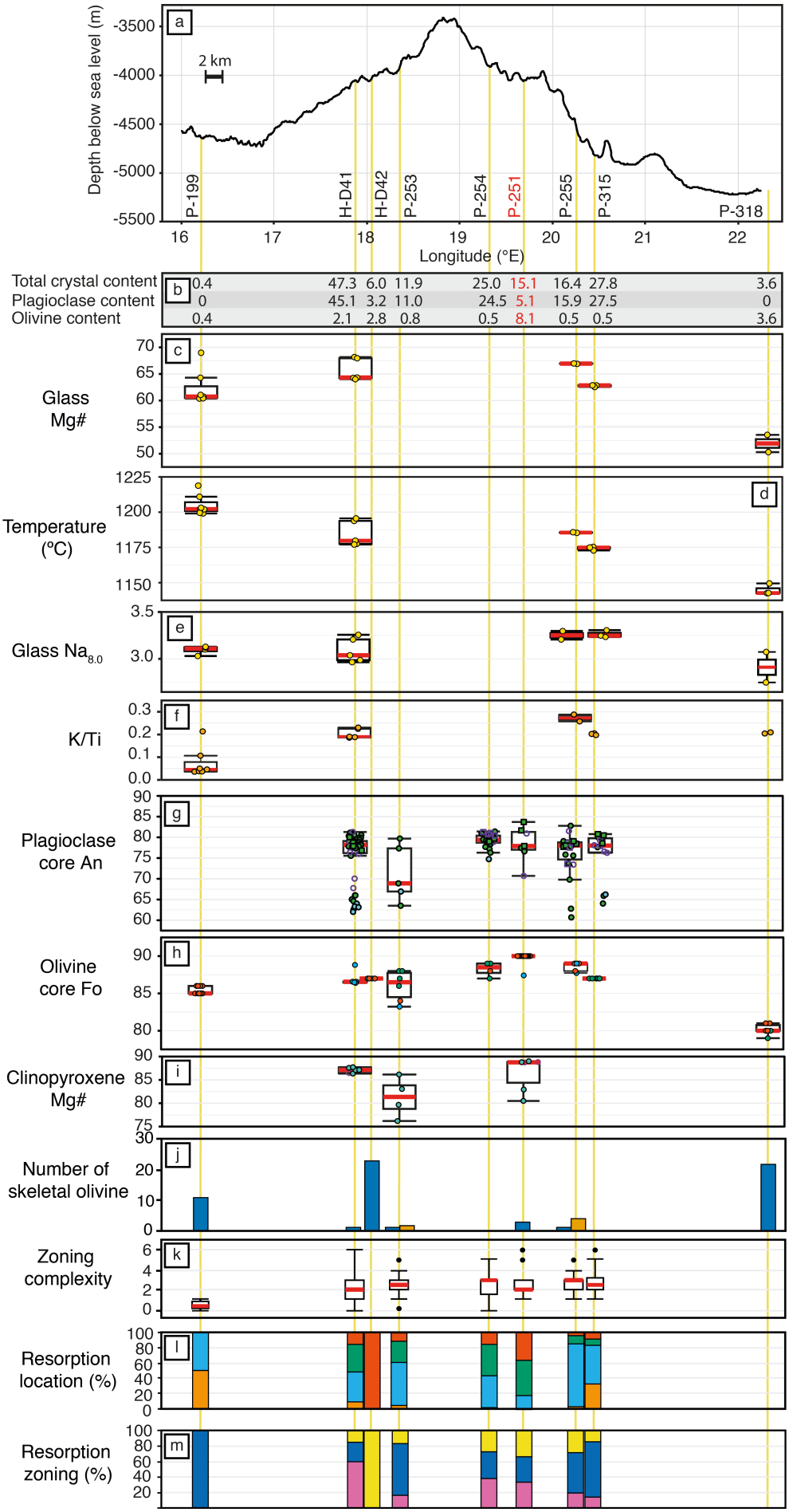
a
Depth below sea level (m)
-3500
-4000
-4500
-5000
-5500
2 km
P-199
H-D41
H-D42
P-253
P-254
P-251
P-255
P-315
P-318
16
17
18
19
20
21
22
Longitude (°E)
Total crystal content
Plagioclase content
Olivine content
b
0.4
47.3 6.0 11.9
25.0 15.1 16.4 27.8
3.6
0
45.1 3.2 11.0
24.5 5.1 15.9 27.5
0
0.4
2.1 2.8 0.8
0.5 8.1 0.5 0.5
3.6
c
Glass Mg#
70
65
60
55
50
d
Temperature (°C)
1225
1200
1175
1150
e
Glass Na8.0
3.5
3.0
f
K/Ti
0.3
0.2
0.1
0.0
g
Plagioclase core An
90
85
80
75
70
65
60
h
Olivine core Fo
90
85
80
i
Clinopyroxene Mg#
90
85
80
75
j
Number of skeletal olivine
30
20
10
0
k
Zoning complexity
6
4
2
0
l
Resorption location (%)
100
80
60
40
20
0
m
Resorption zoning (%)
100
80
60
40
20

← **Fig. 8.4:** Local-scale variation at 18°50'E Basement Ridge. See Figure 8.2 caption for explanation of symbols used in each of the panels.

8.3 Discussion

Using the results presented above, the following discussion will focus on the degree to which melt transport at the Gakkel Ridge is vertical and/or lateral.

8.3.1 Melt transport at the Gakkel Ridge: 2°W Axial Volcanic Ridge and 18°50'E Basement Ridge

Geochemically, trends of increasing degree of fractionation and crystal content away from magmatic centres towards the flanks have previously been interpreted as evidence for lateral melt transport (e.g., Thompson et al. 1985). In addition to glass Mg# and crystal content, glass K/Ti ratios can be used to examine melt transport; K/Ti ratios are often used to interpret variations in mantle source compositions (e.g., Standish et al. 2008). If lateral transport has occurred from a central magma reservoir, one might expect K/Ti ratios to be similar at the centre and flanks; in contrast eruptions from reservoirs fed by different, or heterogenous, mantle sources would have different K/Ti. For example, spatial variations in K/Ti ratios between and within individual flow fields at the Galapagos Spreading Centre (e.g., Colman et al. 2012) demonstrate that not only does the composition of the mantle source change temporally, but that multiple parent magmas from multiple mantle sources are involved in individual eruptions.

K/Ti ratios at 2°W AVR show minimal lateral variation (Fig. 8.2f), consistent with lateral transport away from a central reservoir. However, basalts become progressively more primitive (i.e., higher Mg# and temperature; Fig. 8.2c,d) and crystal-poor towards the flanks (Fig. 8.2b). Mirroring basalt compositions, on the whole plagioclase and olivine compositions become more primitive towards the distal portions of the AVR (Fig. 8.2 g,h). These trends are inconsistent with increased degrees of fractionation and crystal content during lateral transport outward from a central magmatic centre. One way to explain the observed spatial variations is if the nature of the erupted products changes temporally during the eruption. Indeed, early eruption products may have been characterised by primitive basalts that were transported, upon eruption, laterally towards the flanks of the AVR; as the eruption proceeds more crystal-rich regions of the plumbing system, characterised by more evolved glass and mineral compositions, are erupted. These crystal-rich samples are restricted to the central region of the AVR due to their increased viscosity. However, if all eruptions are sourced from a single reservoir, one might have expected a greater overlap in plagioclase compositions; instead we observe a shift to more primitive plagioclase compositions toward the flanks. Alternatively,

observations at 2°W AVR can be reconciled in a model whereby following melt influx from a homogeneous mantle source (similar K/Ti ratios), the resulting magma reservoir evolves ununiformly, forming distinct regions which experience differing degrees of differentiation. Such non-uniform magma chamber evolution is similar to that proposed at the Rekjanes Ridge by Sinha et al. (1998). Here, they suggest that the magma reservoir does not form or crystallise at a uniform rate and can therefore comprise melt- and crystal-dominated regions at different stages of its evolution. It follows that these regions may evolve in isolation from one another. Whilst we have no direct constraints on crystallisation pressures at the flanks, it is possible, that similar to primitive melts erupted in Hawaii (e.g., Helz et al. 2015), more primitive melt and mineral compositions erupted at the flanks have been sourced from reservoirs at greater depths where hotter temperatures limit the extent of fractionation. Alternatively, primitive compositions may have been preserved if melts either bypassed the central magma reservoir (e.g., Sides et al. 2014) or resided for shorter timescales in the system than more evolved melts at the centre of the ridge as suggested in Chapter 7 for basalts erupted at 48°E Deep Seafloor. In order to determine which of the above scenarios is applicable to 2°W AVR, detailed seafloor mapping is needed to constrain whether samples are from the same eruptive unit. Either way, the AVR was fed predominantly vertically, delivering basalts with distinct crystallisation histories along different portions of the ridge.

Samples at the flanks of the 18°50'E Basement Ridge are more evolved (both glass and mineral compositions) than samples located towards the centre of the ridge. However, in contrast to 2°W AVR, K/Ti ratios at 18°50'E Basement Ridge are spatially variable (Fig. 8.4f). In principle, such variations could reflect variations in mantle source composition, extent of melting or fractionation. Firstly, the lack of correlation between $Na_{8.0}$ and K/Ti indicates that K/Ti is not a function of degree of partial melting. Secondly, the LLD of a primitive basalt from 18°50'E Basement Ridge shows only ~0.01 change in K/Ti over a large range of MgO (5.5-9.5%; Fig. 8.5), thus highlighting the inability of fractionation to explain the range of observed K/Ti (0.04-0.29) in this location. It is therefore likely that variations in K/Ti arise from variations in mantle source composition and that eruptions originate from reservoirs fed by melt influx from distinct mantle regions. Enhanced melt focussing in the mantle beneath 18°50'E Basement Ridge might allow melts from distinct regions to be collected together (Fig. 7.29). Subsequent intrusion of these melts into the vertically extensive magma plumbing system (Chapter 7) will result in regions of the plumbing system characterised by different K/Ti ratios; these magma reservoirs undergo differing degrees of evolution and maturation. Vertical transport from these regions results in the eruption of basalts that preserve evidence of

mantle source heterogeneity and differing extents of lithospheric evolution (i.e., magmatic fractionation). For example, the fractionated nature of samples at P-318 indicates that they have been sourced from a reservoir which has undergone protracted fractionation and maturation. In contrast, samples located closer to the centre of the magmatic system, with higher glass Mg# and temperatures (e.g., P-255), have been sourced from a reservoir that is not only fed by moderately more enriched melts, but that has also undergone less fractionation. For both magmatic systems discussed above, vertical transport from chemically distinct regions formed within the plumbing system results in the eruption of basalts whose geochemistry and crystal cargo do not support the occurrence of lateral melt transport. Whilst not discussed in detail in this chapter, spatial variation in K/Ti at 48°E Deep Seafloor (Appendix 3, Fig. A3.10l) supports the occurrence of vertical melt transport from chemically distinct mantle sources.

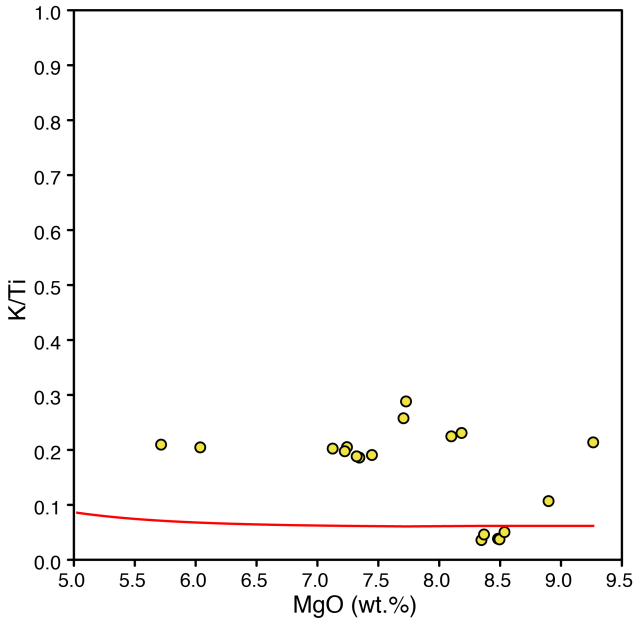

Fig. 8.5: K/Ti variation versus MgO of basalts from 18°50'E Basement Ridge. The liquid line of decent (LLD) of a primitive basalt from the region of 18°50'E Basement Ridge is shown by the red line. The LLD was modelled using rhyolite MELTS v.1.2 (Gaulda et al. 2012) using a pressure of 2.5 kbar, oxygen fugacity of QFM-1 and water content of 0.4 wt.%. The ΔK/Ti over 5.5-9.5 wt.% MgO is only ~0.01 and cannot account for the observed K/Ti in samples from 18°50'E Basement Ridge.

Furthermore, classical lateral dyke migration patterns are absent in teleseismic earthquake records from the Gakkel Ridge; these swarms are instead interpreted to reflect the complex interplay between dyking and fault reactivation over broad areas (Schlindwein 2012). To summarise, whereas lateral melt transport has been argued to occur at the ultraslow-spreading Southwest Indian Ridge (Cannat et al. 2006, 2008; Jian et al. 2017b), multiple lines of geochemical evidence from two magmatic systems of the

Gakkel Ridge are inconsistent with lateral melt transport, and are instead consistent with the occurrence of vertical transport.

8.4 Conclusions

Using a wide range of tools (e.g., basalt geochemistry, crystal contents, mineral geochemistry and textures and ridge bathymetry) it has been possible to constrain the mode of melt transport in several Gakkel Ridge magmatic systems. The data presented from two magmatic systems along the Gakkel Ridge are inconsistent with the occurrence of lateral transport from a centralised magmatic system. Instead spatial variations in geochemistry and crystal content at 2°W AVR and 18°50'E Basement Ridge are consistent with vertical melt transport from distinct regions of the plumbing system. Vertical melt transport is consistent with conclusions drawn from teleseismic earthquake records at 85°E where classical epicentre migration patterns, indicative of lateral melt transport seen to occur at fast-spreading ridges, are not observed.

Blank page

Chapter 9
Synthesis

Chapter 9

The research presented and discussed in Chapters 5 though 8 represents the first systematic and comprehensive crystal-scale study of the Gakkel Ridge magma plumbing system and addressed the following research questions introduced in Chapter 1:

- What is the relative importance of the different magmatic processes occurring within the Gakkel Ridge magma plumbing system, and what is their record on the crystal scale?
- What is the vertical extent of the Gakkel Ridge magma plumbing system?
- What is the physical nature (i.e., crystal vs. melt content and chemical maturity) of the Gakkel Ridge magma plumbing system?
- Do any of the above change along axis and/or correlate with spreading rate?

The following sections will directly address these questions by drawing together the findings from Chapters 5 through 8, placing them into a broader framework that addresses their implications not only for mid-ocean ridge plumbing systems but also mafic magmatic systems in other geo-tectonic settings.

9.1 Magmatic processes in mid-ocean ridge plumbing systems

Mid-ocean ridges are often seen as simple end-member magmatic systems due to their relatively uniform compositions (i.e., tholeiitic basalts), low water contents (Michael 1995; Danyushevsky 2001) and occurrence of either variable (Soule et al. 2012) or no volatile degassing (Saal et al. 2002). However, the observed variability and complexity in plagioclase textures and compositions presented in this thesis attest to the occurrence of complex magmatic processes; textures of individual crystals are a function of their respective histories of (under)cooling, magma mixing and decompression. Not only is the level of complexity comparable to that observed in some compositionally variable volcanic arc settings (e.g., Ginibre 2002; Ginibre and Worne 2007; Cashman and Blundy 2013), but importantly it demonstrates that even in systems that are nominally “simple”, magmatic processes can be complex. This adds to our growing understanding of the complexity of processes occurring within mid-ocean ridge plumbing systems (e.g., Pan and Batiza 2003; Ridley et al. 2006; Costa et al. 2009; Lange et al. 2013). Not only does the plagioclase database presented herein serve as a template for the interpretation of plagioclase textures in mid-ocean ridge basalts, it can serve as a basis for the classification of plagioclase textures in mafic magmatic systems elsewhere.

9.2 The melt inclusion record of crystallisation depths at mid-ocean ridges

Melt inclusions have been used extensively over the last decade to constrain the depths of magma chambers at mid-ocean ridges. However, to date the depths of crystallisation beneath on-axis mid-ocean ridge segments have been constrained exclusively using olivine-hosted melt inclusions. These studies have shown that crystallisation is generally restricted to depths of seismically imaged melt lenses (Wanless and Shaw 2012) and crustal depths (Wanless and Shaw 2012; Wanless et al. 2014b; Colman et al. 2015). Here, through the use of plagioclase-hosted melt inclusions, it has been shown, contrary to current constraints, that the magmatic plumbing systems, at least at ultraslow-spreading ridges, are vertically extensive and have roots that extend up to 16.4 km into the lithospheric mantle. Furthermore, the dichotomy identified between Gakkel Ridge olivine- and plagioclase-hosted melt inclusion pressures indicates that these two minerals are capturing different portions of the crystallisation record. Importantly, this dichotomy demonstrates that using olivine-hosted melt inclusions alone may provide a bias sampling of crystallisation processes beneath mid-ocean ridges because they record, in general, crystallisation occurring in the shallower portions of the plumbing system. This in part may explain the similarity in crystallisation pressures recorded by olivine-hosted melt inclusion from fast- to ultraslow-spreading mid-ocean ridges. If predictions of increased depths of crystallisation with decreasing spreading rate due to more efficient conductive cooling are correct (e.g., Reid and Jackson, 1981; Bown and White 1994; Coakley and Cochran 1998), systematically deeper crystallisation pressures would have been expected at slower spreading rates. This not only has implications for our ability to fully reconstruct the magmatic architecture of mid-ocean ridges, but also that of other mafic plumbing systems that traditionally rely on olivine-hosted melt inclusions alone. In order to ensure that crystallisation processes occurring within magmatic systems are not selectively sampled, melt inclusion crystallisation pressure studies, when possible, need to adopt a multi-mineral approach.

This study also highlights the importance of understanding the textures and growth mechanisms of the host crystals, with many shallower crystallisation pressures occurring within skeletal olivine interpreted to grow during late-stage undercooling in shallow portions of the plumbing system. Similarly, the observation that morphologies of melt inclusions trapped in the plagioclase crystals are associated with specific host crystal textures indicates there is a link between plagioclase crystallisation processes and melt inclusion entrapment; again, this has important implications for the interpretation of melt inclusions and demonstrates the importance of understanding how particular mineral textures form.

9.3 The physical nature of the Gakkel Ridge magma plumbing system

Magma plumbing systems at fast- to slow-spreading ridges have been proposed to comprise regions of both melt and crystal mush (e.g., Sinton and Detrick 1992; Singh et al. 1998; Sinha et al. 1998; Marjanović et al. 2015; Lissenberg et al. 2019). The ultraslow-spreading Gakkel Ridge appears to be no different in that both modal data and mineral textures indicate the presence of both melt- and crystal-rich regions within the plumbing system. However, despite comparisons of modal data from fast- to ultraslow-spreading ridges that clearly illustrate plumbing systems are increasingly crystal-dominated at slower spreading rates, there is no systematic relationship between spreading rate and crystal content along the Gakkel Ridge. Whilst this in part reflects the small change in spreading rate along the Gakkel Ridge (3 $mmyr^{-1}$), it also suggests that the physical nature of the ultraslow-spreading plumbing system may not be a simple function of spreading rate. Indeed, variations in both the efficiency and degree of melt focussing and extent of partial melting likely play a major role at ultraslow-spreading ridges.

Similarly, spreading rate alone cannot account for variations in plumbing system maturity, volcanic morphology or crystallisation pressures observed at the Gakkel Ridge. Using glass and mineral chemistry it has been possible to identify magma plumbing systems and mush zones that represent different stages of maturity; much like chemical variations along the propagating Galapagos spreading ridge, maturity at the Gakkel Ridge can be related to variations in melt supply. Variations in melt supply along the Gakkel Ridge can be related to variations in the degree of melt focussing, and in the case of the WVZ, to large-scale tectonic rifting events. Indeed, the presence of the most mature plumbing systems within the WVZ can be related to the separation of Greenland and Svalbard that resulted in the influx of North Atlantic mantle into the WVZ and the onset of robust magmatism here. It is the enhanced degrees of partial melting in the WVZ that resulted in thinner lithosphere, and in turn, formation of shallower magma plumbing systems. In contrast, plumbing systems are poorly developed or absent in regions of decreased partial melting. Here, seamount volcanism is common, and melts may ascend from depth without undergoing significant compositional modification. As melt focussing increases, the time averaged melt supply to a single point along the ridge is increased. This leads to the formation of long-lived, vertically extensive magma plumbing systems that manifest on the seafloor as large circular volcanic edifices and basement-perpendicular ridges. In some instances, enhanced melt focussing can generate conditions within the lithosphere that are favourable to the occurrence of enhanced degrees of magmatic fractionation; such conditions result in the eruption of highly variable glass and mineral compositions.

Whilst the nature of the Gakkel Ridge magma plumbing system does not correlate with spreading rate, comparisons of glass chemistry from the Gakkel Ridge, East Pacific Rise and Mid-Atlantic Ridge demonstrate that the East Pacific Rise, where melt supply is higher, is characterised by lower crystal contents and more evolved glass compositions than the Gakkel Ridge. This indicates that at the global scale there is a relationship between the nature of the plumbing systems and spreading rate that relates to melt supply. Importantly, unlike glass chemistry, mineral chemistry appears to be decoupled from spreading rate. Additionally, whilst it was expected that clinopyroxene would be a more common phase in Gakkel Ridge basalts due to the occurrence of melt evolution at higher pressures, the abundance of clinopyroxene in basalts from the East Pacific Rise, which have relatively more evolved compositions, suggests that the presence of clinopyroxene in basalts is a function of the extent of fractionation, not pressure of melt evolution.

9.4 Future work

This investigation, though comprehensive, only characterises the physical nature of the Gakkel Ridge magma plumbing system and processes occurring within it. In the future, seismic studies would allow further constraints to be placed on the physical state (i.e., crystal vs. melt content) and vertical extent of the Gakkel Ridge magma plumbing system. To gain a more comprehensive understanding of this magma plumbing system, it is important that future studies seek to understand its geochemical nature. For example detailed crystal-scale isotope studies, both on individual grains and melt inclusions, will help to address questions such as:

- How heterogenous is the mantle beneath the Gakkel Ridge, and does its composition change along axis?
- Do melt inclusions preserve a greater range in isotopic variability than mid-ocean ridge basalts?
- Is the isotopic record of olivine- and plagioclase-hosted melt inclusions different?
- Do melt inclusions trapped at different pressures preserve different isotopic records?

In addition, diffusion studies of both olivine and plagioclase will provide further information on the timescales of magmatic processes such as magma mixing and mush disaggregation as well as magma transport. Finally, in order to fully understand if and/or how the physical nature and processes occurring within mid-ocean ridge magma plumbing systems change with spreading rate, further systematic and quantitative studies of basalt crystal cargo, including both textural and melt inclusion studies, from additional ridge segments at a range of spreading rates are needed. This will help address the following questions:

- Is the crystallisation pressure record of plagioclase-hosted melt inclusions spreading rate dependent?
- Do plagioclase-hosted melt inclusions provide a more extensive record of crystallisation occurring at mid-ocean ridges than olivine-hosted melt inclusions?
- Does the relative importance of specific magmatic processes change across the full spreading rate spectrum?
- Do the timescales of magmatic processes such as magma mixing vary with spreading rate?

Bibliography

Allan J.F., Batiza, R., Perfit M.R. et al. 1989. Petrology of lavas from the Lamont seamount chain and adjacent East Pacific Rise, 10 N. *Journal of Petrology*, 30:1245-1298.

Allègre C.J., Hamelin B. and Dupré B.1984. Statistical analysis of isotopic ratios in MORB: the mantle blob cluster model and the convective regime of the mantle. *Earth and Planetary Science Letters,* 71:71–84. doi: 10.1016/0012-821X(84)90053-0

Allison, C.M., Roggensack, K. and Clarke, A.B. 2019. H_2O–CO_2 solubility in alkali-rich mafic magmas: new experiments at mid-crustal pressures. Contributions to Mineralogy and Petrology, 174;58.

Anderson A.T. and Brown G.G. 1993. CO_2 contents and formation pressures of some Kilauean melt inclusions. *American Mineralogist,* 78:794–803

Anonymous, 1972. Penrose field conference on ophiolites. *Geotimes*, *17*(12), pp.24-25.

Batiza R. and Niu Y.L. 1992. Petrology and Magma Chamber Processes at the East Pacific Rise 9°30'N. *Journal of Geophysical Research: Solid Earth,* 97:6779–6797. doi: 10.1029/92jb00172

Batiza R., Allan, J.F., Bach, W. et al. 1995. Petrology, geochemistry, and petrogenesis of Leg 142 basalts—synthesis of results. *In* Batiza, R., Storms, M.A., and Allan, J.F. (eds.), *Proceedings of the ODP, Science Results,* 142: College Station, TX (Ocean Drilling Program), 3–8. doi:10.2973/odp.proc.sr.142.101.1995

Batiza R., Niu Y.L., Karsten J.L., et al. 1996. Steady and non-steady state mamgma chembers below the East Pacific Rise. *Geophysical Research Letters,* 7:486–508. doi: 10.1063/1.2756072

Batiza R., Rosendahl B.R. and Fisher R.L. 1977. Evolution of oceanic crust: 3. Petrology and chemistry of basalts from the East Pacific Rise and the Siqueiros Transform Fault. *Journal of Geophysical Research,* 82:265–276. doi: 10.1029/jb082i002p00265

Bédard J.H. 2005. Partitioning coefficients between olivine and silicate melts. *Lithos*, 83:394–419. doi: 10.1016/j. Lithos.2005.03.011

Bergmanis E.C., Sinton J. and Rubin K.H. 2007. Recent eruptive history and magma reservoir dynamics on the southern East Pacific Rise at 17°30'S. *Geochemistry, Geophysics, Geosystems*. doi: 10.1029/2007GC001742

Berry A.J., Stewart G.A., O'Neill H.S.C., et al. 2018. A re-assessment of the oxidation state of iron in MORB glasses. *Earth and Planetary Science Letters*, 483:114–123. doi: 10.1016/j.epsl.2017.11.032

Blundy, J. and Cashman, K. 2005. Rapid decompression-driven crystallization recorded by melt inclusions from Mount St. Helens volcano. *Geology*, *33:*793-796.

Blythe A.E. and Kleinspehn K.L. 1998. Tectonically versus climatically driven Cenozoic exhumation of the Eurasian plate margin, Svalbard: Fission track analyses. *Tectonics,* 17:621. doi: 10.1029/98TC01890

Bottinga Y. and Weill D.F. 1972. The viscosity of magmatic silicate liquids: a model for calculation. *American Journal of Science,* 438–475

Bottinga Y., Kudo A. and Weill D.1966. Some observations on oscillatory zoning and crystallization of magmatic plagioclase. *American Mineralogist,* 51:792

Bouvet de Maisonneuve C., Costa F., Huber C., et al. 2016. How do olivines record magmatic events? Insights from major and trace element zoning. *Contributions to Mineralogy and Petrology,* 171:1–20. doi: 10.1007/s00410-016-1264-6

Bown J.W. and White R.S. 1994. Variation with spreading rate of oceanic crustal thickness and geochemistry. *Earth and Planetary Science Letters,* 121:435–449. doi: 10.1016/0012-821X(94)90082-5

Brozena J.M., Childers V.A., Lawver L.A., et al. 2003. New aerogeophysical study of the Eurasia Basin and Lomonosov Ridge: Implications for basin development. *Geology*, 31:825–828. doi: 10.1130/G19528.1

Bryan W. 1979. Regional variation and petrogenesis of basalt glasses from the FAMOUS area, Mid-Atlantic Ridge. *Journal of Petrology*, 20:293-325.

Bryan W.B. 1983. Systematics of modal phenocryst assemblages in submarine basalts: petrological implications. *Contributions to Mineralogy and Petrology,* 83:62–74

Bryan W.B., Thompson, G. and Ludden, J.N. 1981. Compositional variation in normal MORB from 22°–25° N: Mid-Atlantic Ridge and Kane Fracture Zone. *Journal of Geophysical Research: Solid Earth*, 86:11815-11836.

Canales J.P., Detrick R.S., Carbotte S.M., et al. 2005. Upper crustal structure and axial topography at intermediate spreading ridges: seismic constraints from the southern Juan de Fuca Ridge. *Journal of Geophysical Research*: *Solid Earth,* 110:1–27. doi: 10.1029/2005JB003630

Cann J.R. 1974. A model for mid oceanic crustal structure developed. *Geophysical Journal International,* 39:169–187. doi: 10.1111/j.1365-246X.1974.tb05446.x

Cannat M., Céline R.J. and Fujimoto H. 2003. Melt supply variations to a magma-poor

ultra-slow spreading ridge (Southwest Indian Ridge 61° to 69°E). *Geochemistry, Geophys Geosyste,* 4:1–21. doi: 10.1029/2002GC000480

Cannat M., Sauter D., Bezos A., et al. 2008. Spreading rate, spreading obliquity, and melt supply at the ultraslow spreading Southwest Indian Ridge. *Geochemistry, Geophyics, Geosystems*, 9:1–26. doi: 10.1029/2007GC001676

Cannat M., Sauter D., Mendel V., et al. 2006. Modes of seafloor generation at a melt-poor ultraslow-spreading ridge. *Geology*, 34:605–608. doi: 10.1130/G22486.1

Carbotte S.M., Marjanović M., Carton H., et al. 2013. Fine-scale segmentation of the crustal magma reservoir beneath the East Pacific Rise. *Nature Geoscience,* 6:866–870. doi: 10.1038/ngeo1933

Carbotte, S., Mutter, C., Mutter, J. et al. 1998. Influence of magma supply and spreading rate on crustal magma bodies and emplacement of the extrusive layer: Insights from the East Pacific Rise at lat 16°N. *Geology*, *26*:455-458.

Cashman K. and Blundy J. 2013. Petrological cannibalism: The chemical and textural consequences of incremental magma body growth. *Contributions to Mineralogy and Petrology,* 166:703–729. doi: 10.1007/s00410-013-0895-0

Cashman K.V., Sparks R.S.J. and Blundy J.D. 2017. Vertically extensive and unstable magmatic systems: A unified view of igneous processes. *Science,* 355. doi: 10.1126/science.aag3055

Chakraborty S. 1997. Rates and mechanisms of Fe-Mg interdiffusion in olivine at 980°–1300°C. *Journal of Geophysical Research,* 102:12317. doi: 10.1029/97jb00208

Chakraborty S. 2008. Diffusion in Solid Silicates: A Tool to Track Timescales of Processes Comes of Age. *Annual Review of Earth and Planetary Sciences,* 36:153–190. doi: 10.1146/annurev.earth.36.031207.124125

Chen Y.J. and Lin J. 2004. High sensitivity of ocean ridge thermal structure to changes in magma supply: The Galápagos Spreading Center. *Earth and Planetary Science Letters*, 221:263–273. doi: 10.1016/S0012-821X(04)00099-8

Chesner C.A. and Luhr J.F. 2010. A melt inclusion study of the Toba Tuffs, Sumatra, Indonesia. Journal of Volcanology and Geothermal Research 197:259–278. doi: 10.1016/j.jvolgeores.2010.06.001

Christie D.M. and Sinton J.M. 1981. Evolution of abyssal lavas along propagating segments of the Galapagos spreading center. Earth and Planetary Science Letters 56:321–335. doi: 10.1016/0012-821X(81)90137-0

Ciazela J., Dick, H.J., Koepke, J., et al. 2017. Thin crust and exposed mantle control sulfide differentiation in slow-spreading ridge magmas. *Geology*, *45*:935-938.

Coakley B.J. and Cochran J.R. 1998. Gravity evidence of very thin crust at the Gakkel Ridge (Arctic Ocean). Earth and Planetary Science Letters 162:81–95. doi: 10.1016/S0012-821X(98)00158-7

Cochran J.R. 2003. The Gakkel Ridge: Bathymetry, gravity anomalies, and crustal accretion at extremely slow spreading rates. *Journal of Geophysical Research*. doi: 10.1029/2002JB001830

Cochran J.R. 2005. Northern Red Sea: Nucleation of an oceanic spreading centre within a continental rift. *Geochemistry, Geophysics, Geosystems*, *6*.

Cochran J.R. 2008. Seamount volcanism along the Gakkel Ridge, Arctic Ocean. Geophys J Int 174:1153–1173. doi: 10.1111/j.1365-246X.2008.03860.x

Colman A., Sinton J.M. and Wanless V.D. 2015. Constraints from melt inclusions on depths of magma residence at intermediate magma supply along the Galápagos Spreading Center. Earth and Planetary Science Letters 412:122–131. doi: 10.1016/j.epsl.2014.12.007

Colman A., Sinton J.M., White S.M., et al. 2012. Effects of variable magma supply on mid-ocean ridge eruptions: Constraints from mapped lava flow fields along the Galápagos Spreading Center. Geochemistry, Geophysics, Geosystems, 13. doi: 10.1029/2012GC004163

Connelly D.P., Copley J.T., Murton B.J., et al. 2012. Hydrothermal vent fields and chemosynthetic biota on the world's deepest seafloor spreading centre. Nature Communications, 3. doi: 10.1038/ncomms1636

Coogan L. A. 2014. The lower oceanic crust. In: Turekian, K. K.& Holland, H. D. (eds) Treatise on Geochemistry, 2nd edn. Elsevier, pp. 497–541.

Coote A.C. and Shane P. 2016. Crystal origins and magmatic system beneath Ngauruhoe volcano (New Zealand) revealed by plagioclase textures and compositions. Lithos 260:107–119. doi: 10.1016/j.lithos.2016.05.017

Cordier C., Benoit M., Hémond C., et al. 2010. Time scales of melt extraction revealed by distribution of lava composition across a ridge axis. Geochemistry, Geophys Geosystems 11. doi: 10.1029/2010GC003074

Costa F. and Dungan M. 2005. Short time scales of magmatic assimilation from diffusion modeling of multiple elements in olivine. Geology 33:837. doi: 10.1130/G21675.1

Costa F., Chakraborty S. and Dohmen R. 2003. Diffusion coupling between major and trace elements and a model for the calculation of magma chamber residence times

using plagioclase. Geochim Cosmochim Acta 67:2189–2200. doi: 10.1016/S0016-7037(00)01345-5

Costa F., Coogan L.A. and Chakraborty S. 2009. The time scales of magma mixing and mingling involving primitive melts and melt-mush interaction at mid-ocean ridges. Contributions to Mineralogy and Petrology159:371–387. doi: 10.1007/s00410-009-0432-3

Coumans J.P., Stix J., Clague D.A. and Minarik W.G. 2015 The magmatic architecture of Taney Seamount-A, NE Pacific Ocean. *Journal of Petrology,* 56:1037–1067. doi: 10.1093/petrology/egv027

Coumans J.P., Stix J., Clague D.A., et al. 2016. Melt-rock interaction near the Moho: Evidence from crystal cargo in lavas from near-ridge seamounts. Geochim Cosmochim Acta 191:139–164. doi: 10.1016/j.gca.2016.07.017

Crawford W. C. and Webb S. C. 2002. Variations in the distribution of magma in the lower crust and at the Moho beneath the East Pacific Rise at 9°–10°N. *Earth and Planetary Science Letters,* 203:117–130.

Crawford W.C., Webb S.C., Hildebrand J.A. and Rise N. 1999. Constraints on melt in the lower crust and Moho at the East Pacific Rise, 9°48'N, using seafloor compliance measurements. *Journal fo Geophysical Research: Solid Earth,* 104:2923–2939

Crisp J.A. 1984. Rates of magma emplacement and volcanic output. *Journal of Volcanology and Geothermal Research,* 20:177–211. doi: 10.1016/0377-0273(84)90039-8

Cullen A., Vicenzi E. and McBirney A.R. 1989. Plagioclase-ultraphyric basalts of the Galapagos Archipelago. *Journal of Volcanology and Geothermal Research,* 37:325–337. doi: 10.1016/0377-0273(89)90087-5

D'Errico M.E., Warren J.M. and Godard M. 2016. Evidence for chemically heterogeneous Arctic mantle beneath the Gakkel Ridge. *Geochimica et Cosmochimica Acta,* 174:291–312. doi: 10.1016/j.gca.2015.11.017

Danyushevsky L.V. 2001. The effect of small amounts of H_2O on crystallisation of mid-ocean ridge and backarc basin magmas. *Journal of Volcanology and Geothermal Research,* 110:265–280. doi: 10.1016/S0377-0273(01)00213-X

Danyushevsky L.V., McNeill A.W. and Sobolev A.V. 2002. Experimental and petrological studies of melt inclusions in phenocrysts from mantle-derived magmas: an overview of techniques, advantages and complications. *Chemical Geology,* 183:5–24. doi: 10.1016/S0009-2541(01)00369-2

Danyushevsky, L.V. and Plechov, P. 2011. Petrolog3: Integrated software for modelling crystallization processes. Geochemistry, Geophysics, Geosystems, 12.

DeMets C., Gordon R.G., Argus D.F. and Stein S. 1990. Current plate motions. *Geophysical Journal International,* 101:425–478. doi: 10.1111/j.1365-246X.1990.tb06579.x

Detrick R.S., Buhl P., Vera E., et al. 1987. Multi-channel seismic imaging of a crustal magma chamber along the East Pacific Rise. *Nature,* 326:35

Dick H.J.B., Lin J. and Schouten H. 2003. An ultraslow-spreading class of ocean ridge. *Nature*, 426:405–412. doi: 10.1038/nature02128

Dick H.J.B., Tivey M.A. and Tucholke B.E. 2008. Plutonic foundation of a slow-spreading ridge segment: Oceanic core complex at Kane Megamullion, 23°30′N, 45°20′W. *Geochemistry, Geophysics, Geosystems*. doi: 10.1029/2007GC001645

Dick, H.J. and Bullen, T. 1984. Chromian spinel as a petrogenetic indicator in abyssal and alpine-type peridotites and spatially associated lavas. *Contributions to mineralogy and petrology*, 86:54-76.

Dick, H.J., Natland, J.H. and Ildefonse, B. 2006. Deep drilling in the oceanic crust and mantle. *Oceanography, 19:.*72-80.

Dixon J.E. and Stolper E.M. 1995. An experimental study of water and carbon dioxide solubilities in mid-ocean ridge basaltic liquids. Part II: Applications to degassing. *Journal of Petrology,* 36:1633–1646

Dixon J.E., Stolper E.M. and Holloway, J.R. 1995. An experimental study of water and carbon dioxide solubilities in mid-ocean ridge basaltic liquids Part I: Calibration and solubility models. *Journal of Petrology,* 36:1607–1631

Dmitriev, Y.I. 1980. Basalts from the East Pacific Rise near 9°N drilled on DSDP Leg 54 compared with marginal-basin and ocean-island basalts. *Initial Reports of the Deep Sea Drilling Project*, 54:695-704.

Drignon M.J., Nielsen R.L., Tepley F.J. and Bodnar R.J. 2018. Upper mantle origin of plagioclase megacrysts from plagioclase-ultraphyric mid-oceanic ridge basalt. *Geology*, 47:43–46. doi: 10.1130/g45542.1

Dungan M.A., Long P.E. and Rhodes J.M. 1978. Magma mixing at mid-ocean ridges: evidence from Legs 45 and 46-DSDP. *Geophysical Research Letters,* 5:423–425

Dungan M.A., Long P.E. and Rhodes J.M. 1979. The petrography, mineral chemistry, and one-atmosphere phase relations of basalts from Site 395. *Initial Reports Deep Sea Drilling Project,* 45. doi: 10.2973/dsdp.proc.45.120.1979

Dunn R.A., Lekić V., Detrick R.S. and Toomey D.R. 2005. Three-dimensional seismic structure of the Mid-Atlantic Ridge (35°N): Evidence for focused melt supply and lower crustal dike injection. *Journal of Geophysical Research*: *Solid Earth,* 110:1–17. doi: 10.1029/2004JB003473

Dziak R.P. and Fox C.G. 1999. The January 1998 earthquake swarm at axial volcano, Juan de Fuca Ridge: Hydroacoustic evidence of seafloor volcanic activity. *Geophysical Research Letters,* 26:3429–3432. doi: 10.1029/1999GL002332

Dziak R.P., Fox G. and Schreiner A.E. 1995 The June-July 1993 seismo-acoustic event at CoAxial segment, Juan de Fuca Ridge: Evidence for a lateral dike injection. *Geophysical Research Letters,* 22:135–138. doi: 10.1029/94GL01857

Eguchi, J. and Dasgupta, R. 2018. A CO_2 solubility model for silicate melts from fluid saturation to graphite or diamond saturation. Chemical Geology, 487: 23-38.

Einarsson P. and Brandsdottir B. 1978. Seismological evidence for Lateral magma intrusion during the July 1978 deflation of the Krafla volcano in NE-Iceland. *Journal of Geophysics*, 47:160–165. doi: 10.2172/890964

Elderfield H. and Schultz A. 1996. Mid-Ocean Ridge Hydrothermal Fluxes and the Chemical Composition of the Ocean. *Annual Review of Earth and Planetary Sciences,* 24:191–224. doi: 10.1146/annurev.earth.24.1.191

Elkins L.J., Sims K.W.W., Prytulak J., et al. 2014. Melt generation beneath Arctic Ridges: Implications from U decay series disequilibria in the Mohns, Knipovich, and Gakkel Ridges. *Geochimica et Cosmochimica Acta*, 127:140-170

Eriksson P.I., Riishuus M.S., Sigmundsson F. and Elming S.Å. 2011. Magma flow directions inferred from field evidence and magnetic fabric studies of the Streitishvarf composite dike in east Iceland. *Journal of Volcanology and Geothermal Research*, 206:30–45. doi: 10.1016/j.jvolgeores.2011.05.009

Escrig S., Capmas F., Dupre B. and Allegre C.J. 2004. Osmium isotopic constraints on the nature of the DUPAL anomaly from Indian mid-ocean ridge basalts. *Nature*, 431:59–63. doi: 10.1029/2004GL019911

Faure F. and Schiano P. 2004. Crystal morphologies in pillow basalts: implications for mid-ocean ridge processes*. Earth and Planetary Science Letters*, 220:331–344. doi: 10.1016/S0012-821X(04)00057-3

Faure F. and Schiano P. 2005. Experimental investigation of equilibration conditions during forsterite growth and melt inclusion formation. *Earth and Planetary Science Letters,* 236:882–898. doi: 10.1016/j.epsl.2005.04.050

Flower M.F.J. 1980. Accumulation of calcic plagioclase in ocean-ridge tholeiite: an

indication of spreading rate? *Nature,* 287.

Flower, M.F.J., Ohnmacht, W., Schmincke, H.U. et al. 1979. Petrology and geochemistry of basalts from Hole 396B, Leg 46. *Initial Reports of the Deep Sea Drilling Project*, 46:179-213.

Fox C.G. and Dziak R.P. 1998. Hydroacoustic detection of volcanic activity on the Gorda Ridge, February-March 1996. *Deep Res Part II: Topical Studies in Oceanography,* 45:2513–2530. doi: 10.1016/S0967-0645(98)00081-2

Francheteau, J., Armijo, R., Cheminée, J.L. et al. 1990. 1 Ma East Pacific Rise oceanic crust and uppermost mantle exposed by rifting in Hess Deep (equatorial Pacific Ocean). *Earth and Planetary Science Letters*, 101:281-295.

Gale A., Dalton C.A., Langmuir C.H., et al. 2013. The mean composition of ocean ridge basalts. *Geochemistry, Geophysics, Geosystems,* 14:489–518. doi: 10.1029/2012GC004334

Gale A., Langmuir C.H. and Dalton C.A. 2014. The Global Systematics of Ocean Ridge Basalts and their Origin. *Journal of Petrology,* 55:1051–1082. doi: 10.1093/petrology/egu017

Gao Y., Hoefs J., Hellebrand E., et al. 2007. Trace element zoning in pyroxenes from ODP Hole 735B gabbros: Diffusive exchange or synkinematic crystal fractionation? *Contributions to Mineralogy and Petrology,* 153:429–442 . doi: 10.1007/s00410-006-0158-4

Gaulda G.A.R., Ghiorso M.S., Lemons R.V. and Carley T.L. 2012. Rhyolite-MELTS: A modified calibration of MELTS optimized for silica-rich, fluid-bearing magmatic systems. *Journal of Petrology,* 53:875–890. doi: 10.1093/petrology/egr080

Geshi N. 2008. Vertical and lateral propagation of radial dikes inferred from the flow-direction analysis of the radial dike swarm in Komochi Volcano, Central Japan. *Journal of Volcanology and Geothermal Research,* 173:122–134. doi: 10.1016/j.jvolgeores.2008.01.001

Ghiorso M.S. and Gualda G.A.R. 2015. An H_2O–CO_2 mixed fluid saturation model compatible with rhyolite-MELTS. *Contributions to Mineralogy and Petrology,* 169:1–30. doi: 10.1007/s00410-015-1141-8

Ginibre C. and Wörner G. 2007. Variable parent magmas and recharge regimes of the Parinacota magma system (N. Chile) revealed by Fe, Mg and Sr zoning in plagioclase. *Lithos,* 98:118–140. doi: 10.1016/j.lithos.2007.03.004

Ginibre C., Wörner G. and Kronz A. 2002. Minor- and trace-element zoning in plagioclase: implications for magma chamber processes at Parinacota volcano,

northern Chile. *Contributions to Mineralogy and Petrology,* 143:300–315. doi: 10.1007/s00410-002-0351-z

Goldstein S.L., Soffer G., Langmuir C.H., et al. 2008. Origin of a “Southern Hemisphere” geochemical signature in the Arctic upper mantle. *Nature,* 453:89–93. doi: 10.1038/nature06919

Grandin R., Jacques E., Nercessian A., et al. 2012. Seismicity during lateral dike propagation: Insights from new data in the recent Manda Hararo-Dabbahu rifting episode (Afar, Ethiopia). *Geochemistry, Geophysics, Geosystems,* 12:1–24. doi: 10.1029/2010GC003434

Grove T.L., Baker M.B. and Kinzler R.J. 1984. Coupled CaAl-NaSi diffusion in plagioclase feldspar: experiments and applications to cooling rate speedometry. *Geochimica et Cosmochimica Acta,* 48:2113–2121. doi: 10.1016/0016-7037(84)90391-0

Grove T.L., Kinzler R.J. and Bryan W.B. 1992. Fractionation of mid-ocean ridge basalt (MORB). *Gephysical Monograph, Geophysical Union,* 71:281–310. doi: 10.1029/GM071p0281

Hansen H. and Grönvold K. 2000. Plagioclase ultraphyric basalts in Iceland: the mush of the rift. *Journal of Volcanology and Geothermal Research,* 98:1–32

Hart S.R. 1984. A large-scale isotope anomaly in the Southern Hemisphere mantle. *Nature,* 309:753-757. doi:10.1038/309753a0.

Hartley M.E., Bali E., Maclennan J, et al. 2018. Melt inclusion constraints on volatile systematics and degassing history of the 2014–2015 Holuhraun eruption, Iceland. *Contributions to Mineralogy and Petrology,* 173:1–23. doi: 10.1007/s00410-017-1434-1

Hekinian R., Bideau D., Hebert R. and Niu Y. 1995. Magmatism in the Garrett transform fault. *Journal of Geophysical Research,* 100:10163–10185

Hellebrand E., Snow J.E. and Mühe R. 2002. Mantle melting beneath Gakkel Ridge (Arctic Ocean): Abyssal peridotite spinel compositions. *Chemical Geology,* 182:227–235. doi: 10.1016/S0009-2541(01)00291-1

Hellevang B. and Pedersen R.B. 2008 Magma ascent and crustal accretion at ultraslow-spreading ridges: constraints from plagioclase ultraphyric basalts from the Arctic mid-ocean ridge. *Journal of Petrology,* 49:267–294. doi: 10.1093/petrology/egm081

Helo C., Longpré M-A., Shimizu N., et al. 2011. Explosive eruptions at mid-ocean ridges driven by CO_2-rich magmas. *Nature Geoscience,* 4:260–263. doi: 10.1038/ngeo1104

Helz R.T., Clague D.A., Mastin L.G. and Rose T.R. 2015. Evidence for Large Compositional Ranges in Coeval Melts Erupted from Kilauea's Summit Reservoir. *American Geophysical Union Monograph,* 208:125–145. doi:10.1002/9781118872079.ch7

Herron E.M., Dewey J.F. and Pitman III W.C. 1974. Geology Plate Tectonics Model for the Evolution of the Arctic. *Geology*, 2:377–380. doi: 10.1130/0091-7613(1974)2<377

Herzberg C. 2004. Partial crystallization of mid-ocean ridge basalts in the crust and mantle. *Journal of Petrology,* 45:2389–2405. doi: 10.1093/petrology/egh040

Hirschmann, M.M., Ghiorso, M.S. and Stolper, M. 1999. Calculation of peridotite partial melting from thermodynamic models of minerals and melts. II. Isobaric variations in melts near the solidus and owing to variable source composition. *Journal of Petrology*, 40:297-313.

Hodges, F.N. 1978. Petrology and chemistry of basalts from DSDP Leg 46. *Initial Reports of the Deep Sea Drilling Project*, 46:227-233.

Holness M.B., Cheadle M.J. and McKenzie D. 2005. On the use of changes in dihedral angle to decode late-stage textural evolution in cumulates. *Journal of Petrology,* 46:1565–1583. doi: 10.1093/petrology/egi026

Holness, M.B., Anderson, A.T., Martin, V.M., et al. 2007. Textures in partially solidified crystalline nodules: a window into the pore structure of slowly cooled mafic intrusions. *Journal of Petrology*, 48:1243-1264.

Holness, M.B., Stock, M.J. and Geist, D. 2019. Magma chambers versus mush zones: constraining the architecture of sub-volcanic plumbing systems from microstructural analysis of crystalline enclaves. *Philosophical Transactions of the Royal Society A*, *377*

Humler E. and Whitechurch H. 1988. Petrology of basalts from the Central Indian Ridge (lat. 25°23′S, long. 70°04′E): estimates of frequencies and fractional volumes of magma injections in a two-layered reservoir. *Earth and Planetary Science Letters,* 88:169–181 . doi: 10.1016/0012-821X(88)90055-6

Humphris S.E., Herzig P.M., Miller D.J., et al. 1995. The internal structure of an active sea-floor massive sulfide deposit. *Nature,* 377:713–716

Iacono-Marziano, G., Morizet, Y. Le Trong, E. and Gaillard, F., 2012. New experimental data and semi-empirical parameterization of H_2O–CO_2 solubility in mafic melts. Geochimica et Cosmochimica Acta, 97;1-23.

Jackson, H.R., Reid, I. and Falconer R.K.H. 1982. Crustal Structure Near the Arctic Mid-

Ocean Ridge. *Journal of Geophysical Research: Solid Earth,* 87:1773–1783

Jackson, M.D., Blundy, J. and Sparks, R.S.J. 2018. Chemical differentiation, cold storage and remobilization of magma in the Earth's crust. *Nature*, 564:405.

Jakobsson M., Mayer L., Coakley B., et al. 2012. The International Bathymetric Chart of the Arctic Ocean (IBCAO) Version 3.0. *Geophysical Research Letters,* 39:1–6. doi: 10.1029/2012GL052219

Jian H., Chen Y.J., Singh S.C., et al. 2017a. Seismic structure and magmatic construction of crust at the ultraslow-spreading Southwest Indian Ridge at 50°28'E. *Journal of Geophysical Research*: *Solid Earth,* 122:18–42. doi: 10.1002/2016JB013377

Jian H., Singh S.C., Chen Y.J. and Li J. 2017b. Evidence of an axial magma chamber beneath the ultraslowspreading Southwest Indian Ridge. *Geology,* 45:143–146 . doi: 10.1130/G38356.1

Jokat W. and Schmidt-Aursch M.C. 2007. Geophysical characteristics of the ultraslow spreading Gakkel Ridge, Arctic Ocean. *Geophysical Journal International,* 168:983–998. doi: 10.1111/j.1365-246X.2006.03278.x

Jokat W., Ritzmann O., Schmidt-Aursch M.C., et al. 2003. Geophysical evidence for reduced melt production on the Arctic ultraslow Gakkel mid-ocean ridge. *Nature,* 423:962–965 . doi: 10.1038/nature01706

Kamenetsky V.S., Eggins S.M., Crawford A.J., et al. 1998. Calcic melt inclusions in primitive olivine at 43°N MAR: evidence for melt-rock reaction/melting involving clinopyroxene-rich lithologies during MORB generation. *Earth and Planetary Science Letters,* 160:115–132. doi: 10.1016/S0012-821X(98)00090-9

Katz, R.F., Spiegelman, M. and Holtzman, B. 2006. The dynamics of melt and shear localization in partially molten aggregates. *Nature*, 442:676.

Kelemen P.B., Hirth G., Shimizu N., et al. 1997. A review of melt migration processes in the adiabatically upwelling mantle beneath oceanic spreading ridges. *Philosophical Transactions of the Royal Society A: Mathatical Physical and Engineering Sciences,* 355:283–318 . doi: 10.1098/rsta.1997.0010

Kelley D.S., Karson J.A., Blackman D.K., et al. 2001. An off-axis hydrothermal vent field near the Mid-Atlantic Ridge at 30°N. *Nature,* 412:145-149. doi: Doi 10.1038/35084000

Kent A.J.R. 2008. Melt Inclusions in Basaltic and Related Volcanic Rocks. *Reviews in Mineraogy andl Geochemistry,* 69:273–331. doi: 10.2138/rmg.2008.69.8

Kimura J.I. and Sano S. 2012. Reactive melt flow as the origin of residual mantle

lithologies and basalt chemistries in mid-ocean ridges: Implications from the red hills peridotite, New Zealand. *Journal of Petrology,* 53:1637–1671. doi: 10.1093/petrology/egs028

Kirkpatrick R.J. and Jolla L. 1976. Processes of crystallization in pillow basalts , Hole 396B , DSDP Leg 46. *Intitial Resports of the Deep Sea Drilling Project,* 271–282

Kirkpatrick R.J., Klein L., Uhlmann D.R. and Hays J.F. 1979. Rates and processes of crystal growth in the system anorthite-albite. *Journal of Geophysical Research,* 84:3671–3676

Kirkpatrick, R.J. 1978. Petrology of basalts: Hole 396B DSDP leg 46. *Initial Reports of the Deep Sea Drilling Project*, 46:165-178.

Klein E.M. and Langmuir C.H. 1987. Global correlations of ocean ridge basalt chemistry with axial depth and crustal thicknes. *Journal of geophysical Research: Solid Earth,* 92.

Koepke J., France L., Mller T., et al. 2011. Gabbros from IODP Site 1256, equatorial Pacific: Insight into axial magma chamber processes at fast spreading ocean ridges. *Geochemistry, Geophysics, Geosystems*, 12. doi: 10.1029/2011GC003655

Korger, E.I.M. and Schlindwein, V. 2012. Performance of localization algorithms for teleseismic mid-ocean ridge earthquakes: the 1999 Gakkel Ridge earthquake swarm and its geological interpretation, *Geophysical Journal International*, 188,doi:10.1111/j.1365246X.2011.05282.x.

Kress V.C. and Ghiorso M.S. 2004. Thermodynamic modeling of post-entrapment crystallization in igneous phases. *Journal of Volcanology and Geothermal Research,* 137:247–260. doi: 10.1016/j.jvolgeores.2004.05.012

Kuo L-C. and Kirkpatrick R.J. 1982. Pre-eruption history of phyric basalts from DSDP Legs 45 and 46: evidence from morphology and zoning patterns in plagioclase. *Contributions to Mineralogy and Petrology,* 79:13–27

Kvassnes A.J.S. and Grove T.L. 2008. How partial melts of mafic lower crust affect ascending magmas at oceanic ridges. *Contributions to Mineralogy and Petrology,* 156:49–71 . doi: 10.1007/s00410-007-0273-x

Lambart, S., Laporte, D. and Schiano, P. 2009. An experimental study of pyroxenite partial melts at 1 and 1.5 GPa: Implications for the major-element composition of Mid-Ocean Ridge Basalts. *Earth and Planetary Science Letters*, 288:335-347.

Lambart, S., Laporte, D. and Schiano, P. 2013. Markers of the pyroxenite contribution in the major-element compositions of oceanic basalts: Review of the experimental constraints. *Lithos*, 160:14-36.

Lange A.E., Nielsen R.L., Tepley F.J. and Kent A.J.R. 2013. The petrogenesis of plagioclase-phyric basalts at mid-ocean ridges. *Geochemistry, Geophys Geosystems,* 14:3282–3296. doi: 10.1002/ggge.20207

Langmuir C.H., Bender J.F. and Batiza R. 1986 Petrological and tectonic segmentation of the East Pacific rise, 5°30′-14°30′N. *Nature,* 322:422–429. doi: 10.1038/322422a0

Langmuir H., Klein E.M. and Plank T. 1992. Petrological Systematics of Mid-Ocean Ridge Basalts: Constraints on Melt Generation Beneath Ocean Ridges. *Mantle Flow and Melt Generation at Mid-Ocean Ridges,* 71.

Larsen H.C., Cannat M., Ceuleneer G., et al. 2009. Oceanic Crustal Structure and Formation. *IODP Thematic Review, Report Series, 2:*65

Laubier, M., Gale, A. and Langmuir, C.H. 2012. Melting and crustal processes at the FAMOUS segment (Mid-Atlantic Ridge): new insights from olivine-hosted melt inclusions from multiple samples. *Journal of Petrology, 53*:665-698.

Laubier, M., Schiano, P., Doucelance, R., Ottolini, L. and Laporte, D. 2007. Olivine-hosted melt inclusions and melting processes beneath the FAMOUS zone (Mid-Atlantic Ridge). *Chemical Geology*, *240*:129-150.

Lehnert K., Su Y., Langmuir C.H., et al. 2000. A global geochemical database structure for rocks. *Geochemistry, Geophysics, Geosystems,* 1:1. doi: 10.1029/1999GC000026

Lehnert, K., Su, Y., Langmuir, C.H., Sarbas, B. and Nohl, U. 2000. A global geochemical database structure for rocks. *Geochemistry, Geophysics, Geosystems*, 1.

Lissenberg C.J. and Dick H.J.B. 2008. Melt–rock reaction in the lower oceanic crust and its implications for the genesis of mid-ocean ridge basalt. *Earth and Planetary Science Letters,* 271:311–325 . doi: 10.1016/j.epsl.2008.04.023

Lissenberg C.J. and MacLeod C.J. 2016. A reactive porous flow control on mid-ocean ridge magmatic evolution. *Journal of Petrology,* 57:2195–2220. doi: 10.1093/petrology/egw074

Lissenberg C.J., MacLeod C.J. and Bennett E.N. 2019. Consequences of a crystal mush-dominated magma plumbing system: a mid-ocean ridge perspective. *Philosophical Transactions of the Royal Society A: Mathamatical Physical and Engineering Science*. doi: 10.1098/rsta.2018.0014

Lissenberg C.J., MacLeod C.J., Howard K.A. and Godard M. 2013. Pervasive reactive melt migration through fast-spreading lower oceanic crust (Hess Deep, equatorial Pacific Ocean). *Earth and Planetary Science Letters,* 361:436–447. doi:

10.1016/j.epsl.2012.11.012

Liu C-Z., Snow J.E., Hellebrand E., et al. 2008. Ancient, highly heterogeneous mantle beneath Gakkel ridge, Arctic Ocean. *Nature,* 452:311–316. doi: 10.1038/nature06688

Lofgren G. 1972. Temperature induced zoning in synthetic plagioclase feldspar. In: WS MacKenzie, J Zussman (eds.) The Feldspars. Manchester University Press, Manchester, England, pp.362-375.

Lofgren G. 1974. An Experimental Study of Plagioclase Crystal Morphology: isothermal Crystallization. *American Journal of Science,* 274:243–273

Lowenstern J.B. 1995. Applications of silicate-melt inclusions to the study of magmatic volatiles. *Magmas, Fluids and Ore Deposits*, 23:71–99

Maaløe S. 1976. The zoned plagioclase of the skaergaard intrusion, East Greenland. *Journal of Petrology,* 17:398–419. doi: 10.1093/petrology/17.3.398

Macgregor L.M., Constable S. and Sinha M. C. 1998. The RAMESSES experiment-III. Controlled-source electromagnetic sounding of the Reykjanes Ridge at 57°45'N. *Geophysical Journal International,* 773–789

Maclennan J. 2008. Lead isotope variability in olivine-hosted melt inclusions from Iceland. *Geochimica et Cosmochimica Acta,* 72:4159–4176. doi: 10.1016/j.gca.2008.05.034

Maclennan J. 2017. Bubble formation and decrepitation control the CO_2 content of olivine-hosted melt inclusions. *Journal of Geophysical Research: Solid Earth*. doi: 10.2113/2.4.476

Maclennan, J. 2019. Mafic tiers and transient mushes: evidence from Iceland. *Philosophical Transactions of the Royal Society A*, *377:*.20180021.

Magde L.S. and Sparks D.W. 1997. Three-dimensional mantle upwelling, melt generation, and melt migration beneath segment slow spreading ridges. *Journal of Geophysical Research: Solid Earth,* 102:20571–20583. doi: 10.1029/97JB01278

Magde, L.S., Barclay, A.H., Toomey, et al. J.A., 2000. Crustal magma plumbing within a segment of the Mid-Atlantic Ridge, 35 N. *Earth and Planetary Science Letters*, 175:55-67.

Mallick, S., Salters, V.J. and Langmuir, C.H. 2019. Geochemical variability along the northern East Pacific Rise: Coincident source composition and ridge segmentation. *Geochemistry, Geophysics, Geosystems*.

Marjanović M., Carbotte S.M., Carton H., et al. 2014. A multi-sill magma plumbing system beneath the axis of the East Pacific Rise. *Nature Geoscience,* 7:825–829. doi:

10.1038/ngeo2272

Marjanović M., Carton H., Carbotte S.M., et al. 2015. Distribution of melt along the East Pacific Rise from 9°30' to 10°N from an amplitude variation with angle of incidence (AVA) technique. *Geophysical Journal International,* 203:1–21. doi: 10.1093/gji/ggv251

Marsh B.D. 1989. Magma chambers. *Annual Review of Earth and Planetary Science,* 12:439–474

Mckenzie D. and Bickle M.J. 1988. The volume and composition of melt generated by extension of the lithosphere. *Journal of Petrology,* 29:625–679. doi: 10.1093/petrology/29.3.625

Melson, W.G. and O'Hearn, T. 2003. Smithsonian volcanic glass file. *Petrological Database of the Ocean Floor*.

Meyer P.S. and Shibata T. 1990. Complex zoning in plagioclase feldspars form ODP Site 648. *Proceedinds of the Ocean Drilling Program, Science Results,* 106/109:123–142

Meyer, B., Saltus, R. and Chulliat, A. 2017. EMAG2: Earth magnetic anomaly grid (2-arc-minute resolution) version 3. *National Centers for Environmental Information, NOAA, Model*.

Michael P. 1995. Regionally distinctive sources of depleted MORB: evidence from trace elements and H_2O. *Earth and Planetary Science Letters,* 131:301–320. doi: 10.1016/0012-821X(95)00023-6

Michael P.J., Langmuir C.H., Dick H.J.B., et al. 2003. Magmatic and amagmatic seafloor generation at the ultraslow-spreading Gakkel ridge, Arctic Ocean. *Nature,* 423:956–96. doi: 10.1038/nature01704

Michael P.J., McDonough W.F., Nielsen R.L. and Cornell W.C. 2002. Depleted melt inclusions in MORB plagioclase: messages from the mantle or mirages from the magma chamber? *Chemical Geology,* 183:43–61. doi: 10.1016/S0009-2541(01)00371-0

Michael, P.J. and Chase, R.L. 1987. The influence of primary magma composition, H_2O and pressure on mid-ocean ridge basalt differentiation. *Contributions to Mineralogy and Petrology*, 96:245-263.

Montési L.G.J., Behn M.D., Hebert L.B., et al. 2011. Controls on melt migration and extraction at the ultraslow Southwest Indian Ridge 10°-16°E. *Journal of Geophysical Research: Solid Earth,* 116:1–19. doi: 10.1029/2011JB008259

Moore A., Coogan L.A., Costa F. and Perfit M.R. 2014. Primitive melt replenishment and

crystal-mush disaggregation in the weeks preceding the 2005-2006 eruption 9°50 'N, EPR. *Earth and Planetary Science Letters*, 403:15–26. doi: 10.1016/j.epsl.2014.06.015

Morgan J.P. 1987. Melt migration beneath mid-ocean spreading centers. *Geophysical Research Letters,* 14:1238–1241. doi: 10.1029/GL014i012p01238

Morse S.A. 1984. Cation Diffusion in Plagioclase Feldspar. *Science*, 225:504–505. doi: 10.1126/science.225.4661.504

Mosar J., Lewis G. and Torsvik T. 2002. North Atlantic sea-floor spreading rates: implications for the Tertiary development of inversion structures of the Norwegian-Greenland Sea. *Journal od the Geological Society of London,* 159:503–515. doi: 10.1144/0016-764901-093

Moune S., Sigmarsson O., Schiano P., et al. 2012. Melt inclusion constraints on the magma source of Eyjafjallajökull 2010 flank eruption. *Journal of Geophysical Research: Solid Earth,* 117:1–13. doi: 10.1029/2011JB008718

Mühe R., Bohrmann H., Garbe-Schönberg D. and Kassens H. 1997. E-MORB glasses from the Gakkel Ridge (Arctic Ocean) at 87°N: evidence for the Earth's most northerly volcanic activity. *Earth and Planetary Science Letters,* 152:1–9. doi: 10.1016/S0012-821X(97)00152-0

Mühe R., Devey C.W. and Bohrmann H. 1993. Isotopes and trace element geochemistry of MORB from the Nansen-Gakkel Ridge at 86 north. *Earth and Planetary Science Letters,* 120:103–109

Muir I.D., Tilley C.E. and Scoon J.H. 1966. Basalts from the Northern part of the Mid-Atlantic ridge. *Journal of Petrology,* 7:193–201. doi: 10.1093/petrology/7.2.193

Müller, C. & Jokat, W., 2000. Seismic evidence for volcanic activity discovered in central Arctic. EOS, Transactiona American Geophysical Union, 81, doi:10.1029/00EO00186.

Nabelek P.I. and Langmuir C.H. 1968. The significance of unusual zoning in olivines from FAMOUS area basalt 527-1-1. *Contributions to Mineralogy and Petrology,* 93:1–8

Nakamura M. and Shimatika S. 1998. Dissolution origin and syn-entrapment compositional changes of melt inclusions in plagioclase. *Earth and Planetary Science Letters*, 161:119–133

Namur, O., Charlier, B., Toplis, M.J. and Vander Auwera, J. 2012. Prediction of plagioclase-melt equilibria in anhydrous silicate melts at 1-atm. Contributions to Mineralogy and Petrology, 163:133-150.

Neave D.A., Buisman I. and Maclennan J. 2017. Continuous mush disaggregation during the long-lasting Laki fissure eruption, Iceland. American Mineralogist, 102:2007–2021. doi: 10.2138/am-2017-6015CCBY

Neave D.A., Hartley M.E., Maclennan J., et al. 2017. Volatile and light lithophile elements in high-anorthite plagioclase-hosted melt inclusions from Iceland. *Geochimica et Cosmochimica Acta,* 205:100–118. doi: 10.1016/j.gca.2017.02.009

Neave D.A., Maclennan J., Hartley M.E., et al. 2014. Crystal storage and transfer in basaltic systems: the Skuggafjöll eruption, Iceland. *Journal of Petrology,* 55:2311_2346. doi: 10.1093/petrology/egu058

Nelson S.T. and Montana A. 1992. Sieve-textured plagioclase in volcanic rocks produced by rapid decompression. *American Mineralogist,* 77:1242–1249

Newman S. and Lowenstern J.B. 2002. Volatile Calc: a silicate melt – H_2O – CO_2 solution model written in Visual Basic for excel. *Computers & Geoscience,* 28:597–604. doi:10.1016/S0098-3004(01)00081-4

Nielsen R.L., Crum J., Bourgeois R., et al. 1994. Local diversity of MORB parent magmas: evidence from melt inclusions in high-An feldspar from the Gorda Ridge. *Mineral Magazine,* 58A:651–652. doi: 10.1180/minmag.1994.58A.2.75

Niu Y. 2016. The meaning of global ocean ridge basalt major element compositions. *Journal of Petrology,* 57:2081–2103. doi: 10.1093/petrology/egw073

Niu Y. and O'Hara M.J. 2008. Global correlations of ocean ridge basalt chemistry with axial depth: A new perspective. *Journal of Petrology,* 49:633–664. doi: 10.1093/petrology/egm051

O'Donnell T.H. and Prensall D.C. 1980. Chemical variations of the glass and mineral phases in basalts dredges from 25°-30°N along the Mid-Atlantic Ridge. *American Journal of Science,* 280:845–868

Oeser M., Dohmen R., Horn I., et al. 2015. Processes and time scales of magmatic evolution as revealed by Fe-Mg chemical and isotopic zoning in natural olivines. *Geochimica et Cosmochimica Acta,* 154:130–150. doi: 10.1016/j.gca.2015.01.025

Okino K., Curewitz D., Asada M., et al. 2002. Preliminary analysis of the Knipovich Ridge segmentation: Influence of focused magmatism and ridge obliquity on an ultraslow spreading system. *Earth and Planetary Science Letters,* 202:275–288. doi: 10.1016/S0012-821X(02)00790-2

Pan Y. and Batiza R. 2002. Mid-ocean ridge magma chamber processes: constraints from olivine zonation in lavas from the East Pacific Rise at 9°30′N and 10°30′N. *Journal of Geophysical Research: Solid Earth,* 107:9–13. doi:

10.1029/2001JB000435

Pan Y. and Batiza R. 2003. Magmatic processes under mid-ocean ridges: a detailed mineralogic study of lavas from East Pacific Rise 9°30′N, 10°30′N, and 11°20′N. *Geochemistry, Geophysics, Geosystems,* 4. doi: 10.1029/2002GC000309

Panjasawatwong Y, Danyushevsky L.V., Crawford A.J. and Harris K.L. 1995. An experimental study of the effects of melt composition on plagioclase - melt equilibria at 5 and 10 kbar : implications for the origin of magmatic high-An plagioclase. *Contributions to Mineralogy and Petrology,* 118:420–432. doi: 10.1007/s004100050024

Papale, P., Moretti, R. and Barbato, D. 2006. The compositional dependence of the saturation surface of H_2O + CO_2 fluids in silicate melts. Chemical Geology, 229;78-95.

Parfitt E.A. and Wilson L. 1994. The 1983-86 Pu'u 'O'o eruption of Kilauea Volcano, Hawaii: a study of dike geometry and eruption mechanisms for a long-lived eruption. *Journal of Volcanology and Geothermal Research,* 59:179–205. doi: 10.1016/0377-0273(94)90090-6

Parfitt E.A., Gregg T.K.P. and Smith D.K. 2002. A comparison between subaerial and submarine eruptions at Kilauea Volcano, Hawaii: Implications for the thermal viability of lateral feeder dikes. *Journal of Volcanology and Geothermal Research* , 113:213–242. doi: 10.1016/S0377-0273(01)00259-1

Passmore E., Maclennan J., Fitton G. and Thordarson T. 2012. Mush disaggregation in basaltic magma chambers: evidence from the AD 1783 Laki eruption. *Journal of Petrology,* 53:2593–2623. doi: 10.1093/petrology/egs061

Perfit M.R., Fornari D.J., Ridley W.I., et al. 1996. Recent volcanism in the Siqueiros transform fault: picritic basalts and implications for MORB magma genesis. *Earth and Planetary Science Letters,* 141:91–108. doi: 10.1016/0012-821X(96)00052-0

Perfit M.R., Fornari D.J., Smith M.C., et al. 1994. Small-scale spatial and temporal variations in mid-ocean ridge crest magmatic processes. *Geology,* 22:375–379

Phipps-Morgan J. and Chen Y.J. 1993a. Dependence of ridge-axis morphology on magma supply and spreading rate. *Letters to Nature,* 366:461–464

Phipps-Morgan J. and Chen Y.J. 1993b. The Genesis of Oceanic Crust: Magma Injection, Hydrothermal Circulation, and Crustal Flow. *Journal of Geophysical Research* 98:6283–6297

Phipps-Morgan, J. 1987. Melt migration beneath mid-ocean spreading centers. *Geophysical Research Letter,* 14:1238-1241

Pietranik A., Koepke J. and Puziewicz J. 2006. Crystallization and resorption in plutonic

plagioclase: Implications on the evolution of granodiorite magma (Gesiniec granodiorite, Strzelin Crystalline Massif, SW Poland). *Lithos,* 86:260–280. doi: 10.1016/j.lithos.2005.05.008

Pollock M.A., Klein E.M., Karson J.A. and Tivey M.A. 2005. Temporal and spatial variability in the composition of lavas exposed along the Western Blanco transform fault. *Geochemistry, Geophysics, Geosystems,* 6. doi: 10.1029/2005GC001026

Portnyagin M.V., Plechov P.Y., Matveev S.V., et al. 2005. Petrology of avachites, high-magnesian basalts of Avachinsky volcano, Kamchatka: I. General characteristics and composition of rocks and minerals. *Petrology*, 13:99–121

Pringle G.J., Trembath L.T. and Pajari G.E. 1974. Crystallization history of a zoned plagioclase. *Mineral Magazine,* 39:867–877. doi: 10.1180/minmag.1974.039.308.06

Purdy, G.M., Kong, L.S.L., Christeson, G.L. et al. 1992. Relationship between spreading rate and the seismic structure of mid-ocean ridges. *Nature*, 355:815-817.

Regelous M, Niu Y.L., Wendt J.I., et al. 1999. Variations in the geochemistry of magmatism on the East Pacific Rise at 10°30'N since 800 ka. *Earth and Planetary Science Letters,* 168:45–63

Reid I. and Jackson, H.R. 1981. Oceanic spreading rate and crustal thickness. *Marine Geophysical Research,* 5:165-172.

Reynolds J.R., Langmuir C.H., Bender J.F., et al. 1992. Spatial and temporal variability in the geochemistry of basalts from the East Pacific Rise. *Nature,* 359, 493-499. 6:493–499

Rhodes J.M., Dungan M.A., Blanchard D.P. and Long P.E. 1979. Magma mixing at mid-ocean ridges: evidence from basalts drilled near 22°N on the Mid-Atlantic Ridge. *Tectonophysics,* 55:35–61. doi: 10.1016/0040-1951(79)90334-2

Ridley W.I., Perfit M.R., Smith M.C. and Fornari D.J. 2006. Magmatic processes in developing oceanic crust revealed in a cumulate xenolith collected at the East Pacific Rise, 9°50′N. *Geochemistry, Geophysics, Geosystems,* 7. doi: 10.1029/2006GC001316

Riedel, C. and Schlindwein, V. 2010. Did the 1999 earthquake swarm on Gakkel Ridge open a volcanic conduit? A detailed teleseismic data analysis, Journal of seismology, 14:505–522.

Rioux, M., Lissenberg, C.J., McLean, N., Bowring, S.A., MacLeod, C.J., Hellebrand, E., Shimizu, N. 2012. Time scales of accretion of the lower crust at fast-spreading ridges. *Nature Geoscience,* 5, 275–278.

Roedder E. 1965. Liquid CO_2 inclusions in olivine-bearing nodules and phenocrysts from basalts. Am Mineral 50:356–366

Roedder E. 1984. Fluid Inclusions; Reviews in mineralogy 12. *Mineralogical Society of America*.

Roeder, P.L. and Emslie, R. 1970. Olivine-liquid equilibrium. *Contributions to mineralogy and petrology*, *29*:275-289.

Rona P.A., Klinkhammer G, Nelsen T.A., et al. 1986. Black smokers, massive sulphides and vent biota at the Mid-Atlantic ridge. *Nature,* 321:33–37. doi: 10.1038/321033a0

Rubin K.H. and Sinton J.M. 2007. Inferences on mid-ocean ridge thermal and magmatic structure from MORB compositions. *Earth and Planetary Science Letters,* 260:257–276. doi: 10.1016/j.epsl.2007.05.035

Rubin K.H., Sinton J.M., Maclennan J. and Hellebrand E. 2009. Magmatic filtering of mantle compositions at mid-ocean-ridge volcanoes. *Nature Geoscience,* 2:321–328. doi: 10.1038/ngeo504

Ryan M.P. 1988. The mechanisms and three-dimensional internal structure of active magmatic systems: Kilauea volcano, Hawaii. *Journal of Geophysical Research,* 93:4213–4248

Ryan W.B.F., Carbotte S.M., Coplan J.O., et al. 2009. Global multi-resolution topography synthesis. *Geochemistry, Geophysics, Geosystems,* 10. doi:10.1029/2008GC002332d

Saal A.E., Hart S.R., Shimizu N., et al. 2005. Pb isotopic variability in melt inclusions from the EMI-EMII-HIMU mantle end-members and the role of the oceanic lithosphere. *Earth and Planetary Science Letters,* 240:605–620. doi: 10.1016/j.epsl.2005.10.002

Saal A.E., Hauri E.H., Langmuir C.H. and Perfit M.R. 2002. Vapour undersaturation in primitive mid-ocean-ridge basalt and the volatile content of Earth's upper mantle. *Nature,* 419:451–455. doi: 10.1038/nature01073

Sauter D., Mendel V., Rommevaux-Jestin C., et al. 2004. Focused magmatism versus amagmatic spreading along the ultra-slow spreading Southwest Indian Ridge: Evidence from TOBI side scan sonar imagery. *Geochemistry, Geophysics, Geosystems,* 5:1–20. doi: 10.1029/2004GC000738

Schilling, J.G., Zajac, M., Evans, R. et al. 1983. Petrologic and geochemical variations along the Mid-Atlantic Ridge from 29 degrees N to 73 degrees N. *American Journal of Science*, 283:510-586.

Schlindwein V. 2012. Teleseismic earthquake swarms at ultraslow spreading ridges:

Indicator for dyke intrusions? *Geophysical Journal International,* 190:442–456. doi: 10.1111/j.1365-246X.2012.05502.x

Schlindwein V. and Schmid F. 2016. Mid-ocean-ridge seismicity reveals extreme types of ocean lithosphere. *Nature,* 535:276–279. doi: 10.1038/nature18277

Schmidt-Aursch M.C., Jokat W. 2016. 3D gravity modelling reveals off-axis crustal thickness variations along the western Gakkel Ridge (Arctic Ocean). *Tectonophysics,* 691:85–97. doi: 10.1016/j.tecto.2016.03.021

Searle R. 2015. Mid-Ocean Ridges. Cambridge University Press

Sekretov S. 2002. Structure and tectonic evolution of the Southern Eurasia Basin, Arctic Ocean. *Tectonophysics,* 351:193–243. doi: 10.1016/S0040-1951(01)00278-5

Shaw A.M., Behn M.D., Humphris S.E., et al. 2010. Deep pooling of low degree melts and volatile fluxes at the 85°E segment of the Gakkel Ridge: evidence from olivine-hosted melt inclusions and glasses. *Earth and Planetary Science Letters,* 289:311–322. doi: 10.1016/j.epsl.2009.11.018

Shishkina T.A., Botcharnikov R.E., Holtz F, et al. 2014. Compositional and pressure effects on the solubility of H_2O and CO_2 in mafic melts. *Chemical Geology,* 388:112–129. doi: 10.1016/j.chemgeo.2014.09.001

Shishkina T.A., Botcharnikov R.E., Holtz F., et al. 2010. Solubility of H_2O- and CO_2-bearing fluids in tholeiitic basalts at pressures up to 500 MPa. *Chemical Geology,* 277:155-125. doi: 10.1016/j.chemgeo.2010.07.014

Sides I.R., Edmonds M., Maclennan J., et al. 2014. Eruption style at Kilauea Volcano in Hawai'i linked to primary melt composition. *Nature Geoscience,* 7:464–469. doi: 10.1038/ngeo2140

Singh S.C., Crawford W.C., Carton H., et al. 2006. Discovery of a magma chamber and faults beneath a Mid-Atlantic Ridge hydrothermal field. *Nature,* 442:1029–1032. doi: 10.1038/nature05105

Singh S.C., Kent G.M., Collier J.S., et al. 1998. Melt to mush variations in crustal magma properties along the ridge crest at the southern East Pacific Rise. *Nature,* 394:874–878. doi: 10.1038/29740

Sinha M.C., Constable S.C., Peirce C., et al. 1998. Magmatic processes at slow spreading ridges: Implications of the RAMESSES experiment at 57°45'N on the Mid-Atlantic Ridge. *Geophysical Journal International,* 135:731–745. doi: 10.1046/j.1365-246X.1998.00704.x

Sinton J.M. and Detrick R.S. 1992. Mid-ocean ridge magma chambers. *Journal of Geophysical Research,* 97:197. doi: 10.1029/91JB02508

Sinton J.M., Bergmanis E.C., Rubin K.H., et al. 2002. Volcanic eruptions on mid-ocean ridges: New evidence from the superfast spreading East Pacific Rise, 17°–19°S. *Journal of Geophysical Research,* 107:65–67. doi: 10.1029/2000JB000090

Sinton J.M., Mahoney J.J. and Macdonald K.C. 1991. Magmatic Processes at Superfast Spreading Ridges ' Glass Compositional Variations Along the East Pacific Rise 13°-23°S. *Journal of Geophysical Research,* 96:6133–6155

Sinton J.M., Wilson D.S., Christie D.M., et al. 1983. Petrological consequences of rift propagation on oceanic spreading ridges. *Earth and Planetary Science Letters,* 62:193–207

Smith D.K. and Cann J.R. 1999. Constructing the upper crust of the Mid-Atlantic Ridge: A reinterpretation based on the Puna Ridge, Kilauea Volcano. *Journal of Geophysical Research*: *Solid Earth,* 104:25379–25399. doi: 10.1029/1999JB900177

Smith R.K. and Lofgren F.E. 1979. The physio-chemical and crystal growth kinetics necessary for zonal development in plagioclase. *Geologial Society of America Abstract Progrogram,* 7:520

Snow J. and Edmonds H.N. 2007. Ultraslow-Spreading Ridges: Rapid Paradigm Changes. *Oceanography,* 20:9. doi: 10.5670/oceanog.2007.83

Sobolev A.V. 1996. Melt Incusions in Minerals as a source of princple petrological information. *Petrology*, 4:209–220

Sobolev A.V. and Shimizu N. 1993. Ultra-depleted primary melt included in an olivine from the Mid-Atlantic Ridge. *Letters to Nature,* 363:151–154

Sohn R.A., Willis C, Humphris S, et al. 2008. Explosive volcanism on the ultraslow-spreading Gakkel ridge, Arctic Ocean. *Nature,* 453:1236–1238. doi: 10.1038/nature07075

Solano J.M.S, Jackson M.D., Sparks R.S.J. and Blundy J. 2014. Evolution of major and trace element composition during melt migration through crystalline mush: implications for chemical differentiation in the crust. *American Journal of Science*. 314:895–939. doi:10.2475/05.2014.01

Solano, J.M.S., Jackson, M.D., Sparks, R.S.J. et al. 2012. Melt segregation in deep crustal hot zones: a mechanism for chemical differentiation, crustal assimilation and the formation of evolved magmas. *Journal of Petrology*, 53:1999-2026.

Solomon S. 1989. Just how do Ocean Ridges Vary?: Characteristics and Population Statistics of Ocean Ridges. In: Dick HJB (ed) *Drilling the Oceanic Lower Crust and Mantle, JOI/USSAC Workshop Report*. Woods Hole Oceanographic Institution,

Woods Hole, MA, pp 73–74

Soule S.A., Nakata D.S., Fornari D.J., et al. 2012. CO_2 variability in mid-ocean ridge basalts from syn-emplacement degassing: Constraints on eruption dynamics. *Earth and Planetary Science Letters,* 327–328:39–49. doi: 10.1016/j.epsl.2012.01.034

Sours-Page R., Johnson K.T.M., Nielsen R.L. and Karsten J.L. 1999. Local and regional variation of MORB parent magmas: evidence from melt inclusions from the Endeavour Segment of the Juan de Fuca Ridge. *Contributions to Mineralogy and Petrology,* 134:342–363. doi: 10.1007/s004100050489

Sparks D.W. and Parmentier E.M. 1991. Melt extraction from the mantle beneath spreading centers. *Earth and Planetary Science Letters,* 105:368–377. doi: 10.1016/0012-821X(91)90178-K

Spiegelman M. and McKenzie D. 1987. Simple 2-D models for melt extraction at mid-ocean ridges and island arcs. *Earth and Planetary Science Letters,* 83:137–152. doi: 10.1016/0012-821X(87)90057-4

Stakes D.S., Perfit M.R., Tivey M.A., et al. 2006. The Cleft revealed: Geologic, magnetic, and morphologic evidence for construction of upper oceanic crust along the southern Juan de Fuca Ridge. *Geochemistry, Geophysics, Geosystems,* 7. doi: 10.1029/2005GC001038

Standish J.J., Dick H.J.B., Michael P.J., et al. 2008. MORB generation beneath the ultraslow spreading Southwest Indian Ridge (9-25°E): Major element chemistry and the importance of process versus source. *Geochemistry, Geophysics, Geosystems,* 9. doi: 10.1029/2008GC001959

Statham, P., Penman, C., Chaldecott, J. et al. Validating a New Approach to the Mapping of Phases by EDS by Comparison with the Results of Simultaneous Data Collection by EBSD. *Microscopy and Microanalysis,* 19:752–53. Doi: 10.1017/S1431927613005758

Stewart, M.A., Klein, E.M., Karson, J.A. and Brophy J.G. 2003. Geochemical relationships between dikes and lavas at the Hess Deep Rift: Implications for magma eruptibility. *Journal of Geophysical Research: Solid Earth*, *108*.

Stracke A., Snow J.E., Hellebrand E., et al. 2011. Abyssal peridotite Hf isotopes identify extreme mantle depletion. *Earth and Planetary Science Letters,* 308:359–368. doi: 10.1016/j.epsl.2011.06.012

Sugawara T. 2000. Empirical relationships between temperature, pressure, and MgO content in olivine and pyroxene saturated liquid. *Journal of Geophysical Research,* 105:8457–8472

Sun S.S., McDonough W.F. 1989. Chemical and isotopic systematics of oceanic basalts: implications for mantle composition and processes. *Geological Society of London, Special Publications,* 42:313–345. doi: 10.1144/GSL.SP.1989.042.01.19

Thompson G., Bryan W.B., Ballard R., et al. 1985. Axial processes along a segment of the East Pacific Rise, 10°-12°N. *Nature,* 318:429–433. doi: 10.1038/318429a0

Tolstoy, M., Bohnenstiel, D., Edwards, M. and Kurras, G. 2001. Seismic character of volcanic activity at the ultraslow-spreading Gakkel Ridge, Geology, 29:1139–1142, doi:10.1130/0091-7613(2001)029.

Ustunisik G, Kilinc A. and Nielsen R.L. 2014. New insights into the processes controlling compositional zoning in plagioclase. *Lithos,* 200–201:80–93. doi: 10.1016/j.lithos.2014.03.021

van der Zwan F.M., Devey C.W., Hansteen T.H., et al. 2017. Lower crustal hydrothermal circulation at slow-spreading ridges: evidence from chlorine in Arctic and South Atlantic basalt glasses and melt inclusions. *Contributions to Mineralogy and Petrology*, 172. doi: 10.1007/s00410-017-1418-1

Vance J.A. 1965. Zoning in igneous plagioclase: patchy zoning. *The Journal of Geology,* 73:637–651

Vance J.A. and Gilreath J.P. 1967. The effect of synneusis on phenocryst distribution patterns in some porphyritic igneous rocks. *American Mineralogist,* 52:529–536

Varga R.J., Gee J.S., Staudigel H and Tauxe L. 1998. Dike surface lineations as magma flow indicators within the sheeted dike complex of the Troodos Ophiolite, Cyprus. *Journal of Geophysical Research,* 103:5241. doi: 10.1029/97JB02717

Viccaro M, Giacomoni P.P., Ferlito C. and Cristofolini R. 2010. Dynamics of magma supply at Mt. Etna volcano (Southern Italy) as revealed by textural and compositional features of plagioclase phenocrysts. *Lithos,* 116:77–91. doi: 10.1016/j.lithos.2009.12.012

Villiger S, Müntener O. and Ulmer P. 2007. Crystallization pressures of mid-ocean ridge basalts derived from major element variations of glasses from equilibrium and fractional crystallization experiments. *Journal of Geophysical Research*: *Solid Earth,* 112:1–18. doi: 10.1029/2006JB004342

Vogt P.R., Taylor P.T., Kovacs L.C. and Johnson G.L. 1979. Detailed aeromagnetic investigation of the Arctic Basin. *Journal of Geophysical Research,* 84:1071–1089. doi: 10.1029/JB086iB07p06323

Wallace P.J., Kamenetsky V.S. and Cervantes P. 2015. Melt inclusion CO_2 contents, pressures of olivine crystallization, and the problem of shrinkage bubbles. *American*

Mineralogist, 100:787–794. doi: 10.2138/am-2015-5029

Wanless V.D. and Behn M.D. 2017. Spreading rate-dependent variations in crystallization along the global mid-ocean ridge system. *Geochemistry, Geophysics, Geosystems,* 116:1–12. doi: 10.1002/2017GC006924

Wanless V.D. and Shaw A.M. 2012. Lower crustal crystallization and melt evolution at mid-ocean ridges. *Nature Geoscience,* 5:651–655. doi: 10.1038/ngeo1552

Wanless V.D., Behn M.D., Shaw A.M. and Plank T. 2014a. Variations in melting dynamics and mantle compositions along the Eastern Volcanic Zone of the Gakkel Ridge: insights from olivine-hosted melt inclusions. *Contributions to Mineralogy and Petrology,* 167:1005. doi: 10.1007/s00410-014-1005-7

Wanless V.D., Shaw A.M., Behn M.D., et al. 2014b. Magmatic plumbing at Lucky Strike volcano based on olivine-hosted melt inclusion compositions. *Geochemistry, Geophysics, Geosystems,* 4692–4711. doi: 10.1002/2015GC005918.

Welsch B., Hammer J. and Hellebrand E. 2014. Phosphorus zoning reveals dendritic architecture of olivine. *Geology,* 42:867–870. doi: 10.1130/G35691.1

White R.S., Edmonds M and Maclennan J, et al. 2019. Melt movement through the Icelandic crust. *Philosophical Transactions of the Royal Society A,* 377:20180010. doi: 10.1098/rsta.2018.0010

White, W.M., Klein, E.M., Holland, H.D. and Turekian, K.K. 2014. 4.13–Composition of the oceanic crust. Treatise on geochemistry, *4*.

Xu M., Pablo Canales J. and Carbotte S.M., et al. 2014. Variations in axial magma lens properties along the East Pacific Rise (9°30'N-10°00'N) from swath 3-D seismic imaging and 1-D waveform inversion. *Journal of Geophysical Research*: *Solid Earth,* 119:2721–2744. doi: 10.1002/2013JB010730

Yang H.J., Kinzler R.J. and Grove T.L. 1996. Experiments and models of anhydrous, basaltic olivine-plagioclase-augite saturated melts from 0.001 to 10 kbar. *Contributions to Mineralogy and Petrology,* 124:1–18. doi: 10.1007/s004100050169

Yoder H.S. 1968. Experimental studies bearing on the origin of anorthosites. In: Isachsen Y.W. (ed) Origin of anorthosite and related rocks. pp. 13–22

Zellmer G.F., Blake S., Vance D., et al. 1999. Plagioclase residence times at two island arc volcanoes (Kameni Islands, Santorini, and Soufriere, St. Vincent) determined by Sr diffusion systematics. *Contributions to Mineralogy and Petrology,* 136:345–357. doi: 10.1007/s004100050543

Zellmer G.F., Dulski P, Iizuka Y. and Perfit M.R. 2012. Rates and processes of crystallization in on-axis and off-axis MOR basaltic melts. *Lithos*, 154:1–15. doi:

10.1016/j.lithos.2012.07.019

Zellmer G.F., Rubin K.H., Dulski P., et al. 2011. Crystal growth during dike injection of MOR basaltic melts: evidence from preservation of local Sr disequilibria in plagioclase. *Contributions to Mineralogy and Petrology*, 161:153–173. doi: 10.1007/s00410-010-0518-y

Zeng L., Cheng L., Cheng Q. and Zhang S. 2014. A refinement of Lange's plagioclase-liquid hygrometer/thermometer based on quadratic log-contrast models for experiments with mixtures. *Journal of Chemical Exploration,* 141:89–99. doi: 10.1016/j.gexplo.2013.12.008

Zhang G.L., Zeng Z.G., Yin X.B., et al. 2008. Periodical mixing of MORB magmas near East Pacific Rise 13°N: Evidence from modeling and zoned plagioclase phenocrysts. *Science in China Series D: Earth Science,* 51:1786–1801. doi: 10.1007/s11430-008frubin-0139-8

Appendix 1

EDS and SIMs standard analysis

Appendix 1

The following appendix contains information relating to the standards used during EDS and SIMs analysis. The accuracy and precision of standard measurements, along with the equations used to calculate them, are included. Accuracy and precision of LA-ICP-MS analysis can be found in Electronic Appendix 4.

Primary EDS standards

Table A1.1: Primary standards used during EDS analysis

Element	Plagioclase	Olivine	Pyroxene	Spinel	Glass
SiO_2	Albite	Almandine	Jadeite	Diopside	Jadeite
MgO	Diopside/ MgO	Chrome Diopside/ Pyrope	Diopside	Chromite	Diopside
Al_2O_3	Albite		Jadeite	Chromite	Jadeite/ Almandine
FeO	Olivine/ FeO	Chromite/ Almandine	Chromite/ Magnetite	Magnetite/ Chromite	Chromite
Na_2O	Jadeite/ Albite		Jadeite		Albite/ Jadeite
CaO	Diopside		Diopside		BIR
K_2O	Orthoclase				Orthoclase
TiO_2			Rutile	Rutile	Rutile
Cr_2O_3			Chromite	Chromite	
NiO		Pentlandite		Nickel	
V_2O_5				Vanadium	
ZnO				Sphalerite	
P_2O_5					GaP
MnO					Manganese
SO_2					Pyrite

Glass and mineral EDS standard information

Glass standard data in Tables A1.2 and A1.3 excludes melt inclusion glass analysis which is shown separately in tables A1.7 and A1.8.

Table A1.2: BCR-2 standard analysis data

			BCR-2			
Element	Accepted value (wt.%)	Average* (wt.%)	2SD		Offset from reference	
			Absolute	%	Absolute	%
SiO_2	54.10	54.55	0.24	0.43	0.45	0.83
TiO_2	2.26	2.33	0.04	1.61	0.07	3.10
Al_2O_3	13.50	13.42	0.10	0.71	-0.08	-0.59
FeO	12.42	12.41	0.07	0.58	-0.01	-0.06
MgO	3.59	3.55	0.04	1.12	-0.04	-1.11
CaO	7.12	7.17	0.05	0.69	0.05	0.70
Na_2O	3.16	3.16	0.05	1.45	0.00	0.00
K_2O	1.79	1.81	0.03	1.79	0.02	1.12
P_2O_5	0.35	0.34	0.05	14.20	-0.01	-2.86
MnO	0.20	0.21	0.03	12.30	0.01	5.00

*** Average of 15 standard analyses**

Table A1.3: BHVO-2 standard analysis data

			BHVO-2			
Element	Accepted value (wt.%)	Average* (wt.%)	2SD		Offset from reference	
			Absolute	%	Absolute	%
SiO_2	49.90	50.06	0.40	0.80	0.16	0.32
TiO_2	2.73	2.77	0.04	1.31	0.04	1.47
Al_2O_3	13.5	13.42	0.14	1.05	-0.08	-0.59
FeO	11.07	11.05	0.14	1.27	-0.02	-0.16
MgO	7.23	7.20	0.05	0.75	-0.03	-0.45
CaO	11.40	11.43	0.11	0.95	0.03	0.26
Na_2O	2.22	2.23	0.03	1.46	0.01	0.45
K_2O	0.52	0.53	0.02	3.38	0.01	1.92
P_2O_5	0.27	0.24	0.03	11.65	-0.03	-11.11
MnO	0.17	0.18	0.02	10.63	0.01	5.88

*** Average of 15 standard analyses**

Standard analyses in Table A1.4 relate to plagioclase compositions used throughout this thesis, those presented in Table A1.9 relate to plagioclase analyses used in the PEC correction.

Table A1.4: ASTIMEX Plagioclase standard analysis data

			2SD (precision)			Offset from reference (accuracy)	
Oxide	Accepted value (wt.%)	Average*	Absolute	%	RSD (%)	Absolute	%
Na_2O	4.36	4.3	0.1	1.2	0.59	-0.1	-1.38
MgO	0.10	0.1	0	30.2	18.57	0	-20
Al_2O_3	29.35	29.8	0.2	0.6	0.32	0.4	1.53
SiO_2	53.12	52.27	0.5	0.9	0.45	-0.4	-0.81
K_2O	0.24	0.4	0	8	4.28	0.2	54.17
CaO	11.93	12.1	0.1	0.7	0.37	0.2	1.68
FeO	0.34	0.4	0	8.9	4.01	0.1	29.41
An	60.2	60.96	0.34	0.55	0.28	0.8	1.33

*** Average of 141 standard analyses**

Clinopyroxene analysis standard information

Table A1.5: ASTIMEX Chrome Diopside standard analysis data

	ASTIMEX Chrome Diopside					
Element		Average*	2SD		Offset from reference	
	Accepted value (wt.%)	(wt.%)	Absolute	%	Absolute	%
SiO_2	54.92	55.35	0.36	0.65	0.42	0.76
Al_2O_3	0.3	0.33	0.03	9.00	0.03	10.00
FeO	1.28	1.42	0.04	2.89	0.14	10.94
MgO	17.72	17.48	0.15	0.85	-0.24	-1.35
CaO	24.67	24.50	0.19	0.77	-0.17	-0.69
Na_2O	0.44	0.42	0.06	13.97	-0.02	-4.55
TiO_2	0.09	0.09	0.02	22.82	0.00	0.00
Cr_2O_3	0.55	0.52	0.12	22.67	-0.03	-5.45

*** Average of 18 standard analyses**

Olivine analysis standard information

Table A1.6: ASTIMEX Olivine standard analysis data

		ASTIMEX Olivine				
Element	Accepted value (wt.%)	Average* (wt.%)	2SD		Offset from reference	
			Absolute	%	Absolute	%
SiO_2	41.61	41.29	0.34	0.82	-0.31	-0.75
MgO	50.97	51.25	0.61	1.18	0.28	0.55
FeO	7.26	7.27	0.15	2.05	0.02	0.28
NiO	0.37	0.46	0.03	7.48	0.09	24.32

* **Average of 9 standard analyses**

Standard analysis relating to melt inclusion analysis (Table A1.7-A1.10)

Table A1.7: BCR-2 standard analysis data during melt inclusion analysis

		BCR-2				
Element	Accepted value (wt.%)	Average* (wt.%)	2SD		Offset from reference	
			Absolute	%	Absolute	%
SiO_2	54.10	54.54	0.78	1.44	0.44	0.81
TiO_2	2.26	2.31	0.07	3.07	0.05	2.21
Al_2O_3	13.50	13.75	0.30	2.22	0.25	1.85
FeO	12.42	12.43	0.29	2.36	0.01	0.10
MgO	3.59	3.63	0.13	3.51	0.04	1.11
CaO	7.12	7.13	0.13	1.88	0.03	0.42
Na_2O	3.16	3.16	0.08	2.56	-0.01	-0.32
K_2O	1.79	1.81	0.05	2.49	0.02	1.12
P_2O_5	0.35	0.30	0.03	11.62	-0.05	-14.29
MnO	0.20	0.19	0.04	20.17	-0.01	-5.00

* **Average of 18 standard analyses**

Table A1.8: BHVO-2 standard analysis data during melt inclusion analysis

	BHVO-2					
Element	Accepted value (wt.%)	Average* (wt.%)	2SD		Offset from reference	
			Absolute	%	Absolute	%
SiO_2	49.90	49.87	0.71	1.42	-0.03	-0.06
TiO_2	2.73	2.74	0.06	2.12	0.01	0.37
Al_2O_3	13.5	13.63	0.27	2.00	0.13	0.96
FeO	11.07	10.98	0.24	2.21	-0.09	-0.79
MgO	7.23	7.28	0.15	2.03	0.05	0.69
CaO	11.40	11.40	0.19	1.70	0.00	0.00
Na_2O	2.22	2.23	0.05	2.42	0.01	0.45
K_2O	0.52	0.54	0.02	4.11	0.02	3.85
P_2O_5	0.27	0.23	0.05	19.61	-0.04	-14.81
MnO	0.17	0.16	0.03	15.93	-0.01	-5.88

*** Average of 18 standard analyses**

Table A1.9: ASTIMEX Plagioclase standard analysis data during melt inclusion host analysis

	ASTIMEX Plagioclase					
Element	Accepted value (wt.%)	Average* (wt.%)	2SD		Offset from reference	
			Absolute	%	Absolute	%
SiO_2	53.12	52.68	0.52	0.99	-0.44	-0.83
Al_2O_3	29.36	29.88	0.56	1.88	0.52	1.76
FeO	0.35	0.44	0.03	7.43	0.09	26.67
MgO	0.10	0.04	0.08	206.73	-0.06	-59.80
CaO	11.94	12.14	0.22	1.83	0.20	1.72
Na_2O	4.37	4.30	0.09	2.21	-0.07	-1.54
K_2O	0.24	0.37	0.03	7.88	0.13	53.58

*** Average of 27 standard analyses**

Table A1.10: ASTIMEX Olivine standard analysis data during melt inclusion host analysis

	ASTIMEX Olivine					
Element	Accepted value (wt.%)	Average* (wt.%)	2SD		Offset from reference	
			Absolute	%	Absolute	%
SiO_2	41.61	41.54	0.43	1.03	-0.07	-0.16
MgO	50.97	50.53	0.34	0.67	-0.44	-0.87
FeO	7.26	7.28	0.06	0.84	0.02	0.33
NiO	0.37	0.46	0.03	6.05	0.09	24.65

*** Average of 9 standard analyses**

SIMs analysis

Uncertainty and accuracy of SIMS analysis can be found in Table A1.11 and Figure A1.1 respectively.

Table A1.11: Uncertainty of SIMS secondary standard measurements

	Number of analyses		Concentration		Relative standard	
Standard	CO_2	H_2O	CO_2 (ppm)	H_2O (wt.%)	CO_2	H_2O
M10	4	7	341	0.75	2	6
M40	9	7	2183	3.07	4	4
M36	3	-	1392		1	-
M21	3	-	1051		4	-
M5	7	-	990		6	-

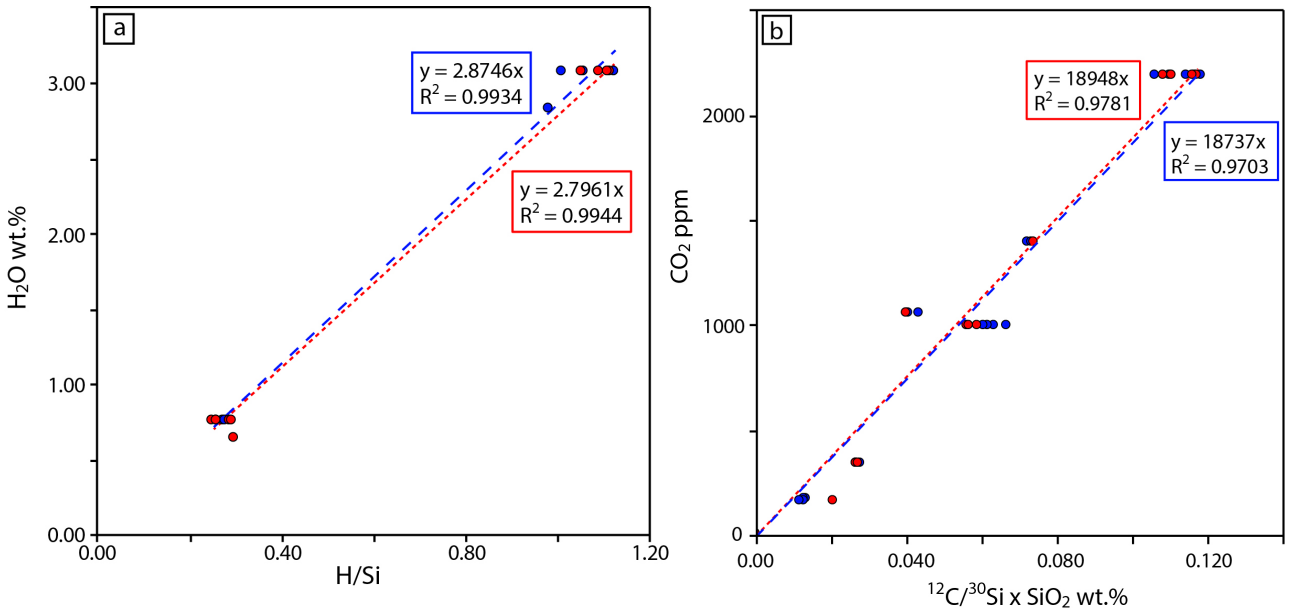

Fig. A1.1: Calibration curves for CO_2 and H_2O SIMS analysis. Calibration curves for both H_2O (**a**) and CO_2 (**b**). The different coloured lines in each panel indicate different sessions.

Accuracy and precision

The following equations were used to calculate the accuracy and precision of standard measurements:

Precision

Sample standard deviation is calculated using the following equations:

$$x_a = \frac{\sum x}{n}$$

where x_a is the average element concentration, x is the element concentration and n is the number of analyses. Standard deviation, σ, is calculated using the following formula:

$$\sigma = \frac{\sqrt{\sum(\mathrm{x} - \mathrm{x_a})^2}}{\mathrm{n} - 1}$$

The coefficient of variance or % relative standard deviation (RSD) is calculated using the following equation:

$$RSD\ (\%) = \frac{\sigma}{x_a} \times 100$$

Accuracy

$$\text{Absolute offset from reference} = \text{Measured value} - \text{Certified value}$$

$$\%\ \text{offset from reference} = \left(\frac{\text{Measured values} - \text{Certified value}}{\text{Certified values}}\right) \times 100$$

Appendix 2

Plagioclase crystal cargo statistics

Appendix 2

Table A2.1 Individual plagioclase habit, abundance, size and composition

Crystal habit	Individual crystals							Glomerocryst components	
	Total (%)	Size range (mm)	Average size (mm)	♦An range	♠Median maximum An	Zoning complexity		Mono-mineralic	Poly-mineralic
						Range	Median		
Tabular	61	0.07-14	2.2	42-87	79	0-8	2	51.8*	27*
Resorbed	30	0.15-13	2.5	52-86	78	0-10	2	16.9*	3*
Skeletal	7	0.21-7.68	1.6	50-83	68	0-5	1	0.6*	11*
Acicular	2	0.18-6.36	1.1	62-78	75	0-3	0	0*	0*
Multi-habit	-	-	-	-	-	-	-	30.7	59

♠ The maximum anorthite content is calculated for each crystal; the median of these values is then found for each crystal habit.

♦The minimum and maximum anorthite content of each crystal is determined. For each crystal habit the range of these values is then determined. This includes plagioclase cores, mottled cores, skeletal cores, mantles, rims, and melt inclusion rims.

*Percentage of glomerocrysts composed of entirely one type of crystal habit

Table A2.3 Types of zoning present in individual plagioclase and glomerocrysts

Zoning	Individual plagioclase zoning (%)	Mono-mineralic (%)	Poly-mineralic (%)
Unzoned	8.1	4	3
Normal only	1.4	2	10
Reverse only	11.1	7	5
Oscillatory only	6.1	11	30
Sector only	0.2	1	0
Patchy only	16.3	5*	2**
Complex	56.7	57	51

*Patchy zoning is present in 38% of all mono-mineralic glomerocrysts
**Patchy zoning is present in 25% of poly-mineralic glomerocrysts

Table A2.2 Individual and glomerocryst zoning and zoning complexity

Zoning	Individual crystals (%)	Mono-mineralic glomerocrysts (%)	Poly-mineralic glomerocrysts (%)
Unzoned	8.1	4	3
One type of zoning*	18.8	26	44
Complex zoning♦	73	70	53
Zoning complexity (range)	0-10	0-6**	0-3**
Zoning complexity (average)	2	2**	2**

**Values account for zoning in the entire glomerocrysts not its individual components
♦Includes Patchy zoning
*Excludes patchy zoning

Table A2.4 Percentage of individual plagioclase that contain each of the different zoning types

Zoning	%
Normal	35
Reverse	62
Patchy	43
Oscillatory	30
Sector	1

Table A2.5 Resorption location in individual and euhedral plagioclase and mono-mineralic glomerocrysts

Type of resorption	Type of crystal		
	Individual plagioclase (%)	Euhedral plagioclase (%)	Mono-mineralic glomerocrysts (%)
Internal	41	41	35
External	29	11	29
Internal and external	14	4	17
None	16	44	18

Table A2.6 Number of resorption events in each individual plagioclase habit category

Crystal habit	Average number of resorption events per crystal (%)	≥ 1 resorption event (%)	≥ 2 resorption event (%)
Tabular	1.22	85	29
Resorbed	1.33	100	26
Skeletal	0.34	31	2
Acicular	0.12	8	4

Table A2.7 Melt inclusion average and maximum size

Melt inclusion habit	Average size range (um)	Maximum size (um)
Circular	8-37	446
Negative crystal	7-41	342
Elongate	17-141	1610
Boxy	22-229	3220
Amoeboid	47-383	4947

Table A2.8 Glomerocryst configuration and component contacts

	Configuration (%)		Component contacts (%)		
Glomerocryst type	Open	Closed	Point	Planar	Embedded
Mono-mineralic	10	90	28*	51*	75*
Poly-mineralic	51	49	47*	18*	98*

*Percentage of glomerocrysts that contain that type of contact, not the percentage with only that contact type

Appendix 3

Local-scale variations within Gakkel Ridge plumbing systems

Appendix 3

The following appendix contains profiles of five magmatic systems not discussed in Chapter 8, this includes; 5°W Axial Volcanic Ridge (AVR), 3°E Seamounts, 12°40'W AVR, 31°E Basement Ridge and 48°E Deep Seafloor.

8.3.1 5°W Axial Volcanic Ridge (Fig. A3.1)

Extending for 36 km along axis in the Western Volcanic Zone, this AVR rises from 4063 mbsl to 2758 mbsl at its shallowest point. The AVR tapers along axis from its central high towards both the northeast and southwest (Fig. A3.1) and bifurcates in the southwest due to normal faulting that produces stair-step morphology; normal faults can also be observed on the northwest valley wall. Three samples have been dredged from both the axial ridge (H-D12, H-D14 and H-D15) and from the valley walls (H-D13, P-222 and P-223). Samples H-D12 and H-D14 are situated closest to the centre of the AVR, whilst H-D15 is located east towards its flank. Samples H-D12 and P-223 are approximately located along a flow line extending from the ridge axis for a distance equivalent to ~1 Myr. The centre of the AVR is located between H-D12 and H-D14 (Fig. 8.1).

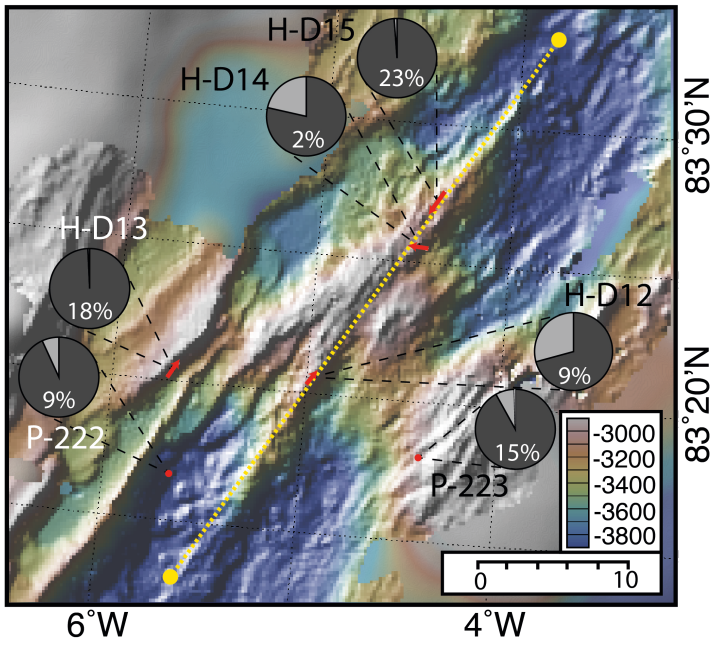

Fig. A3.1: Bathymetric map of 5°W Axial Volcanic Ridge. Pie charts represent the average proportions of plagioclase (dark grey), olivine (middle grey) and clinopyroxene (light grey) present in samples analysed from the dredges. Orange circles indicate the presence of spinel. White numbers show the total crystal content (this is an average if >1 sample was analysed from each dredge). Red dots indicate the on-bottom depth of each dredge; red arrows indicate the directions of dredges from on- to off-bottom depths. The yellow dashed line indicates the bathymetric profile line used for Fig. A3.2a. The bathymetric map was made using GeoMapApp and uses a combination of bathymetric data from the Global Multi-Resolution Topography (Ryan et al. 2009) and data from the AMORE 2001 expedition (e.g., Michael et al. 2003).

8.3.1.1 Local-scale geochemical and textural variation

Moving towards the flank from H-D14 to H-D15 there is an increase in total crystal content from ~2 to 23% (Fig. A3.2b) and corresponding increase in Mg# and temperature variability and decrease in both median $Na_{8.0}$ and K/Ti (Fig. A3.2c-f). The increase in Mg# and temperature variability from H-D14 to H-D15 coincides with an increase in both plagioclase core anorthite content (Fig A3.2g) and the proportion of plagioclase exhibiting external resorption (Fig. A3.2l). Whilst H-D12 was dredged from a similar depth and distance from the centre of the magmatic system to H-D14 (Fig. A3.2a), the only similarity between these two dredges is their median $Na_{8.0}$. Instead H-D12 is characterised by higher crystal content, glass Mg# and temperature and lower K/Ti. Additionally, plagioclase anorthite contents in H-D12 are more similar to H-D15 located towards the flank (Fig. A3.2g) and olivine is more primitive than that at H-D14.

Comparison of samples that are approximately orthogonal to one another (H-D13 and P-223 off-axis (i.e., valley wall) vs. H-D12 on-axis) reveals several differences between off- and on-axis samples. Firstly, off-axis samples have higher total crystal contents (14-18%, Fig. A3.2b) compared to H-D12 (9%). Secondly, whilst glass from P-223 has $Na_{8.0}$ and K/Ti values that fall within the range of samples from H-D12, median glass Mg# and temperature are higher in this valley wall sample. Thirdly, off-axis plagioclase core anorthite compositions cover the same range as plagioclase in on-axis samples (Fig. A3.2g) but olivine forsterite contents are higher (Fig. A3.2h). Finally, plagioclase in valley wall samples has lower zoning complexity values (Fig. A3.2k) and more evidence of internal resorption (Fig. A3.2l) followed by reverse zoning (Fig. A3.2m) than plagioclase in on-axis samples.

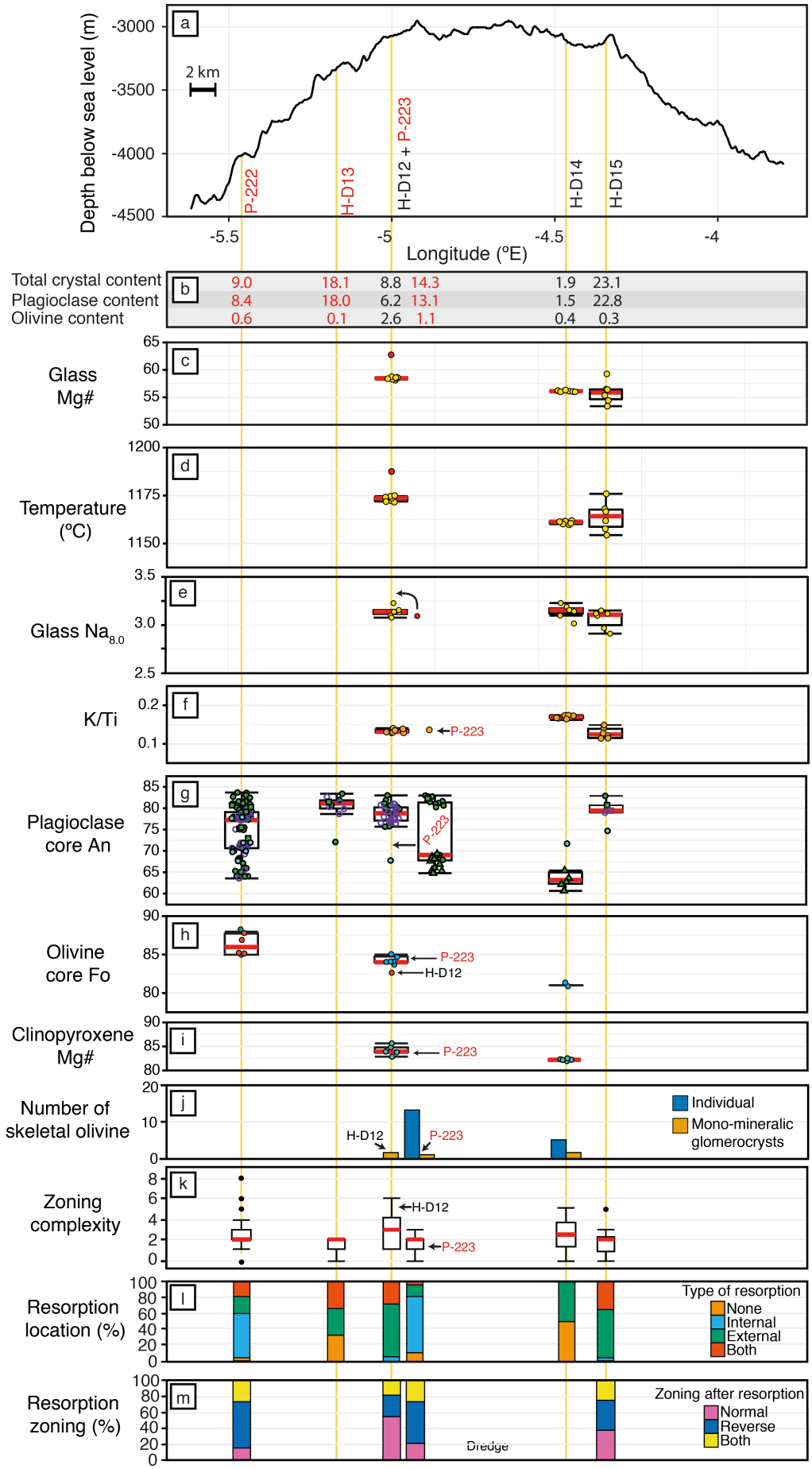
a
Depth below sea level (m)
-3000
-3500
-4000
-4500
2 km
P-222
H-D13
H-D12 + P-223
H-D14
H-D15
-5.5
-5
-4.5
-4
Longitude (ºE)
b
Total crystal content
Plagioclase content
Olivine content
9.0 18.1 8.8 14.3 1.9 23.1
8.4 18.0 6.2 13.1 1.5 22.8
0.6 0.1 2.6 1.1 0.4 0.3
c
Glass Mg#
d
Temperature (ºC)
e
Glass Na8.0
f
K/Ti
P-223
g
Plagioclase core An
P-223
h
Olivine core Fo
P-223
H-D12
i
Clinopyroxene Mg#
P-223
j
Number of skeletal olivine
H-D12
P-223
Individual
Mono-mineralic glomerocrysts
k
Zoning complexity
H-D12
P-223
l
Resorption location (%)
Type of resorption
None
Internal
External
Both
m
Resorption zoning (%)
Dredge
Zoning after resorption
Normal
Reverse
Both

←**Fig. A3.2:** Local-scale variation at 5°W Axial Volcanic Ridge. **a** Bathymetric profile of 5°W Axial Volcanic Ridge; on-axis and valley wall samples are shown in black and red respectively. **b** Variations in average total crystal, olivine and plagioclase content. Glass geochemistry: Mg# (**c**); temperature (**d**)**;** $Na_{8.0}$ (**e**); and K/Ti (**f**). Mineral chemistry: plagioclase core anorthite (**g**); olivine core forsterite (**h**); and clinopyroxene Mg# (**i**)**. j** Absolute number of both individual skeletal olivine and skeletal olivine in poly-mineralic glomerocrysts. Plagioclase textures: zoning complexity (**k**); resorption location (**l**); and type of zoning following resorption events (**m**)**.** Yellow and red points in **c-f** indicate samples from on-axis and valley wall locations respectively. Symbols in **g-i** are the same as in Figure 7.12.

8.3.2 3°E Seamounts (Fig. A3.3)

This magmatic system straddles a bathymetric high situated at ~84°30'N and is adjacent to the left-stepping non-transform fault offset that marks the transition between the WVZ and SMZ (Fig. A3.3). To the north of the bathymetric high samples (P-234) have been dredged from a ~1 km round seamount that swells from 4095-4025 mbsl. To the south, samples (H-D27 and H-D26) have been dredge from a flat-topped seamount and from a location with no obvious volcanic morphology respectively. Here, dredge H-D27 is treated as the magmatic centre with H-D26 and P-234 located at the flanks of the system.

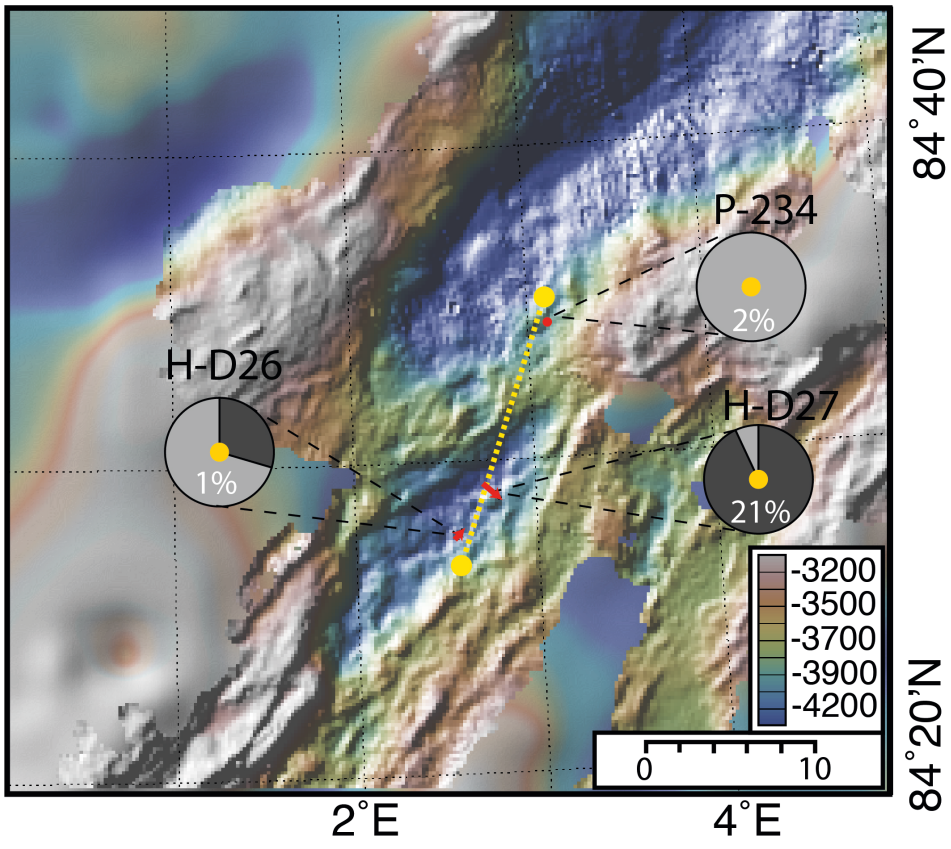

Fig. A3.3: Bathymetric profile of 3°E Seamounts. Pie charts and all symbols shown are the same as in Fig. A3.1. Yellow dashed line corresponds to the bathymetric profile line in Fig. A3.4**.**

8.3.2.1 Local-scale geochemical and textural variation (Fig. A3.4)

Multiple parameters, including crystal content, glass geochemistry and mineral geochemistry and textures change systematically away from the magmatic centre at H-D27 (Fig. A3.4). Moving away from H-D27, crystal contents decreases form ~21% to >~2% at the flank (Fig. A3.4b). Compared to H-D27 which is plagioclase-rich, these flank locations contain predominantly olivine; the median olivine core forsterite contents is moderately lower at the flanks than the centre (Fig. A3.4g). Similarly, median glass Mg# and temperature decrease towards the flanks (Fig. A3.4c,d). Whilst median glass $Na_{8.0}$ decreases from H-D27 to H-D26 and becomes more variable, there is no significant change from H-D27 to P-234 (Fig. A3.4e). Glasses from each of the locations show similar K/Ti ratios (Fig. A3.4l). Finally, plagioclase from H-D27 are texturally more complex than those from H-D26. This is evident from both the higher median zoning complexity and greater range (Fig. A3.4i), and the greater variety of resorption location (Fig. A3.4j) and type of zoning after resorption (Fig. A3.4k).

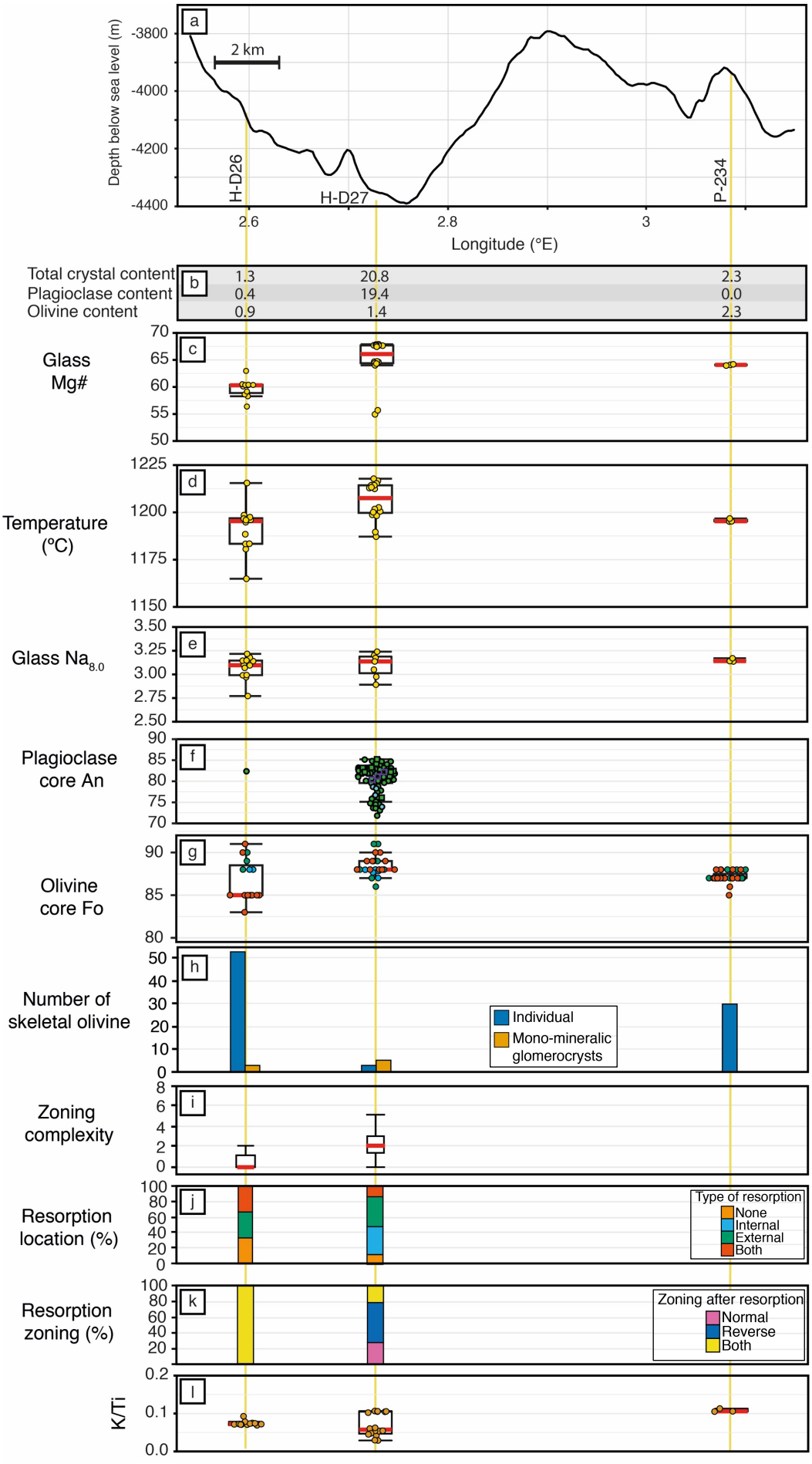
a
2 km
Depth below sea level (m)
-3800
-4000
-4200
-4400
H-D26
H-D27
P-234
2.6
2.8
3
Longitude (°E)
b
Total crystal content
Plagioclase content
Olivine content
1.3
0.4
0.9
20.8
19.4
1.4
2.3
0.0
2.3
c
Glass Mg#
70
65
60
55
50
d
Temperature (°C)
1225
1200
1175
1150
e
Glass Na8.0
3.50
3.25
3.00
2.75
2.50
f
Plagioclase core An
90
85
80
75
70
g
Olivine core Fo
90
85
80
h
Number of skeletal olivine
50
40
30
20
10
0
Individual
Mono-mineralic glomerocrysts
i
Zoning complexity
8
6
4
2
0
j
Resorption location (%)
100
80
60
40
20
0
Type of resorption
None
Internal
External
Both
k
Resorption zoning (%)
100
80
60
40
20
Zoning after resorption
Normal
Reverse
Both
l
K/Ti
0.2
0.1
0.0

←**Fig. A3.4:** Local-scale variation at 3°E Seamounts. **a** Bathymetric profile of 3°E Seamounts. **b** Variations in average total crystal, olivine and plagioclase content. Glass geochemistry: Mg# (**c**); temperature (**d**)**;** and $Na_{8.0}$ (**e**). Mineral chemistry: plagioclase core anorthite (**f**); olivine core forsterite (**g**). **h** Absolute number of both individual skeletal olivine and skeletal olivine in poly-mineralic glomerocrysts. Plagioclase textures: zoning complexity (**i**); resorption location (**j**); and type of zoning following resorption events (**k**)**.** Glass K/Ti Ratios in **l**.

8.3.3 12°40'E Axial Volcanic Ridge (Fig. A3.5)

From 3°E to 12°40'E, the axial valley is not characterised by volcanic topography (Michael et al. 2003). This location, an AVR, marks the first volcanic edifice within the SMZ. Its tapering morphology is similar to those AVRs located in the WVZ; however it is shorter, extending 22 km along axis. This AVR is also deeper, the ridge swelling from 4821 to 3952 mbsl at its shallowest point. H-D36 samples a location close to the centre of the AVR, whilst H-D38 is located towards the flank of the system.

8.3.3.1 Local-scale geochemical and textural variation (Fig. A3.6)

Multiple geochemical parameters show trends moving away from the AVR centre (H-D36) towards the system flank (H-D38) (Fig. A3.6). One exception to this is crystal content which shows no significant change; both locations are characterised by low crystal content (<2%) and contain predominantly olivine (Fig. A3.6b). In contrast, median glass Mg# and temperature (Fig. A3.6c,d), plagioclase anorthite content and olivine forsterite content (Fig. A3.6f,g) all increase from H-D36 to H-D38. In addition, plagioclase anorthite content and olivine forsterite content become more variable at H-D38 (fig. A3.6f,g). Texturally, there are trends of both increasing number of skeletal olivine (Fig. A3.6h) and plagioclase zoning complexity median and range from H-D36 to H-D38 (Fig. A3.6i); the resorption record also becomes more complex (Fig. A3.6j).

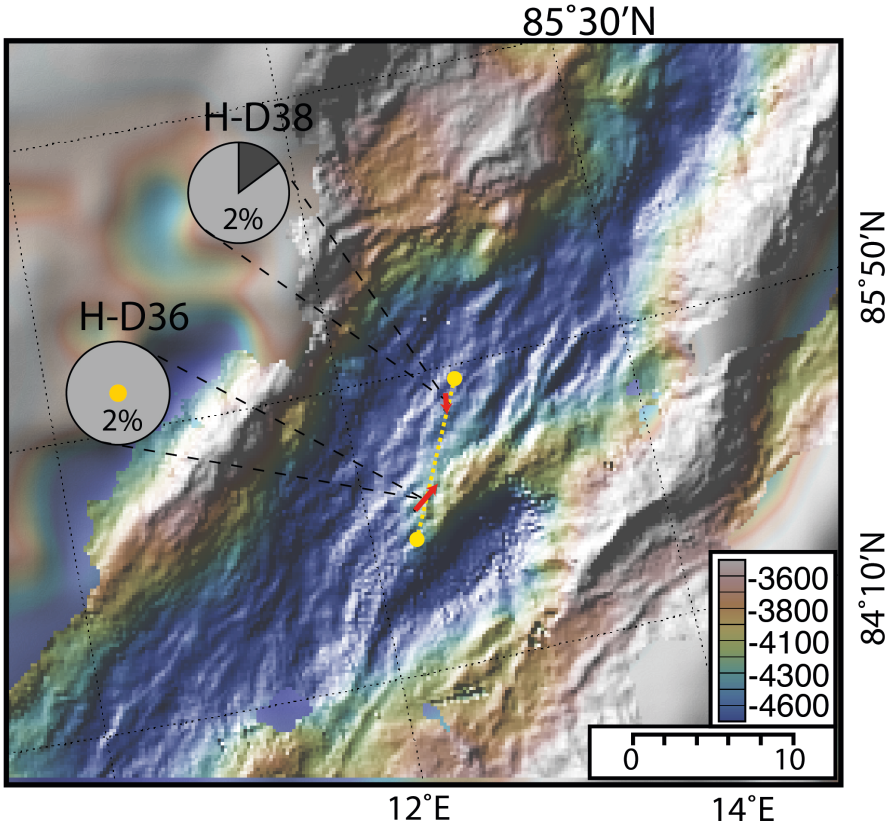

Fig. A3.5: Bathymetric profile of 12°40E W Axial Volcanic Ridge. Pie charts and all symbols shown are the same as in Fig. A3.1. Yellow dashed line corresponds to the bathymetric profile line in Fig. A3.6).

→**Fig. A3.6:** Local-scale variation at 12°40'E Axial Volcanic Ridge. **a** Bathymetric profile of 12°40'E Axial Volcanic Ridge. **b** Variations in average total crystal, olivine and plagioclase content. Glass geochemistry: Mg# (**c**); temperature (**d**); and $Na_{8.0}$ (**e**). Mineral chemistry: plagioclase core anorthite (**f**); olivine core forsterite (**g**). **h** Absolute number of both individual skeletal olivine and skeletal olivine in poly-mineralic glomerocrysts. Plagioclase textures: zoning complexity (**i**); resorption location (**j**); and type of zoning following resorption events (**k**). Glass K/Ti Ratios in **l**.

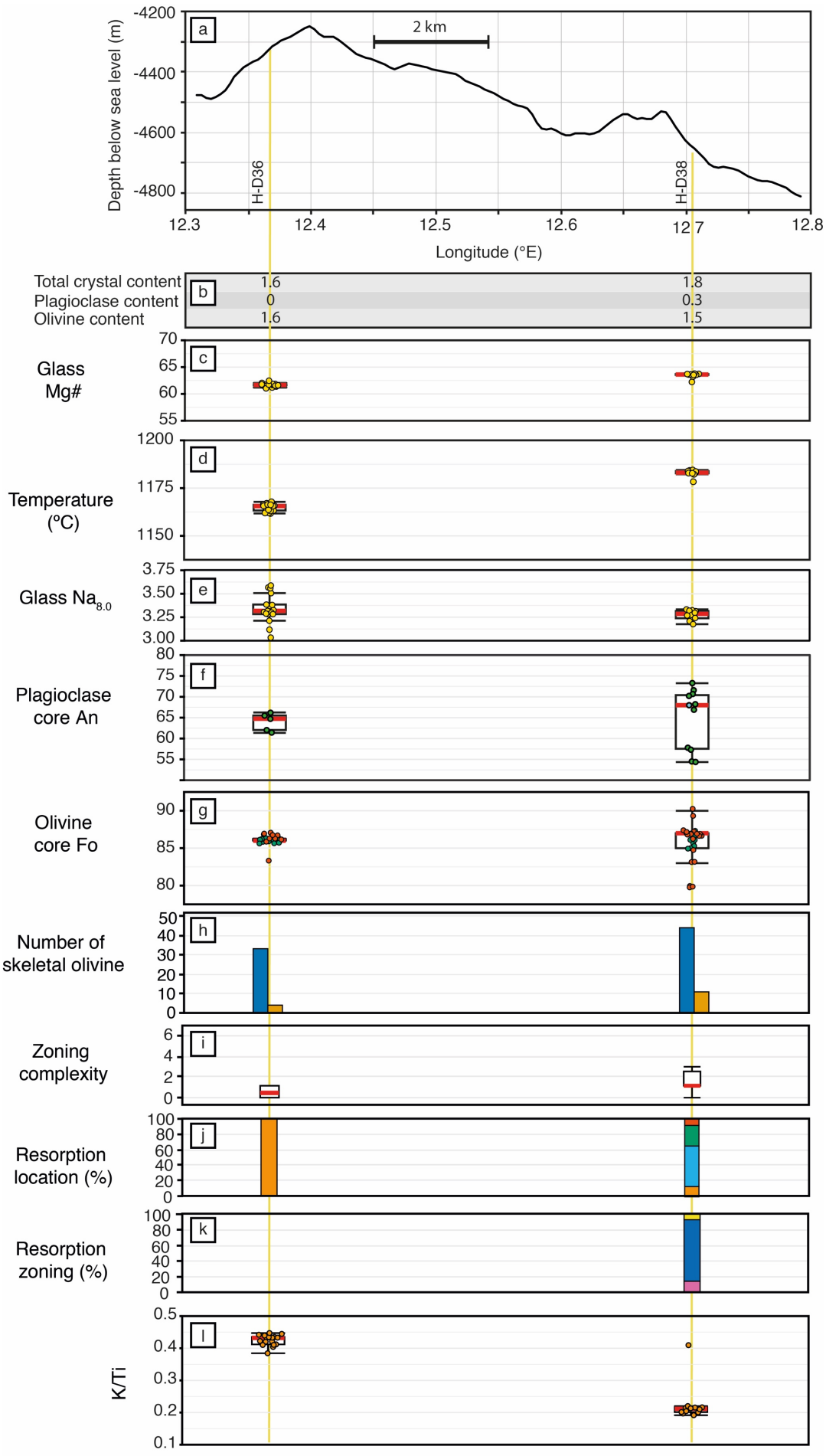
a
2 km
Depth below sea level (m)
-4200
-4400
-4600
-4800
H-D36
H-D38
12.3
12.4
12.5
12.6
12.7
12.8
Longitude (°E)
b
Total crystal content
Plagioclase content
Olivine content
1.6
0
1.6
1.8
0.3
1.5
c
Glass Mg#
70
65
60
55
d
Temperature (°C)
1200
1175
1150
e
Glass Na8.0
3.75
3.50
3.25
3.00
f
Plagioclase core An
80
75
70
65
60
55
g
Olivine core Fo
90
85
80
h
Number of skeletal olivine
50
40
30
20
10
0
i
Zoning complexity
6
4
2
0
j
Resorption location (%)
100
80
60
40
20
0
k
Resorption zoning (%)
100
80
60
40
20
0
l
K/Ti
0.5
0.4
0.3
0.2
0.1

8.3.4 31°E Basement Ridge (Fig. A3.6)

This basement ridge runs perpendicular to the ridge axis and can be traced 57 km southeast and 112 km northwest off axis. This location marks the only occurrence of an axial volcanic ridge within the axial valley outside of the WVZ (Cochran et al. 2003). Two samples (H-D48 and H-D49) have been dredged from the axial volcanic ridge, whilst two other dredges have been collected from the rift valley walls (H-D95 and P-310). Excluding the two valley wall dredges, the centre and flank of the magmatic system are approximated by H-D48 and H-D49 respectively.

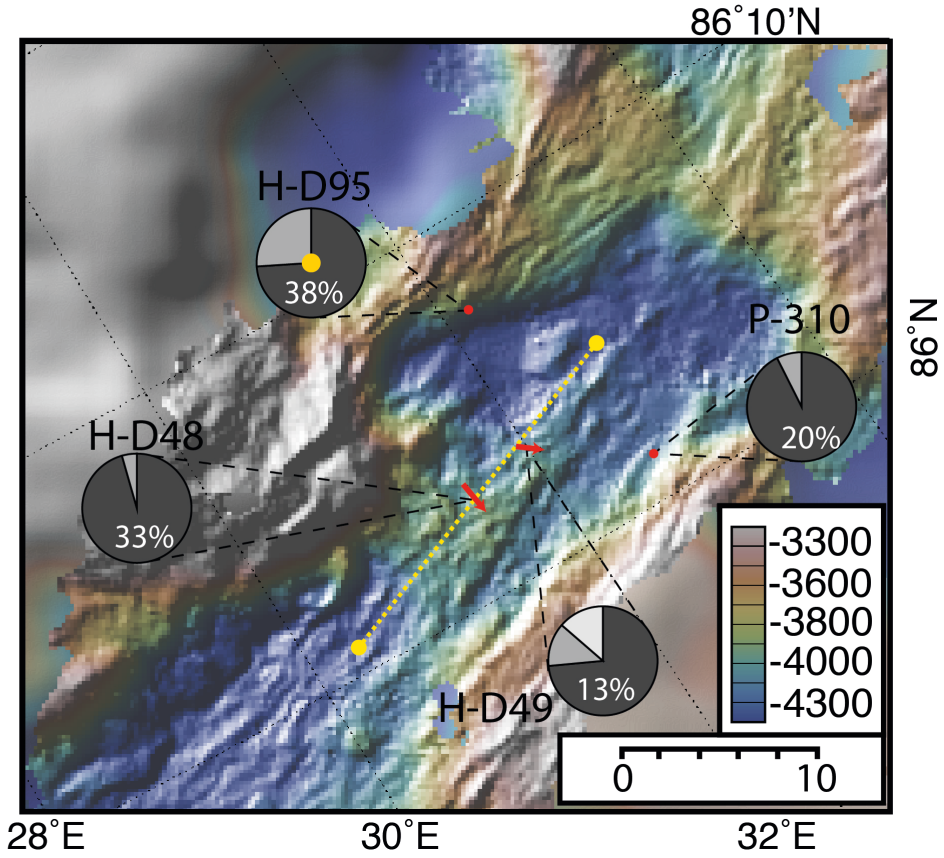

Fig. A3.7: Bathymetric profile of 31°E Basement Ridge. Pie charts and all symbols shown are the same as in Fig. A3.1. Yellow dashed line corresponds to the bathymetric profile line in Fig. A3.8).

8.3.4.1 Local-scale geochemical and textural variation (Fig. A3.8)

Moving toward the flank of the system there is a reduction in total crystal content from ~33% at H-D48 to 13% at H-D49; plagioclase makes up ≥73% of the crystal cargo at each of these locations (Fig. A3.8b). Glass geochemistry show similar trends of decreasing median Mg#, temperature and $Na_{8.0}$ towards the flank of the system; both Mg# and temperature become more variable, whilst $Na_{8.0}$ variability reduces (Fig. A3.8c-e). Mineral geochemistry correlates with changes in glass geochemistry, with both

median plagioclase anorthite content and olivine forsterite content becoming lower at H-D49 (Fig. A3.8f,g). The number of skeletal olivine increases from H-D48 to H-D49 (Fig. A3.8i). Texturally, plagioclase from H-D48 are more complex than those in H-D49; plagioclase have a greater range in zoning complexity values (Fig. A3.8j) and more varied resorption characteristics in terms of both the types of resorption and adjacent zoning (Fig. A3.8k,l). The flank is characterised by more internal resorption events and more reverse zoning after resorption than plagioclase from H-D48.

Dredges from the valley walls (P-310 and H-D95) show some geochemical and textural similarities to on-axis samples. First, both median plagioclase core anorthite compositions and the range are similar to H-D48 at the magmatic centre. Secondly, plagioclase from these two locations exhibit both similar ranges in zoning complexity and types of resorption and zoning after these resorption events. Despite these similarities, glass and olivine compositions are markedly different; glass compositions exhibit higher median glass Mg#, temperature and $Na_{8.0}$ values (H-D95) (Fig. A3.8c-e) and olivine extend to more primitive compositions than typical of the on-axis dredges (Fig. A3.8g).

→**Fig. A3.8:** Local-scale variation at 31°E Basement Ridge. **a** Bathymetric profile of 31°E Basement Ridge. **b** Variations in average total crystal, olivine and plagioclase content. Glass geochemistry: Mg# (**c**); temperature (**d**)**;** and $Na_{8.0}$ (**e**). Mineral chemistry: plagioclase core anorthite (**f**); olivine core forsterite (**g**); clinopyroxene Mg# (**h**). **i** Absolute number of both individual skeletal olivine and skeletal olivine in poly-mineralic glomerocrysts. Plagioclase textures: zoning complexity (**j**); resorption location (**k**); and type of zoning following resorption events (**l**)**.** Glass K/Ti Ratios in **m**.

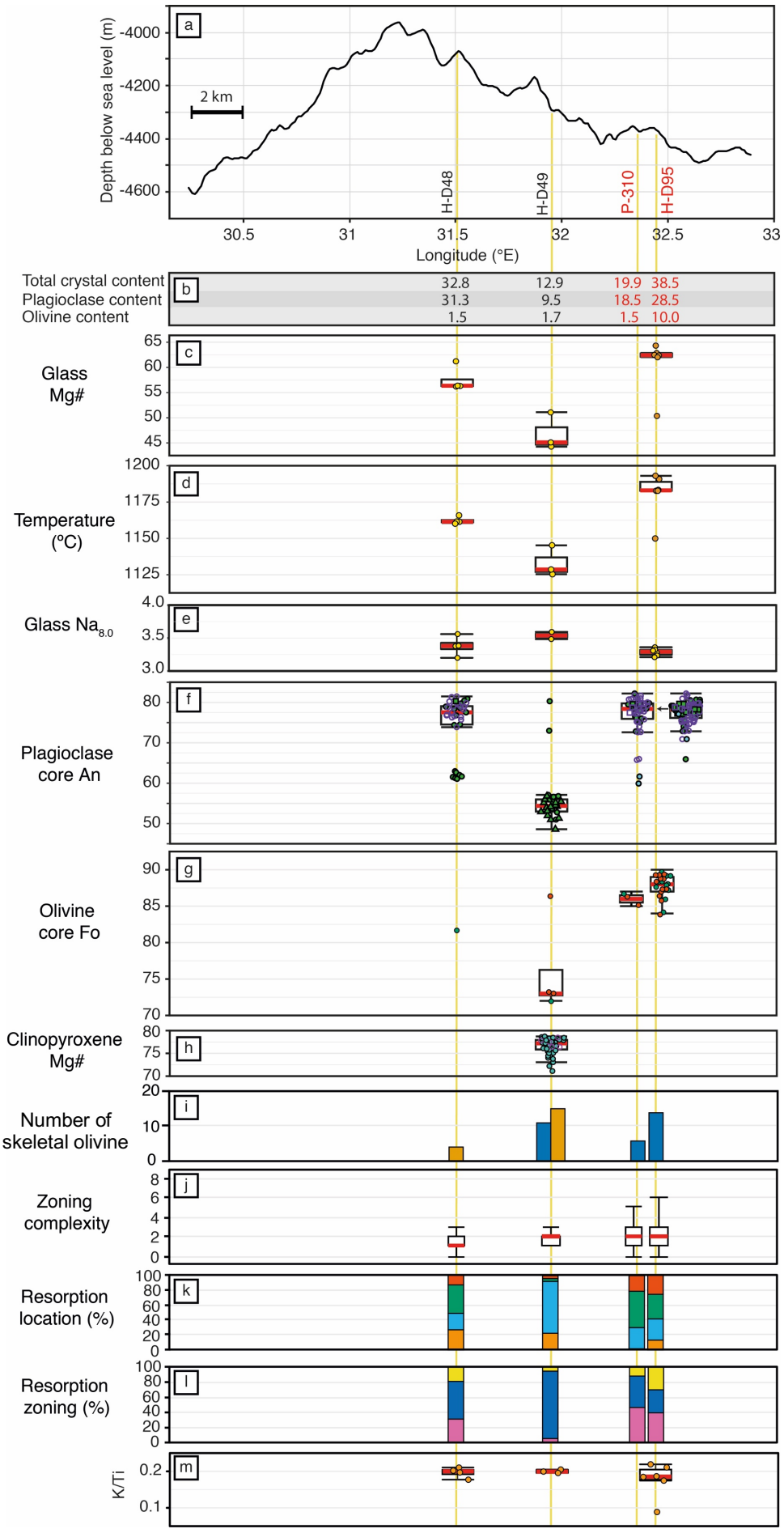
a
Depth below sea level (m)
-4000
-4200
-4400
-4600
2 km
H-D48
H-D49
P-310
H-D95
30.5
31
31.5
32
32.5
33
Longitude (°E)
Total crystal content
Plagioclase content
Olivine content
b
32.8
31.3
1.5
12.9
9.5
1.7
19.9
18.5
1.5
38.5
28.5
10.0
Glass Mg#
c
Temperature (°C)
d
Glass Na8.0
e
Plagioclase core An
f
Olivine core Fo
g
Clinopyroxene Mg#
h
Number of skeletal olivine
i
Zoning complexity
j
Resorption location (%)
k
Resorption zoning (%)
l
K/Ti
m

8.3.5 48°E Deep Seafloor (Fig. A3.9)

As the name suggests, seven dredges have been collected from a region of deep seafloor that swells from 5095 to 4853 mbsl. The region is characterised by a broad valley floor bound by normal faults. Seamounts are common within the region and are located at the edges of the valley floor and on fault scarps; they range in height from ~106 to ~265 m. The samples have been dredged from the edges of the valley floor, valley wall fault scarps and seamounts (P-297 and likely H-D77 and P-270). Dredges cover 32 km along axis. Local-scale variations, moving away from the seamount sampled by dredge P-297, are presented below.

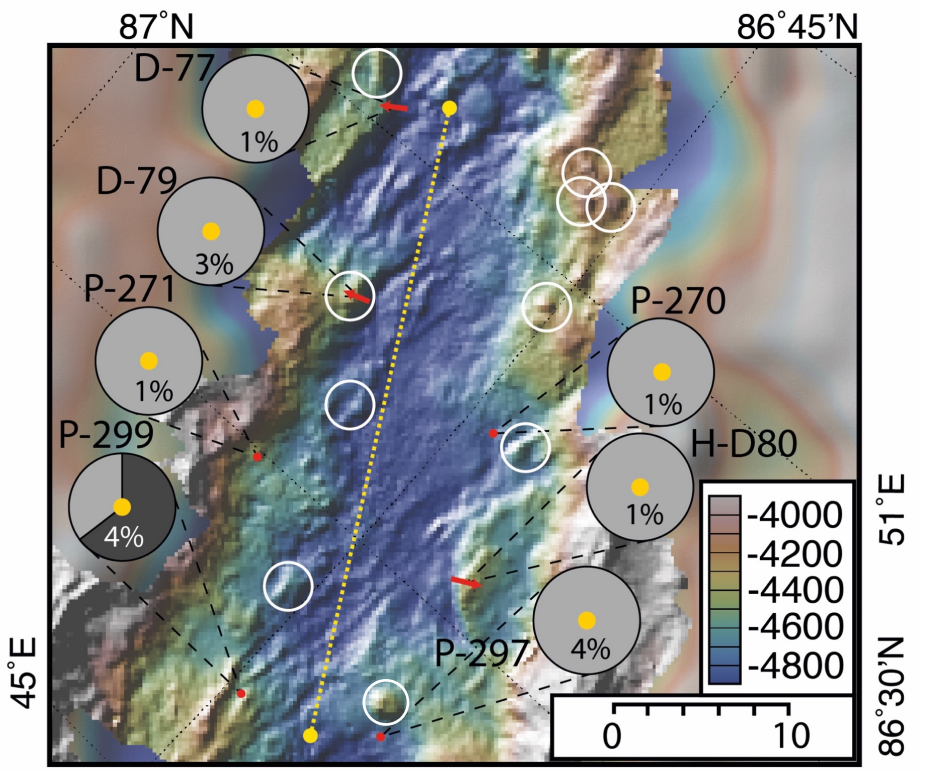

Fig. A3.9: Bathymetric profile of 48°E Deep Seafloor. Pie charts and all symbols shown are the same as in Fig. 8.1. Yellow dashed line corresponds to the bathymetric profile line in Fig. A3.10**.** White circles indicate the locations of seamounts identified by Chochran (2008).

8.3.5.1 Local-scale geochemical and textural variation (Fig. A3.10)

Other than dredge H-D79, crystal content generally decreases from ~4% at P-299 and P-297 to between 0.5-1.4% in samples to the east; all samples east of P-299 and P-297 contain olivine only (Fig. A3.10b). Glass Mg# are lowest at P-299 and then remain relatively stable from P-297 to H-D77 (Fig. A3.10c). Glass temperatures are relatively constant along much of the ridge, other than at P-299 where temperatures are higher (Fig. A3.10d). Glass K/Ti ratios are variables along the ridge; K/Ti ratios are lowest and

highest at P-297 and P-270 respectively (Fig. A3.l). Median olivine core forsterite contents mirror trends seen in glass Mg# with olivine becoming generally more primitive towards the east away from P-297 and P-299 (Fig. A3.10g). Whilst few data points exist, glass $Na_{8.0}$ decreases toward the east (Fig. A3.10e).

Texturally there are few local-scale variations. Whilst the number of skeletal olivine does not change systematically away from P-299 and P-297, only these two locations contain poly-mineralic glomerocrysts (Fig. A3.10h). Plagioclase in these two locations show 81pa decrease in the median and range of zoning complexity values (Fig. A3.10i). A reduction in complexity is similarly indicated by an increase in the proportion of plagioclase exhibiting no resorption (Fig. A3.10j); despite this reverse zoning becomes more common (Fig. A3.10k).

→**Fig. A3.10:** Local-scale variation at 48°E Deep Seafloor. **a** Bathymetric profile of 48°E Deep Seafloor. **b** Variations in average total crystal, olivine and plagioclase content. Glass geochemistry: Mg# (**c**); temperature (**d**)**;** and $Na_{8.0}$ (**e**). Mineral chemistry: plagioclase core anorthite (**f**); olivine core forsterite (**g**). **h** Absolute number of both individual skeletal olivine and skeletal olivine in poly-mineralic glomerocrysts. Plagioclase textures: zoning complexity (**i**); resorption location (**j**); and type of zoning following resorption events (**k**)**.** Glass K/Ti Ratios in **l**.

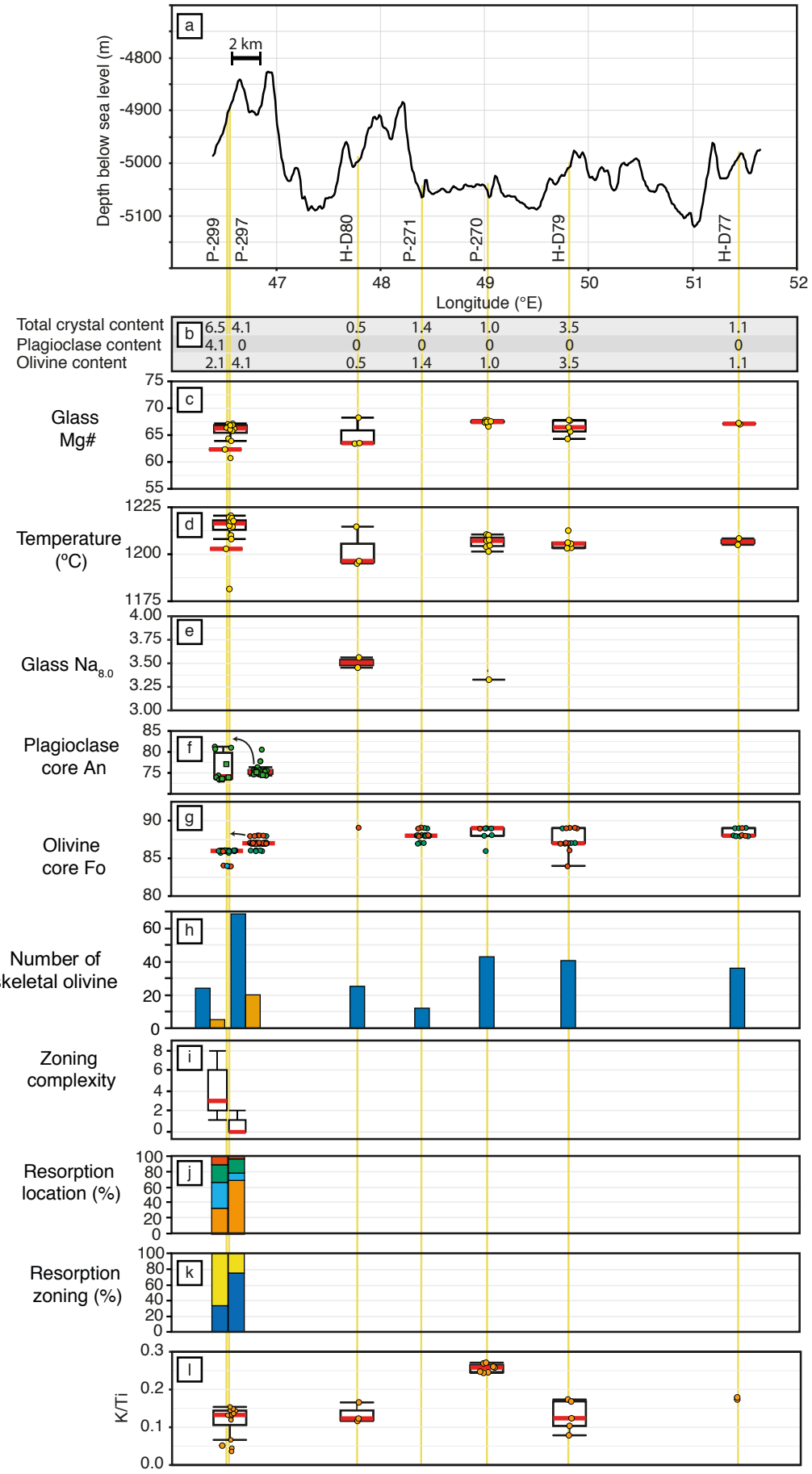
a
2 km
Depth below sea level (m)
-4800
-4900
-5000
-5100
P-299
P-297
H-D80
P-271
P-270
H-D79
H-D77
47
48
49
50
51
52
Longitude (°E)
Total crystal content
Plagioclase content
Olivine content
b
6.5 4.1 0.5 1.4 1.0 3.5 1.1
4.1 0 0 0 0 0 0
2.1 4.1 0.5 1.4 1.0 3.5 1.1
Glass Mg#
c
Temperature (°C)
d
Glass Na8.0
e
Plagioclase core An
f
Olivine core Fo
g
Number of skeletal olivine
h
Zoning complexity
i
Resorption location (%)
j
Resorption zoning (%)
k
K/Ti
l